Titre: Title:	Electric and Magnetic One- And Two-Dimensionally Tuned Parameter-Agile Substrate Integrated Waveguide Components and Devices
Auteur: Author:	Sulav Adhikary
Date:	2014
Type:	Mémoire ou thèse / Dissertation or Thesis
Référence: Citation:	Adhikary, S. (2014). Electric and Magnetic One- And Two-Dimensionally Tuned Parameter-Agile Substrate Integrated Waveguide Components and Devices [Ph.D. thesis, École Polytechnique de Montréal]. PolyPublie. https://publications.polymtl.ca/1374/

UNIVERSITÉ DE MONTRÉAL

ELECTRIC AND MAGNETIC ONE- AND TWO-DIMENSIONALLY TUNED PARAMETER-AGILE SUBSTRATE INTEGRATED WAVEGUIDE COMPONENTS AND DEVICES

SULAV ADHIKARI

DÉPARTEMENT DE GÉNIE ÉLECTRIQUE

ÉCOLE POLYTECHNIQUE DE MONTRÉAL

THÈSE PRÉSENTÉE EN VUE DE L'OBTENTION

DU DIPLÔME DE PHILOSOPHIAE DOCTOR

(GÉNIE ÉLECTRIQUE)

AVRIL 2014

UNIVERSITÉ DE MONTRÉAL

ÉCOLE POLYTECHNIQUE DE MONTRÉAL

Cette thèse intitulée:

ELECTRIC AND MAGNETIC ONE- AND TWO-DIMENSIONALLY TUNED PARAMETER-AGILE SUBSTRATE INTEGRATED WAVEGUIDE COMPONENTS AND DEVICES

présentée par : ADHIKARI Sulav

en vue de l'obtention du diplôme de : Philosophiæ Doctor

a été dûment acceptée par le jury d'examen constitué de :

M. AKYEL Cevdet, Ph.D., président

M. WU Ke, Ph.D., membre et directeur de recherche

M. GHIOTTO Anthony, Ph.D., membre et codirecteur de recherche

M. NERGUIZIAN Chahé, Ph.D., membre

M. KISHK Ahmed, Ph.D., membre

DEDICATION

To my parents

To my wife and my twins

ACKNOWLEDGEMENTS

It is my great pleasure to express my gratitude to all who have made this thesis possible.

First of all, I would like to thank my supervisor Professor Ke Wu for accepting me as a Ph.D. student at Poly-Grames Research Center. I would have never been able to write and complete my thesis, without his support and guidance. Throughout my Ph.D., he provided me with sound advices, encouragement, and lots of new ideas to work on. His door was always open, whenever I had any questions or doubts. Perhaps number of times I was taking a wrong way or making a wrong decision. In all these difficult times, he has shown me the right way, so that I could come back to the correct path. I am deeply grateful to his valuable advices and recommendations, when I was looking for industrial positions. I will always be missing Professor Wu and Poly-Grames Research Center.

I would also like to express my deep gratitude to my co-supervisor Associate Professor Anthony Ghiotto. I met Professor Ghiotto during the first year of my Ph.D. study at Poly-Grames Research Center. From the beginning he has been very supportive to me. He not only provided me with valuable ideas, but also supported me during the measurements in laboratories. His patience, despite my lots of questions and faults, is greatly appreciated. It was my great pleasure to do my thesis under his supervision.

I would like to express gratitude to Mr. Jules Gauthier for providing me lots of technical ideas. He has in fact built a set-up that could cut the ferrites into any shapes and dimensions precisely. Without his innovative ideas, my circuits would have never met the best performances. I would like to thank Mr. Traian Antonescu and Mr. Steve Dubé for fabricating my circuits precisely and in time. I would like to thank Mr. Maxime Thibault for his precise and accurate mountings of all microwave components and devices on the circuit boards. I would also like to take chance to thank Mr. Jean-Sebastien Décarie for all the IT related supports even during the weekends and holidays.

I am also thankful to Dr. Simon Hemour, who has been very interested and supportive to my works. He has provided me with number of interesting ideas and discussions that have helped me elevate the quality of my work.

I would like to thank my group members and former colleagues, Ajay-Babu Guntpalli, Nasser Ghassemi, Shabnam Ladan, Ali Doghri, Deng Ya, Lydia Chioukh, Louis-Philippe Carignan, Pascal Burasa, David Dousset, Yan Ding, Liang Han, Zhenyu Zhang, Fanfan He, Jawad Attari, Alvaro Diaz-Bolado, Shulabh Gupta, Yong-Ju Ban, Jiang Tao, Jaber Moghaddasi, Hoda Nematollahi, Leandro Miguel Rufail, Seyyid M. Dilek, Van-Hoang Nguyen, Zhebin Wang for all their supports and friendliness.

I would like to thank my parents and my parents-in-law for always being there during my toughest time. Without their love and support I would have never achieved my goals in my life.

I would like to thank my wife Astha for her love, encouragement and support. During the toughest times, she has been so strong and supportive. On number of occasions I even thought of discontinuing my Ph.D., during those hard times she stayed strong and kept me moving. Thank you for always being there.

Finally, I would like to thank my twin daughters Milie and Julie for showering our lives with joy and happiness. Thank you for giving a new meaning to my life.

RÉSUMÉ

Les composants micro-ondes et millimétriques accordables constituent des éléments importants rencontrés dans les systèmes de radiocommunications et radars. En effet, ils donnent la possibilité à ces derniers d'être adaptables et ajustables. Or, ces deux caractéristiques sont importantes puisqu'elles permettent aux systèmes de s'adapter à des changements de leurs spécifications sans avoir à changer leurs circuits. Il peut y avoir en effet plusieurs raisons qui amèneraient à procéder à des modifications de spécifications d'un système : des variations des conditions environnementales (liées à la température, l'humidité, ou encore aux vibrations), et des changements liés à des contraintes de nouveaux clients comme par exemple l'utilisation de nouvelles bandes de fréquence ou de canaux. Il serait vraiment peu efficace d'avoir à reconcevoir l'ensemble du système afin de satisfaire de nouvelles performances. Ainsi, il est important de concevoir le système de façon à ce qu'il puisse s'ajuster ou se corriger pour toutes modifications qui pourraient arriver. Par exemple, si la réponse fréquentielle d'un filtre passe-bas commence à glisser vers des fréquences plus basses avec une augmentation de la température, le système le mettant en œuvre pourrait ne plus être en mesure de recevoir ou transmettre de l'information dans cette bande de fréquence. Cependant, si le même filtre peut être ajusté en fréquence, il sera alors possible de le corriger et de le refaire fonctionner dans ses spécifications d'origine.

Dans la littérature, on trouve de nombreuses méthodes qui permettent de concevoir des éléments et composants ajustables aux fréquences micro-ondes. Les méthodes employées les plus populaires mettent en œuvre : des composants semi-conducteurs (tels que des diodes varicaps, des diodes PIN et des transistors), des microsystèmes électromécaniques (ou MEMS pour micro-electro-mechanical systems), des matériaux ferroélectriques et des matériaux ferromagnétiques. Dans certaines de ces conceptions, des combinaisons de ces différentes méthodes ont également été adoptées afin d'obtenir de meilleures performances.

Ce travail présente de nouveaux types de composants micro-ondes ajustables basés sur les Guides d'onde Intégrés au Substrat (GIS). La technologie GIS peut être considérée comme une forme planaire de la technologie guide d'onde conventionnelle, dont elle hérite de la plupart des propriétés. Par exemple, comme pour les guides d'onde conventionnels, les guides GIS sont faibles pertes et peuvent être mis en œuvre pour de fortes puissances. Bien que le GIS soit similaire au guide d'onde sur de nombreux aspects, il présente une taille et un coût plus réduit.

Les guides d'onde conventionnels sont habituellement réalisés à partir de tubes métalliques creux de section rectangulaire ou cylindrique. Ainsi pour une même fréquence, leurs tailles est bien plus grandes que les lignes planaires conventionnelles telles que les lignes micro-rubans ou coplanaires. Ainsi, même si les guides d'ondes rectangulaires offrent des performances remarquables, ils ne peuvent pas être directement utilisés pour la conception de circuits planaires compacts. Puisque la technologie GIS hérite de quasiment toutes les propriétés des guides d'ondes rectangulaires et qu'elle est aussi planaire par nature, elle est particulièrement adaptée pour la conception de circuits et systèmes planaires aux fréquences millimétriques et micro-ondes. Cependant les GIS sont fabriqués à partir de matériaux diélectriques, ainsi leur capacité de tenue en puissance et leurs performances en terme de pertes sont largement dépendantes du substrat.

Dans ce travail, un nouveau type de composants GIS micro-ondes ajustables basés sur les matériaux ferromagnétiques (ou ferrite) est présenté. La perméabilité de ces matériaux peut être modifiée avec l'application d'un champ magnétique extérieur. Or, la constante de propagation d'une onde électromagnétique est directement proportionnelle à la racine carrée de la permittivité et de la perméabilité. De ce fait, en utilisant de la ferrite, des éléments reconfigurables peuvent être conçus. Une autre caractéristique importante de la ferrite est qu'elle peut avoir un comportement non réciproque. Ce qui signifie que les signaux radiofréquences (RF) se propageant dans différentes directions à l'intérieur de la ferrite, peuvent voir des caractéristiques de propagation différentes. Cela est une propriété très intéressante qui peut être utilisée non seulement pour réaliser des éléments ajustables, mais aussi des éléments non réciproques. Ces éléments non réciproques incluent : les isolateurs, les gyrateurs, et les circulateurs. Dans la bibliographie, on peut s'apercevoir que la plupart des éléments non réciproques et ajustables utilisant de la ferrite sont conçus à partir de la technologie guide d'onde conventionnelle. En effet, les propriétés de faibles pertes et de fortes tenues en puissance rendent les guides d'onde conventionnels attractifs pour la conception d'éléments basés sur la ferrite. De plus, pour un guide d'onde opérant dans son mode dominant TE_{10}, l'intensité maximale du champ électrique se trouve dans la région centrale, alors que l'intensité maximale du champ magnétique se trouve le long des parois. Cette distribution du champ magnétique et du champ électrique permet de positionner la ferrite dans les régions ayant un fort champ magnétique sans avoir à perturber le champ électrique. Puisque la ferrite interagit fortement avec le champ magnétique, elle est placée

dans les régions ou le champ magnétique est le plus intense. Bien que les guides d'onde rectangulaires soient une technologie prometteuse pour la conception d'éléments magnétiquement ajustables ayant une forte tenue en puissance, ils ne peuvent être intégrés de façon planaire. Un des objectifs de cette thèse est de réaliser des éléments GIS magnétiquement ajustables et planaires par nature, tout en préservant les qualités offertes par les guides d'onde rectangulaires.

Dans ce travail, des éléments clefs magnétiquement ajustables, incluant des résonateurs, filtres passe-bande, oscillateurs, interrupteurs, décaleurs de phase, circulateurs, et amplificateurs de puissance, sont présentés. Il est également démontré qu'en utilisant seulement des ferrites, la plage d'ajustabilité des performances est limitée. Cependant, en combinant simultanément une ajustabilité électrique et magnétique, l'ajustabilité totale peut-être significativement améliorée, et également, l'élément peut avoir des performances améliorées. C'est ainsi que dans ce travail de recherche, un nouveau concept d'accordabilité en deux dimensions est introduit. Ce concept est utilisé afin de réaliser des éléments complètement adaptables. Une cavité, un filtre passe-bas, et une antenne, tous basés sur ce concept, sont présentés.

ABSTRACT

Microwave and millimeter wave tunable devices, circuits and components are one of the most important parts in any communication and radar system design. The tunable devices, circuits and components which are integrated into a system enable it to become more adaptive and flexible in nature. The adaptive and flexible system can be reconfigured to follow the changes that occur into its variable or adjustable specifications without changing its hardware design. There may be several reasons that could lead to the change in the system specifications: changes in the environmental conditions (related to temperature, humidity, and vibration), and changes due to new customer requirements, for example, the inclusion of a new operating frequency band or channel. It would be very impractical to re-design all the system components just to meet the new performance criteria. Hence, it is important to design the system in a way that it can adjust or correct itself for any changes that might occur. For example, if a band-pass filter frequency response begins to drift towards a lower frequency value with the increase in temperature, it might not be able to receive or transmit valuable information at this frequency band. However, if the same band pass filter can be made frequency tunable, it will be able to get self-corrected and bring its frequency response back to the original value.

In literature, there are many methods that are used in realizing tunable microwave circuits and components. The most popular methods in the realization of tunable components make use of semiconductor elements and devices (including varactor diodes, PIN diodes, and transistors), micro-electro-mechanical systems (MEMS) switches and capacitors, ferroelectric materials, and ferromagnetic materials. In some of the designs to achieve a better tuning performance, even combinations of two different tuning methods have also been adopted.

In this work, new types of microwave tunable devices, circuits and components based on substrate integrated waveguide (SIW) are presented. SIW technology can be considered as a synthesized planar form of rectangular waveguide, and inherits almost all of its properties. For example, similar to rectangular waveguide, SIW is lower in loss, it can be used for higher power applications compared to conventional planar counterparts, and it is lower in cost. Although SIW is similar to rectangular waveguide in many aspects, it holds a significant difference in terms of size. Rectangular waveguide is usually made of hollow metallic tube (rectangular or circular), therefore at a given frequency, its size is much larger than the conventional planar transmission

lines (microstrip or coplanar). Thus, even though rectangular waveguide being capable of delivering outstanding RF performance cannot be directly used in realizing compact planar circuits. Since SIW technology inherits almost all the properties of rectangular waveguide and also it is planar in nature, it is an outstanding candidate in realizing microwave and millimeter wave planar integrated circuits. However, SIW is usually fabricated on dielectric substrate, thus its power handling capabilities and its performance in terms of losses are largely dependent upon substrate material used and structure topology.

In this work, SIW-based microwave tunable devices, circuits and components using ferromagnetic materials are presented. Ferrites or ferromagnetic material permeability value can be controlled through the application of an external DC magnetic bias. Since the propagation constant of an RF signal is directly proportional to the square root of the material permittivity and permeability. Therefore, any change in the permeability component also changes the propagation constant of the electromagnetic wave. Thus, using ferrite materials allow the realization of very interesting reconfigurable devices. Another important characteristic of ferrite materials is that they display non-reciprocal behaviour. This means that RF signals, propagating in two different directions in the ferrite material can have different characteristic behaviours. This is a very interesting feature, which can be used not only to realize tunable microwave devices, but also devices that are non-reciprocal in nature. Some of the ferrite-based non-reciprocal devices include isolator, gyrator, and circulator. In literature, it can be observed that most of the non-reciprocal and tunable devices using ferrite materials are designed based on rectangular waveguide technology. The low loss and high power handling property of rectangular waveguide make them an attractive candidate in realizing ferrite based tunable devices. Moreover, for a rectangular waveguide operating with dominant TE_{10} mode, the maximum magnitude of its electric field occurs at the central region, whereas the maximum magnitude of its magnetic field occurs along the sidewalls. This distribution of electric and magnetic fields, allows placing the ferrite materials in the regions of the highest magnetic field without perturbing the electric field distribution. Since the ferrite materials interact strongly with magnetic field, they are usually placed in the regions where the magnetic field concentration is highest. Although rectangular waveguide is a very promising technology in realizing high power magnetically tunable devices, they cannot be readily integrated in a planar form. Therefore, one of the purposes of this thesis is

to realize SIW based magnetically tunable ferrite loaded microwave devices that are planar in nature and at the same time retain all the good qualities offered by the rectangular waveguide.

In this work, key microwave magnetically tunable devices, circuits and components including resonator, band pass filter, oscillator, switch, phase shifter, circulator, and power amplifier are presented. It is also demonstrated that using only ferrite materials, the device total tuning range and performance are limited. However, by combining an innovative simultaneous electric tuning with the magnetic tuning, the total tuning range can be significantly extended, and also the circuit performance can be improved. Therefore, in this work, a new concept of two-dimensional tuning (simultaneous electric and magnetic tuning) is also introduced and demonstrated. This concept is then used to realize fully-adaptable and reconfigurable band pass filter, resonator and antenna. Special features of the proposed two-dimensional parameter tuning are revealed and discussed.

TABLE OF CONTENTS

LIST OF TABLES

LIST OF FIGURES

LIST OF ACRONYMS AND ABBREVIATIONS

1-D	One-Dimensional
2-D	Two-Dimensional
A/D	Analog to Digital
AC	Alternating Current
ADS	Advanced Design System (Agilent)
AI	Active Inductor
BST	Barium-Strontium-Titanate
BW	Bandwidth
CBCPW	Conductor Backed Coplanar Waveguide
CPW	Coplanar Waveguide
DC	Direct Current
E-field	Electric-Field
ESD	Electro Static Discharge
FET	Field Effect Transistor
FLSIW	Ferrite Loaded Substrate Integrated Waveguide
FM	Frequency-Modulated
FMR	Ferromagnetic Resonance
GaAs	Gallium Arsenide
H-field	Magnetic Field
HFSS	High Frequency Structure Simulator® (ANSYS)
HMSIW	Half Mode Substrate Integrated Waveguide
IDCs	Inter-Digital Capacitors
LNA	Low Noise Amplifier

LPE	Liquid Phase Epitaxy
LPF	Low Pass Filter
MEMS	Micro-Electro-Mechanical Systems
MESFET	Metal Semiconductor Field Effect Transistor
MIM	Metal-Insulator-Metal
Ni	Nickel
PA	Power Amplifier
PCB	Printed Circuit Board
PIN	Positive Intrinsic Negative
PNA	General Purpose Network Analyzer
RF	Radio-Frequency
RX	Receiver
SIW	Substrate Integrated Waveguide
SM	Surface Mount
SOLT	Short Open Load Thru
SPST	Single Pole Single Throw
SSIW	Slotted Substrate Integrated Waveguide
TE	Transverse Electric
TEM	Transverse Electromagnetic
TM	Transverse Magnetic
TRL	Thru- Reflect-Line
TX	Transmitter
UHF	Ultra High Frequency
UWB	Ultra Wide Band

VCO	Voltage Controlled Oscillators
VNA	Vector Network Analyser
WLAN	Wireless local area network
X-band	Standard waveguide band from 7 GHz to 11.2 GHz
YIG	Yttrium Iron Garnet

INTRODUCTION

Since the past decades, there has been a significant development of electronically reconfigurable or tunable circuits, devices, and components in the field of radio frequency (RF) and microwave wireless systems, which is even now moving towards the millimeter-wave domain. This has been fuelled by the emerging needs for multi-band and multi-function specifications within the same compact-structured design platform. Indeed, current communication devices are able to offer multiple functionalities that are generally operating in different frequency bands. In addition to the popular 3G and 4G communication systems, for example, a portable handheld device also supports WLAN and Bluetooth applications. Therefore, it is obvious that wireless systems are becoming more complex and smart due to the inclusion or convergence of multiple standards and applications into a single device. In order to meet the stringent design requirements of those wireless systems, the related RF front ends must be adaptive and flexible in nature. The quality of front-end is directly responsible for the performances of the entire systems as it is directly related to critical electrical specifications of the system such as noise, dynamic range and channelization. This becomes much more involved in multi-band and multi-function systems as the performances should be consistent and uniform for all system states. An adaptive RF front end has been recognized as a viable and effective solution in incorporating multi-band and/or multi-channel circuits with multi-functions to satisfy several wireless system standards. One desirable way of realizing such multi-band or multi-channel systems is through deploying fast and tunable RF and microwave components and circuits, which should be enabled electronically. For example, a frequency agile filter with embedded tuning elements can carry out a switching function between several individual filters in order to have more than one frequency response. Compared with a bulky bank of filters, a single tunable filter offers higher flexibility, better functionality, lighter weight, and the same hardware circuitry can be used to cope with the requirement of multiple purposes, which also reduces the total cost and size.

The replacement of a large and complex circuitry with single tunable device is indeed a very attractive option. However, there are lot of complexities and issues associated with it. One of the biggest challenges of using a single tunable device that covers the multitude of functions is whether it can maintain the same device or system performance at all times or at all states. Usually, in complex systems, there are individual circuit blocks that are optimized or fine-tuned

to carry out specific functionalities. When a single block is designed to perform the same tasks that were previously taken care by a number of individual blocks, then of course, the same performance quality cannot be expected in connection with all the tasks. An example can again be taken of a tunable band-pass filter, which is designed to work continuously over a certain band of frequency. If the filter is designed only with a purpose of tuning the center frequency, it cannot be expected to display the same filter response over the frequency band. As soon as the filter is tuned from one center frequency point to another, the key design parameters that are used in optimizing the filter response change, making the filter response different from the original. Therefore, in order to maintain the best circuit or device performances throughout its tuning range, a certain design strategy must be adopted.

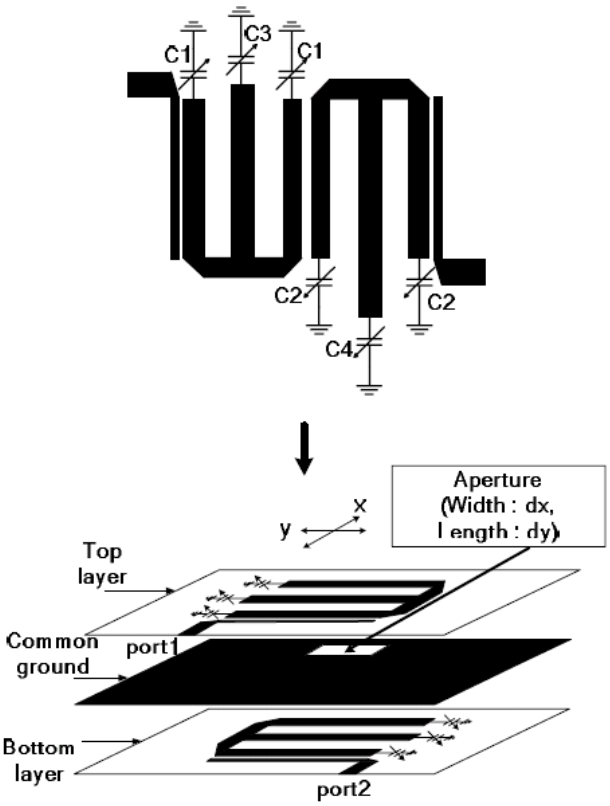

Figure 0.1-1: The structure of an aperture coupled constant bandwidth tunable filter [Moon, et al. (2008)].

In literature, recently there has been a significant amount of works done in the realization of fully-adaptive and reconfigurable filters. In the works carried out by [Joshi, et al. (2009)], [Yi, and Rebeiz (2011)] and [Moon, et al. (2008)] tunable band-pass filter with reconfigurable

bandwidths and center frequencies are presented. In Fig. 0.1-1 and Fig. 0.1-2, the topology of the filter structure and measurement results presented in [Moon, et al. (2008)] are illustrated.

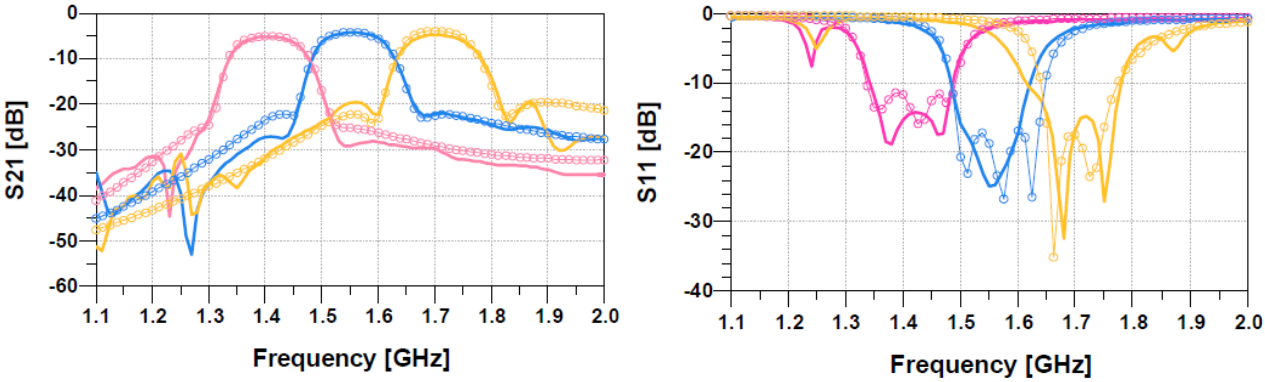

(a) (b)

Figure 0.1-2: Measurement results of the filter illustrating (a) S_{21} parameters (b) S_{11} parameters [Moon, et al. (2008)]

The tunable filter presented in [Moon, et al. (2008)] consists of two sections of hairpin resonators that are coupled to each other by an aperture which lies in an intermediate layer of a multi-layer substrate. The resonators are coupled through an aperture to achieve higher frequency selectivity, and to reduce the total size of the filter. The varactor diodes that are connected at the end of the resonators are used for changing the center frequency of the filter as well as to change its bandwidth. The varactor diodes connected at the end of the resonators change their equivalent length, thereby changing the resonant frequency, at the same time they are also used in changing the inter-resonator couplings to maintain the constant frequency response. The band-pass filter presented in Fig. 0.1-1 and Fig. 0.1-2, uses semiconductor varactor diodes as tuning elements. In order to realize any type of RF and microwave tunable devices, a special tuning element has to be integrated into the device circuitry. The most commonly used tuning elements include: semiconductors (varactor diodes, PIN diodes, and transistor), micro-electro-mechanical systems (MEMS), ferroelectrics materials, and ferromagnetic materials. Each of these tuning elements has their own advantages and disadvantages. Their use largely depends upon, the required type of tunability (discrete or continuous), operating power, design frequency, and also manufacturing complexity and total cost. Previously to this work, few efforts has been made in the design of tunable planar devices based on ferrite material, even if a multitude of three dimensional devices based on bulky waveguide technology has been demonstrated. One of the objectives of this thesis

is to realize fully adaptive and reconfigurable planar filters based on ferrite material as a tuning element. It is also a purpose of this thesis to realize fully adaptive and reconfigurable filters using ferrite material as a tuning element.

In this thesis, a new type of microwave tunable devices based on substrate integrated waveguide (SIW) technology is presented. The SIW based devices are made magnetically tunable by loading planar ferrite slabs inside them. It is demonstrated that, with the application of an external magnetic bias on ferrite loaded SIW (FLSW) structures, a number of interesting and very useful microwave components and devices can be realized. The designed tunable microwave components and devices could then be directly implemented in the realization of a high power radar system design. In Fig.0.1- 3 as an example, a schematic drawing of radar system is presented.

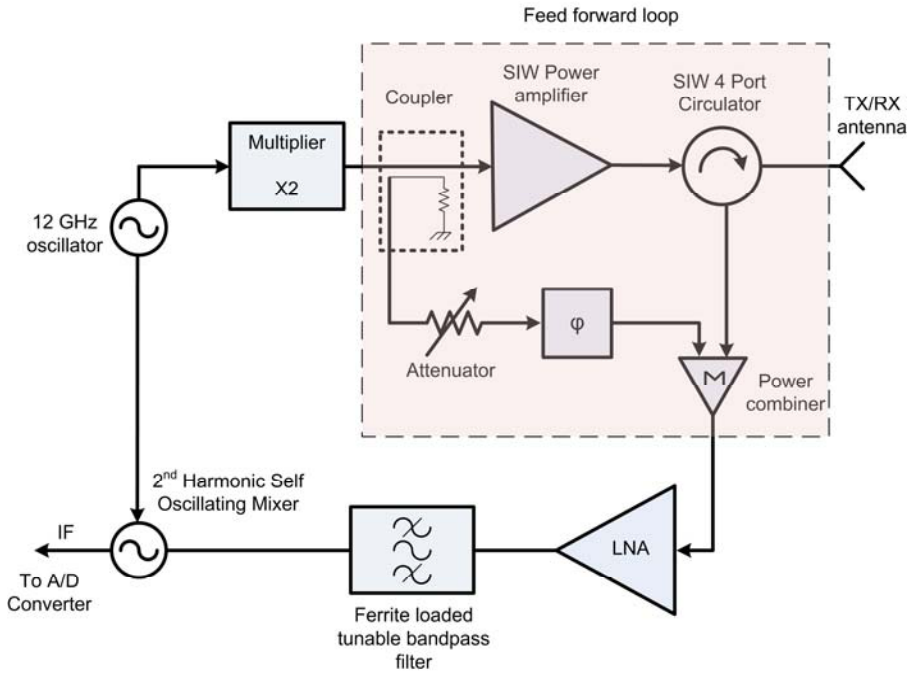

Figure 0.1-3: A schematic of radar system design

It can be seen from Fig. 0.1-3 that, an RF system is made of a number of components and devices including: signal generator, mixer, filters, low-noise amplifier (LNA), power amplifier, antenna, and circulator. In order to realize a fully adaptive and reconfigurable system design, it will be an advantage if in each of the above-mentioned components some degree of tunability can be added. This will allow the system to reconfigure itself to a new system requirement or specification

without a need to change the whole hardware circuitry. Moreover, for a high power application, it will be desirable to have these components capable of handling higher powers. Thus, it is a purpose of this thesis to develop a new type of microwave tunable components with high power handling capabilities.

SIW is an emerging transmission line technology, which is lower in cost, lower in loss, and can also handle high power than other transmission lines. Moreover, it is fully compatible with other planar circuits. Since ferrite materials are also known for their high power handling capability and high tunability, they are used together with SIW technology to realize a new type of highly tunable, planar microwave components and devices for radar application at 12 GHz.

In Chapter 1, a general overview and current status of various tuning elements and related technologies is presented. Each of the technologies is compared to one another in terms of performance, cost and applications. In Chapter 2, an introduction to ferrite material is presented with a brief theoretical review of its microscopic properties. Properties of two different types of ferrite materials to be used in this work are also presented. An introduction to SIW technology and its basic design rules are discussed. In Chapter 3, magnetically tunable microwave devices based on ferrite loaded SIW technology are presented. Tunable radar system components like resonators, oscillators, and switches are introduced. In Chapter 4, a novel concept of simultaneous electric and magnetic two-dimensional tuning is presented, where both ferrite materials and varactor diodes are used to achieve the dual electric and magnetic tuning. It is demonstrated that with the concept of two-dimensional tuning not only the total tuning range can be extended but also the key design parameters like matching, Q–factor, coupling between resonators, and filter shape can be improved. In Chapter 5, non-reciprocal microwave devices are presented, where the non-isotropic behaviour of the ferrite material is used to realize phase-shifters, gyrator and circulator. Finally in Chapter 6, half-mode SIW (HMSIW) devices are introduced. It is shown that the performance of HMSIW devices in terms of tunability and losses are very similar to SIW type of devices. Due to their miniaturized size, they can be used as an alternative to magnetically tunable SIW devices.

CHAPTER 1 TUNABLE RF AND MICROWAVE DEVICES

The current radar and wireless communication systems are becoming more and more complex in terms of performances and functionalities. Military radars for example are desired to be reconfigurable in frequency in order to avoid enemy interferences and in bandwidth to dynamically adjust their resolution depending on the target. Also, a portable hand held communication devices are not only equipped with usual voice-to-voice communication capabilities, but also they can support wireless local area network (WLAN), and Bluetooth. Thus, it is evident that, communication systems are becoming more advanced, smart and complex due to the inclusion or convergence of multiple standards and applications into a single device. In order to meet the requirements of modern wireless communication systems, the RF front ends must therefore be adaptive and flexible in nature. An adaptive RF front ends can be realized by incorporating multi-band or multi-channel circuits to satisfy the several wireless system standards. One way of realizing the multi-band or multi-channel communication systems is by incorporating the tunable microwave components, circuits and devices into them. The tunable devices can be designed to operate not just in one frequency band but in several of them. For example, a single frequency agile filter with embedded tuning elements can replace the requirement of switching between several filters to have more than one frequency response. In comparison to a fixed bank of filters, a single tunable filter is capable of switching the filter response between different frequencies, it is lighter in weight, smaller in footprint, and the same hardware circuitry can be re-used for multiple purposes, which also reduces the total cost. In some cases, the tuning or reconfigurable features are also used in the real-time adjustment of circuit parameters, which are not just limited to frequency tuning.

In order to realize the RF and microwave tunable devices, a special tuning element has to be integrated into the device circuitry. The most widely and commercially used tuning elements include: semiconductors (varactor diodes, PIN diodes, and transistor), micro-electro-mechanical systems (MEMS), ferroelectrics materials, and ferromagnetic materials. Each of these tuning elements or techniques has their own advantages and disadvantages. Their use largely depends upon, the required type of tunability (discrete or continuous), operating power, design frequency, and also manufacturing complexity and total cost. The RF and microwave systems are made up of a number of components and devices including: oscillator, antenna, phase-shifter, amplifier

etc. Each of these devices can be made tunable by incorporating any one of the above mentioned tuning elements. To cover all of the microwave tunable devices is beyond the scope of this chapter. Therefore, a general overview of each tuning element in the realization of a tunable microwave filter is only presented. Since the purpose of this thesis is to realize ferrite loaded magnetically tunable SIW devices, a comparative study of ferrite materials with other tuning elements in terms of performance, cost, and reliability is also discussed and presented.

1.1 Semiconductor tuning elements

In this section, a detailed discussion on RF and microwave tunable band-pass filters that make use of semiconductor as key building elements is presented. Semiconductor is known to be the most popular and widely used technology in the realization of fast tunable integrated RF and microwave components and circuits. They are always associated with low cost, light weight and small footprint, and most importantly they are known to offer a very wide tuning range with adaptive options, depending on diodes and transistor design platforms. However, they can only offer a low Q factor at microwave frequencies [Torregrosa-Penalva et al. (2002)]. For example, the Q factor of a varactor diode is proportional to frequency and junction capacitance at low frequencies (1 MHz) whereas it is inversely proportional at higher frequency (>100 MHz) values [Norwood, and Shatz (1968)]. Moreover, parasitic series resistance of the diode caused by packaging also increases at higher frequency. Thus, the use of varactor techniques is generally limited to frequencies below 10 GHz as they suffer from higher insertion loss. However, an attempt has been made to compensate the loss and increase the Q factor by incorporating FETs as a negative resistance device [Chandler et al. (1968)]. Of course, any active compensation can be made possible at the expense of additional power consumption and potential non-linear effects. There are basically three reported different types of semiconductor devices that are integrated inside a microwave circuit as tuning elements, which include varactor diode, PIN diode, and field effect transistor (FET). Naturally, any active diodes and transistors can be used as tuning elements, depending on their technical merits. The tuning elements are used in the realization of tunable devices that are made either in discrete mode or in continuous mode.

1.1.1 Varactor diode

Varactor diode is also known as a variable reactor, which means a device whose reactance can be made variable by the application of a DC bias voltage. The reactance in the case of a varactor diode is a simple depletion layer capacitance, which is formed at the junction of p-type and n-type semiconductor materials. Depending upon the polarity and the strength of the applied bias voltage, the depletion layer width is changed, which in turn also changes the junction capacitance value. Since the capacitance value of the varactor diode can be changed even by a slight variation of applied bias voltage, it finds application as a continuously tunable device. Varactor diodes are very useful in realizing a variety of devices including tunable filter, tunable phase shifter, and voltage controlled oscillator (VCO), parametric amplifier, and mixer. In this section, a brief overview of tunable filters based on varactor diodes are discussed and presented.

There is a growing interest in the design and realization of RF and microwave systems that have multi-channel and multi-band functionalities. Since filter is one of the most critical parts of the system design, it is highly beneficial to realize such a filter that is fully adaptive to any changes in connection with the system behaviour. Tunable filter can reduce the complexity of a system design by avoiding the need of filter banks, which consist of multiple filters with distinct filter responses for each frequency band. The use of a tunable filter allows the coverage of the whole frequency bandwidth. Early work of tunable filter designs involved the tuning of center frequency using various kinds of tuning devices and materials. Presently, the focus of a tunable filter design has not only been on changing the center frequency but also on making it fully reconfigurable in terms of bandwidth and selectivity. Varactor diode has been one of the most promising technologies that have been widely used in the realization of a wide variety of electronically tunable filters. In the early work of varactor tuned filter developments, the center frequency was tuned by loading the varactor diodes at the ends of resonating stubs [Hunter, and Rhodes (1982)]. It was noticed that, the band stop characteristic of the filter was largely dependent upon the coupling gap between the feeding transmission line and the parallel stubs. Since the coupling gaps of the parallel stubs are highly frequency dependent, it was suggested in [Hunter, and Rhodes (1982)], to tune the capacitance of the gaps in accordance with the tuning capacitances in order to preserve the band stop characteristics. In [Makimoto and Sagawa (1986)], a varactor tuned ring resonator filter using microstrip technology was presented. The center frequency of the filter was configured by changing both

filter's coupling and tuning capacitances. In [Musoll-Anguiano et al. (2002)] a fully adaptable band stop filter, which is able to reconfigure its center frequency, bandwidth, and selectivity, was demonstrated. The bandwidth tuning is achieved by varactor diodes that are used in coupling resonators to transmission line, whereas the center frequency is controlled by varactor diodes connected at the end of transmission line resonators.

Since the varactor diodes are made up of semiconductor materials, they suffer from non-linearity when injected with high power signals. Despite non-linear behaviours of semiconductor materials, it has been demonstrated that the varactor diodes can also be used for realizing high power filters [Swartz et al. (1980)] at UHF band. Recently, a varactor tuned band-pass filter with improved linearity has been presented in [Yu et al. (2012)]. The filter topology consists of an open-ended transmission line with back-to-back varactor diodes loaded at one end. The back-to-back varactor diodes enhance the linearity of the filter while the mixed electric and magnetic coupling scheme keeps the absolute bandwidth at a constant value when the frequency of the filter is tuned. Thus, varactor diode presents itself a very promising low cost, highly tunable, and adaptive semiconductor tuning element that can be used in realizing tunable filters at relatively low tuning voltage.

1.1.2 PIN diode

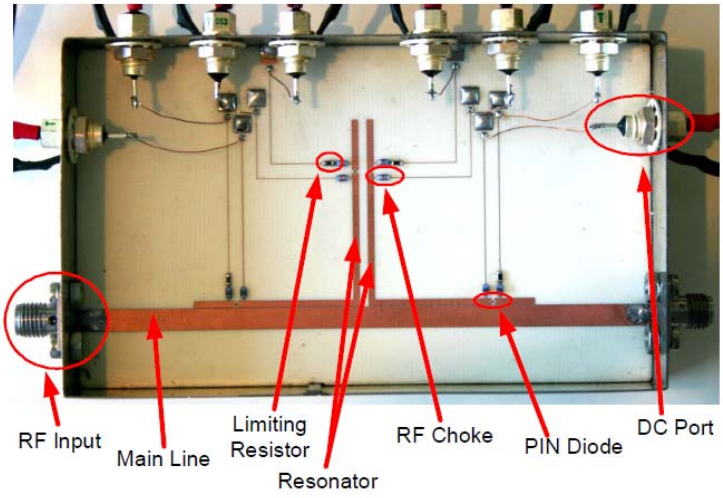

Figure 1.1-1: Photograph of the fabricated switchable band-pass filter [Brito-Brito, et al. (2008)].

PIN diodes are semiconductor based tuning devices, which are popularly used to produce discrete states reconfigurable filters. In this section, a brief review of tunable filters based on PIN diodes is presented. In [Lugo, and Papapolymerou (2004)], a PIN diode based reconfigurable filter for

wireless applications was demonstrated. The designed filter falls into a category of admittance inverter coupled resonator filter, with two discrete bandwidths at 5.6 GHz

The PIN diodes being semiconductor device, non-linear effects of the diode in the filter structure are also studied. In [Brito-Brito, et al. (2008)], a band-pass filter which is switchable between two central frequency states is presented. The designed filter uses PIN diodes for switching, such that in each frequency states a constant bandwidth is maintained. In Fig. 1.1-1, the fabricated prototype of the switchable band-pass filter is illustrated. By changing the polarity of the bias voltage, the filter is switched between 1.5 GHz and 2 GHz center frequencies respectively [Brito-Brito, et al. (2008)]. In [Karim, et al. (2009)] a miniaturized reconfigurable and switchable band pass filter is presented. By shorting the open stubs of the filter using PIN diodes, the UWB filter is reconfigured from band-pass to bandstop response. Moreover, with the addition of half-wavelength stub to the existing reconfigurable filter, it is switched from UWB to 2.4 GHz narrowband filter response.

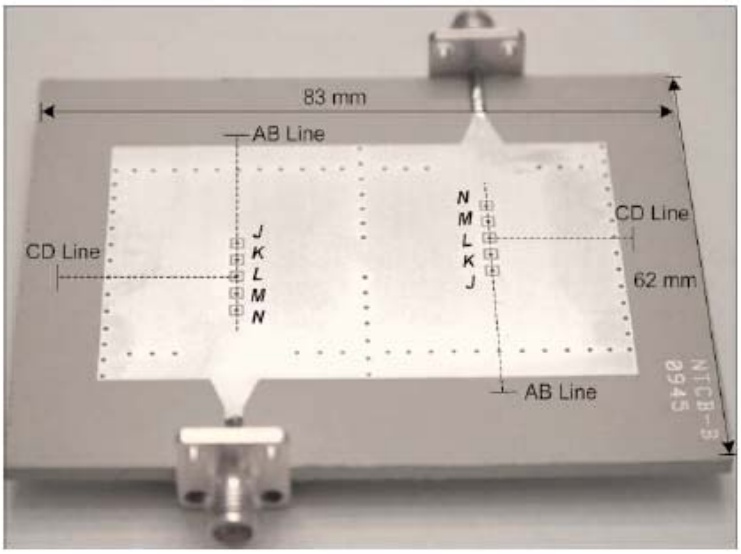

Figure 1.1-2: Fabricated SIW filter with via posts islands for the connection of PIN diodes [Armendariaz, Sekar, and Entesari (2010)].

A new type switchable band-pass filter based on SIW technology and using PIN diodes was presented in [Armendariaz, Sekar, and Entesari (2010)]. The two-pole band-pass filter is switched between six states ranging from 1.55 GHz to 2.0 GHz. The SIW cavity resonators are equipped with multiple via posts, which are either connected or disconnected from the top metal layers using PIN diodes, thus producing different switching states (see Fig. 1.1-2). Another SIW based

digitally tunable band-pass filter was demonstrated in [Sirci, Martinez, and Boria, (2013)], where discrete frequency tuning with nearly 8 equal spaced frequency responses from 4-4.4 GHz is obtained. In [Bakhit, and Wong (2013)], switchable band-pass filter using stepped impedance resonator was presented. The designed operates between two states, in the first stated the filter produces a band-stop response. By switching the PIN diodes to ON state, the filter response then changes from band-stop to all-pass filter characteristics.

1.1.3 Transistors

In [Lin, and Itoh (1992)], using the concept of three-terminal MESFET varactor tunable active band-pass filter was demonstrated. In the two pole filter configuration, one transistor is used to provide center frequency tuning, while the other is used to provide the negative resistance to the circuit. The negative resistance of the transistor improves the overall *Q* factor and improved filter response. In [Torregrosa-Penalva, et al., (2002)], a wideband tunable combline filter using gallium arsenide field effect transistor as a tuning element was presented which is illustrated in Fig. 1.1-3. The filter resonators are loaded with field effect transistors to produce the desired tunability. A systematic approach in designing tunable combline filters and the non-ideal effects in the overall performance of the filter are also discussed.

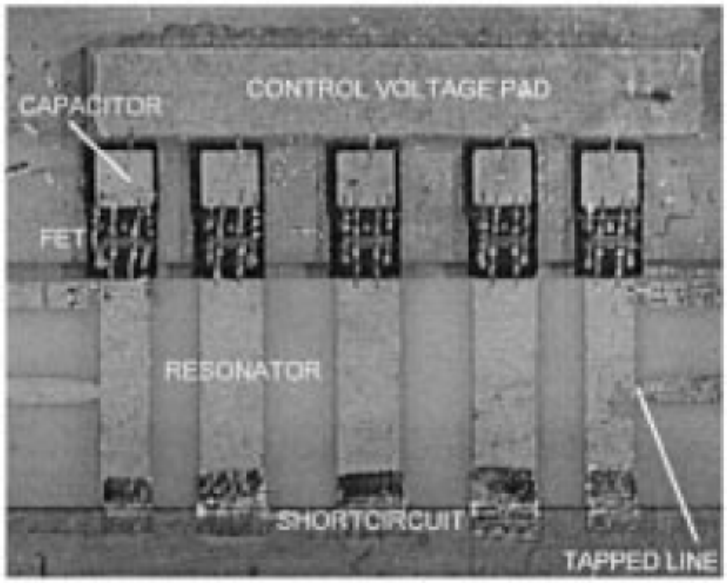

Figure 1.1-3: Fabricated filter prototype [Torregrosa-Penalva, et al., (2002)].

In [Pantoli, Stornelli, and Leuzzi (2012)], a high Q tunable filter with a single transistor active inductor (AI) was presented. The first order band-pass filter has a central frequency of 2400 GHz, the total frequency tuning range is 100 MHz.

1.2 MEMS techniques

Although it has been studied since early 60s, MEMS has become an emerging technology that is very useful in realizing variable capacitors, switches, and reconfigurable RF and microwave devices. Compared with semiconductors, ferrites and ferromagnetic materials based tunable devices; MEMS techniques offer much higher Q factor with very low power consumption. Moreover, as opposed to the solid state devices, they offer linear signal transmission with low signal distortion. Hence, MEMS have attracted much attention, which present very promising scheme in realizing a wide range of RF and microwave tunable components and devices. Tunable filters, realized using MEMS technology generally make use of MEMS switch or MEMS varactors as tuning elements. This section show several filter topologies to produce discrete and continuous tuning of the filter parameters.

1.2.1 Tunable filters using MEMS switches

MEMS switches are generally used for re-routing RF signals and also they are widely used in realizing tunable filters. Since MEMS based switches operate in only two states: on and off, the tunability of filters designed using MEMS switches are discrete in nature. From the structure point of view, such switches are either cantilever types or bridge types. An example of cantilever type MEMS switch is illustrate in Fig. 1.2-4.

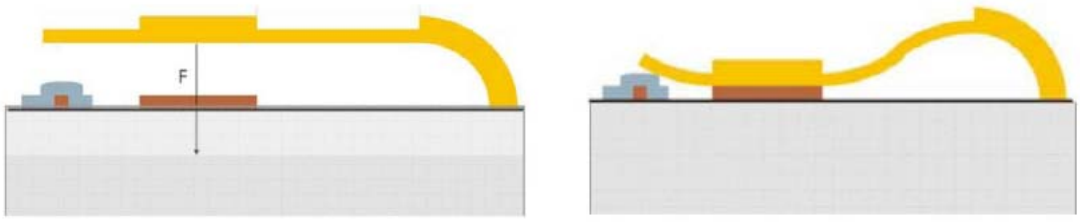

(a) (b)

Figure 1.2-4: Schematic of electro-statically actuated cantilever type RF MEMS switch (a) OFF state (b) ON State [Ocera, et al. (2006)].

The electrical performance of a cantilever type switch largely depends upon the quality of contact in the ON state as illustrated in Fig. 1.2-4(b). There are basically two types of electrical contacts used in MEMS switches: direct contact and contact through a capacitive membrane also known as Metal-Insulator-Metal (MIM) contact. Compared to the MIM contact, the direct contact switches have lower insertion loss and better isolation. However, due to direct contacts between metals, the direct contact switch suffers from metal corrosion and has a shorter life time compared to MIM switches. Two well-known problematic issues in the development of MEMS devices are related to high actuation voltage and relatively low speed because of a mechanical process. In addition, MEMS techniques may not be well suitable for high-power applications even though significant research efforts have been invested to remedy this situation.

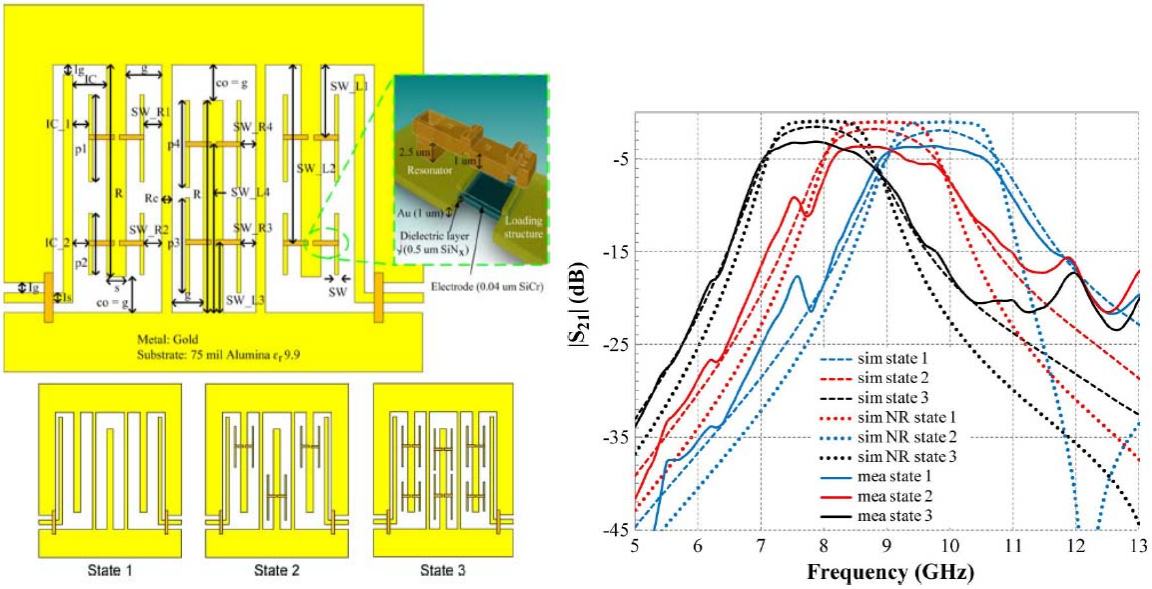

(a) (b)

Figure 1.2-5: Schematic of electro-statically actuated cantilever type RF MEMS switch (a) layout of the filter (b) simulation and measurement results illustrating three states of tuning [Chan, et al. (2012)].

In this section, tunable filters using direct and MIM contact based MEMS switches are presented. The cantilever type MEMS switch illustrated in Fig. 1.2-4 was used to realize a tunable hairpin line filter in [Ocera, et al. (2006)]. The filter tunability is achieved by loading identical MEMS switches at the end of hairpin resonators. When the switches are changed between on and off states, the equivalent electrical lengths of resonators is also changed, thereby making the filter

tunable. Another example of tunable filter using MEMS switch was described in [Chan, et al. (2012)], where the microwave filter is switched between three states. It is a good example in which MEMS switches are used in controlling the resonant frequency, input/output couplings, and couplings between resonators to achieve a fully-reconfigurable band-pass filter at microwave frequency. The measured filter response shows three different states of filters at 8, 9 and 10 GHz respectively. In Fig. 1.2-5(a), the filter layout with tuning elements is presented, and its simulation and measurement results are presented in Fig. 1.2-5(b)

A new type of tunable filter based on SIW technology was presented in [Sekar, et al. (2011)]. The filter topology consists of two SIW cavities that are coupled to each other via an iris window. Commercially available packaged RF MEMS switches are surface mounted in each cavity to tune them separately. The two-pole filter implemented using two-layer SIW circuit has a total tuning range of 28% with reflection loss better than 15 dB. The fabricated filter prototype and the measurement results are illustrated in Fig. 1.2-6 and Fig. 1.2-7 respectively.

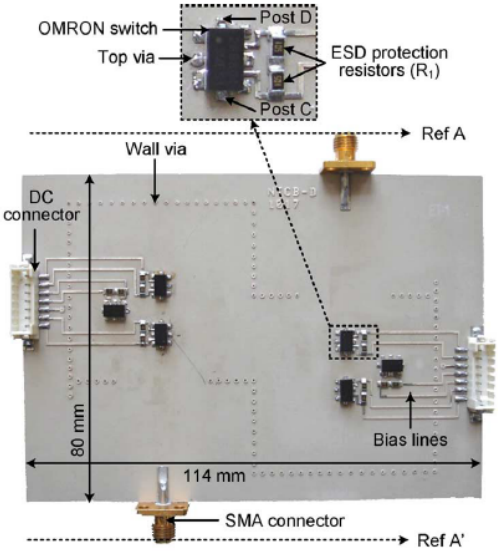

Figure 1.2-6: Fabricated tunable low pass filter using direct contact MEMS switches [Sekar, et al. (2011)].

A coplanar waveguide based fully reconfigurable filter was presented in [Park, et al (2005)]. The filter topology consists of cascaded CPW-based periodic structures which are loaded with MEMS switches for tunability. By suitable combination of MEMS switches a 3-unit CPW lines are combined to form a single-cell low pass filter. In this way the length of the filter is increased by

three-times the original length, and subsequently reducing the low-pass cut-off frequency also by three-times. In a similar way, a reconfigurable band-pass filter was also realized in [Park, et al (2005)], where three band-pass units are cascaded together using MEMS switches to realize a single larger band-pass filter having a filter response at low frequency region.

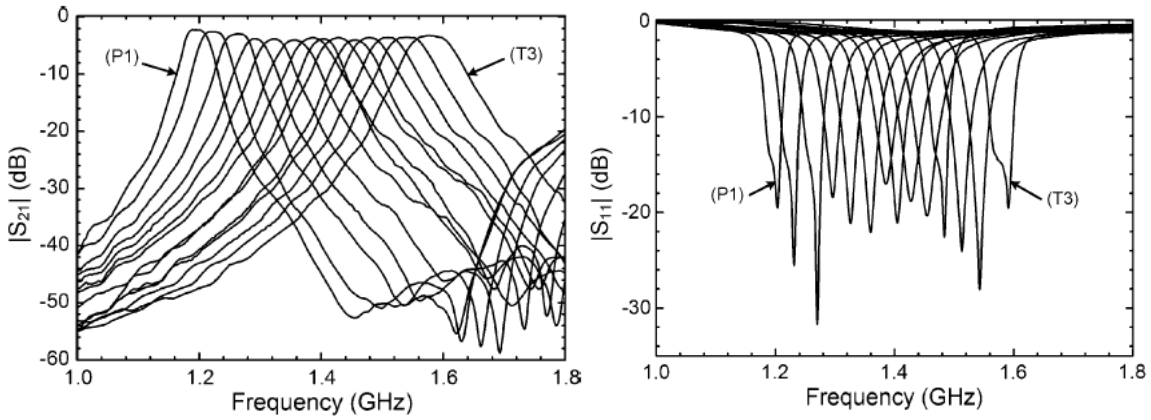

(a) (b)

Figure 1.2-7: Measurement results of tunable band-pass pass filter [Sekar, et al. (2011)].

1.2.2 Tunable filters using MEMS switch capacitors

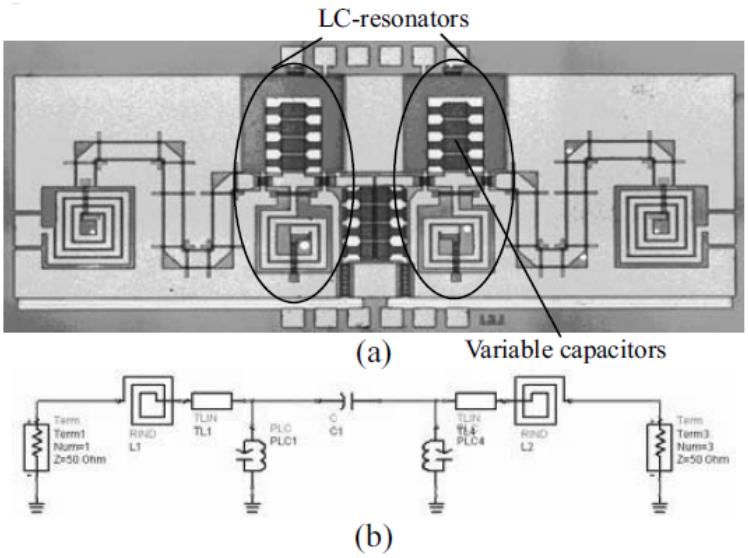

Figure 1.2-8: Lumped element filter using MEMS switch capacitors for tuning (a) fabricated prototype (b) equivalent circuit [Kim, J-M., et al. (2006)].

In this section, an overview of tunable filters based on MEMS switch capacitors is presented. Similar to the direct contact counterparts, the switch capacitors can also be cantilever or bridge

type as illustrated in Fig. 1.2-4. However, in the MEMS switch capacitors, an electrical connection is established not through an ohmic contact but through a capacitive membrane. Therefore, the switch operates between two different capacitance values: one for the ON state and the other for the OFF state. A central frequency and bandwidth controlled filter using MEMS cantilever type capacitive switch was presented in [Fourm, E., et al. (2003)]. The switches are loaded at the end of the coplanar resonators to achieve two center frequency states. The MEMS switch capacitors are also used in realizing the lumped element type tunable filters. A lumped element type tunable filter using MEMS capacitive switch was designed in [Kim, J-M., et al. (2006)] for WLAN applications. The filter is designed to select alternate frequency bands which are at 2.4 and 5.1 GHz. In Fig. 1.2-8, the fabricated prototype of the lumped element filter and equivalent circuit is illustrated.

1.2.3 Tunable filters using MEMS varactors

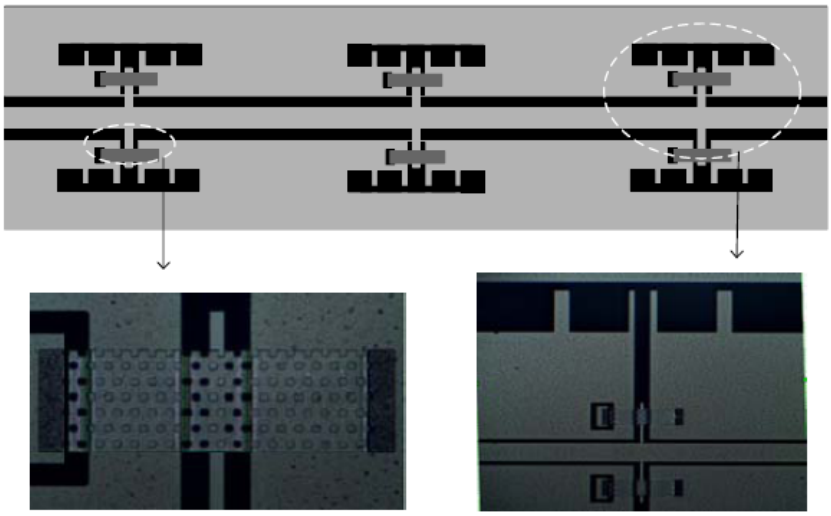

Figure 1.2-9: Fabricated tunable band-pass filter [Zhang, Deng, and Sen (2013)].]

MEMS varactors present an advanced form of MEMS capacitive switches. Similar to the MEMS capacitive switches, they are also composed of capacitive membrane between the two metal contacts. Unlike the capacitive switches that operate only between ON or OFF states, MEMS varactor capacitance membrane can be tuned continuously with an applied analog voltage. From the operation point of view, they are very similar to semiconductor biased varactor diodes and are useful in realizing the continuously tunable RF/microwave filters. They are more attractive than semiconductor varactor diodes in terms of Q factor, power consumption and linearity. However,

they have lower tuning speed and are more sensitive to environmental conditions for example temperature, moisture and vibrations. A lumped element type tunable K-band filter using MEMS bridge varactor was presented in [Kim, Lee, Park, and Kim, (2005)]. The filter consists of J-inverters and shunt-type resonator sections. The variable capacitors are loaded in the shunt type resonators to vary the center frequency of the filter.

In [Abbaspour, Dussopt, and Rebeiz, (2003)] a distributed type band-pass filter was designed using bridge type MEMS varactors. The coplanar transmission line is loaded with MEMS varactors to reconfigure the center frequency of the filter. A coplanar waveguide tunable band-stop filter using RF MEMS variable capacitor was presented in [Zhang, Deng, and Sen (2013)]. The filter is designed to operate from 8.5 to 12.3 GHz with 35% of tunability. This filter is another example of MEMS varactors loaded distributed type of filter. In Fig. 1.2-9, the fabricated prototype of the filter is presented.

1.3 Ferroelectrics

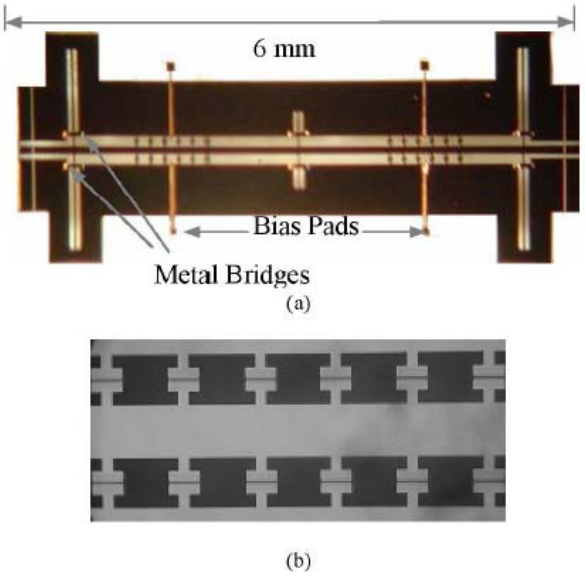

Figure 1.3-10: Photographs of (a) fabricated 2-pole filter and (b) area around CPW line loaded with BST [Papapolymerou, et al. (2006)].

Ferroelectrics are one of the most promising materials in realizing electronically tunable RF and microwave components and circuits for wireless front-end applications. A number of tunable devices including phase shifters, oscillators, and filters have been demonstrated by using ferroelectric materials as key tuning elements. The dielectric constant of ferroelectric materials

varies with the applied DC voltage, ranging from a few hundreds to a few thousands. Therefore, a device incorporating ferroelectric material or loaded with ferroelectric material locally generally in the form of thin-films becomes tunable with respect to the effective permittivity change. Compared to MEMS, ferroelectric materials offer a very fast tuning time like semiconductor techniques, but they have lower *Q*-factor. In addition, the quality and properties of ferroelectric thin-films can be strongly dependent on processing techniques. The most commonly used ferroelectric material in microwave regime is Barium-Strontium-Titanate oxide (BST). In this section, a brief review of tunable microwave filters based on BST is presented.

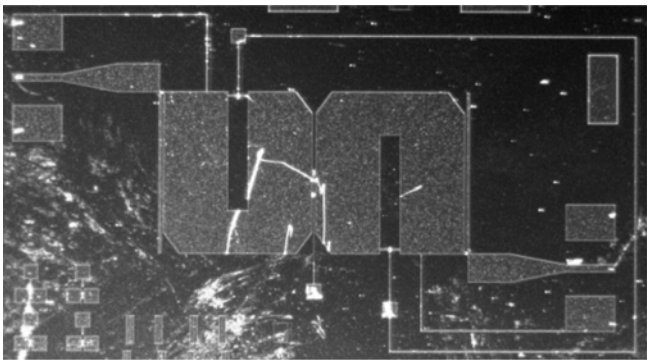

Figure 1.3-11: Fabricated prototype of tunable filter with constant fractional bandwidth and return loss [Courreges, et al. (2009)].

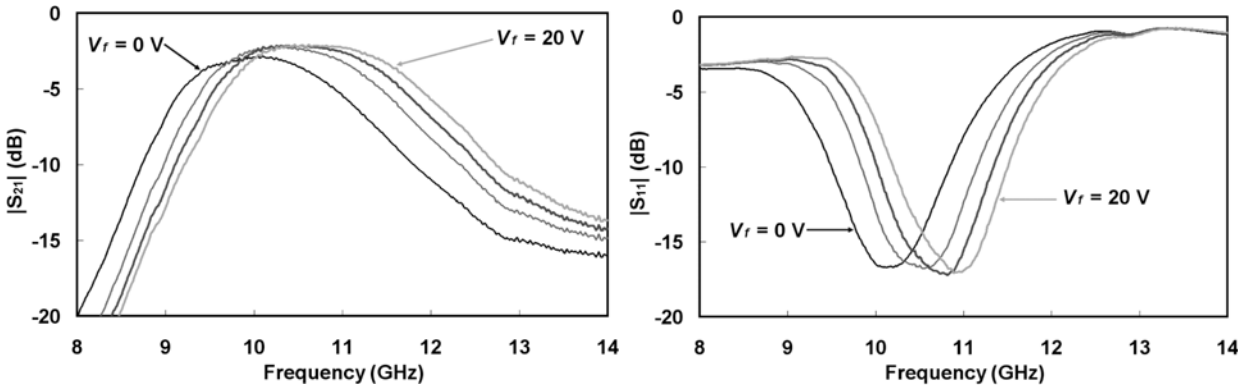

(a) (b)

Figure 1.3-12: Measured frequency responses indicating (a) constant fractional bandwidths and (b) return loss [Courreges, et al. (2009)].

Before beginning with the design of tunable RF and microwave devices using ferroelectric material, it is very important to first characterize in terms of tunability and losses. In [Ouaddari, et al. (2005)], a computer-aided-design model is developed, to characterize the BST thin films in

the frequency range from 1 to 16 GHz. Coplanar waveguides (CPWs) and inter-digital capacitors (IDCs) are fabricated on BST thin films, to determine the complex dielectric constants, voltage tunability and *Q*-factor. Once the material is correctly characterized, very accurate designs of the tunable devices can be realized at a given frequency. In [Papapolymerou, et al. (2006)] a slow wave miniature, tunable 2-pole filter operating from 11.5 GHz to 14 GHz was presented. The filter consists of a section of a coplanar transmission line that is loaded with several ferroelectric BST high *Q* capacitors. The total insertion loss of the device varies from 5.4 to 3.3 dB in the tuning range of the filter. A DC variation between 0-30 V is applied to achieve the tunability of the filter. In Fig. 1.3-10, the photographs of fabricated prototype of the tunable slow wave filter loaded with BST as a tuning element is presented. In order to achieve high tunability using ferroelectric material, in [Delprat, et al. (2007)] a study was performed to establish a correlation between the lattice parameter of BST films with the dielectric tunability. It was concluded that, a broad tunability can be achieved on low cost microwave devices based on BST films provided the internal elastic stress of the film is low. A microstrip based tunable filter with improved selectivity was presented in [Lourandakis, et al. (2009)]. The frequency tuning of the filter is achieved by loading BST based varactor diodes on the microstrip resonators. From the frequency response it was demonstrated that the designed filter had a better frequency response compared to the conventional combline filter in terms of frequency selectivity. In [Courreges, et al. (2009)] a two-pole X-band tunable filter with constant fractional bandwidth and return loss was presented. To achieve the frequency tunability, ferroelectric BST material is used. A total tuning range of 7.4% is achieved with a minimum applied voltage of 30V. In Fig. 1.3-11, the fabricated prototype of the filter is presented, while in Fig. 1.3-12, the measurement result indicating the constant bandwidth and return loss is presented. In [Jiang, et al. (2012)], an asymmetric inductively-coupled tunable band-pass filter using ferroelectric BST as tuning element was presented. Similar to the work in [Courreges, et al. (2009)], the filter is able to tune the center frequency but at the same time maintain a constant fractional bandwidth and return loss.

1.4 Ferromagnetic

Ferrites or ferromagnetics are materials with an electric anisotropy. They are very useful in realizing non-reciprocal devices including circulators, isolators and gyrators. Such non-reciprocal devices are generally fixed frequency types, which are designed for particular applications. The

frequency of operation for a ferrite material largely depends upon the external DC magnetic bias that is applied on it. Therefore, the non-reciprocal devices operating at a constant frequency constitute a fixed permanent magnet that delivers a constant value of magnetic bias to the ferrite material. When the applied magnetic bias value is changed, however the effective permeability value presented by the ferrite material also changes. Note that permeability and permittivity present the same contributions to the change of transmission phase or propagation constant. Since the frequency of an electromagnetic wave is directly proportional to the square root of permeability, any changes in permeability also changes the frequency. Therefore, ferrite materials are not only useful in realizing fixed frequency non-reciprocal type devices but they present also similar features as ferroelectrics in realizing tunable RF, microwave and millimeter wave components and circuits. The evolution of tunable filters based on ferromagnetic materials and their present status are discussed in the following.

From mid-1950's, ferrites materials have drawn considerable interest in the realization of tunable devices including tunable cavities, filters and frequency modulation of the generated signal [Jones (1956)] and [Fay (1956)]. It can be observed that in both works presented in [Jones (1956)] and [Fay (1956)] rectangular waveguide technology is used to realize the desired tunable devices. The higher power handling capabilities, lower loss, and more convenient of biasing ferrites could have been one of few reasons why rectangular waveguide technology would have been used. Moreover, within the rectangular waveguide, the positions of electric and magnetic fields for a given mode of operation (TE_{10} for example) are clearly defined. Since ferrite materials strongly interact with magnetic fields, they can be placed in the positions of the highest magnetic field strength without perturbing electric fields. In this section, tunable filters based on rectangular waveguide technology and their subsequent evolutions into planar forms are briefly discussed.

In [Fay (1956)], a magnetically tunable cavity resonator based on rectangular waveguide technology was presented. The tunability is achieved by placing a slab of YIG along one of the sidewall of the rectangular waveguide, where the magnetic field component of TE_{101} mode is dominant. By the application of an external DC magnetic bias, the resonant frequency of the cavity is tuned towards higher frequency value. The magnetically tunable cavity resonator presented in [Fay (1956)] uses a block YIG slab to achieve the magnetic tunability. Since the ferrite blocks are usually polycrystalline material therefore they suffer from losses when used in

microwave and millimeter wave regions. In order to improve the total tuning range and to reduce the losses, a magnetically-tunable filter consisting of single-crystal YIG was proposed in [Carter (1961)]. It is demonstrated that single-crystal YIG are very useful in realizing low loss and highly tunable microwave filters. In [Carter (1961)] a filter with adjustable 3dB bandwidth and center frequency tunability was demonstrated. However, the filter has a low tuning speed, and possesses fabrication difficulties in precisely placing and biasing the single-crystal YIG sphere.

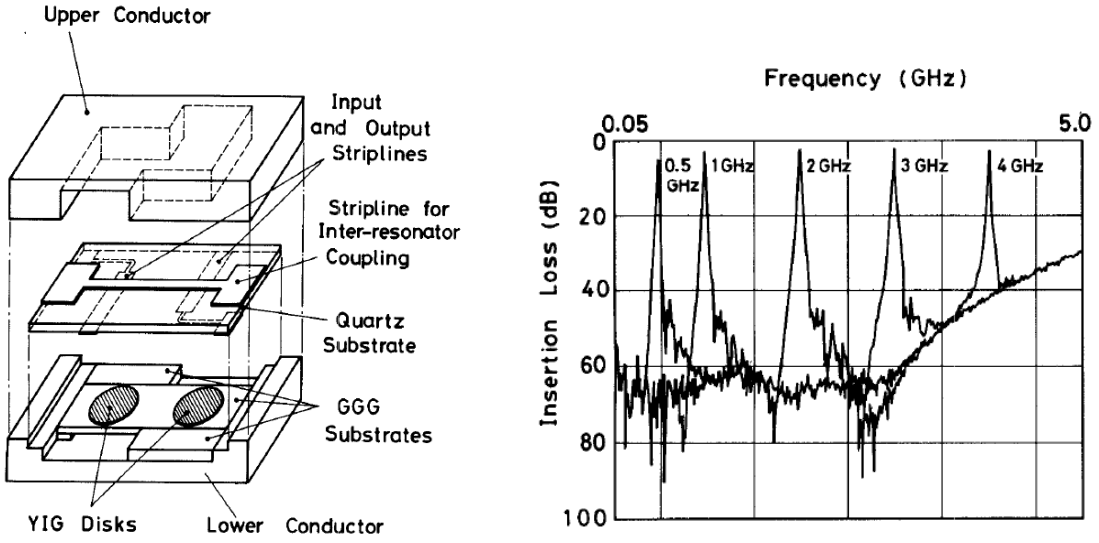

Figure 1.4-13: Structure of planar tunable filter using ferromagnetic disks (a) filter structure (b) frequency response [Murakami, et al. (1987)].

After the earlier works of filter design using rectangular waveguide technology, the interest has slowly shifted in incorporating the ferrite materials in planar form; thereby realizing magnetically tunable planar filter circuits. In [Murakami, et al. (1987)] tunable band-pass filter using YIG film that is grown by Liquid Phase Epitaxy (LPE) was presented. A total tuning range from 0.5 GHz to 4 GHz has been achieved with low insertion loss. In Fig. 1.4-13, the proposed schematic of the filter and the frequency response is presented. A tunable resonator based on ferromagnetic resonance was presented in [Tatarenko, et al. (2006)]. The designed cavity resonator is tunable due to the magnetoelectric interactions between the layers of ferrite and ferroelectric those make up the resonator. In [Oates, Dionne, and Slattery (2009)] a tunable resonator fabricated on a polycrystalline ferrite substrate was presented. It is demonstrated in this work that, the applied stress can influence the magnetization of the ferrite material. Frequency tunability is achieved by

an application of stress on the ferrite substrate. Maximum tunability of 300 MHz is experimentally achieved.

In [Tai, and Qiu (2009)] a tunable band-pass and bandstop filters based on ferromagnetic resonance (FMR) absorption is presented. The schematic of the tunable bandstop filter topology is presented in Fig. 1.4-14.

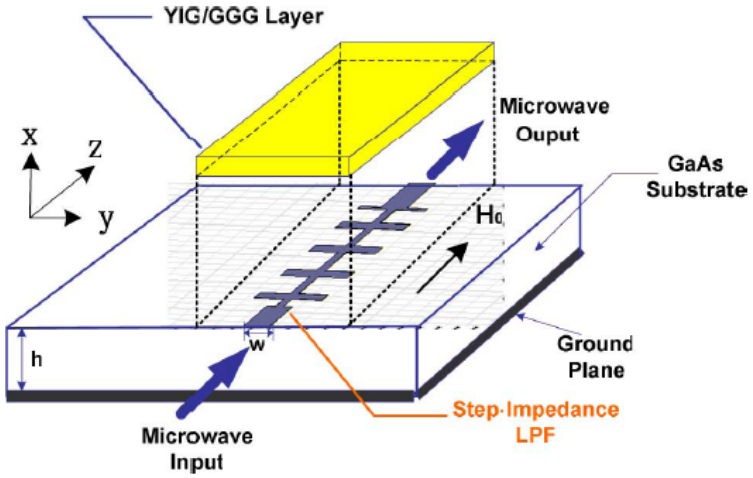

Figure 1.4-14: Schematic of tunable microwave band-stop filter based on FMR [Tai, and Qiu (2009)].

As illustrated in Fig. 1.4-14, the bandstop filter consists of YIG/GGG layer placed upon the microstrip line based upon the GaAs substrate. A bandstop characteristic of the filter occurs, when the incoming microwave signal are absorbed by the YIG/GGG substrate layer. This occurs when the FMR frequency of the YIG/GGG substrate coincides with the frequency of the incoming signal. In [Popov, et al. (2012)] magnetically tunable dielectric band-pass filter based on nickel ferrite was presented. The filter is tunable from 18-36 GHz and has an insertion loss between 2-5 dBm.

1.5 Discussion

Based on the brief overviews of different tuning elements and techniques that are widely used in the realization of tunable microwave cavities and filters, it can be concluded that each scheme has its own advantages and limitations in performance. In the following table, the key parameters of each tuning scheme are compared and summarized in terms of losses, tunability, power consumption and response time, when they are used in the realization of tunable filters.

Table 1.1: Comparison between various tuning elements:

Tunable elements	Q-factor	Tunability	Power consumption	Response time
Semiconductor	Moderate	High	Poor	Fast
MEMS	Very high	Low	Excellent	Slow
Ferroelectric	Moderate	High	Excellent	Very fast
Ferromagnetic	High	Very high	Moderate	Moderate

Semiconductor diodes present lower cost, light weight, easy biasing, low voltage, and small footprint. However, they would inherently produce non-linear effects and suffer from inter-modulation noises and transmission losses. MEMS techniques, on the other hand, are highly linear in comparison to semiconductor schemes. However, the response or the switching time of MEMs is much slower compared to semiconductor counterparts. They are also vulnerable to environmental conditions, for example, temperature, vibration in which they operate. Thus, they may require a stringent packaging condition. Ferroelectric materials are highly suitable for integrated microwave devices because they can be made in thin-film or thick film forms, and they also offer a relatively high tunability. Nevertheless, the dielectric loss tangent of ferroelectric materials is generally very high and the inherent permittivity of ferroelectric materials may present highly dispersive behavior, which may not be good for a wide-ranged frequency tuning. Thus, they offer a very low *Q*-factor with limited bandwidth applications. Tunable devices based on ferromagnetic materials can handle more power compared to semiconductors and MEMS technologies, and they are highly tunable and higher *Q*. However, biasing the ferrite materials requires the use of solenoids wounded with current carrying coils or large permanent magnets. Therefore, the tunable circuit using ferrite materials can sometimes be bulky.

It has been found that the one-dimensional electric or magnetic tuning may not be effective in terms of tuning range and design complexity. In this work, to increase the scopes of tunability and at the same time improve the performance of the device in the whole tuning range, a concept of two-dimensional tuning is proposed. The proposed two-dimensional tuning technique may present an attractive and emerging alternative for simultaneous electric and magnetic tuning, which may fundamentally change the design landscape of tuning structures and circuits.

CHAPTER 2 MAGNETICALLY TUNABLE FERRITE LOADED SUBSTRATE INTEGRATED WAVEGUIDE

In the previous chapter, a general overview on RF and microwave tunable technologies has been presented. State-of-the-art tunable technologies including: semiconductors, MEMS, ferroelectric and ferromagnetic materials and their use in the realization of tunable filters have been discussed and presented. As it was discussed, RF and microwave tunable components and devices can be realised by incorporating tuning elements into circuit topologies that are based either on microstrip, coplanar or metallic hollow waveguide technologies. The exact use of a circuit technology also depends upon user requirements and applications. For example, for high power and some specific millimeter-wave applications, rectangular hollow waveguides are more preferable than planar transmission lines because of loss and power handling issues. On the contrary, for miniaturized and highly integrated circuits applications, planar transmission lines like, microstrip lines, coplanar waveguides and striplines are preferred. Although, planar transmission line and circuits being very useful in realizing miniaturized devices, they are not very suitable for high power applications. On the other hand, the bulkiness of rectangular waveguide technologies does not allow any possible integration amenable into favorable miniature forms. Therefore, there is the pressing need of a technology which can combine the qualities of both rectangular waveguides and planar transmission lines technology into one. SIW technology, which is part of the substrate integrated circuits (SICs) family, is an emerging technology, which combines the features of both rectangular waveguide and planar circuit technologies. SIW inherits almost all the properties of rectangular waveguide including: higher power carrying capabilities, lower in loss, lower in cost and at the same time it is also easily compatible with other planar circuitries. One most important purpose and demonstration of this thesis is to realize tunable microwave components and devices for high power radar or communication application at 12 GHz. SIW being a very promising technology for low-loss and high power applications, it is chosen to be used in the realization of microwave front-end's components and devices. In order to make the SIW devices tunable, ferrite materials are chosen to be placed inside them. Ferrites are also known for their lower-loss and higher power carrying capabilities. Therefore, a new-type of microwave tunable device is proposed in this thesis, which

makes use of SIW technology and ferrite materials. In this chapter, a brief introduction of ferrite materials and SIW technology is presented.

2.1 Ferrites for microwave devices

Ferrite materials possess a property of magnetic anisotropy (tensor permeability), and their behaviour can be influenced with the application of an external DC magnetic bias. In contrary to passive devices (or isotropic devices), the electromagnetic signals propagating through the ferrite material behave differently when travelling in different directions. This non-isotropic behaviour of ferrite has led to the realization of a large number of non-reciprocal devices including: isolators, circulators, and gyrators [Fay, et al. (1965)], [D'Orazio, and Wu (2006)], [Pozar (2005)]. Their use is not only limited to the realization of non-isotropic material, but they are also very useful in the realization of magnetically tunable devices in RF, microwave and millimeter wave regime. The value of an effective permeability of the plane wave propagating in the ferrite material is largely dependent on the value of applied magnetic bias. Since the operating frequency is proportional to the square root of the permeability value, any change in the permeability also changes the frequency of operation. Hence, ferrite materials are very useful in the realization of non-isotropic and magnetically tunable devices.

2.1.1 Basic properties of ferrite materials

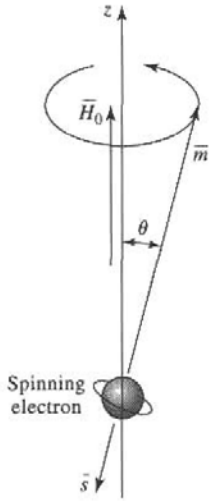

Figure 2.1-1: Illustration of spinning electron with angular momentum vector [Pozar (2005)].

Inside a ferrite material, there are magnetic dipole moments. The dipole moments are due to the electron spin. The spinning electron possesses a spin angular momentum. In Fig. 2.1-1, an

illustration of spinning electron is shown, with magnetic dipole moment $\bar{m}$ and angular momentum $\bar{s}$ vectors.

The spin angular momentum of the electron is related with the Planck's constant which is given as [Fuller (1987)] and [Pozar (2005)],

$$s = \frac{\hbar}{2}. \tag{2.1}$$

The ratio of spin magnetic moment and spin angular momentum of the electron is known as gyromagnetic ratio,whose value is given by,

$$\gamma = \frac{m}{s} = 1.759 \times 10^{11} C / kg. \tag{2.2}$$

When the ferrite material is applied with external magnetic bias $\bar{H}_0$ a torque is exerted on the magnetic dipole that is given by,

$$\bar{T} = -\mu_0 \gamma \bar{s} \times \bar{H}_0. \tag{2.3}$$

Since the time rate of change of angular momentum produces the torque, the following relation is obtained

$$\frac{d\bar{m}}{dt} = -\mu_0 \gamma \bar{m} \times \bar{H}_0. \tag{2.4}$$

The relation given by (2.4) describes the motion of a magnetic dipole moment $\bar{m}$ inside the ferrite material when applied with the external magnetic bias $\bar{H}_0$. The relation given in (2.4) is for a magnetic dipole moment due to single spinning electron. Assuming there is N number of spinning electrons per unit volume, then the total magnetization value is given by,

$$\frac{d\bar{m}}{dt} = -\mu_0 \gamma \bar{M} \times \bar{H}_0, \tag{2.5}$$

where $\bar{M} = N\bar{m}$.

In the absence of external magnetic bias $\bar{H}_0$, the dipole moments are oriented more or less in random directions, producing a net-magnetization value of zero. When the ferrite material is applied with an external magnetic field, the magnetic dipole moments begin to align themselves in the direction of the applied field. At a certain value of the applied field, all the dipole moments

are aligned in one direction and the ferrite material is said to have reached a state of saturation magnetization.

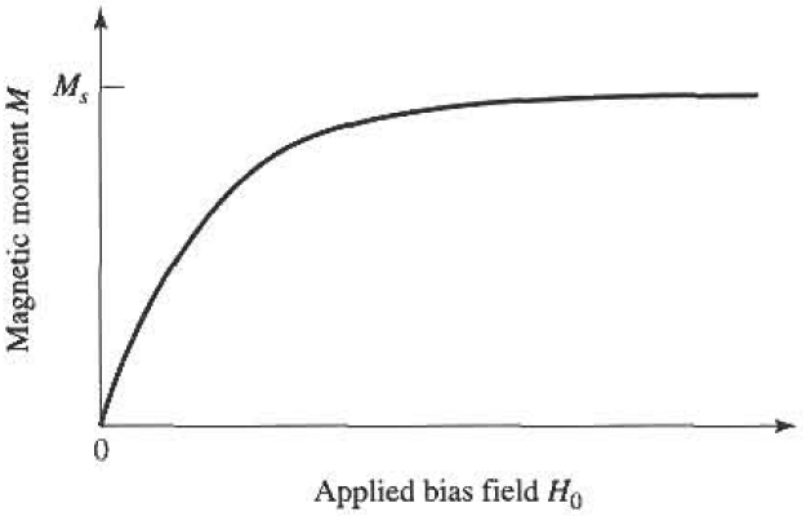

Figure 2.1-2: Magnetic moment of a ferrite material versus applied magnetic field, H_0 [Pozar (2005)].

In Fig. 2.1-2, a relation between the magnetic dipole moment M and the applied bias field is illustrated. It can be noted that the magnetic moment increases linearly with the applied field H_0 until it reaches a state of saturation magnetization M_s.

The relationship given by (2.5) describes the motion of dipole moments in ferrite material when applied with static DC magnetic bias, where the dipole moments are in a natural state of free precession around $\bar{H}_0$ axis. As illustrated in Fig. 2.1-1, it has to be noted that the natural precession of the dipole moments around $\bar{H}_0$ axis, exists as long as the ferrite material is lossless. In the presence of loss or the damping force, the natural precession of the dipole moments cease to exists and its motion will spiral down to align with the axis $\bar{H}_0$.

Until now it has been assumed that, the ferrite material is applied only with the static magnetic bias field. When a magnetically saturated ferrite is applied with small signal AC (microwave) magnetic field, the dipole moments will undergo a forced precession around the $\bar{H}_0$ axis. The frequency of precession of the dipole moments depends upon the frequency of the applied AC field. Hence the total magnetic field and magnetization value become,

$$\bar{H}_t = \bar{H}_0 + \bar{H}. \qquad (2.6)$$

And

$$\bar{M}_t = \bar{M}_S + \bar{M}. \tag{2.7}$$

In (2.6) and (2.7), $\bar{H}_t$ and $\bar{M}_t$ represent the total magnetic field and magnetization values, and $\bar{H}$ and $\bar{M}$ represent the magnetic field and magnetization value due to the small signal AC magnetic field. In [Fuller (1987)] and [Pozar (2005)], a linear relationship between $\bar{H}$ and $\bar{M}$ has been derived which is given by,

$$\bar{M} = [\chi]\bar{H} = \begin{bmatrix} \chi_{xx} & \chi_{xy} & 0 \\ \chi_{yx} & \chi_{yy} & 0 \\ 0 & 0 & 0 \end{bmatrix} \bar{H}, \tag{2.8}$$

where $[\chi]$ is the tensor susceptibility whose elements are given by,

$$\chi_{xx} = \chi_{yy} = \frac{\omega_0 \omega_m}{\omega_0^2 - \omega^2}. \tag{2.9}$$

$$\chi_{xy} = -\chi_{yx} = \frac{j\omega\omega_m}{\omega_0^2 - \omega^2}. \tag{2.10}$$

In the above derivation of components of susceptibility, it has been assumed that the direction of the applied static magnetic bias is along *z*-direction as illustrated in Fig. 2.1-1. In (2.9) and (2.10), $\omega_0 = \mu_0 \gamma H_0$, $\omega_m = \mu_0 \gamma M_S$ and ω is the angular velocity of applied AC signal.

From the tensor susceptibility, the relation for tensor permeability can be derived, which is given by,

$$[\mu] = \mu_0 \left([U] + [\chi] \right) = \begin{bmatrix} \mu & j\kappa & 0 \\ -j\kappa & \mu & 0 \\ 0 & 0 & \mu_0 \end{bmatrix} \tag{2.11}$$

The above relation is for *z*-direction biased ferrite.

The elements of the permeability tensor are given by,

$$\mu = \mu_0 \left(1 + \chi_{xx}\right) = \mu_0 \left(1 + \chi_{yy}\right) = \mu_0 \left(1 + \frac{\omega_0 \omega_m}{\omega_0^2 - \omega^2} \right), \tag{2.12}$$

$$\kappa = -j\mu_0 \chi_{xy} = j\mu_0 \chi_{yx} = \mu_0 \frac{\omega\omega_m}{\omega_0^2 - \omega^2}. \tag{2.13}$$

For *x*- and *y*- direction biased ferrite, the permeability tensor will be of different form. For $\bar{H}_0 = \hat{x} H_0$,

$$[\mu] = \begin{bmatrix} \mu_0 & 0 & 0 \\ 0 & \mu & j\kappa \\ 0 & -j\kappa & \mu \end{bmatrix}. \tag{2.14}$$

Similarly for $\bar{H}_0 = \hat{y}H_0$,

$$[\mu] = \begin{bmatrix} \mu & 0 & -j\kappa \\ 0 & \mu_0 & 0 \\ j\kappa & 0 & \mu \end{bmatrix}. \tag{2.15}$$

In (2.12) and (2.13), when Larmor frequency is equal to the frequency of the applied small signal (AC), then the elements of the permeability tensor becomes infinite. Physically, this happens when the forced precession frequency of the dipole moments becomes equal to the free precession frequency. However, every ferrite materials suffer from magnetic losses, which will avoid this singularity. The effect of the magnetic loss can be taken into consideration by making the resonant frequency complex

$$\omega_0 \Rightarrow \omega_0 + j\alpha\omega. \tag{2.16}$$

In (2.16), α is the damping or the loss factor. Thus, after substituting the value of ω_0 in (2.9) and (2.10), the susceptibility values become complex and their real and imaginary parts can be written as [Pozar (2005)],

$$\chi'_{xx} = \frac{\omega_0\omega_m\left(\omega_0^2 - \omega^2\right) + \omega_0\omega_m\omega^2\alpha^2}{\left[\omega_0^2 - \omega^2\left(1+\alpha^2\right)^2 + 4\omega_0^2\omega^2\alpha^2\right]}. \tag{2.17}$$

$$\chi''_{xx} = \frac{\alpha\omega\omega_m\left[\omega_0^2 + \omega^2\left(1+\alpha^2\right)\right]}{\left[\omega_0^2 - \omega^2\left(1+\alpha^2\right)^2 + 4\omega_0^2\omega^2\alpha^2\right]}. \tag{2.18}$$

$$\chi'_{xy} = \frac{\omega\omega_m\left[\omega_0^2 - \omega^2\left(1+\alpha^2\right)\right]}{\left[\omega_0^2 - \omega^2\left(1+\alpha^2\right)^2 + 4\omega_0^2\omega^2\alpha^2\right]}. \tag{2.19}$$

$$\chi'_{xy} = \frac{2\omega_0\omega_m\omega^2\alpha^2}{\left[\omega_0^2 - \omega^2\left(1+\alpha^2\right)^2 + 4\omega_0^2\omega^2\alpha^2\right]}. \tag{2.20}$$

Using the relationship between tensor permeability and tensor susceptibility as given (2.12) and (2.13), a similar set of equations can be derived for tensor permeability. In the above relations,

the damping factor as represented by α is also related to the line width ΔH of the susceptibility curve near the resonance.

In this work, two different ferrite materials, namely YIG and Nickel ferrite ($NiFe_2O_4$), are considered in the realization of SIW based magnetically tunable devices. YIG is a ferrimagnetic material whereas Nickel ferrite is composed of Nickel and Oxides. Ferrimagnetic materials possess higher resistivity and anisotropy compared to ferromagnetic materials [Pozar (2005)]. Both YIG and Nickel (Ni) ferrite are manufactured at National Magnetics Groups TCI ceramics, PA, USA. The two materials possess completely different properties in terms of losses and magnetization values. YIG is low-loss material, with low value of saturation magnetization and Ni ferrite suffers from higher magnetic losses and its saturation magnetization value is also high. Because of the diverse nature of the two materials, they are considered to be used in the development of novel microwave tunable devices based on SIW technology. In Table 2.1, some of the properties of the two materials are compared:

Table 2.1: Comparison between YIG and Ni ferrite:

Ferrite material	**Saturation Magnetization ($4\pi Ms$)**	**Line width (ΔH)**	**Dielectric constant (ε_r)**
YIG	1780 G	≤17 Oe	15
NiFe2O4	5000 G	≤198 Oe	13.1

Based on the information provided in Table 2.1 and using the relations given by (2.12) and (2.13), the components of the permeability tensor for YIG and Ni ferrite are plotted in Fig. 2.1-3 and Fig. 2.1-4. By considering the effect of magnetic loss as given in (2.6), the components of permeability tensor becomes complex, yielding dissipative and dispersive components of tensor permeability.

In Fig. 2.1-3 and Fig. 2.1-4, calculated dissipative and dispersive components of YIG and Ni ferrite are plotted against the internal magnetic field H_i. The permeability components of an infinite ferrite medium are plotted based on the provided values of Ms and ΔH values of YIG and Ni ferrite. The permeability components are calculated at an intended design frequency of 12 GHz

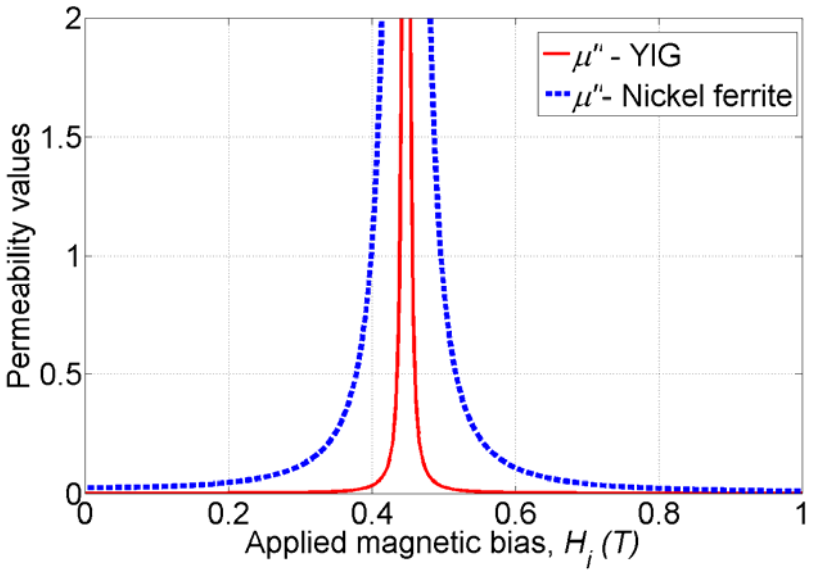

Figure 2.1-3: Calculated dissipative components of YIG and Nickel ferrite's complex tensor permeability. .

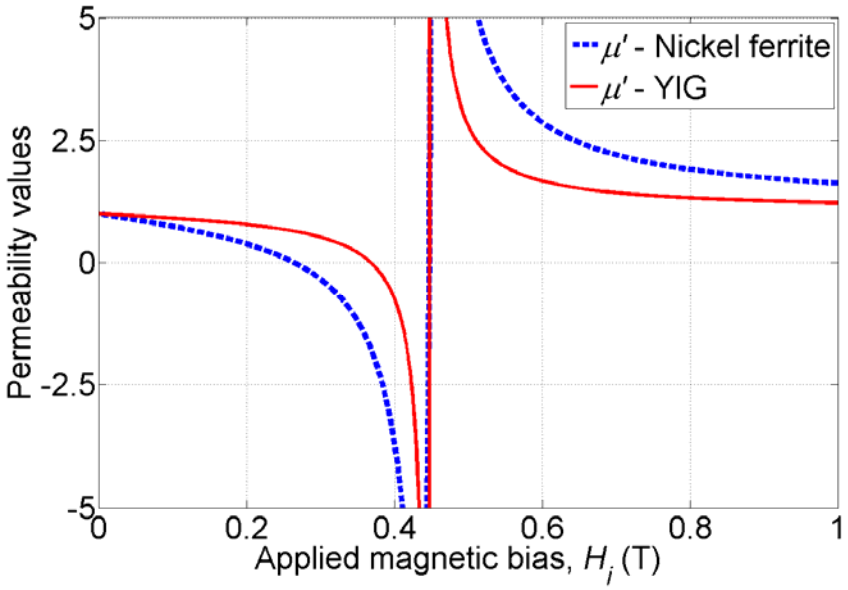

Figure 2.1-4: Calculated dispersive components of YIG and Nickel ferrite's complex tensor permeability. .

In Fig. 2.1-3 and Fig. 2.1-4, the ferromagnetic resonance region occurs near 0.45 T of applied magnetic bias H_i. Since the line width value (ΔH) of Ni ferrite is much higher than YIG, in Fig. 2.1-3, the magnetic loss due to Ni ferrite begins to increase significantly even from 0.2 T of applied magnetic bias H_i. Near the ferromagnetic resonance region, the Ni ferrite suffers from much higher losses compared to YIG. Due to higher magnetic loss near the ferromagnetic resonance region, the tunable devices presented in the next sections will be designed in the region

below the ferromagnetic resonance. Similary in Fig. 2.1-4, it can be noted that the rate of change of dispersive permeability component μ' of Ni ferrite below the ferromagnetic resonance region is much higher compared to YIG. This suggests, even a low value of magnetic bias is sufficient to produce a significant change in the dispersive permeability component value of Ni ferrite. Hence, it can be concluded that, due to the low loss property, YIG is more suitable in the design of low loss devices where the tunablitly is not important. Whereas, Ni ferrite is suitable in the design of highly tunable devices where some magnetic losses are tolerable. Therefore, in this work, YIG is used in the realization of low-loss tunable resonators and filters, while due to high tunability, Ni ferrite is used in the realization of non-reciprocal devices like gyrator and circulator, where all the designs are based on SIW technology.

2.2 Substrate integrated waveguide (SIW)

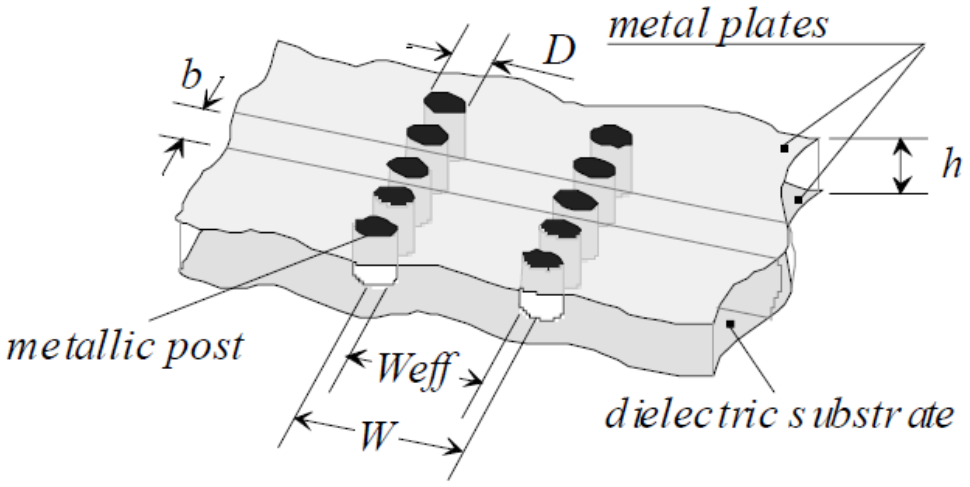

Figure 2.2-5: Schematic of an SIW guide realized on planar dielectric substrate [Wu, Deslandes, and Cassivi (2003)].

SIW is a new type of transmission line, which combines the features of both rectangular waveguide and planar transmission lines. Similar to rectangular waveguide, the SIW is a single conductor device. Therefore, SIW cannot support TEM mode of transmission. As illustrated in Fig. 2.2-5, it consists of a substrate material coated with metal plates on its both sides. Two rows of parallel metallic via posts or slots are made connecting the top and bottom conductors to guide the electromagnetic signal. Since, via posts are placed in a discrete fashion and do not form the continuous wall, they pose the discontinuity for a surface current on the SIW walls. Therefore,

SIW are not capable of supporting TM modes. Being a single conductor device they support only TE type of modes in this case. SIW inherits almost all the properties of a rectangular hollow waveguide. It is lower in loss, and can handle also a higher power compared to other planar transmission lines. However, the power handling capability of SIW is lower and the losses of SIW are higher compared to rectangular hollow waveguide, due to the presence of dielectric material. Thus, the performance of SIW is largely dependent also upon the selection of dielectric material and geometrical topology.

As illustrated in Fig. 2.2-5, the diameter D of holes, the spacing b between holes, and the spacing W between the two rows are the physical parameters that are necessary for the design of the guide. There are basically two design rules that must be followed in realizing the SIW guide given by,

$$D<\lambda_g / 5 \tag{2.21}$$

$$b \leq 2D \tag{2.22}$$

In (2.21), λ_g is the guided wavelength. The above two rules are necessary to follow for realizing an optimal SIW guide with negligible radiation loss. Once the design rules are met, the SIW can be modeled with reference to a conventional rectangular waveguide design.

In Fig. 2.2-6 and Fig. 2.2-7, electric and magnetic field vectors of SIW transmission lines are presented. The field components are plotted for dominant TE_{101} mode of SIW. As it can be seen the field vectors are orthogonal to the direction of propagation of wave. The electric field strength is highest along the central region while the magnetic field strength is highest along the sidewalls.

In this work, a new type of tunable device based on ferrite loaded substrate integrated waveguide (FLSIW) is presented. Unlike the conventional bulky designs, it is a purpose of this work to realize planar ferrite based components and devices. SIW technology inherits almost all the properties of rectangular waveguide, and still it is planar in nature making suitable candidate for the realization of planar ferrite based tunable devices. Moreover, it has a higher power handling capability compared to other planar counterparts; therefore a highly tunable microwave components and devices for high power applications can be realized using the combination of SIW and ferrite materials.

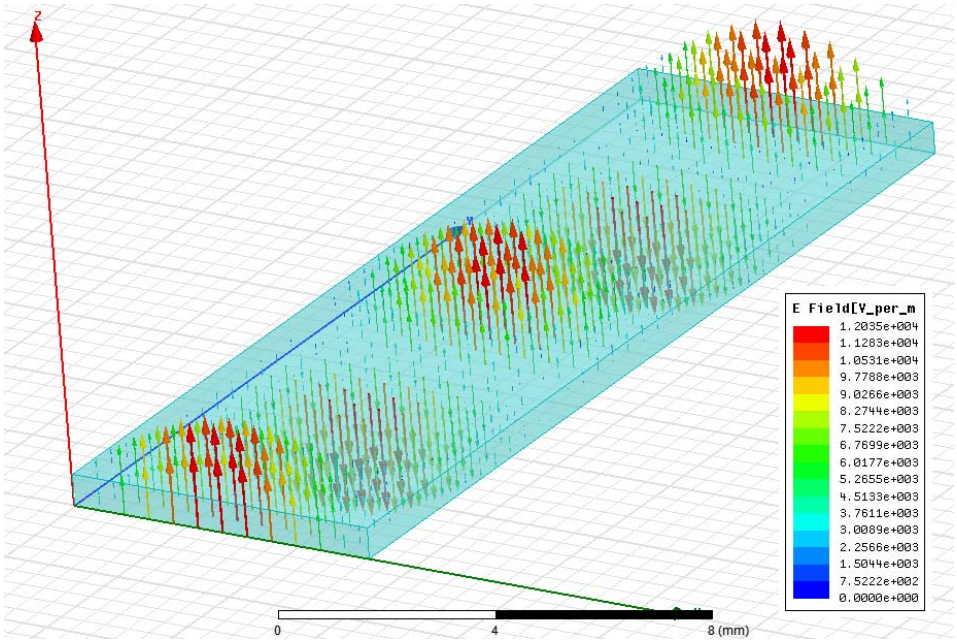

Figure 2.2-6: Simulated SIW transmission line which illustrates the electric field component of dominant TE_{10} mode.

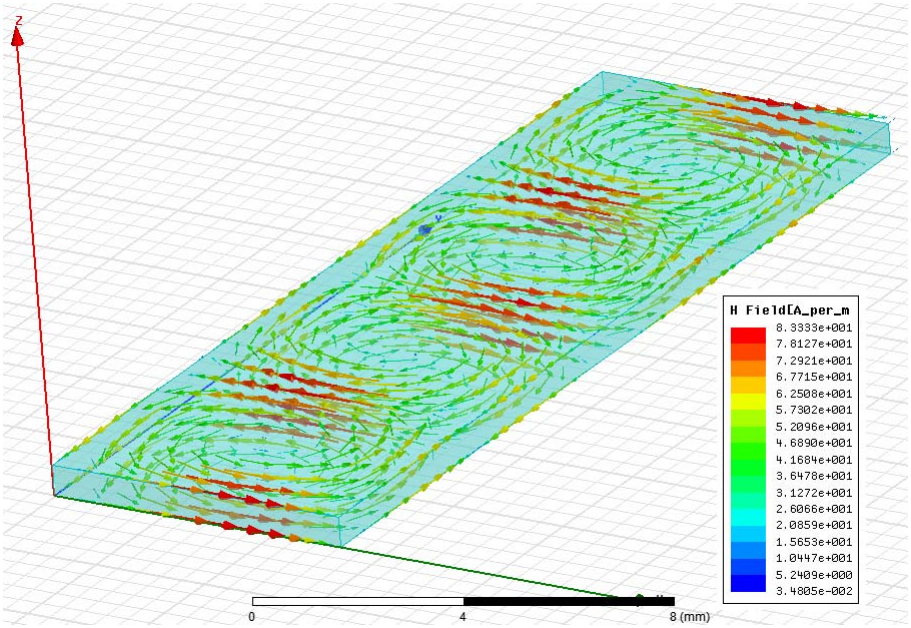

Figure 2.2-7: Simulated SIW transmission line which illustrates the magnetic field component of dominant TE_{10} mode.

CHAPTER 3 MAGNETICALLY TUNABLE SIW BASED DEVICES

In this chapter, magnetically tunable devices based on SIW technology are presented. The magnetic tuning is achieved by loading the ferrite materials onto the sidewalls of SIW lines where the magnetic field strength of the dominant TE_{10} mode is highest. The ferrite materials that are used in this work are polycrystalline ferrites, which are cut into pieces to fit into the slots that are created inside the SIW.

3.1 Ferrite loaded SIW

In literature, it can be found that, most of the ferrite based devices are based on rectangular waveguide technology, which is bulky in nature. However, due to their large geometry, they cannot be easily integrated with other planar circuitries. It is thus, a purpose of this work to bring the ferrite based devices into planar forms and also it suggests a suitable biasing mechanism for it. Since SIW technology inherits almost all the properties of rectangular waveguide, and still is planar in nature, it is a suitable candidate for the realization of planar ferrite based tunable devices. Moreover, it has a higher power handling capability compared to other planar counterparts; therefore a highly tunable microwave components and devices for high power applications can be realized using the combination of SIW and ferrite materials.

3.2 Ferrite loaded SIW cavity resonator

SIW technology is used to design a magnetically tunable ferrite-loaded cavity resonator. The high *Q* characteristic and easy integration of ferrite slabs in SIW based transmission lines present a motivation in the design and realization of this magnetically tunable resonator. The evaluation of ferrite-tuned resonant cavities in a rectangular waveguide was first made by Fay [Fay (1956)]. In [Fay (1956)], a single ferrite slab was loaded along the end wall of the cavity. A DC magnetic field, orthogonal to the direction of the propagation of the electromagnetic field was applied, to tune the cavity`s resonant frequency. In [He, et al (2010)], an electronically tunable SIW cavity at *X*-band was demonstrated, where a varactor diode was used to tune the cavity electronically. In this work, a magnetically tunable SIW cavity resonator is presented and experimentally demonstrated. Planar ferrite slabs are loaded along the sidewalls of the SIW, where the value of magnetic field is the highest. External magnetic bias is applied to alter the effective permeability

of ferrite slabs, which in turn changes the resonant frequency of the cavity. To compare the results obtained from [Fay (1956)], and [He, et al. (2010)], 12 GHz is deliberately chosen to be the design frequency. Measurement and simulation results of frequency tuning ranges and *Q*-factors of single and double ferrite loaded cavities are presented. It is seen from the measurement results that the frequency tuning range is more than 10% at *X*-Band which is significantly higher compared to the varactor tuned cavity resonator reported by [He, et al. (2010)].

3.2.1 Theoretical and topological considerations

SIW cavity design

SIW technology is used to realise a magnetically tunable ferrite loaded cavity resonator. The cavity resonator is designed to resonate at 12 GHz, with TE_{101} as a fundamental mode of operation.

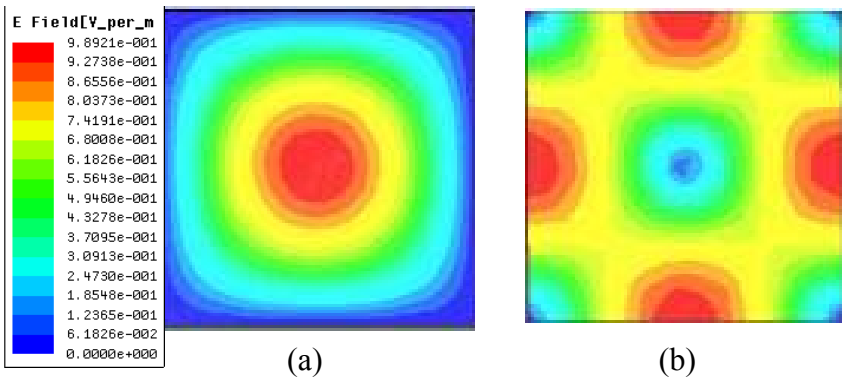

Figure 3.2-1: Top view of a simulated rectangular cavity resonator displaying (a) Electric field of dominant TE_{101} mode and (b) Magnetic field of dominant TE_{101} mode.

In Fig. 3.2-1, the field plot of a cavity resonator obtained from the eigen-mode simulation using Ansoft HFSS 13.0 is presented. As illustrated in Fig. 3.2-1 (a) and Fig. 3.2-1 (b), the dominant TE_{101} mode of the cavity has a maximum value of electric field at its center and a maximum value of magnetic field along its sidewalls. Since ferrite materials interact strongly with the externally applied magnetic field, it is advantageous to place them along the sidewalls of the cavity. Placing the ferrite slabs along the sidewalls not only enhances their interaction with the magnetic field present in the cavity, but also the dielectric loss ($\tan\delta$) which is due to the interaction between the material and the electric field also reduces. Hence, keeping the ferrite

slabs along the sidewalls of the cavity not only enhances the magnetic tunability but at the same time reduces the dielectric losses.

In Fig. 3.2-2 the fabricated prototype of an SIW cavity resonator is presented. As illustrated, the SIW cavity has a square geometry with equal length L and width W. The thickness of the cavity along y-direction is represented by t. The gap between the rectangular metallic slots L_G holds the substrate together and its appropriate size L_S reduces the wave leakages subjected to SIW. The signal is coupled into the cavity by means of a short circuited section of a Conductor Backed Coplanar Waveguide (CBCPW). In 3.2-2, the width of the CBCPW line is represented by C_W and the gap between the line and the ground plane is represented by C_G.

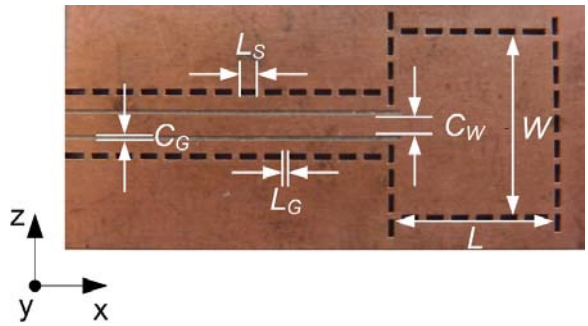

Figure 3.2-2: Fabricated SIW cavity resonator at 12 GHz.

Since the propagation of a TE_{10}-like mode in SIW is similar to the TE_{10} mode of a rectangular cavity, the resonant frequency of the cavity in SIW is given by [Cassivi, Wu (2003)],

$$f_{\mathbf{r}(\mathbf{TE}_{\mathbf{m0q}})} = \frac{c_0}{2 \cdot \sqrt{\mu_{\mathbf{r}} \varepsilon_{\mathbf{r}}}} \sqrt{\left(\frac{m}{W}\right)^2 + \left(\frac{q}{L}\right)^2}. \qquad (3.1)$$

In (3.1), f_r is the resonant frequency of the TE_{m0q} mode, W and L are the width and the length of the cavity, respectively. Since metallic via slots are used in synthesizing the rectangular cavity, it has enabled the use of actual dimensions of the cavity in (3.1) instead of the effective dimensional values.

Ferrite loaded SIW cavity

It has been mentioned in the previous section that, due to the presence of the highest magnetic fields, ferrite slabs are loaded along the sidewalls of the SIW cavity. In Fig. 3.2-3, the top views of the fabricated SIW cavity loaded with two planar ferrite slabs are illustrated. It can be seen that the ferrite slabs are covered with highly conducting tapes on both sides in order to achieve upper

and lower metal covering. For a better contact with the SIW, the conductor tapes are soldered along its periphery.

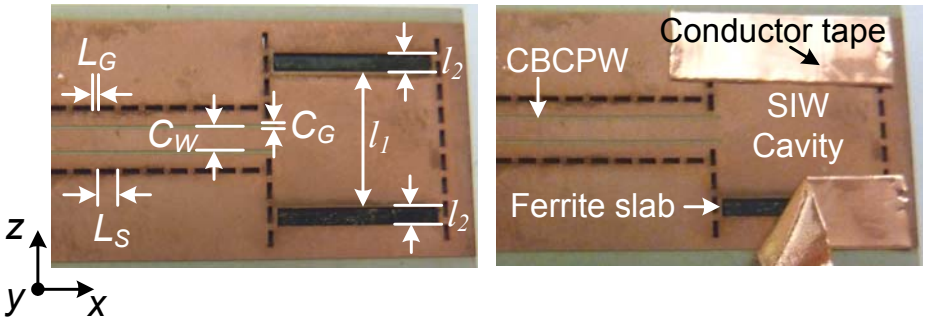

(a) (b)

Figure 3.2-3: Fabricated SIW cavity loaded with two rectangular ferrite slabs along the sidewalls.

In Fig. 3.2-4, the cross-sectional views of the ferrite loaded cavity of Fig. 3.2-3 when viewed in *yz*-plane are presented. In Fig. 3.2-4, the width of the substrate section and the width of the ferrite sections are represented by l_1 and l_2, respectively. Static magnetic bias H_0 is applied along the *y*-direction as indicated, which is parallel to the direction of the electric field vector of the TE_{101} mode.

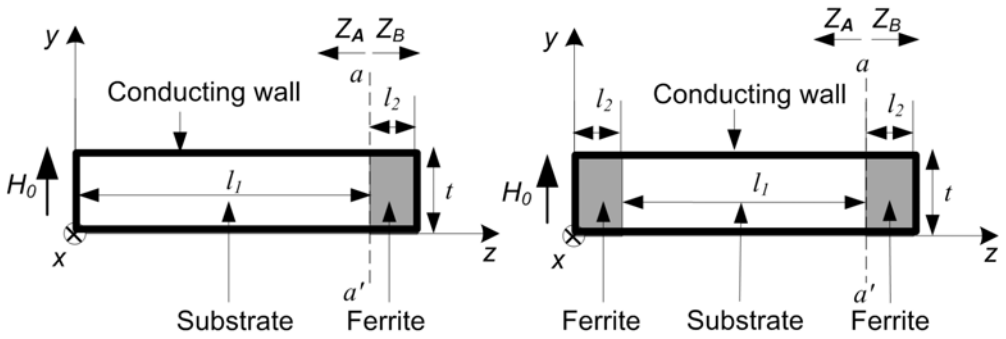

(a) (b)

Figure 3.2-4: Cross-sectional view of the SIW cavity loaded with (a) a single ferrite slab and (b) two ferrite slabs along the side walls.

The width of the substrate section and the width of the ferrite slabs along *z*-direction are represented by l_1 and l_2, respectively. In order to evaluate the property of the ferrite loaded SIW cavity resonator, transmission line theory is used to determine its characteristic equation. The solution of the characteristic equation will provide a relationship between the resonant frequency of the cavity and the applied DC magnetic bias. As illustrated in Fig. 3.2-4(a) and Fig. 3.2-4(b),

single and double ferrite loaded cavity resonators will separately be considered to determine their respective frequency tuning curves.

Single ferrite loaded SIW cavity:

In Fig. 3.2-4(a), the input impedance Z_B seen from the reference plane aa' towards the ferrite loaded section is,

$$Z_B = jZ_{ef} \tan\left(\beta_f l_2\right), \tag{3.2}$$

where Z_{ef} is the wave impedance of the ferrite section, β_f is the propagation constant of the ferrite loaded section. The expression for Z_{ef} is given by,

$$Z_{ef} = \sqrt{\frac{\mu_0 \mu_e}{\varepsilon_0 \varepsilon_f}} \frac{\lambda_{gf}}{\lambda_0}. \tag{3.3}$$

In (3.3), μ_e is the effective permeability of the ferrite material, λ_{gf} is the guided wavelength of the ferrite loaded section, ε_f is the permittivity of the ferrite material and λ_0 is the free space wavelength. The effective permeability μ_e is a tensor permeability given by [Pozar (2005)],

$$\mu_e = \frac{\mu'^2 - \kappa'^2}{\mu'^2}, \tag{3.4}$$

where μ' and κ' are the components of Polder tensor, which describe the permeability of a ferrite material and μ_e is the effective permeability of a plane wave that is propagating transverse to the direction of applied DC magnetic bias. At the cavity resonance frequency, the sum of imaginary parts of the impedances seen looking towards the short-circuited ferrite section and the short-circuited substrate section must be equal to zero,

$$\mathrm{Im}\left\{Z_A\right\} + \mathrm{Im}\left\{Z_B\right\} = 0. \tag{3.5}$$

In (3.5), 'Im' represents the imaginary part of the term inside the parenthesis. Therefore, using the transmission line theory in (3.5), the following characteristic equation is obtained,

$$Z_{ef} \tan\left(\beta_f l_2\right) + Z_{es} \tan\left(\beta_s l_1\right) = 0, \tag{3.6}$$

where Z_{es}, and β_s are wave impedance and propagation constant of the short-circuited substrate section. Thus (3.6) is the characteristic equation of a lossless single ferrite loaded SIW transmission line.

Double ferrite loaded SIW cavity:

In Fig. 3.2-4(b), from reference plane *aa'*, the impedance seen looking towards the short-circuited section containing both ferrite and substrate is given by,

$$Z_A = Z_{es}\frac{jZ_{ef}\tan\left(\beta_f l_2\right)+jZ_{es}\tan\left(\beta_s l_1\right)}{Z_{es}-Z_{ef}\tan\left(\beta_f l_2\right)\tan\left(\beta_s l_1\right)}. \tag{3.7}$$

Similarly, the impedance seen looking towards the short-circuited ferrite loaded section is,

$$Z_B = jZ_{ef}\tan\left(\beta_f l_2\right). \tag{3.8}$$

At the cavity resonance frequency, the sum of the imaginary parts of the impedances given by (3.7) and (3.8) is equal to zero. Hence, the characteristic equation of the two ferrite slabs loaded SIW cavity resonator is given by,

$$Z_{ef}\tan\left(\beta_f l_2\right)+\mathrm{Im}\left\{Z_{es}\frac{jZ_{ef}\tan\left(\beta_f l_2\right)+jZ_{es}\tan\left(\beta_s l_1\right)}{Z_{es}-Z_{ef}\tan\left(\beta_f l_2\right)\tan\left(\beta_s l_1\right)}\right\}=0 \tag{3.9}$$

The solution of (3.6) and (3.9) will yield the frequency tuning curves of single and double ferrite loaded cavity resonators when applied with an external DC magnetic bias.

3.2.2 Theoretical and measurement results

The cavity resonator is fabricated using RT/Duroid 6002 substrate. The dielectric constant of the substrate is $\varepsilon_s = 2.94$, loss tangent ($\tan\delta$) = 0.0012. The cavity is designed to resonate at a frequency of 12.6 GHz, hence from (3.1), the length and the width of the cavity are $W = L = 9.8$ mm, respectively. For the cavity resonators illustrated in Fig. 3.2-2, the length of metallic slots L_s is 0.94 mm and the gap between slots L_G is 0.4 mm. Using Agilent Advanced Design System's line calculation tool, for a 50 Ω CBCPW line, the width C_W and the gap C_G are calculated to be 1.2 mm and 0.2 mm, respectively. Yttrium Iron Garnet (YIG) is chosen as a ferromagnetic material to be placed inside the SIW resonant cavity. YIG is chosen as a frequency tunable element because of its low magnetic loss property. The line width (ΔH) of the YIG is 17 Oe. Its saturation magnetisation value is $Ms = 1780$ Gauss. As indicated in Fig. 3.2-3, the ferrite slab and the substrate have the same thickness of $t = 0.762$ mm along y-direction. As shown in Fig. 3.2-3, rectangular slots are created on the substrate where the ferrite slabs are inserted. In order to create a constant metallic wall for the ferrite, one of the sidewalls of the slot

is completely metalized along its length. As shown in Fig. 3.2-3(a) and Fig. 3.2-3(b), the ferrite slabs are covered by copper conductor tape on both sides of the cavity, in order to provide an upper and lower metal covering. To insure a good contact between the tape and the cavity, tin-lead is soldered around the conductor tapes. The ferrite loaded SIW cavity is also simulated in HFSS 15.0 before fabricating the prototype.

For YIG, with the given values of saturation magnetization Ms = 1780 Gauss and line width ΔH = 17 Oe, the effective permeability value of an infinite ferrite medium is calculated [Pozar (2005)]. Based on (3.4), in Fig 3.2-5, the dispersive and dissipative components of permeability tensor of YIG is presented.

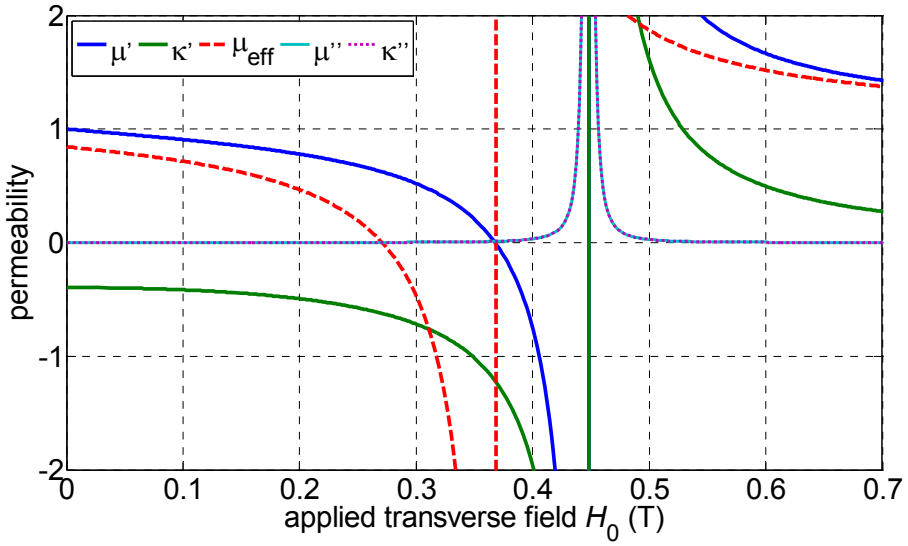

Figure 3.2-5: Calculated relative permeability components of YIG ferrite versus applied magnetic field (H0) in Tesla, μ' and κ' are dispersive permeability components, μ'' and κ'' are dissipative loss components and μ_e is the effective permeability.

In Fig. 3.2-5, the value of μ_e progressively decreases from the initial value of 0.84 as the applied bias field is increased. At 0.27 T, the value of μ_e is equal to zero. Beyond this value, loss increases due to the ferromagnetic resonance that occurs at 0.45 T of applied magnetic bias. Thus, the region below the ferromagnetic resonance is chosen for the tuning purpose as it offers lower loss and low value of applied magnetic bias is required to obtain the desired tuning effect. The permeability components in Fig. 3.2-5 are plotted against the internal magnetic field of the ferrite. In practice, the external field required to bias the ferrite for a given frequency is higher than the value of the internal field. The difference between the internal and the external magnetic

fields is due to the demagnetization factor of the ferrite, which is in turn dependent on the geometry of the ferrite material and the direction of the applied magnetic bias.

In Fig. 3.2-6, measurement results of an SIW resonant cavity containing one single ferrite slab along its sidewall as indicated in Fig. 3.2-4(a) is presented. It can be seen that, with the increasing value of an applied external magnetic field on the cavity, the resonant peaks move towards the higher frequency values.

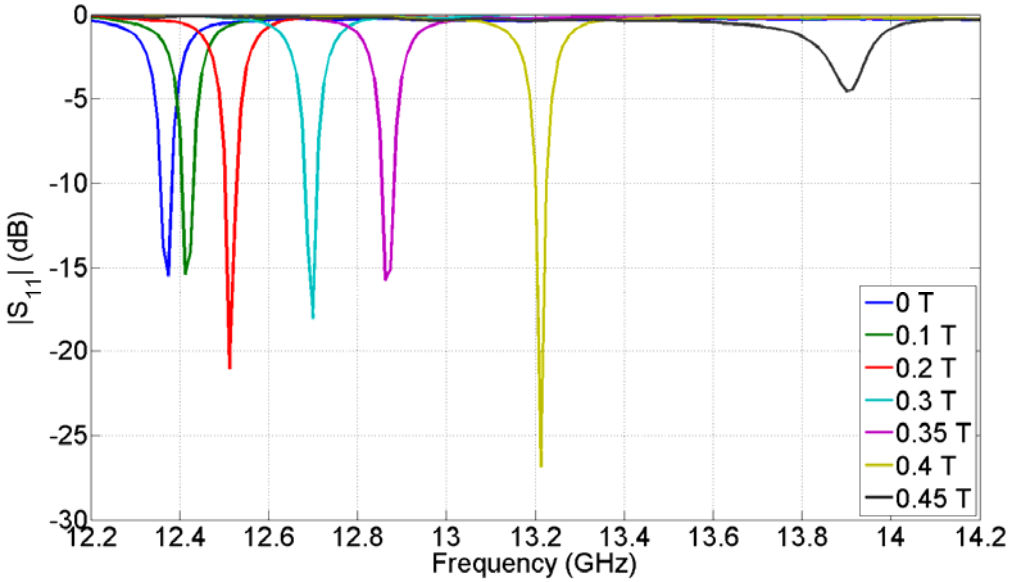

Figure 3.2-6: Measurement results displaying the resonant peaks of a single ferrite loaded cavity resonator versus frequency.

It can be seen from Fig. 3.2-6, there is a non-linear shift of the resonant peaks towards higher frequency value for a linear increase in the values of an applied magnetic bias. This could be explained from Fig. 3.2-5, where the relationship between μ_e values with the applied magnetic bias is also non-linear. Since the resonant frequency is inversely proportional to the square root of permeability, any decrease in the permeability value will result in the increase of the resonant frequency. Hence, the non-linear shift of the resonant peaks towards the higher frequency values is due to the non-linear reduction of μ_e values with the applied magnetic bias.

In Fig. 3.2-5, at 0.27 T of externally applied magnetic bias, the effective permeability value μ_e becomes negative and decreases rapidly until the ferromagnetic resonance region is reached at 0.4 T. Beyond 0.4 T of applied magnetic bias, the magnetic loss due to the property of ferrite material increases sharply. In Fig. 3.2-5, the ferromagnetic resonance region is in the region near 0.4 T of applied magnetic bias, where the dissipative permeability component values μ'' and κ''

increase sharply. In Fig. 3.2-6, at 0.45 T of externally applied magnetic bias, it can be observed that, the resonant peak suffers from a high level of attenuation. Hence it can be concluded, with the increase in the value of applied magnetic bias, the resonant peaks of the cavity move towards a higher frequency value until they suffer from high value attenuation near the ferromagnetic resonance region. Therefore, the designed resonator is suitable to be used only in the region below the ferromagnetic resonance where the magnetic losses of the ferrite material are lowest.

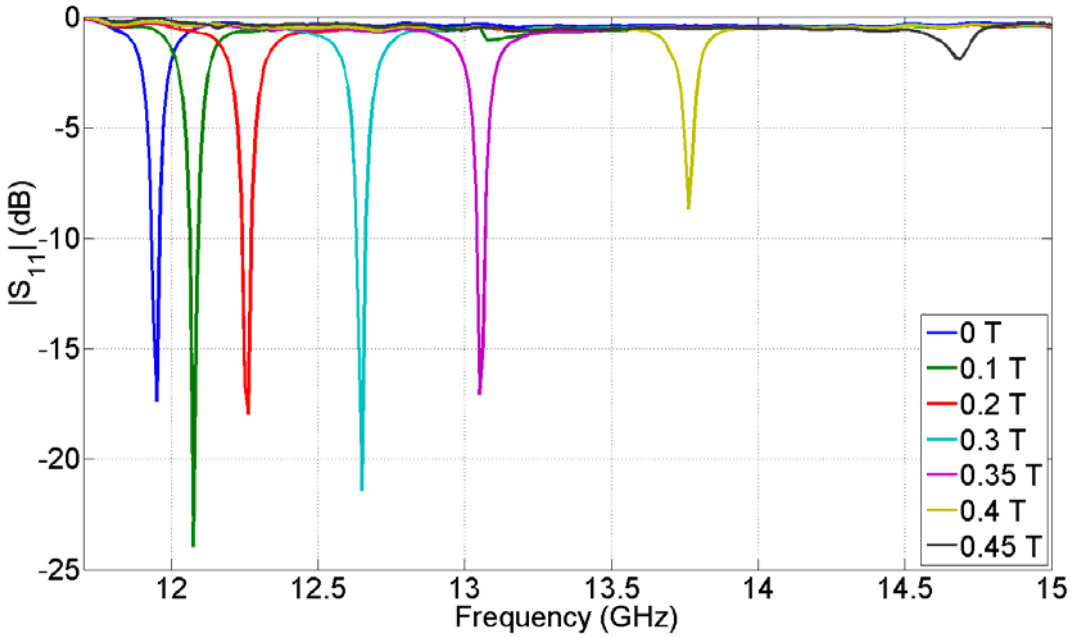

Figure 3.2-7: Measurement results displaying the resonant peaks of a double ferrite slabs loaded cavity resonator versus frequency.

In Fig. 3.2-7, measurement results of an SIW cavity resonator loaded with two ferrite slabs are presented. Similar to the case of the single ferrite loaded cavity resonator, with the application of the applied magnetic bias, the resonant frequency of the cavity shifts towards the higher frequency values. It can be noted that, due to increase in the volume of ferrite material inside the cavity, less amount of magnetic bias is required to achieve the same frequency shift when compared to the scenario of single ferrite loaded cavity resonator. For example, in Fig. 3.2-7 for a double ferrite loaded cavity resonator, when magnetic bias is increased from 0 T to 0.35 T, the net frequency shift is 700 MHz. Whereas in Fig. 3.2-6 when the magnetic bias is increased from 0 T to 0.35 T, the net frequency shift is only 480 MHz. Thus, it can be concluded that increasing the volume of the ferrite also increases the total tunable frequency range for a given value of applied magnetic bias.

A theoretical analysis is made in order to better understand a relationship between the frequency tuning range and the applied magnetic bias. The characteristic equation of (3.6) and (3.9) for a lossless SIW cavity loaded with single and double ferrite slabs are solved analytically to find the resonant frequency tuning curve. Newton Raphson method of iteration [Pozar, 2005] is used to find the frequency roots of the equations given in (3.6) and (3.9).

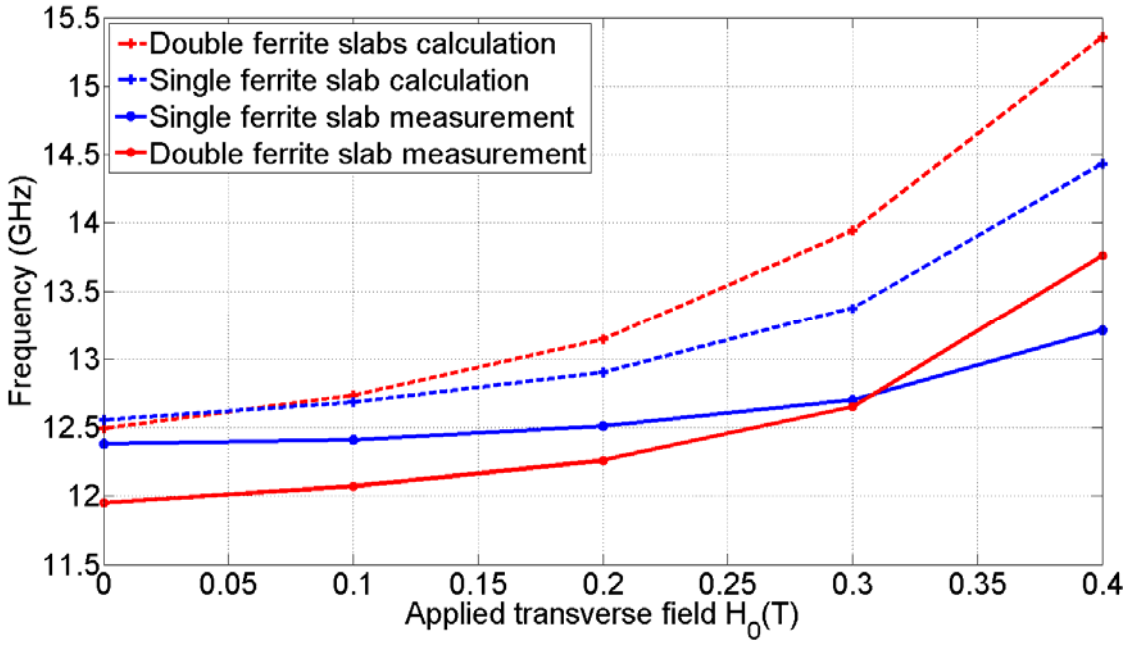

Figure 3.2-8: Calculate and measured tuning curves of single and double ferrite slabs loaded SIW cavity resonator.

Fig. 3.2-8, illustrates the comparison between measured and calculated frequency tuning curves of single and double ferrite slabs loaded SIW cavity resonator. The calculated curves are obtained by finding the roots of (3.6) and (3.9). Both in the measurement and in the calculation, the width of the ferrite slabs is $l_2 = 1$ mm and the width of the substrate section is $l_1 = W\text{-}l_2$ for a single ferrite loaded cavity and $l_1 = W\text{-}2l_2$ for a double ferrite loaded cavity. Calculations do not include magnetic and electric losses. As can be seen, the tuning curves are non-linear functions of applied magnetic bias. The non-linear behaviour increases with the increase of applied magnetic bias. In Fig. 3.2-8, calculated curves are plotted against the internal magnetic field while the measured curves are plotted against the externally applied magnetic field. The difference between the calculated and measured frequency tuning curves can be explained due to tolerance in the fabrication of the prototype, and also due to demagnetization factor of the ferrite slabs. As can be seen with two ferrite slabs loaded SIW cavity resonator, higher frequency tuning range is

achieved compared to the case of single ferrite loaded cavity. Thus, based on the theoretical analysis and measurement results, increasing the volume of the ferrite would increase the total frequency range of the cavity. In Fig. 3.2-9, measurement results of unloaded *Q*-factor of the ferrite loaded SIW cavity resonator are presented. Results are presented for single and double ferrite loaded SIW cavity resonators.

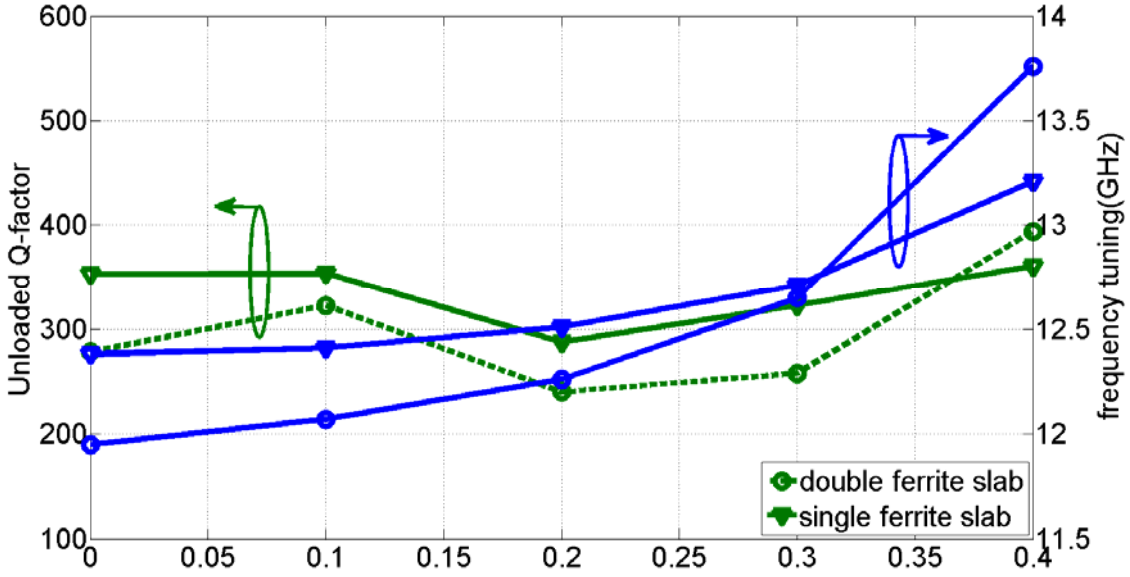

Figure 3.2-9: Measurement results of unloaded Q-factors and resonant frequency versus applied magnetic bias for single and double ferrite loaded SIW cavity resonators.

In Fig. 3.2-9, in order to better understand the effect of losses when tuning the resonant cavity, both frequency tuning curves and unloaded *Q*-factors are plotted in the same figures. The unloaded *Q*-factor is calculated from the resonant frequency and 3-dB bandwidth of measured S_{11} parameter of the under-coupled cavity resonator. As can be seen, compared to single ferrite loaded cavity, double ferrite loaded cavity offers more losses. Thus, based on Fig. 3.2-8 and Fig. 3.2-9, increasing the volume of the ferrite material increases the total frequency tuning range but at the same time the total loss of the cavity also increases.

3.3 Magnetically tunable ferrite loaded SIW oscillator

In this section, a magnetically tunable and planar feedback-loop oscillator on the basis of the SIW technology is presented. The oscillator consists of a magnetically tunable SIW cavity resonator which is connected to the input and output of an amplifier to form a closed feedback loop. In Fig. 3.3-10, the schematic of a feedback loop magnetically tunable oscillator is presented. The

topology consists of a ferrite loaded magnetically tunable cavity resonator connected between the input and output terminals of a broadband amplifier. The total gain of the loop including the cavity and the amplifier is positive and the length of the cavity is adjusted such that the total phase shift around the loop is 0° or $2\pi n$ [Cassivi, Wu (2003)], where n is a positive integer number.

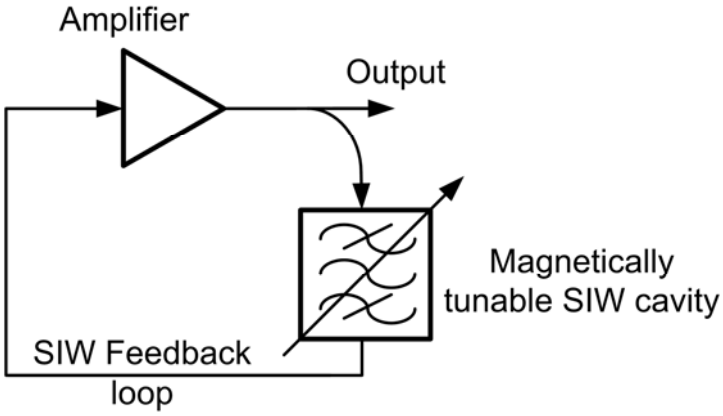

Figure 3.3-10: Schematic of magnetically tunable feedback loop oscillator.

With the application of a transverse external DC magnetic bias on the ferrite loaded cavity, the resonant frequency of the cavity as well as the 0° phase condition of the feedback loop are changed to higher frequency values. Thus, with the application of an external magnetic field, the oscillations occur at the successive frequency values, where the positive loop-gain and the 0° or $2\pi n$ conditions are again satisfied. In [He, et al. (2010)], an electronically tunable *X*-band oscillator based on SIW cavity resonator was presented. The resonant frequency of the SIW cavity was tuned by a DC-voltage bias over a varactor coupled to the cavity. While in this work, by the application of an external static magnetic field, the relative permeability of the ferrite slabs loaded inside the SIW cavity is changed, thereby making the cavity`s resonant frequency tunable. Moreover, it is also demonstrated that, by replacing the applied static DC bias with alternating magnetic bias, the output of the oscillator is modulated by the frequency of the applied AC signal current. In the design of the oscillator, Ansoft's HFSS 13.0 and Agilent's ADS 2009 were used as simulation tools.

3.3.1 Multilayer ferrite loaded SIW (FLSIW) cavity resonator

In Section 3.2, the theoretical and measurement results of an SIW cavity resonator loaded with single and double ferrite slabs along the sidewalls slots were presented. Measured frequency

tuning range of 10% was reported. In this Section, all four sidewalls of SIW cavity are exploited by placing rectangular ferrite slabs on them. The total frequency range of the four ferrite slabs loaded is determined both analytically and experimentally. In the later section, thanks to low loss and high tunability of magnetically tunable cavity resonator, a frequency tunable low phase noise feedback-loop oscillator is developed and presented. Comparison of the total tuning range and the phase noise of the oscillator consisting of cavity resonator separately loaded with single, double and four ferrite slabs are presented and discussed.

Theory of multi-layer SIW cavity resonator

SIW cavity resonator is fabricated in a two-layered printed circuit board and it is fed by SIW sections of transmission lines as shown in Fig. 3.3-11 [Hwang, Pan (2007)].

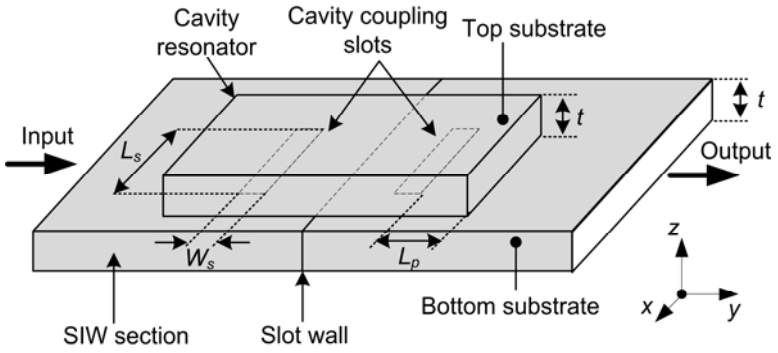

(a)

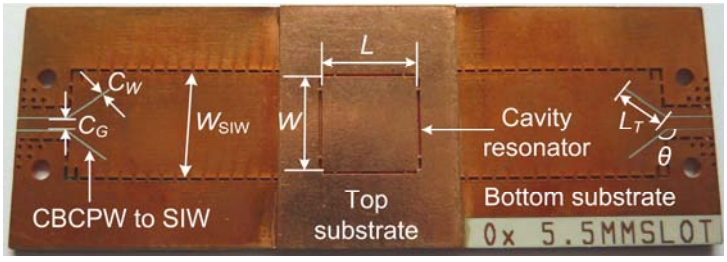

(b)

Figure 3.3-11: Multilayered SIW cavity resonator (a) Cross-sectional schematic with Ls = 5.5 mm, Ws = 0.5 mm, Lp = 3 mm (b) Top view of the fabricated cavity with W_{SIW} = 12 mm, C_W = 1.2 mm, C_G = 0.2 mm, W = 9.8 mm, L = 9.8 mm, L_T = 5.25 mm, θ = 35°.

In Fig. 3.3-11, the cross sectional schematic and fabricated prototype of a multilayer SIW cavity resonator are illustrated. The cavity resonator is on the top layer and the SIW feeding sections are on the bottom layer. The cavity has a square geometry of equal length L and width W. The

thickness of the cavity along *z*-direction is denoted by *t*. In the four ferrite slabs loaded cavity resonator, using CBCPW as a feeding element will create a discontinuity along the ferrite length. Therefore, the cavity resonator is placed in a different layer and fed from the SIW sections using rectangular coupling slots having length L_s and width W_s. A slot wall at the center of the SIW section prevents the direct propagation of the signal from the input port to the output port of the SIW section instead of getting coupled through the cavity. Similar to the single layer cavity resonator, in the multi-layer cavity resonator of Fig. 3.3-11 the dominant mode of resonance is also TE_{101}. Hence, the relation given by (3.10) is also valid for the evaluation of the multi-layer cavity resonator of Fig. 3.3-11.

Theory of SIW cavity loaded with four ferrite slabs

Determination of the characteristic equation of a four ferrite slabs loaded cavity involves three steps. In the first step, propagation constant β_s of an SIW transmission line section of length l_1 loaded with twin ferrite slabs on each side wall as shown in Fig. 3.3-12(a) and 3.3-12(b) is determined. The ferrite slabs are loaded parallel to *xz*-plane. In Fig. 3.3-12, both the ferrite slabs are biased reciprocally along *z*-direction.

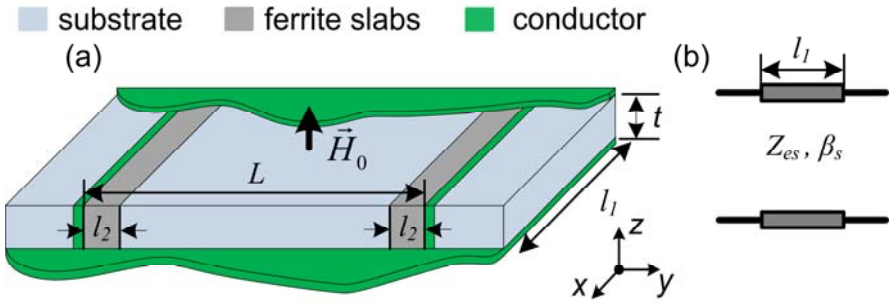

Figure 3.3-12: Twin ferrite slabs loaded SIW section of length l_1 a) schematic representation b) equivalent transmission line model.

In [Lax, and Button (1962)] the characteristic equation of a rectangular waveguide loaded with twin ferrite slabs was presented. Since SIW inherits most of the properties of a rectangular waveguide, hence the characteristic equation presented in [Lax, Button (1962)] is valid to characterize FLSIW transmission line.

The characteristic equation of a waveguide section loaded with twin-ferrite slabs along its sidewalls of Fig. 3.3-12 is given by,

$$\tan\left[\left(k_s\right)\left(L-2l_2\right)\right]=p/q, \tag{3.10}$$

where,

$$p=2\left(K_m\mu_0/\mu_e k_s\right)\cosh\left(K_m l_2\right)\sinh\left(K_m l_2\right), \tag{3.11}$$

$$q=\left[1-\left(\frac{\beta_s\mu_0}{\mu_e\theta k_s}\right)^2\right]\sinh^2\left(K_m l_2\right)-\left(\frac{\mu_0 K_m}{\mu_e k_s}\right)^2\cosh^2\left(K_m l_2\right), \tag{3.12}$$

$$K_m^2=-\omega^2\varepsilon_f\mu_e+\beta_s^2, \tag{3.13}$$

$$k_s^2=\omega^2\varepsilon_s\mu_0-\beta_s^2. \tag{3.14}$$

$$\theta=\frac{\mu'}{-j\kappa'}. \tag{3.15}$$

In (3.11) and (3.12) μ_0 is the free-space permeability. Fig. 3.3-12(b) presents the equivalent transmission line model of FLSIW presented in Fig. 3.3-12(a). The solution of (3.10) yields propagation constant β_s for various values of applied magnetic bias H_0.

In the second step for the determination of a characteristic equation, a cavity resonator loaded with two ferrite slabs along its end-wall is considered. Fig. 3.3-13 represents an SIW cavity resonator loaded with planar ferrite slabs along its two end-walls in *yz*-plane. Unlike Fig. 3.3-12, metallic walls are present on all sides to form a cavity resonator.

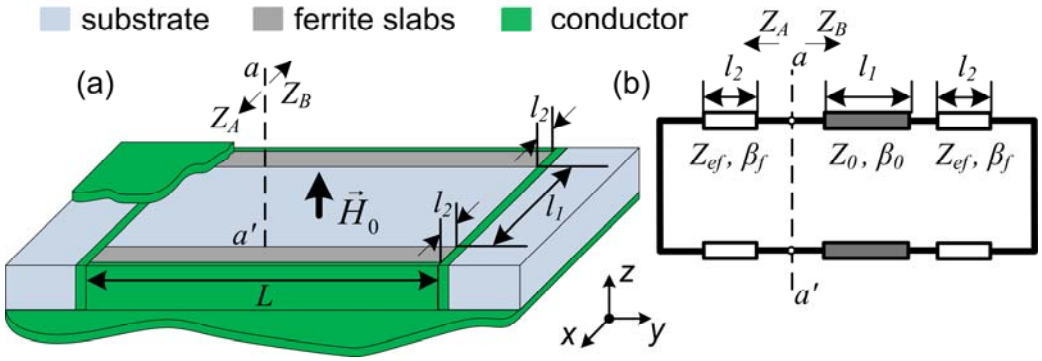

Figure 3.3-13: Double ferrite slabs loaded cavity resonator a) schematic representation b) equivalent transmission line model.

The width of the ferrite slabs is represented by l_2, and the length of a substrate section sandwiched between two ferrite slabs is represented by l_1. The impedance seen from reference plane *aa'* towards the ferrite section (positive *x*-direction) is,

$$Z_A = jZ_{ef}\tan\left(\beta_f l_2\right), \tag{3.16}$$

where,

$$Z_{ef} = \sqrt{\frac{\mu_0\mu_e}{\varepsilon_0\varepsilon_f}}\frac{\lambda_{gf}}{\lambda_0},, \tag{3.17}$$

$$\lambda_{gf} = \frac{\lambda_0}{\sqrt{1-\lambda_0/\left(2L\sqrt{\mu_e\mu_0\varepsilon_r\varepsilon_0}\right)}}. \tag{3.18}$$

In (3.16) and (3.17), Z_{ef} and β_f are wave impedance and propagation constant of the ferrite section and μ_e is the effective permeability of the ferrite material, which is given by,

$$\mu_e = \frac{\mu'^2 - \kappa'^2}{\mu'}. \tag{3.19}$$

In (3.19), μ' and κ' are components of the Polder Tensor, which describe the permeability of the ferrite material [Fay (1956)]. Similarly, the impedance seen from the reference plane *aa′* towards the substrate section of length l_1 and ferrite section l_2 (negative *x*-direction) is,

$$Z_B = Z_0\frac{jZ_{ef}\tan\left(\beta_f l_2\right) + jZ_0\tan\left(\beta_0 l_1\right)}{Z_0 - Z_{ef}\tan\left(\beta_f l_2\right)\tan\left(\beta_0 l_1\right)}, \tag{3.20}$$

where Z_0 and β_f are wave impedance and propagation constant of the substrate section of length l1. For a cavity resonating at a desired frequency, at the reference plane *aa′* the reactance looking into the ferrite section of length l_1 is equal to the negative of the total reactance seen looking towards the sections containing a substrate of length l_1 and ferrite of length l_2. Therefore, at the cavity resonance frequency the sum of the imaginary parts of the impedances seen looking from the reference plane *aa′* is equal to zero and it is given by the following relation,

$$0 = Z_{ef}\tan\left(\beta_f l_2\right) + \mathrm{Im}\left[Z_0\frac{jZ_{ef}\tan\left(\beta_f l_2\right) + jZ_0\tan\left(\beta_0 l_1\right)}{Z_0 - Z_{ef}\tan\left(\beta_f l_2\right)\tan\left(\beta_0 l_1\right)}\right]. \tag{3.21}$$

In (3.21) ‘Im’ represents the imaginary part of the impedance enclosed inside the parenthesis. The relation given by (3.21) is a characteristic equation of the cavity containing two ferrite slabs as illustrated in Fig. 3.3-13(a) and Fig. 3.3-13(b).

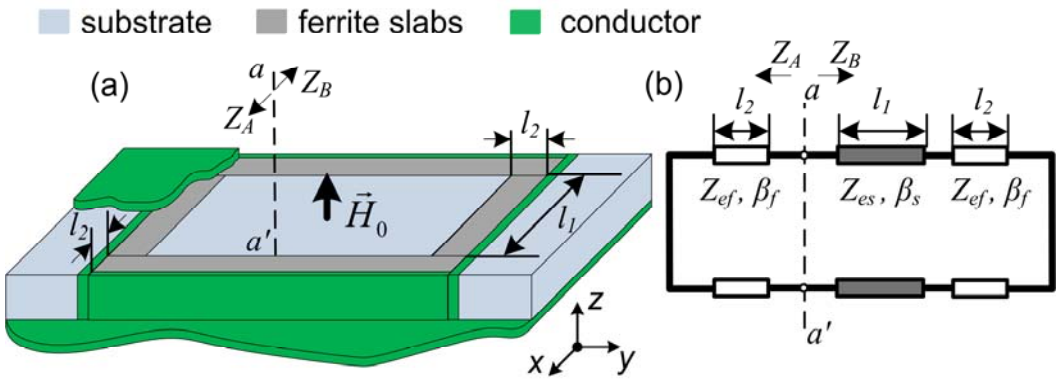

Figure 3.3-14: Four ferrite slabs loaded cavity resonator a) schematic representation b) equivalent transmission line model.

The cavity containing four ferrite slabs as illustrated in Fig. 3.3-14 can be viewed as a result of combining two ferrite slabs loaded SIW section of length l_1 of Fig. 3.3-12 with two ferrite slabs loaded cavity resonator of Fig. 3.3-13. Therefore, in the third step, the characteristic equation given by (3.21) will now represent the characteristic equation of four ferrite slabs loaded cavity of Fig. 3.3-14, if β_0 and Z_0 values are replaced by β_s and Z_{es} values in (3.21). Consequently, the characteristic equation for ferrite slabs loaded cavity resonator can be written as,

$$0 = Z_{ef}\tan\left(\beta_f l_2\right) + \mathrm{Im}\left[Z_{es}\frac{jZ_{ef}\tan\left(\beta_f l_2\right) + jZ_{es}\tan\left(\beta_s l_1\right)}{Z_{es} - Z_{ef}\tan\left(\beta_f l_2\right)\tan\left(\beta_s l_1\right)}\right]. \qquad (3.22)$$

For the applied magnetic field H_0, the solution of (3.22) will yield the resonant frequency value for the cavity resonator loaded with four ferrite slabs.

Calculation and measurement results

SIW cavity resonator and feedback loop oscillator are fabricated on RT/duroid 6002 substrate with thickness $t = 0.762$ mm, dielectric constant $\varepsilon_s = 2.94$ and dielectric loss $\tan\delta = 0.0012$. Rectangular slabs of YIG with low magnetic loss ($\Delta H \leq 17$ Oe) and low value of saturation magnetization ($4\pi M_S = 0.178$ T) are chosen to be placed inside the SIW cavity. The dielectric constant of the YIG is $\varepsilon_f = 15.1$.

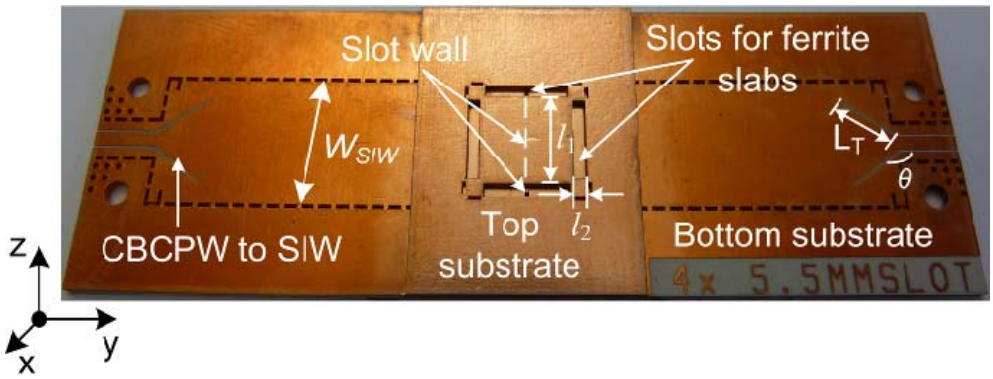

Figure 3.3-15: Top view of multilayered SIW cavity resonator containing four empty slots for loading ferrite slabs around the periphery of the cavity with $W_{SIW} = 12$ mm, $l_2 = 1.0$ mm, $l_1 = 8.8$ mm, $L_T = 5.25$ mm, $\theta = 35°$.

Fig. 3.3-15 illustrates a fabricated prototype of SIW cavity resonator. The cavity resonator is mounted on top of SIW feeding transmission line sections. The side-walls of the cavity resonator are cut to form rectangular hollow sections in order to accommodate the ferrite slabs. In order to hold the middle portion of the resonant cavity on the substrate, the corner square sections are still kept intact. Since the strength of magnetic field in the corner areas of the cavity is small, their effects in theoretical calculations are therefore neglected.

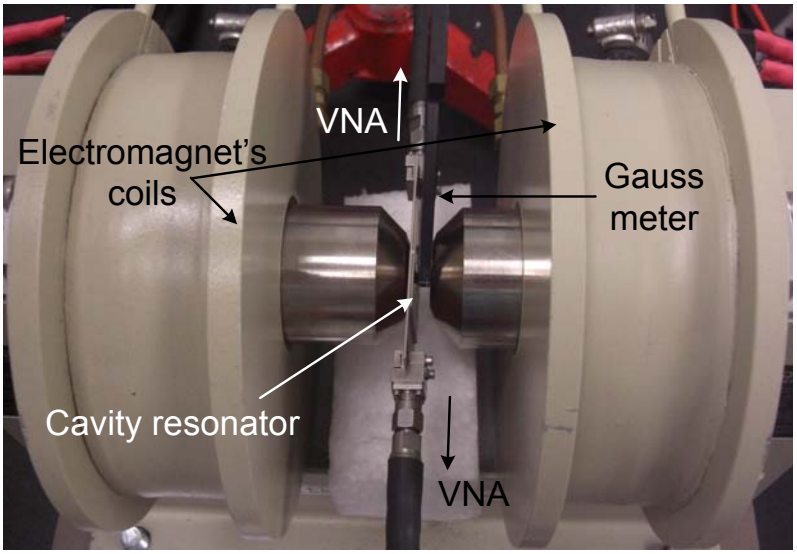

Figure 3.3-16: Measurement set-up of a ferrite-loaded cavity resonator.

Fig. 3.3-16 illustrates a set-up for the measurement of magnetically tunable SIW cavity resonator. To measure the transmission coefficients, the SIW cavity resonator is directly connected to the

input and output ports of a Vector Network Analyzer (VNA). In order to vary the resonance frequency, the ferrite loaded SIW cavities are placed between the two rods of the electromagnet, where the static magnetic field perpendicularly crosses the ferrite loaded cavity. For accurate measurements, Through-Reflect-Line (TRL) method is used to calibrate and de-embed the CBCPW to SIW transitions. The size of the ferrite slabs placed inside the cavity is 1 mm x 10 mm, which is much smaller than the (45 mm) diameter of the electromagnet's rod, hence the magnetic field inside the ferrite slabs is assumed to be uniform.

In Fig. 3.2-5, the permeability components of an infinite YIG ferrite medium [Pozar (2005)] are plotted. As can be seen, the ferromagnetic resonance occurs for an internal magnetic bias of approximately 0.45 T. Since SIW tunable cavity resonators and feedback-loop oscillator are operated in the region below the ferromagnetic resonance, the increase in magnetic loss at 0.45 T of internal magnetic field sets an upper limit in their tunability. The plotted permeability components of Fig. 3.2-5 refer to an infinite ferrite medium, and it can be noted that the effective permeability value μ_e, decreases non-linearly with the applied value of magnetic bias H_i. It can be noted from (3.10) that, the resonant frequency of a cavity is inversely proportional to the square root of the permeability value. Therefore, the cavity resonant frequencies f_0 is also expected to have a non-linear dependency with H_i. It is thus, a purpose of Fig. 3.2-5 to estimate the variation of f_0 curve against the applied magnetic field H_i, even before f_0 values are calculated or measured. In Fig. 3.2-5, the permeability components are plotted against the internal magnetic field H_i of the ferrite material. In practice, however, the value of H_i cannot be measured directly. A Gauss meter is generally used to measure the amount of magnetic bias applied to a ferrite material, but this measured value of magnetic field corresponds to external field. For orthogonally biased rectangular ferrite slab, a relationship between external and internal magnetic fields is given by [Pozar (2005)],

$$H_i = H_0 - N_z M, \tag{3.23}$$

where H_i is the internal magnetic field, H_0 is the external field applied perpendicularly to the ferrite material, M is the magnetization value of the ferrite material, and N_z is the demagnetization factor. The value of N_z is dependent on the direction of the applied external magnetic field, and the shape of the ferrite material. In [Aharoni (1998)], a closed-form relationship of the demagnetization factor of a rectangular prism is derived. For a YIG with length, l_1 = 8.8 mm,

width l_2 = 1 mm and thickness t = 0.762 mm, the value of demagnetization factor is calculated to be Nz = 0.53 [Aharoni (1998)].

From (3.23) it can be noted that, if the values of H_i and H_0 are known then for a given value of N_z, the magnetization value M can be easily obtained. Hence, in order to determine the values of M for a given value of internal or external magnetic bias H_i, a cavity resonator loaded with a single ferrite slab at the end-wall is considered. The characteristic equation of a single ferrite loaded cavity is solved to obtain the desired theoretical frequency tuning curve. The measurement tuning curve is obtained by measuring the resonant frequency of the cavity for increasing values of externally applied magnetic field H_0.

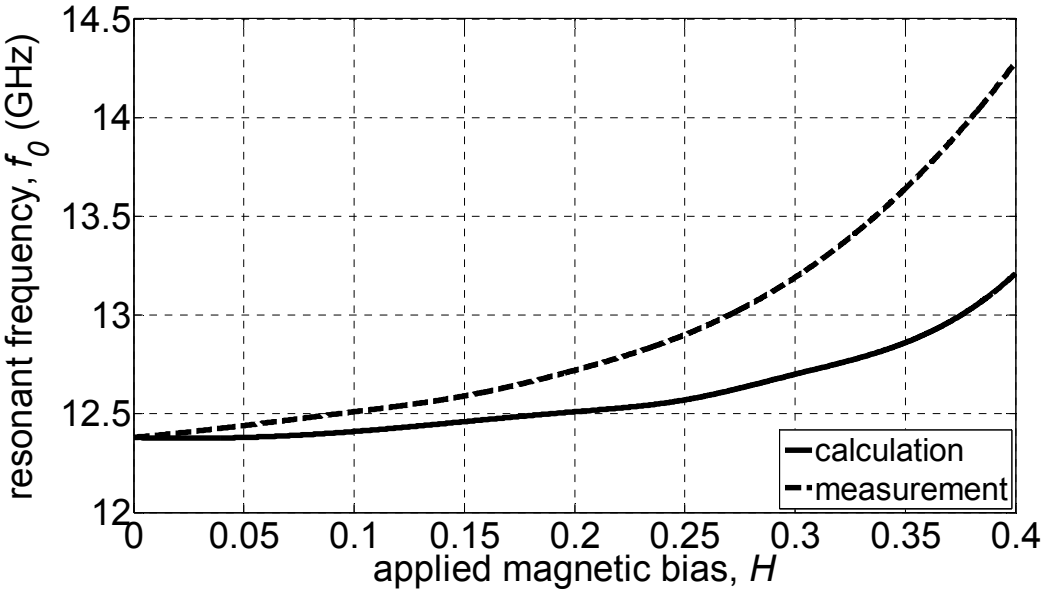

Figure 3.3-17: Measured and calculated frequency tuning curves of SIW cavity resonator loaded with a single ferrite slab.

In Fig. 3.3-17, the measured and calculated frequency tuning curves of an SIW cavity resonator loaded with a single ferrite slab is presented. The calculated tuning curve is plotted against H_i values, while the measured tuning curve is plotted against H_0 values. For a given value of the cavity resonant frequency, once the values of H_i and H_0 are determined, using (3.23), the magnetization value M of the ferrite material can be easily determined. For the calculation of magnetization values, the values of H_i and H_0, corresponding to the same cavity resonant frequency, are considered.

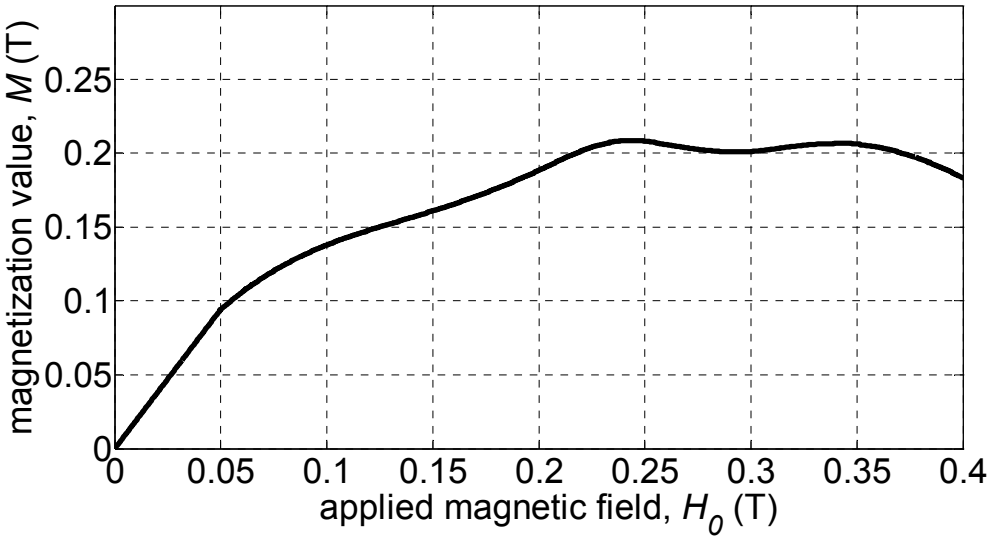

Figure 3.3-18: Calculated magnetization value of rectangular YIG prism, where the length and width of the rectangular prism are 8.8 mm and 1 mm respectively.

Fig. 3.3-18, a calculated M value of YIG is plotted against the externally applied magnetic field H_0. The calculated magnetization M values are due to the material property of YIG. It indicates how the ferrite material behaves and attains its saturation magnetization, when applied by static or DC magnetic bias in a given direction. Thus, for a given shape and size of YIG, and with the calculated M and N_z values, the relationship between internal H_i and external H_0 magnetic fields can be easily established.

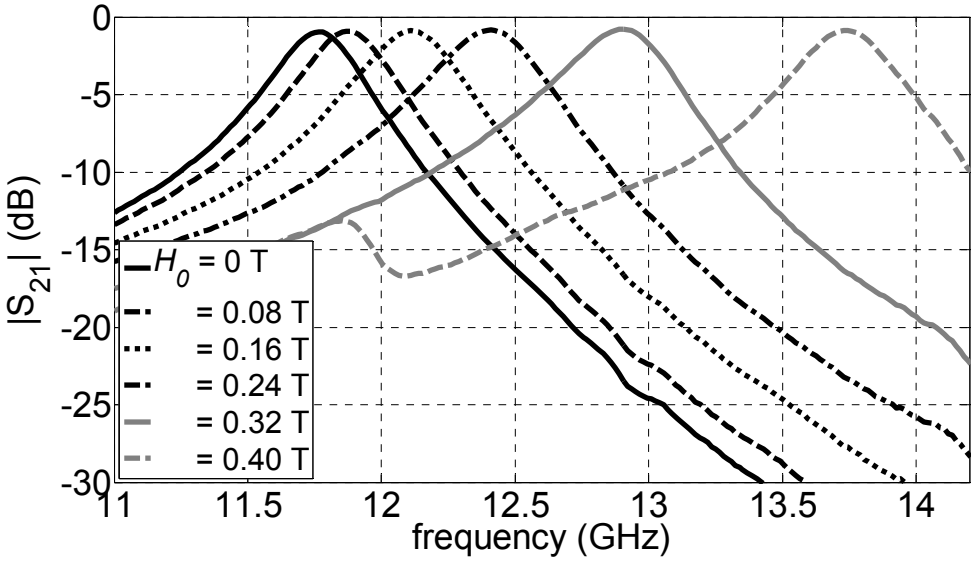

Figure 3.3-19: Measurement results of multi-layer cavity resonator.

Fig. 3.3-19 illustrates the two port measurement results of a four ferrite loaded SIW cavity

resonator. It can be seen that with the increase of applied magnetic bias, the resonant frequency of the cavity move towards the higher frequency values. In Fig. 3.3-19, for $H_0 = 0$ T, the cavity resonant frequency is 11.7 GHz, and for $H_0 = 0.4$ T the cavity resonant frequency is 13.74 GHz. Therefore, the total frequency tuning range is approximately 16%. This value of total tuning range is a significant improvement compared to the results presented for single and double ferrite slabs loaded cavities and to the results presented in [He and Wu (2009)], where the frequency tuning range was limited to 10%. Therefore, the cavity frequency tuning range depends upon the volume of ferrite material loaded inside it. Thus, instead of only loading the ferrite slabs along the sidewalls of the cavity, even higher frequency tunability can be achieved by completely filling the cavity with a ferrite slab. However, for a cavity operating in a dominant TE_{101} mode, the highest value of magnetic fields exists only along the sidewalls and the highest value of electric field occurs at the central region. Therefore, increasing the ferrite width up to the center of the cavity will increase the dielectric loss not only due to the presence of maximum value of electric field, but also due to the absence of magnetic field not a significant improvement in tuning will be achieved. Therefore, completely filling a cavity operating in dominant TE_{101} with a ferrite material inside is not advantageous.

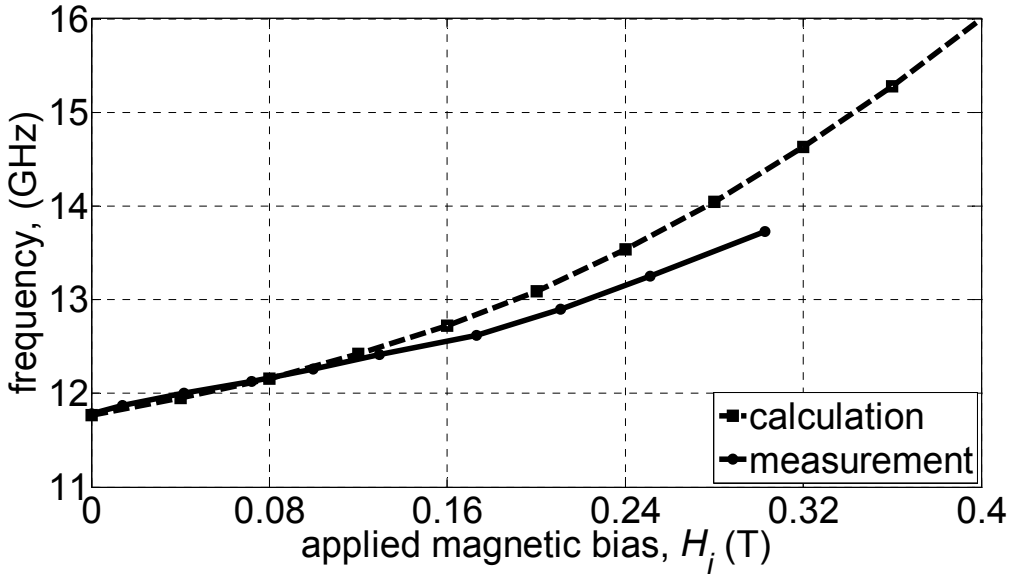

Figure 3.3-20: Plot of calculated and measured frequency tuning curves of four ferrite slabs loaded SIW cavity resonator.

In Fig. 3.3-20, the frequency tuning curves of a four ferrite loaded cavity resonator obtained from the solution of (3.22) and from the measurement result of Fig. 3.3-19 are plotted together. Both

the tuning curves are plotted against the internal magnetic bias H_i of the ferrite. The measured and calculated results are in close agreement for lower values of H_i, the maximum deviation between these two curves is approximately equal to 5% at $H_i = 0.3027$ T. As mentioned previously, using a Gaussmeter, it is only possible to measure the applied magnetic field H_0 external to the ferrite material. However, for the given value of demagnetization factor $N_z = 0.53$ and the magnetization value obtained from Fig. 3.3-18, the value of internal magnetic field H_i is calculated from H_0 based on the relation given by (3.23). Therefore, in Fig. 3.3-20, the frequency points do not correspond to the same value of H_i.

3.3.2 Measurement results of magnetically tunable SIW oscillator

In this section, measurement results of a magnetically tunable oscillator are presented. Measurements are performed for the cavity resonator loaded with single, double and four ferrite slabs along its sidewalls respectively.

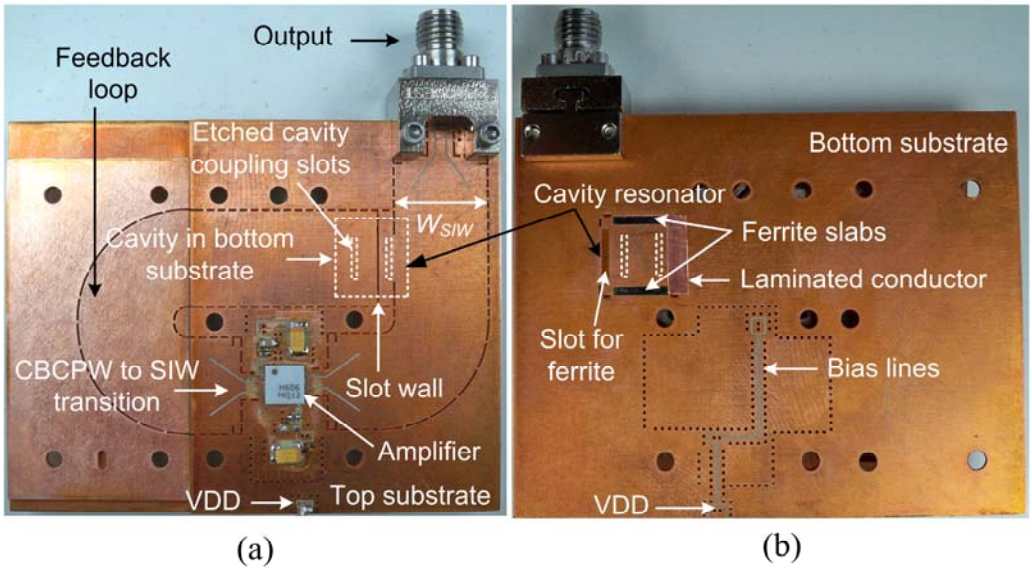

Figure 3.3-21: Fabricated multilayered magnetically tunable SIW feedback-loop oscillator (a) top view (b) bottom view.

Fig. 3.3-21 illustrates the top and bottom views of the fabricated SIW feedback-loop oscillator that consists of a magnetically tunable ferrite loaded SIW cavity resonator. The top substrate of the fabricated oscillator consists of an amplifier, CBCPW to SIW transitions, an output coupler and feedback loop, while the cavity resonator is placed on the bottom substrate as indicated by

the dotted white marks in Fig. 3.3-21. The cavity is fed from the SIW sections by using cavity couplings slots etched in the inner conductor layer as also indicated by the white marks. As previously mentioned, in order to place four ferrite slabs around the periphery of an SIW cavity, a multi-layered topology of the oscillator is chosen. The cavity is connected in a feedback loop with Hittite's HMC606LC5 amplifier. Rectangular ferrites slabs of width $l_2 = 1$ mm are placed along the sidewall slots of the cavity, where the magnetic field of the dominant TE_{101} mode is the highest. The feedback loop oscillator including the SIW cavity resonator is fabricated on Rogers RT/duroid substrate, which has a dielectric constant value of $\varepsilon_s = 2.94$ and thickness $t = 0.762$ mm.

Open-loop measurement results

For a feedback type circuit, oscillation occurs for positive loop gain and $0°$ or $2\pi n$ phase shift conditions around the loop are satisfied. In order to get a better insight into gain and phase relationship of the magnetically tuned oscillator, an open loop measurement involving the amplifier, the ferrite loaded cavity resonator and a section of the feedback loop is performed. The open loop measurement provides valuable information such as the unusual effects due to biasing network and possibility of out of band oscillation conditions.

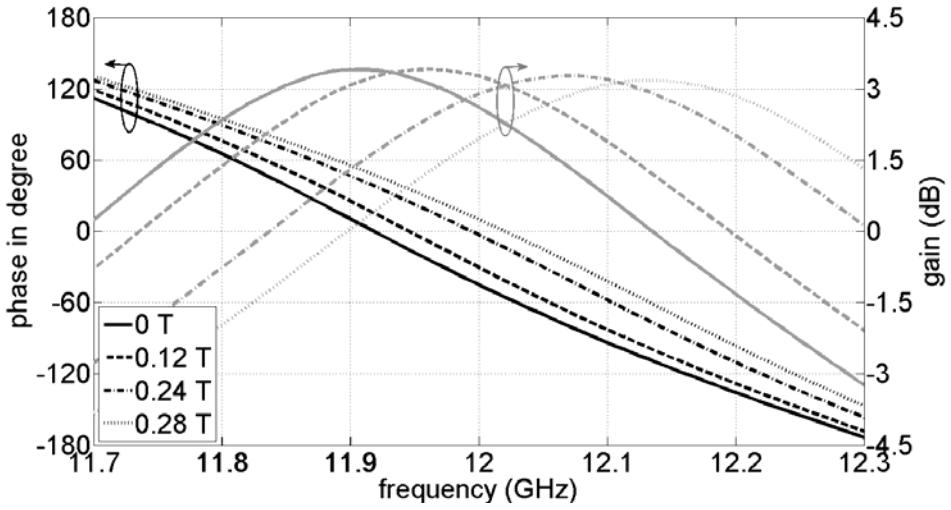

Figure 3.3-22: Measurement of open-loop gain and phase versus applied magnetic field H_0 for a single ferrite loaded SIW cavity with ferrite width $l_2 = 1$mm.

In Fig. 3.3-22, the open loop measurement of the magnetically tunable oscillator is presented. The measurement results are obtained for the SIW cavity when loaded with one ferrite slab along

its sidewall slots. As it can be seen from Fig. 3.3-22, by increasing the external magnetic bias, the gain and the phase curves shift towards the higher frequency values. It can be noted that the gain and the phase shifting are not synchronous with the applied magnetic bias. When the applied magnetic bias is 0 T, the open loop gain peak and the zero phase crossing are aligned at 11.92 GHz. As the bias is increased to 0.12 T, the open loop gain peak is at 11.96 GHz while the zero phase crossing is at 11.94 GHz. Similarly, at 0.28 T of applied magnetic bias, the peak of the open loop is at 12.14 GHz, while the zero phase crossing is still at 12.02 GHz. Thus, it can be observed that this synchronous shifting of the open loop gain and zero phase crossing increases with the applied magnetic bias. Due to such an asynchronous shifting of the gain and phase curve, at a very high value of the applied magnetic field, the condition of positive loop gain and zero phase crossing is no longer satisfied, thus putting an upper limit in the total tuning range of the oscillator. However, by keeping the length of the feedback loop as short as possible and increasing the gain margin up to the maximum acceptable value of 8 dB [Meskoob, and Prasad (1992)] can improve the tunability of the oscillator. Thus, the limitation of the oscillator tunability relies on the total phase of the feedback loop and the gain of the amplifier

Close-loop measurement results

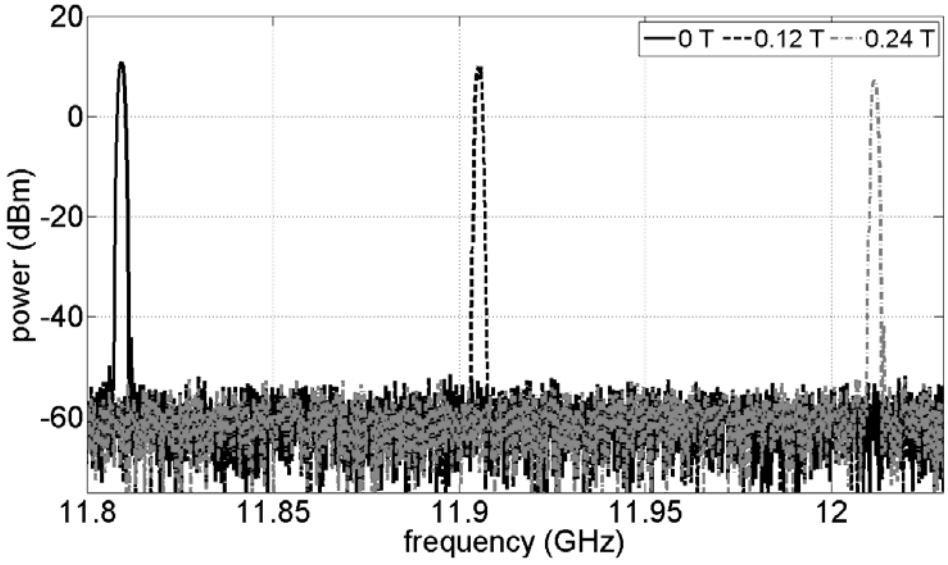

Figure 3.3-23: Spectrum of the magnetically tunable oscillator with SIW cavity resonator loaded with four ferrite slabs.

In Fig. 3.3-23, measurement results of a tunable oscillator are presented, which are obtained by closing the feedback loop. The measurement is performed using Agilent's E4440A spectrum

analyser. In Fig. 3.3-23, the measurement results are for an oscillator whose cavity is loaded with four ferrite slabs. The oscillation frequencies are illustrated for 0 T, 0.12 T and 0.24 T of external DC magnetic field. For the four ferrite loaded cavity resonator of Fig. 3.3-15, the total frequency tuning range at 0.24 T is approximately 630 MHz, while for the oscillator the tuning range at 0.24 T is 200 MHz. As explained previously, the tunability of the oscillator is less compared to the pure cavity case because the zero phase crossing of the feedback loop lags behind the loop gain for increasing values of external magnetic bias, which can be improved by making the feedback loop shorter and increasing the gain of the amplifier over the broader frequency range.

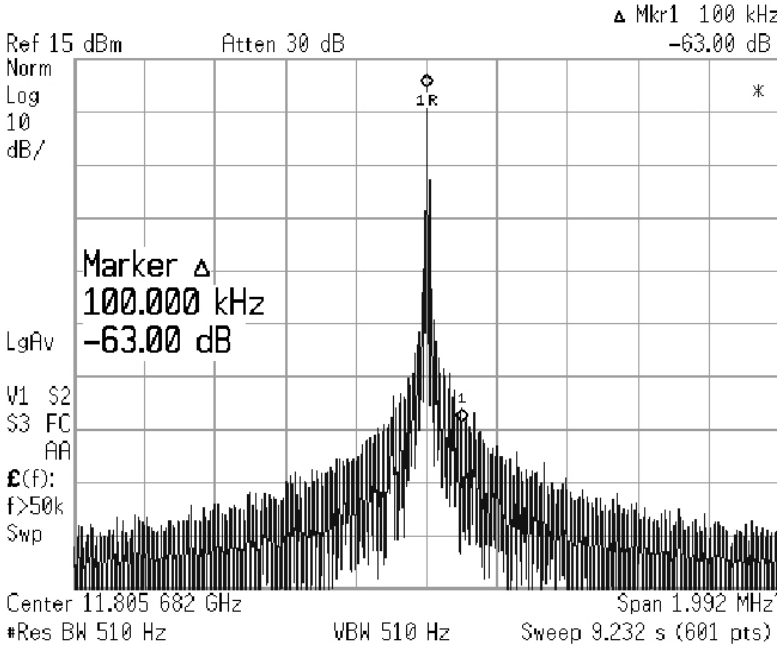

Figure 3.3-24: Spectrum of the oscillator output when the SIW cavity resonator loaded with four ferrite slabs and applied magnetic bias is 0 T.

In Fig. 3.3-24, spectrum of the magnetically tunable oscillator whose resonant cavity is loaded with four ferrite slabs is presented. The output of the oscillator is measured using Agilent's E4440A spectrum analyser with resolution bandwidth (RBW) = 510 Hz and span = 2 MHz. The sideband level is measured at 100 kHz offset, where the difference between the carrier and the sideband level is -63 dB. The following relation is used to calculate the phase noise performance of the oscillator [Cassivi, and Wu (2003)],

$$P_{NOISE} = P_{CARRIER} - P_{SIDEBAND} + 10\log(RBW). \qquad (3.24)$$

For $P_{CARRIER}$-$P_{SIDEBAND}$ = 63 dB at 100 kHz offset and for RBW = 510 Hz, the measured phase noise is approximately equal to 90 dBc/Hz.

In Fig. 3.3-25, measurement results of oscillator frequency tuning and phase noise versus the applied external magnetic bias are presented. The measurement results are plotted for the SIW cavity resonator loaded with one, two and four ferrite slabs along its sidewall slots.

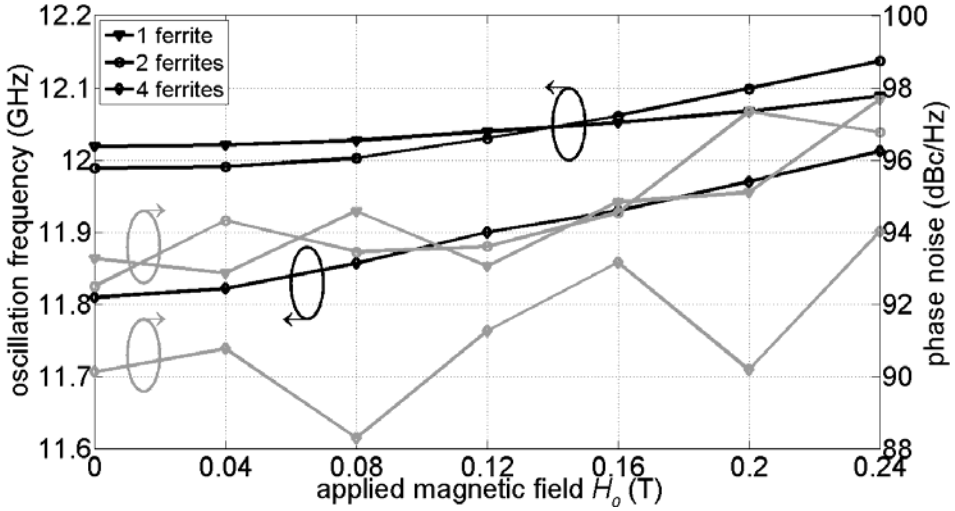

Figure 3.3-25: Oscillator frequency tuning range and phase noise performance versus applied magnetic bias.

It is evident from Fig. 3.3-25 that, the same amount of frequency shift can be achieved with a low value of magnetic bias if the number of ferrite slabs loaded inside the cavity resonator is also increased. For 0.24 T of external magnetic bias, the four ferrite slabs loaded cavity produces 200 MHz of frequency tuning, while single ferrite loaded cavity produces 70 MHz, and for the two ferrite slabs, the frequency tuning range is 150 MHz. The phase noise performance of the oscillator for single and two ferrite slabs loaded cavity is almost similar, while for the four ferrite slabs loaded cavity it is slightly degraded by 5 dBc/Hz.

Frequency modulation technique for ferrite loaded magnetically tunable SIW oscillator

In this section, a method to generate a frequency-modulated (FM) output of an FLSIW based oscillator is presented. In the previous section, it was shown that the oscillation frequency of FLSIW oscillator is tuned by the application of an external DC magnetic bias. However, when the external DC source is replaced by an alternating magnetic source, a frequency-modulated output of an oscillator is produced.

Fig. 3.3-26 illustrates a cross-sectional schematic of the biasing mechanism of an SIW cavity resonator when loaded with two ferrite slabs along its sidewall slots.

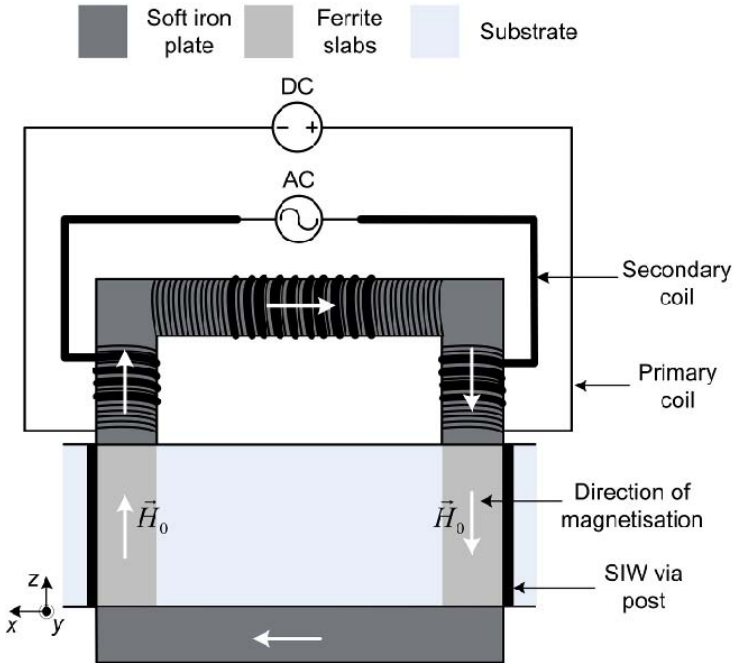

Figure 3.3-26: Biasing mechanism of ferrite loaded SIW cavity resonator to produce frequency tuning and frequency modulation.

In Fig. 3.3-26, soft iron plates are used in order to confine and guide the magnetic field generated by the current carrying coil winded around the core. The generated magnetic fields are made to pass through the ferrite slabs that are loaded along the sidewall slots of the SIW cavity. The amount of magnetic field generated in the core depends upon the current and the number of turns in the solenoid.

Fig. 3.3-26 illustrates one example of biasing the ferrite loaded cavity. Two separate soft iron cores for two ferrite slabs in order to achieve symmetrical biasing condition can also be readily used. As indicated in Fig. 3.3-26, the metal core is winded by two different wires. The primary wire contains a higher number of turns and it is supplied by a DC current source, while the secondary or FM (frequency modulation) wire contains a less number of turns and it is supplied by an alternating current (AC) source. The DC current source creates a static magnetic field around the iron core and is used to achieve the frequency tuning of the oscillator. While the AC current source creates an alternating magnetic field around the steel core to frequency modulate

the oscillator's carrier frequency. In this way, two sets of wires can be used to obtain the frequency tuning and the frequency modulation of the oscillator, simultaneously.

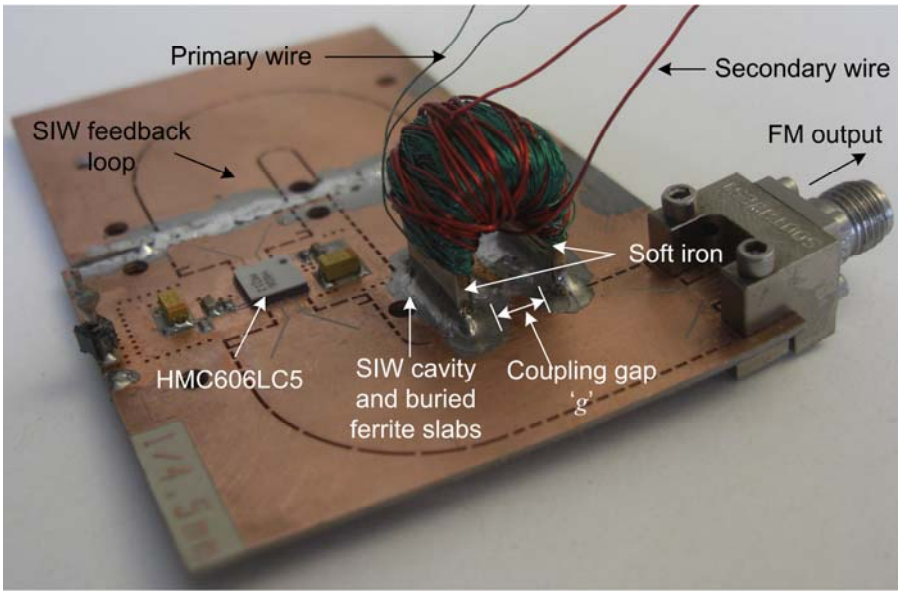

Figure 3.3-27: Fabricated single substrate ferrite loaded SIW oscillator, containing SIW cavity loaded with two ferrite slabs and copper wires winded around the soft iron core to produce the frequency tuning and frequency modulated output, with coupling gap g = 4.5 mm.

In Fig. 3.3-27, a fabricated prototype of single substrate FLSIW oscillator is shown. Two ferrite slabs are placed inside the cavity resonator along its sidewall slots. Similar to Fig. 3.3-21, the ferrite loaded cavity is connected in a feedback loop with Hittite's HMC606LC5 amplifier. A biasing mechanism as illustrated in Fig. 3.3-17 is used to bias the ferrite slabs. The soft iron core is placed on top of the two ferrite slabs that are loaded inside the SIW cavity.

In Fig. 3.3-27, for approximately 40 turns of secondary wire, a sensitivity of 80 kHz/A is obtained. The value of sensitivity also depends on the number of turns and thus can be increased by increasing the number of turns around the soft iron core. Moreover, the contact between the soft iron core and ferrite slabs is also an important factor in determining the sensitivity. The soft iron core is placed on top of the ferrite slabs and for a better contact, soldering lead is applied around the contact. However, it is difficult to avoid a small air-gap between the soft iron core and the ferrite slabs. The air-gap creates reluctance along the path of the generated magnetic field, which will have a tendency to reduce the desired sensitivity value. The time domain frequency modulated signal is given by [Rhea (2011)],

$$f(t) = A_c \cos\left[2\pi f_c t + m_f \times \sin\left(2\pi f_m t\right)\right], \tag{3.25}$$

where A_c and f_c are respectively the amplitude and the frequency of the carrier signal, f_m is the frequency of the modulating signal and m_f is the modulation index, which is given by,

$$m_f = \left(\frac{k_f A_m}{2\pi f_m}\right). \tag{3.26}$$

In (3.26), k_f is the modulation constant or the sensitivity of the FM wire, A_m is the maximum current amplitude of the control signal. The Fourier transform of (3.25) for the given values of modulation index and modulation frequency gives the output spectrum of the oscillator. The calculated frequency-modulated spectrum from (3.25) is used to verify the measurement results of the single substrate oscillator of Fig. 3.3-27. The measurement is performed by connecting the secondary wire to HP 33210A arbitrary waveform generator.

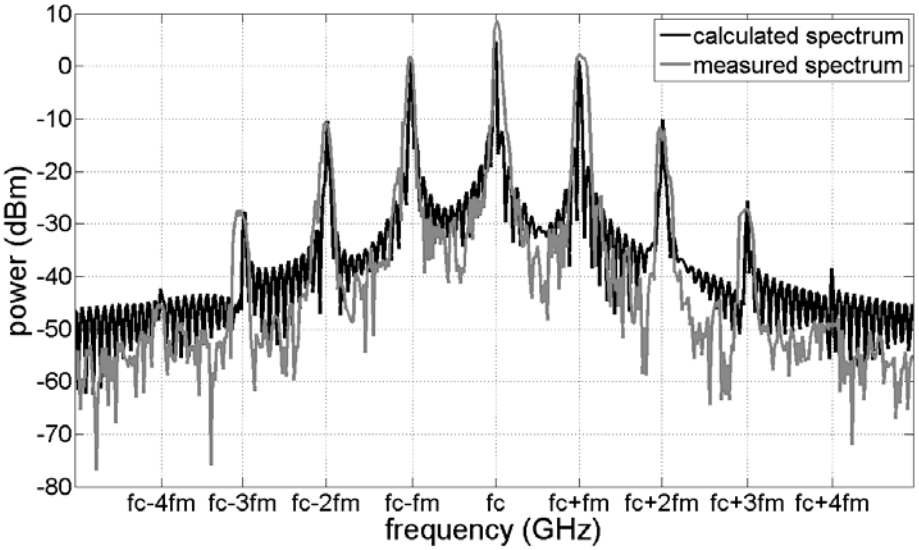

Figure 3.3-28: Calculated and measured frequency-modulated spectrums of magnetically tunable SIW oscillator for modulation index value $m_f \approx 1$.

Fig. 3.3-28 illustrates a comparison between the calculated and measured spectrums of the ferrite loaded SIW oscillator of Fig. 3.3-27. Using HP 33210A arbitrary waveform generator, a sinusoidal modulating signal of frequency $f_m = 10$ kHz with a maximum voltage amplitude of $V_{max} = 42$ mV is applied across the secondary wire. For the given value of voltage, a current of $A_m = 124$ mA is measured in the secondary wire. From (3.26), it is noted that for the given values of k_f, A_m, and f_m the value of modulation index is $m_f \approx 1$. In Fig. 3.3-28, the calculated and

measured output spectrums of the oscillator for $m_f \approx 1$ condition are plotted. The output spectrum is measured using Rohde&Schwarz FSIQ 40 signal analyzer. It can be observed that for the given modulating signal, the measured and calculated results agree very well with each other, which validates the frequency modulation of the oscillator using the biasing mechanism as illustrated in Fig. 3.3-26.

3.4 Ferrite-loaded SIW (FLSIW) switch

Switches are essential components that can be found in many microwave system applications. There are different types of microwave switches, namely electro-mechanical switches, solid state and high power solid state switches, micro-electro-mechanical systems (MEMS) switches and ferrite switches. In this section, a magnetically controlled switch on the basis of the SIW technology is presented [Cassivi, and Wu (2003)]. In [Xu, Izquierdo, and Young (2011)], a switchable SIW was proposed with PIN diodes, allowing the SIW to switch between Slotted Substrate Integrated Waveguide (SSIW) and Half Mode Substrate Integrated Waveguide (HMSIW). In this work, through an external transverse magnetic field, the permeability of the ferrite slabs loaded inside the SIW cavity is tuned, thereby making the SIW mode cut-off frequency change and achieving the desired switching function. Compared to [Xu, Izquierdo, and Young (2011)], the advantages of the proposed technique can be seen by, first of all, a higher expected power handling capability as it is not limited by the maximum power rating of a solid state device, and second, a better immunity to perturbation or interference as the SIW structure is not compromised by radiating slots. In [Soohoo (1959)] a single ferrite slab waveguide switch based on the cut-off phenomenon in transversely-magnetized ferrite was reported. In this work, a magnetically controlled switch is studied and demonstrated on the basis of a detailed theoretical analysis of the FLSIW properties when biased with a transverse DC magnetic field.

Properties of ferrite loaded SIW line

Fig. 3.4-29 illustrates the geometry of a ferrite loaded SIW (FLSIW) section of length L consisting of an SIW section of width W loaded with rectangular ferrite slabs of width w_f along the conducting sidewall.

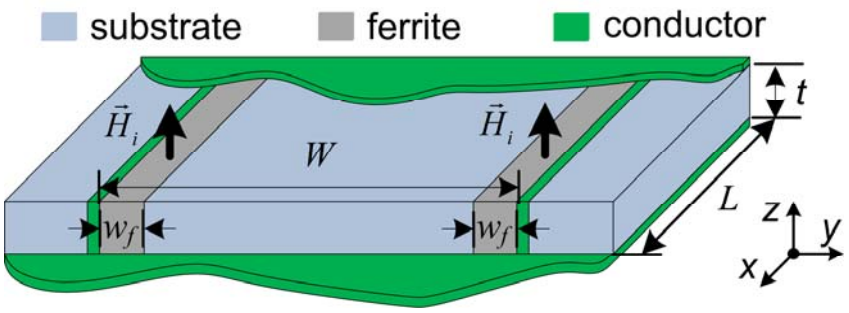

Figure 3.4-29: Geometry of two ferrite slabs loaded SIW section.

In Section 3.3, the characteristic equations for propagation constant β of the fundamental TE_{10}-like mode of an arrangement consisting of a ferrite loaded waveguide were presented. The same set of equations given in (3.10)-(3.15) are used for the evaluation of two ferrite slabs loaded SIW transmission line of Fig. 3.4-29. To obtain the FLSIW cut-off frequency f_c, the condition $\beta = 0$ in (3.10) yields:

$$0 = \left(\frac{|\mu_f| \varepsilon_s}{\mu_s \varepsilon_f} \right) \tanh^2 \left[2\pi f_c w_f \sqrt{|\mu_f| \varepsilon_f} \right] - \frac{1 + \cos\left[2\pi f_c (W - 2w_f) \sqrt{\mu_s \varepsilon_s} \right]}{1 - \cos\left[2\pi f_c (W - 2w_f) \sqrt{\mu_s \varepsilon_s} \right]}. \tag{3.27}$$

Properties of ferrite material

YIG-1780-17 Yttrium Iron Garnet (YIG) ferrite from TCI Ceramics is used for the design of a ferrite loaded SIW switch. Calculated from (3.19), Fig. 3.4-30 illustrates the YIG relative effective permeability $\mu_{rf} = \mu_f / \mu_0$ against frequency f for internal transverse magnetic fields $H_i = 0$ T, 0.17 T and 0.24 T (Fig. 3.4-30(a)) and against the internal transverse magnetic fields H_i for frequencies $f = 9$ GHz, 10 GHz and 11 GHz (Fig. 3.4-30 (b)).

It can be seen from Fig. 3.4-30(a) that μ_{rf} has a resonance that occurs at frequency $f_r = 6.8$ GHz for $H_i = 0.17$ T, and at $f_r = 8.8$ GHz when the magnetic field value is increased to $H_i = 0.24$ T. When considering a fixed bias, for frequencies $f > f_r$, the ferrite is operated below this resonance, and inversely, for frequencies $f < f_r$, the ferrite is operated above this resonance (Fig. 3.4-30(b)).

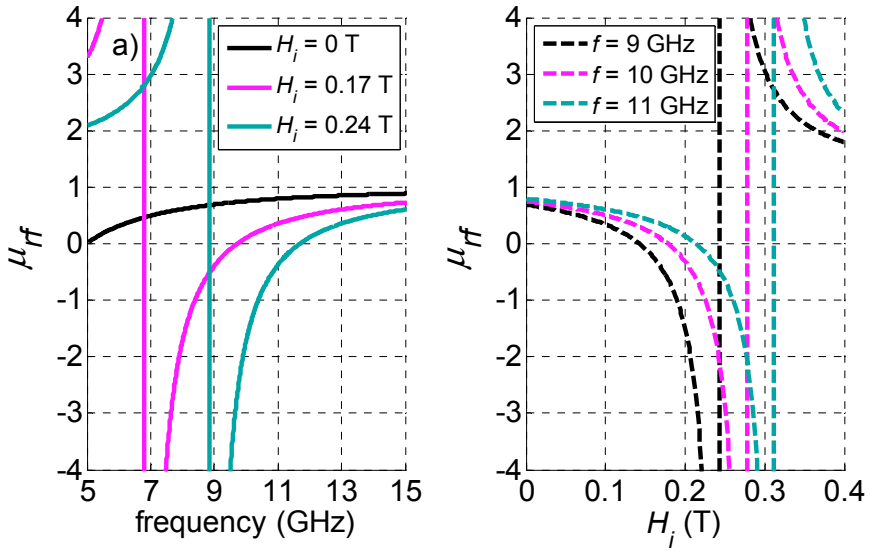

(a) (b)

Figure 3.4-30: Calculated μ_{rf} of YIG ferrite, a) versus frequency at internal magnetic fields $H_i = 0$ T, 0.17 T and 0.24 T, b) versus internal magnetic field H_i at frequencies $f = 9$ GHz, 10 GHz and 11 GHz.

FLSIW switching properties

Fig. 3.4-31 presents μ_{rf} of YIG ferrite, attenuation constant α and propagation constant β versus frequency for two different magnetic biases: $H_i = 0$ T and 0.17 T. α and β are both calculated using the Newton-Raphson method of iteration to solve the transcendental equation (3.10) for an FLSIW with $W = 9.8$ mm, $w_f = 1$ mm and substrate RT/duroid 6002 with thickness $t = 0.762$ mm, relative permitivity $\varepsilon_{rs} = 2.94$ and relative permeability $\mu_{rs} = 1$.

As shown in Fig. 3.4-31, μ_{rf} decreases with decreasing frequency from an initial value close to 1. As μ_{rf} decreases with decreasing frequency, it will reach a certain value corresponding to the FLSIW cut-off frequency f_c determined by (3.1). For $f > f_c$, the relationship given by (3.10) results in real values of β, which implies that the FLSIW is in the state of propagation.

At a certain frequency of f_μ, shown in Fig. 3.4-31 for 0.17 T of internal magnetic bias, μ_{rf} value becomes zero and negative hereafter.

For $f_\mu < f < f_c$, the relationship given by (3.10) results in an imaginary value of β, meaning that the fundamental TE_{10}-like mode is evanescent. In this case, (3.10) can be used to calculate the attenuation constant α as it results in an imaginary β. This suggests that all field components

decay exponentially with the FLSIW section length L. And the insertion loss IL in decibels is given by $IL = 8.686\alpha L$.

For $f < f_\mu$, μ_{rf} is negative and the FLSIW supports a mode that exists below the usual cut-off frequency f_c of the dominant TE_{10}-like mode.

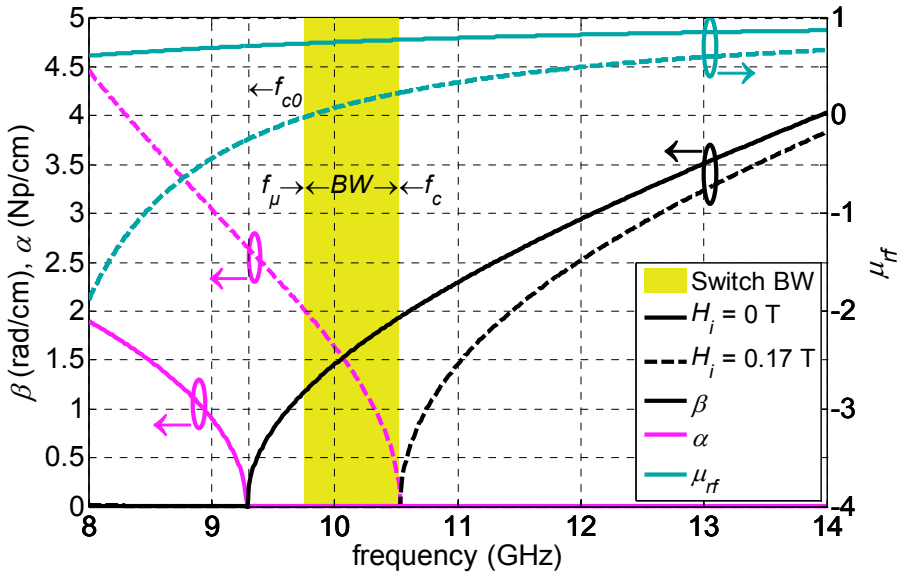

Figure 3.4-31: Calculated β, α and μ_{rf} versus frequency at applied magnetic field $H_i = 0.17$ T for $W = 9.8$ mm and $w_f = 1$ mm.

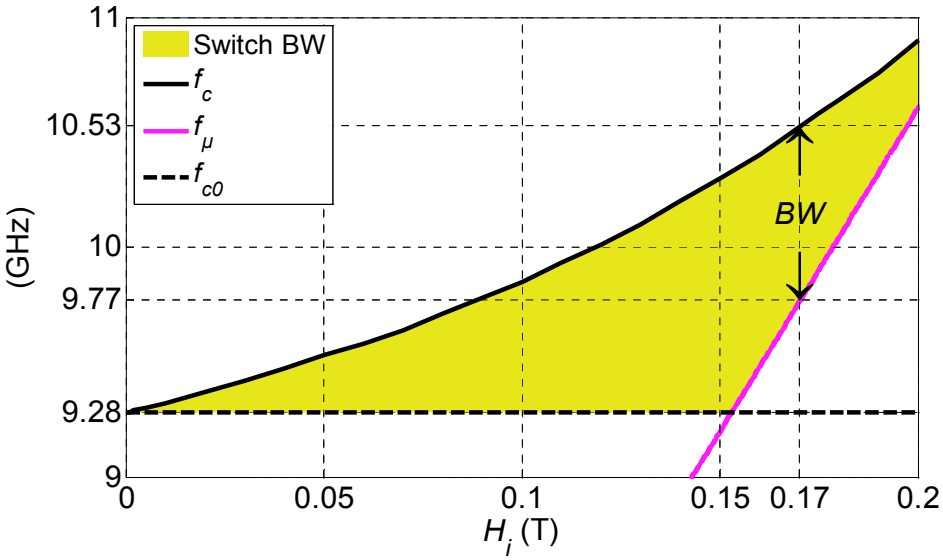

Figure 3.4-32: Calculated f_c and f_μ versus H_i for $w_f = 1$ mm.

Fig. 3.4-32 shows the calculated frequency bandwidth (BW) for which the FLSIW is evanescent and the value of the BW is:

$$BW = \min(f_c - f_\mu; f_c - f_{c0}), \tag{3.28}$$

where f_{c0} is the cut-off frequency at $H_i = 0$ T. As can be seen from Fig. 3.4-32, the upper limit of BW is given by f_c, while the lower limit is determined by the highest value between f_{c0} and f_μ. An optimum value of BW is obtained around $H_i = 0.15$ T of the internal magnetic field.

It is the purpose of this work to take advantages of the magnetically controlled frequency bandwidth BW for which the FLSIW is evanescent in order to demonstrate a magnetically controlled switch.

3.4.1 Measurement and simulation results

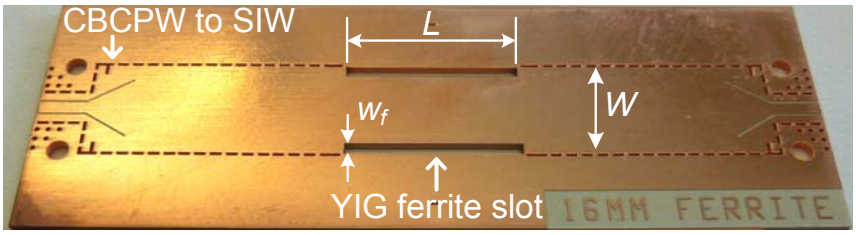

Figure 3.4-33: Fabricated FLSIW switch, $W = 9.8$ mm, $L = 16$ mm, $w_f = 1$ mm.

To demonstrate the switching properties of the FLSIW, a 16 mm long FLSIW switch loaded with 1 mm wide ferrite slabs is considered. The FLSIW is simulated using Ansoft's HFSS package (version 13). Fig. 3.4-33 illustrates the fabricated device for which conductor tape is used to cover the ferrite. To measure its performances, transitions from SIW to CBCPW are again used. In our measurement, CBCPW transitions are de-embedded using a TRL calibration. An SIW section of width $W = 9.8$ mm is used to feed the FLSIW, section. Its cut-off frequency is $f_{cSIW} = 8.93$ GHz. For characterization, the device is biased with an electromagnet, and external applied transverse magnetic field H_e is measured using a Gauss meter.

From HFSS electromagnetic simulation and measurement results, a demagnetization factor of $N_z = 0.73$ is determined using (3.23). An internal field $H_i = 0.17$ T is chosen to demonstrate the operational bandwidth BW shown in Fig. 3.4-32. With the values of $N_z = 0.73$ and $H_i = 0.17$ T, using (3.23) the value of an external field $H_e = 0.3$ T is calculated.

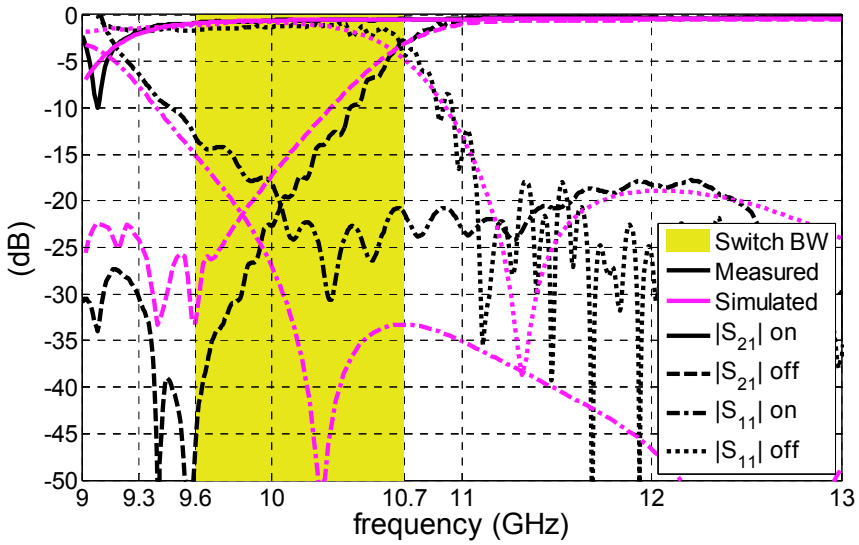

Figure 3.4-34: Calculated and measured S-parameters for different magnetic bias (on state for $H_e = 0$ T or $H_i = 0$ T and off state for $H_e = 0.3$ T or $H_i = 0.17$ T).

Table 3.1: Comparison of reported reflective SPST switches

Device	**Technology**	**Size (mm x mm)**	**BW (GHz)**	**S11 (dB)**	**IL in dB (on/off)**
[Xu]	PIN diode / SIW	120 x 21	3 – 4.2	-10	3 / 20
[Soohoo]	Ferrite / waveguide	70 x 17.7	8.8 – 9.5	-16.4	0.4 / 60
This work	FLSIW	16 x 9.8	9.5 - 10	-10	1 / 20

Fig. 3.4-34 shows the simulated and measured S-parameters for external fields $H_e = 0$ T and 0.3 T, respectively, corresponding to the on and off states of the switch. Simulated and measured results agree well with the theoretical results shown in Fig. 3.4-30 and Fig. 3.4-31. When no bias is applied, the cut-off frequency f_c is about 9.3 GHz. Once the bias is applied, f_c switches to approximately 10.7 GHz. In Fig. 3.4-34, the frequency f_μ can be observed at about 9.6 GHz. For $f < f_\mu$, the isolation deteriorates due to a mode existing for $\mu_{rf} < 0$ but stays better than -20 dB. In the on state, the insertion loss is better than 1 dB over the switchable bandwidth. With this design, an isolation of -20 dB and a matching bandwidth of -10 dB are achieved over the bandwidth of 9.5 to 10 GHz. In accordance with (3.28), a longer length will increase the attenuation. A maximum operation bandwidth of 9.5 to 10.7 GHz is achievable for this design. A switching speed of 500 µs is obtained. It includes the electromagnet and control circuit effects

which could be further optimized. Table 3.1 1lists the performances of some reported reflective SPST switches.

In this section, an *X*-band reflective type SPST switch based on an FLSIW section has been demonstrated. The cut-off properties of the FLSIW transition line have been analyzed. As the proof of concept, an FLSIW switch was studied, fabricated and measured. It has achieved a 1 dB insertion loss with an isolation of 20 dB. Theoretical predictions, simulated and measured results all agree well with each other. In comparison with other substrate based circuits, this type of switch is very suitable for high-power microwave and millimeter-wave applications based on SIW technology.

CHAPTER 4 SIMULTANEOUS ELECTRIC AND MAGNETIC TWO-DIMENSIONALLY TUNED PARAMETER-AGILE SIW DEVICES

Frequency-agile RF and microwave devices have gained much attention from growing demands for dynamic spectrum management in cognitive and software-define radio designed platforms and phase-controlled systems for both military and civilian applications. A large number of previous papers have suggested different types of reconfigurable devices to solve this challenging topic [Djoumessi, Tatu and Wu (2010)], [Zhang, et al. (2012)], [Fukuda, et al. (2007)]. Most reported reconfigurable devices have addressed frequency tuning issues utilizing various tuning techniques. Among them are four typical tuning methods as follows: magnetic materials such as Yttrium Iron Garnet (YIG) [Fay (1956)], semiconductor varactor [Musoll Anguiano, et al. (2002)], ferroelectric (e.g. BST) [Papapolymerou, et al. (2006)] and micro-electromechanical systems (MEMS) [Ocera, et al. (2006)]. With a limited degree of freedom, those devices, however, can achieve a limited tuning range and do not provide an optimal design regarding the other key parameters over the whole tuning range, which are generally interplayed with each other in the design. In this chapter, a novel approach is proposed to design outstandingly parameter-agile devices. This approach consists in simultaneous electric (E) and magnetic (H) two-dimensional (2D) tuning allowing an increased tuning range and at the same time optimizing other key design parameters. The proposed approach that is demonstrated in this chapter again makes use of SIW technology. In order to achieve the best possible RF performance, it is important to have a circuit that has high Q value and wide frequency tunability. SIW is a promising technology that inherits almost all the characteristics of a rectangular waveguide and planar structure.

First, a two dimensionally (2-D) tuned cavity resonator is theoretically and experimentally studied. The frequency tunable resonator is a key building block component in designing tunable band-pass filters, oscillators, mixers and antennas that can finally make-up the whole cognitive system. In [He, et al. (2009)], an electrically tunable SIW cavity resonator was presented, where the resonant frequency of the cavity was tuned by a DC-voltage bias over a varactor coupled to the cavity. A magnetically tunable SIW cavity resonator realized by loading planar ferrite slabs along the sidewall slots of the cavity was presented in the previous chapter. In [He, et al. (2009)], the limited capacitance variation of the varactor diode had set an upper limit in the total tuning

range of the cavity resonator. While in magnetically tunable resonator of the previous chapter, suffers from a high magnetic loss near the ferromagnetic resonance region and the requirement of a high external magnetic bias limits the total frequency tuning range. It is thus a purpose of this research work, to increase the frequency tunability by incorporating both electric and magnetic tuning in the same cavity. It is also a purpose to study theoretically and experimentally if the limitation due to electric frequency tuning can be compensated by magnetic manner and vice-versa. In [Yang, et al. (2011)], results of dual E-field and H-field tunable band-pass filter at 2 GHz were presented, where H-field tunability was achieved by using single crystal Yttrium Iron Garnet (YIG) film and E-field tunability was achieved by bonding YIG film to a piezoelectric substrate. The preliminary result presented in [Yang, et al. (2011)] depicts that it requires approximately 8 kV/cm of electric field to achieve the tuning of 200 MHz. In this chapter, the two-dimensional electric and magnetic tuning is achieved by using commercially available low cost bulk ferrite material and Surface Mount (SM) capacitor/varactor diode, which require low values of magnetic and voltage bias to achieve the desired tuning at 12 GHz. Based on the two dimensionally tuned cavities, a parameter-agile second order band-pass filter achieving simultaneous frequency and bandwidth tuning is introduced with theoretical and experimental results. In the literature, a large number of papers presented tunable filters only dealing with frequency tuning [Hunter, and Rhodes (1980)]-[Torregrosa-Penalva, et al. (2002)] due to the lack of methods to control inter-resonator coupling coefficients. Compared to what were reported in literature, this work shows a distinct design method based on the simultaneous control of the E- and H-fields of an SIW cavity. The dual tuning allows tuning of the cavity frequency along with inter-resonator coupling control.Finally, the concept of simultaneous electric and magnetic 2D tuning is again applied to the design of a tunable cavity-backed slot antenna. Using the proposed dual tuned cavity, the tuning range is significantly increased and the antenna return loss optimized to increase the antenna overall efficiency.

4.1 Electrically and magnetically tunable SIW cavity resonator

4.1.1 Theory of 2-D tuned SIW cavity resonator

In this section, a theoretical analysis of an SIW cavity resonator loaded with both electric and magnetic tuning elements is presented. The thorough understanding of such a building block

element is critical for the development of any further circuits and structures based on such two-dimensional tuning scheme. The magnetic tuning element is a planar ferrite slab, which is loaded along one of the electrically shorted-end-walls of the cavity, while the electric tuning element is a lumped capacitor connected between the upper and lower conductor at the central region of the cavity where the electric fields are maximally confined. The use of lumped capacitors can be replaced by a continuously tuning capacitive element such as varactor. In this work, the investigation of electrical tuning is done with lumped capacitors to simplify the theoretical and experimental studies as the capacitors can be accurately determined. Continuous tuning is accommodated in the late stage for our design demonstrations. At the cavity resonance frequency, a simple transmission line theory is used to derive a characteristic equation of the cavity loaded with dual tuning elements for which higher-order modes and parasitic effects are ignored. The solution of the characteristic equation, gives a relationship between the cavity resonant frequency and its variation with electric and magnetic tuning element values.

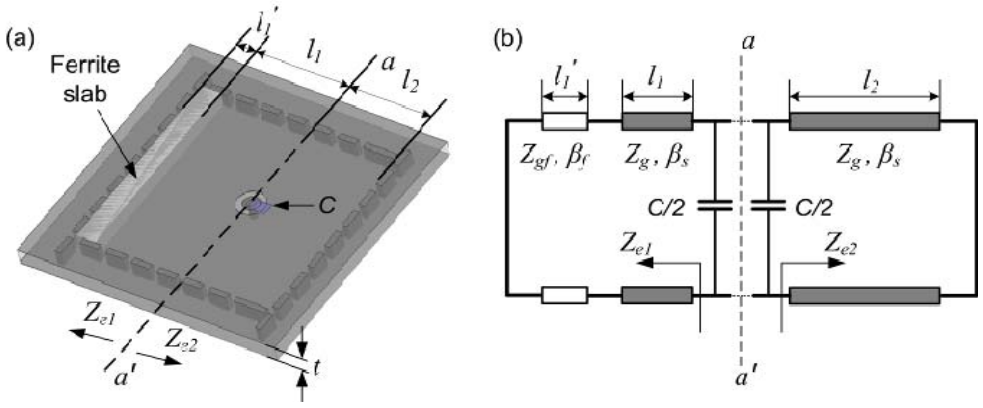

Figure 4.1-1: Simultaneous electrically and magnetically tunable cavity resonator, a) SIW cavity resonator loaded with a lumped capacitor and a ferrite slab, b) equivalent transmission line model.

Fig. 4.1-1 represents SIW cavity resonator loaded with a ferrite slab along its end-wall and a surface mounted capacitor C at the central region of the cavity. Fig. 4.1-1(b) is the equivalent transmission line model of the cavity, where short-circuited section of a ferrite slab is represented by a transmission line of length l_1', substrate section between the lumped capacitor C and the ferrite slab is represented by l_1, and a short circuited substrate section is represented by l_2.

From the transmission line theory, the equivalent impedance seen looking from reference plane aa' towards the short-circuited SIW section of length l_2 is,

$$Z_{e2} = jZ_g \tan \beta_s l_2, \tag{4.1}$$

where Z_g is the guide impedance and β_s is the propagation constant of the SIW transmission line section. Similarly, the impedance seen looking towards the short-circuited ferrite section of length l_1' and substrate section of length l_1 is,

$$Z_{e1} = Z_g \frac{jZ_{gf} \tan\left(\beta_f l_1'\right) + jZ_g \tan\left(\beta_s l_1\right)}{Z_g - Z_{gf} \tan\left(\beta_f l_1'\right) \tan\left(\beta_s l_1\right)}, \tag{4.2}$$

where Z_{gf} and β_f are the guide impedance and the propagation constant of the ferrite loaded cavity section of length l_1'. The propagation constant β_f of the ferrite loaded cavity section is given by,

$$\beta_f = \frac{2\pi}{\lambda_0} \sqrt{\mu_f \varepsilon_{rf}} \sqrt{1 - \left(\frac{\lambda_0}{\lambda_c \sqrt{\mu_f \varepsilon_{rf}}} \right)}. \tag{4.3}$$

In (4.3), λ_c is the cut-off wavelength, ε_{rf} is the relative permittivity of the ferrite material, and μ_f is the effective permeability of the ferrite material given by,

$$\mu_f = \frac{\mu'^2 - \kappa'^2}{\mu'}, \tag{4.4}$$

where μ' and κ' are the components of the Polder tensor that describe the permeability of the ferrite material [Fay (1956)]. At the cavity resonance frequency f_0, seen from the reference plane aa' the sum of the imaginary parts of (4.1) and (4.2) should be equal to zero, thus the following characteristic equation is obtained,

$$\mathrm{Im}\left[\frac{Z_{e1} \cdot (2X_c)}{Z_{e1} + (2X_c)} + \frac{Z_{e2} \cdot (2X_c)}{Z_{e2} + (2X_c)} \right] = 0. \tag{4.5}$$

In (4.5), "Im" represents the imaginary part of the terms written inside the parenthesis, and X_C is the reactance of the capacitor at a given frequency. The solution of (4.5) yields a theoretical frequency tuning curve of the cavity resonator in relation to the applied magnetic bias on ferrite material, and the capacitance C values.

4.1.2 Calculation and measurement results

In this section, calculated and measurement results of the SIW cavity resonator of Fig. 4.1-1, are presented. Fig. 4.1-2 illustrates the fabricated prototype of SIW cavity resonator loaded with both electric and magnetic tuning elements.

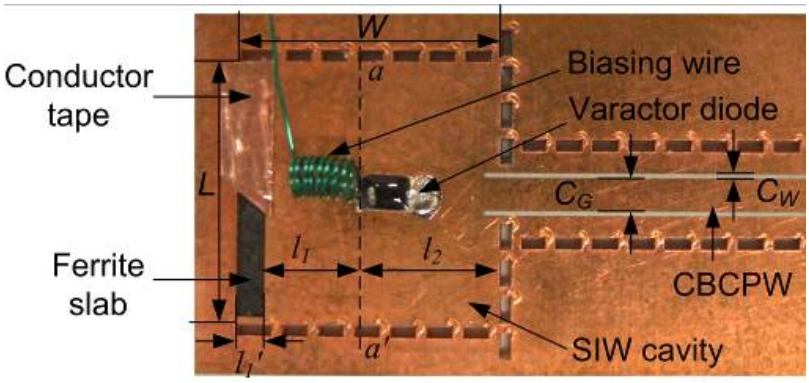

Figure 4.1-2: Fabricated SIW cavity resonator with C_W = 1.2 mm, C_G = 0.2 mm, l_2 = 5.9 mm, l_1 =1 mm, $L = W$ = 9.8 mm.

The SIW cavity resonator is fabricated on Rogers RT/duroid 6002 substrate. The planar ferrite slab placed at the end-wall of the cavity as shown in Fig. 4.1-2 is YIG-1780. The same YIG ferrite slabs were also used in the design of magnetically tunable resonator, oscillator and switch as presented in Chapter 3. For the dimensions given in Fig. 4.1-2, the resonant frequency of a cavity having a dimension of $L = W$ = 9.8 mm without ferrite slab and varactor/capacitor surface mounted is approximately 12.6 GHz. A current probe consisting of 50 Ω CBCPW is used to feed the cavity.

For the given cavity dimensions, substrate and YIG ferrite materials, the characteristic equation given by (4.5) is solved using Newton Raphson method of root finding [Pozar (2005)] to theoretically determine the cavity resonance frequency versus applied magnetic bias H_i on ferrite slabs and capacitance C values.

In (4.5), the impedance Z_{e1} is dependent upon the effective permeability value μ_f of the ferrite material as given by (4.3) and (4.4). In Fig. 3.2-5, calculated permeability components of a given infinite YIG ferrite material are plotted as a function of internal magnetic bias H_i at 12.6 GHz. As can be seen, at below ferromagnetic resonance region, μ_e progressively reduces from an initial value of approximately 1 to a value of zero at 0.27 T of H_i. Since the ferrite loaded SIW cavity

resonator will be operated in a region below the ferromagnetic resonance, the resonant frequency of the SIW cavity is expected to follow the inverse variation of μ_e curve for the applied values of transverse magnetic bias H_i.

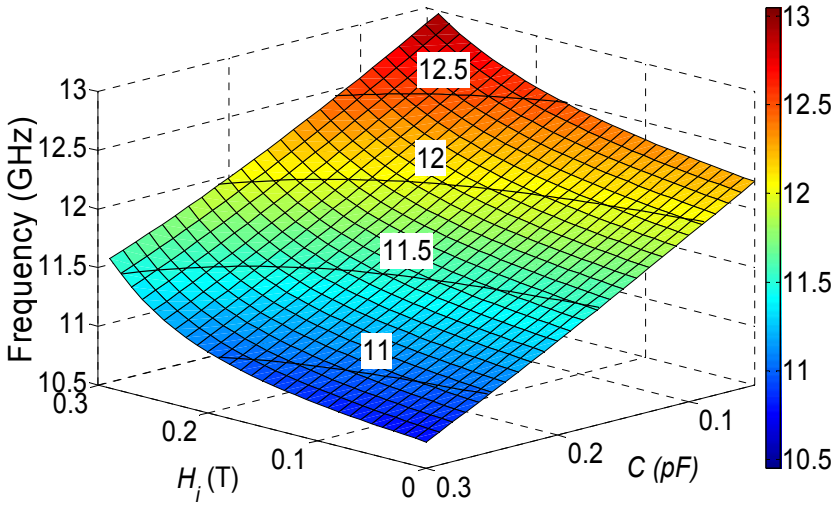

Figure 4.1-3: Theoretically calculated resonant frequency curve of YIG planar slab and capacitor loaded SIW cavity resonator.

In Fig. 4.1-3 a theoretically calculated frequency tuning curve of SIW cavity resonator of Fig. 4.1-1 and Fig. 4.1-2 is presented. The frequency tuning curve is obtained from the solution of (4.5). In Fig. 4.1-3, the cavity resonant frequency decreases linearly with the increase in the lumped capacitor value from 0.05 pF to 0.3 pF, while it increases when the ferrite internal magnetic field H_i is increased from 0 T to 0.3 T. It can be noted that, keeping the capacitance value constant at 0.3 pF, and increasing the magnetic field H_i from 0 T to 0.3 T, the resonant frequency value increases from 10.73 GHz to 11.6 GHz. Therefore, the tuning frequency range is 7% at 12 GHz. But at the same time, if the capacitance value is reduced to 0.05 pF, the maximum frequency that can be attained with 0.3 T would be 12.98 GHz, which is approximately 18% of tuning range. Thus, theoretically, it can be observed that, for the same value of applied internal magnetic field H_i, the frequency tuning range can be increased by 2.5 times if the lumped capacitor value is changed in a suitable way. Therefore, it rules out a possibility that higher frequency tuning range can be obtained for lower values of applied magnetic field H_i.

After the determination of the theoretical frequency tuning curve, measurement of a single port SIW cavity resonator of Fig. 4.1-2 is performed for the proof of concept. The first measurement

consists of SIW cavity resonator loaded with a single planar ferrite slab and high Q UQCL2AXXXBAT2A series ceramic capacitors from AVX Corporation. The measurement is performed to determine the change in the resonant frequency of the cavity for the given value of applied magnetic bias H_0 and capacitance values C. The applied magnetic bias H_0 in this case is the external magnetic field measured outside the ferrite slab using a Gauss meter.

In Fig. 4.1-4, measurements results of cavity resonator loaded with both electric and magnetic tuning elements are presented. The measurement is performed for an SIW cavity loaded with a single ferrite slab at its end-wall and surface mounted capacitors at the central region of the cavity. In Fig. 4.1-4, it can be seen that the use of capacitor has reduced the resonant frequency from the initial value of 11.98 GHz to 11.48 GHz for 0.1 pF and 11.1 GHz for 0.05 pF, thus significantly expanding the total tuning range. When no capacitors are mounted, the frequency range only due to externally applied magnetic field H_0 is from 11.98 GHz to 13.49 GHz, which is 12% at 12 GHz. But with capacitor mounted into the structure, the total frequency range is significantly increased to 20%. Therefore, the measurement results supports the theoretical prediction presented in Fig. 4.1-3, that using two-dimensional tuning a higher frequency tuning range can be achieved.

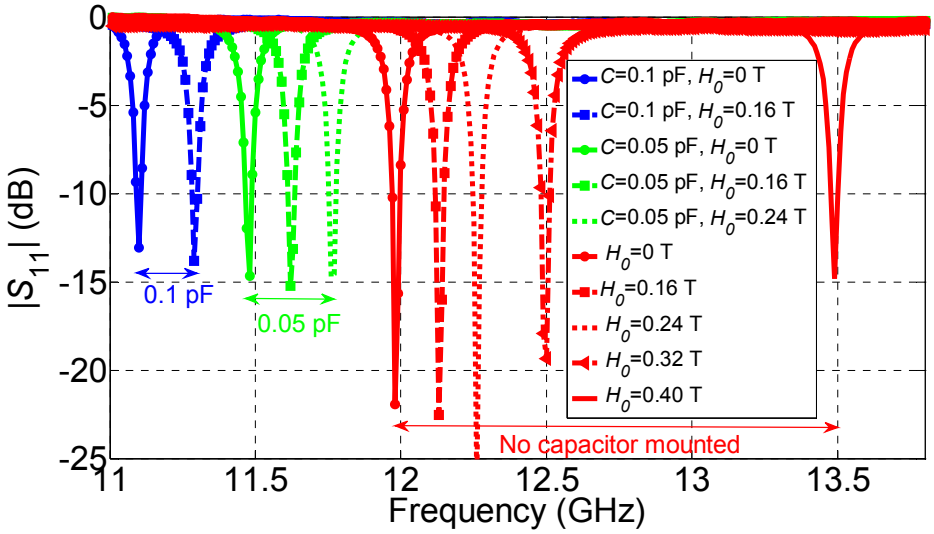

Figure 4.1-4: Measurement results for different lumped capacitor C and external applied magnetic field H_0 values.

To perform the electrical tuning of the cavity, a varactor diode MSV34060-0805-2 from Aeroflex is used. For an applied bias voltage in the range of $V_b = 4$ V to 30 V, the variation of the nominal capacitance is between 0.5 pF and 0.3 pF. However, it was found that these values of capacitance

are too high to obtain a good matching for the cavity. Therefore, in order to reduce the total capacitance value, two varactor diodes and a capacitor of value 0.05 pF are connected in series to get the total capacitance range of C = 45.45-42.9 fF.

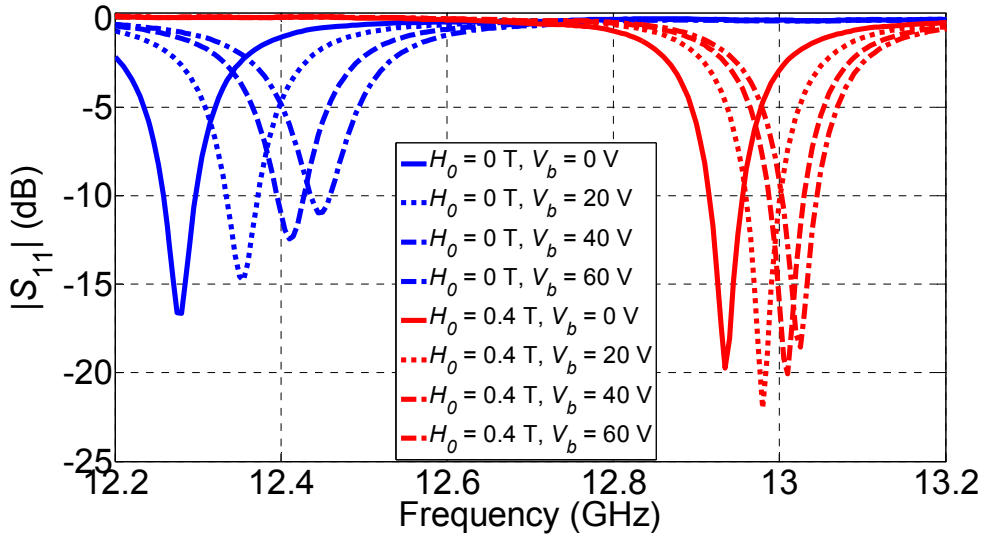

Figure 4.1-5: Measurement results for two-dimensionally tuned SIW cavity resonator using a single ferrite slab and a varactor diode.

Fig. 4.1-5 illustrates the measurement results, for the 2-D tuned cavity of Fig. 4.1-2 using varactor diode and ferrite. Since the equivalent capacitance tuning range is limited to $\Delta C = 2.55$ fF, the electric frequency tuning range is limited to about 170 MHz. Ferromagnetic resonance of the ferrite and limited capacitance variability of the varactor diode have set an upper limit in the total tuning range. In Fig. 4.1-5, measurement results for simultaneous electric and magnetic tuning are presented. The resonant frequency increases non-linearly with increased value of H_0 and V_b, due to the non-linear change of effective permeability value of YIG ferrite and the capacitance value of the varactor diode.

In Fig. 4.1-6(a) and (b), measured frequency tuning curves of the two-dimensionally tuned cavity resonator are presented. It can be seen in Fig. 4.1-6(a), at lower values of H_0 ($H_0 = 0$ T), the frequency tuning curve changes linearly with the increase in varactor diode voltage V_b. As the applied magnetic field H_0 increases towards higher values ($H_0 = 0.4$ T), the variation of the resonant frequency with increasing V_b also reduces.

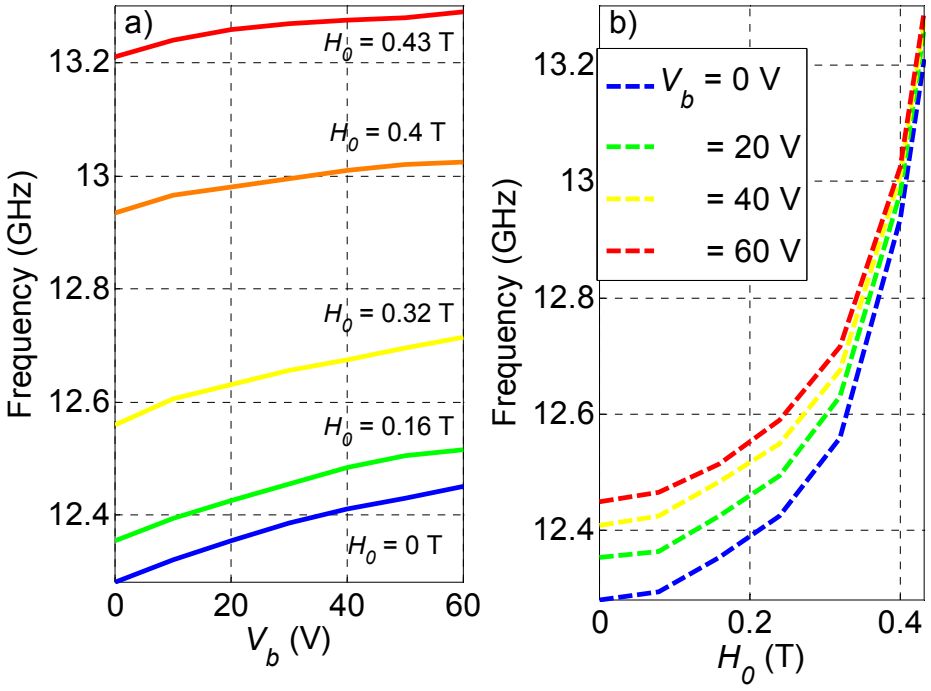

Figure 4.1-6: Two-dimensional measurement results showing variation of resonant frequency a) versus V_b, b) versus H_0.

This behavior is related due to the frequency limited operation of MSV34060-0805-2 varactor diode. Similar variation of the resonant frequency can also be observed in Fig. 4.1-5, where the rate of increase of cavity resonant frequency at lower frequency values is higher. Similarly in Fig. 4.1-6(b), measured frequency tuning curve of the cavity resonator plotted against H_0 is presented. As predicted theoretically in Fig. 4.1-3, the variation of the resonant frequency exhibits as a non-linear function of the applied magnetic bias H_0.

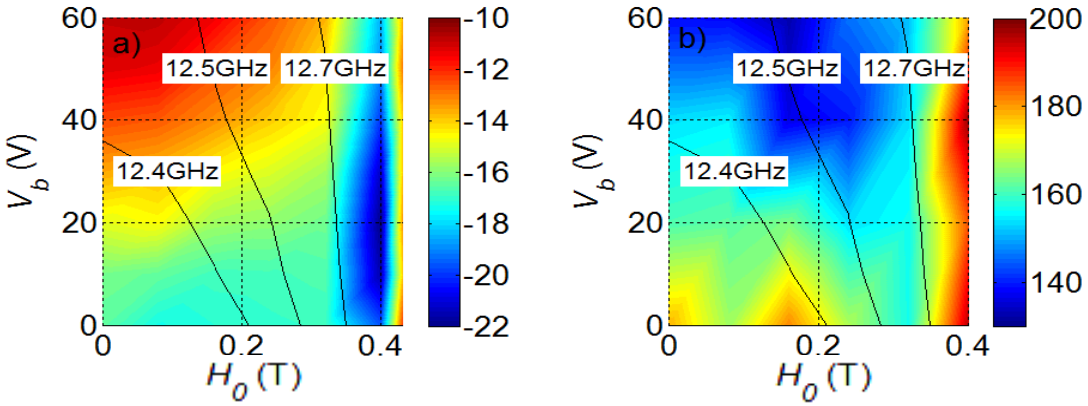

Figure 4.1-7: Measurement results for a) $|S_{11}|$ (dB), b) Q_u.

In Fig. 4.1-7, isofrequency curves are plotted together with S_{11} and Q_u. As different biasing point allows achieving the same resonant frequency, it is possible to optimize either S_{11}, Q_u, the required tuning energy or a function of those parameters.

4.2 Two dimensionally (2-D) tunable SIW band-pass filter

With the concept of simultaneous electric and magnetic tuning, a simultaneous frequency and bandwidth tunable band-pass filter is theoretically and experimentally demonstrated. The designed band-pass filter is reconfigurable in both frequency and bandwidth. It can achieve frequency tunable constant-bandwidth and constant-frequency variable-bandwidth operations at the same time.

4.2.1 Filter topology

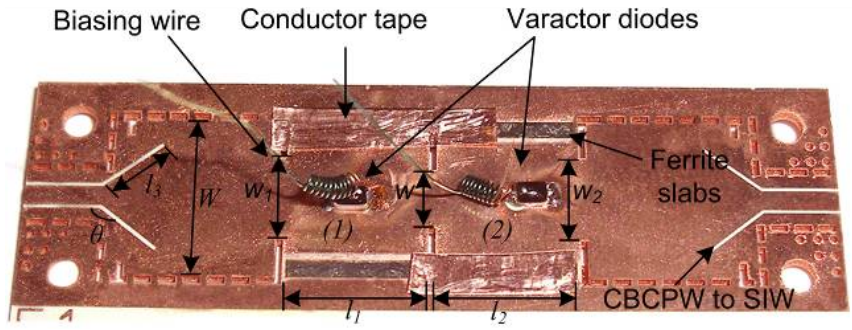

(a)

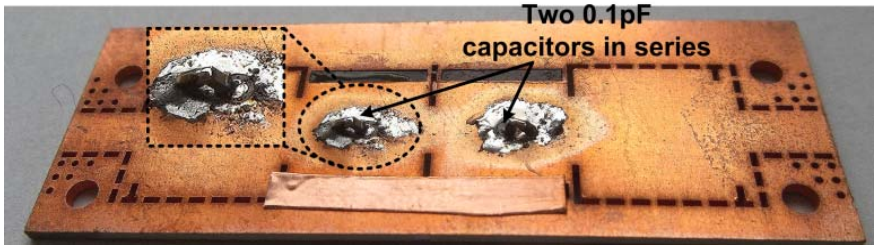

(b)

Figure 4.2-8: Fabricated SIW second order Tchebyscheff band-pass filter with a) Top-view W = 10 mm, w_1 = 5.2 mm, w =3.9 mm, w_2 = 5.2 mm, l_1 =8.3 mm, l_2 =8.3 mm (b) bottom view with two 0.1 pF capacitors connected in series.

Fig. 4.2-8 illustrates the fabricated band-pass filter based on SIW technology. It consists of two SIW cavities *(1)* and *(2)* cascaded to form a second order Tschebyscheff band-pass filter. The filter is fabricated on Rogers RT/duroid 6002 substrate. The ferrite material used in the design is

YIG with $4\pi M_s = 1780$ G, and $\Delta H \leq 17$ Oe. The thickness of the YIG slab is equal to the thickness of the substrate $t = 0.762$ mm.

The principal mode of operation of the filter is the TE_{10} mode. Since TE_{10} is the dominant mode of operation, is up to the cut-off frequency of TE_{20} mode. Similar to SIW cavity resonator presented in the previous section, simultaneous electric and magnetic tuning is achieved by loading ferrite slabs and capacitors/varactor diodes along the sidewalls and at the center of the cavity respectively. Unlike in the case of an SIW cavity resonator of Fig. 4.1-2, each cavity of the band-pass filter of Fig. 4.2-8 is loaded with two ferrite slabs instead of one. It is apparent that, by increasing the volume of the ferrite material inside a cavity, the frequency tuning range of the cavity also increases. Therefore, to increase the frequency tunability of the whole filter, two ferrite slabs are loaded along the sidewalls of each cavity. Moreover, with two ferrite slabs the filter structure becomes symmetric in a given plane, which will keep the theoretical analysis using transmission line method straightforward.

4.2.2 Theory of dual electric and magnetic tunable filter

In this section, the concept of simultaneous electric and magnetic tuning is further exploited to realize both frequency-tunable constant-bandwidth, and constant-frequency variable-bandwidth band-pass filter. A theoretical analysis is performed to lay out a design guideline, which shows an ideal relationship between magnetic bias H_i applied to the ferrite material and change in the values of varactor capacitance C in order to realize a tunable filter with a constant filter shape and bandwidth and vice-versa.

In the design of a simultaneous electric and magnetic tunable filter, the following 2 design-steps are followed:

1) For given filter specifications, the low-pass prototype parameters are obtained and the corresponding impedance-invert values are calculated from the following relations [Matthaei, Young, Jones (1964)],

$$\frac{k_{01}}{Z_0} = \sqrt{\frac{\lambda}{2}\frac{w_\lambda}{g_0 g_1 w_1'}}, \quad \left.\frac{k_{j,j+1}}{Z_0}\right|_{j=1 to n-1} = \frac{\pi w_\lambda}{2w_1'}\frac{1}{\sqrt{g_j g_{j+1}}}$$
$$\frac{k_{n,n+1}}{Z_0} = \sqrt{\frac{\lambda}{2}\frac{w_\lambda}{g_n g_{n+1} w_1'}} \qquad (4.6)$$

where $g_0, g_1, \ldots, g_{n+1}$ are low-pass prototype parameters and w_λ is the guide wavelength fractional bandwidth. The inverters of the band-pass filter presented in Fig. 4.2-8 are shunt-inductance type and the structure operates like a filter with series resonators. The equivalent circuit for a shunt-inductance-coupled filter is a T-network consisting of a shunt-inductance and series capacitances.

After the calculation of impedance-invert values, they are physically realized by the simulation of metallic via window indicated by w_1, w and w_2 in Fig. 4.2-8 using Ansoft HFSS version 13. From the S-parameters obtained from the simulation, the following parameters are calculated [Uher, Bornemann, and Arndt (1991)],

$$\begin{aligned} &\phi = -\tan^{-1}\left(2x_p + 2x_s\right) - \tan^{-1}\left(x_s\right), jx_s = \frac{1 - S_{12} + S_{11}}{1 - S_{11} + S_{12}} \\ &jx_p = \frac{2S_{12}}{\left(1 - S_{11}\right)^2 - {S_{12}}^2} \end{aligned} \tag{4.7}$$

The impedance-inverter value of the metallic-via window and the length of the SIW cavity L_j (j = 1, 2, …, n) are obtained using

$$\begin{aligned} &\frac{k}{Z_0} = \left|\tan\left(\frac{\phi}{2}\right) + \tan^{-1}\left(x_p\right)\right|, \theta_j = \pi + \frac{1}{2}\left(\phi_{j-1,j} + \phi_{j,j+1}\right) \\ &L_j = \frac{\left(\lambda_g\right)_0 \theta_j}{2\pi} \end{aligned} \tag{4.8}$$

Finally the size of the metallic via window is varied until the impedance-inverter value obtained from (4.8) is close to the calculated value given by (4.6). Based on the above calculation and simulation results a second-order Tschebyscheff filter with 0.1 dB ripple is designed and fabricated and it is presented in Fig. 4.2-8. The filter is designed at the center frequency of 12 GHz. The design does not include ferrite slabs and capacitance loading, which are added later.

After the initial design of the SIW cavity based filter, it is made E- and H- tunable by loading it with planar ferrite slabs along its end-wall and varactor/capacitance at the center of each cavity. Then, the next step is to determine a design guide line in order to maintain the constant bandwidth over the whole frequency range and variable-bandwidth at one particular frequency. In order to maintain constant filter response and shape, the

resonator slope parameters of the filter's end resonators *(1)* and *(2)* of Fig. 4.2-8 take the following forms [Matthaei, Young, Jones (1964)],

$$\alpha_1 = (\alpha_1)_m \left[\frac{f_0}{(f_0)_m} \right]^3, \tag{4.9}$$

$$\alpha_2 = (\alpha_2)_m \left[\frac{f_0}{(f_0)_m} \right]^3, \tag{4.10}$$

where $(\alpha_1)_m$ and $(\alpha_2)_m$ are the slope parameters of end-resonators *(1)* and *(2)* at the cavity's mean tuning frequency $(f_0)_m$, and the cavity resonant frequency f_0. The SIW cavity resonator exhibits series type resonance, and its reactance slope parameter is given by,

$$\alpha_j = \pi f_0 \left. \frac{dX_j}{df} \right|_{f=f_0}, \tag{4.11}$$

where X_j is the reactance of the resonator j. Based on the cavity resonator and ferrite slabs dimension, and loaded capacitance C value, the cavity's resonator slope parameter for each resonators *(1)* and *(2)* given by (4.11) is separately calculated. At a selected value of $(f_0)_m$, and for a given values of C and H_i, the calculated values from (4.11) are compared with the ideal slope parameters values given by (4.9) and (4.10). At a given frequency of resonance, the applied magnetic field H_i, and the value of C are changed until the two resonator slope parameter values are in close agreement with one another.

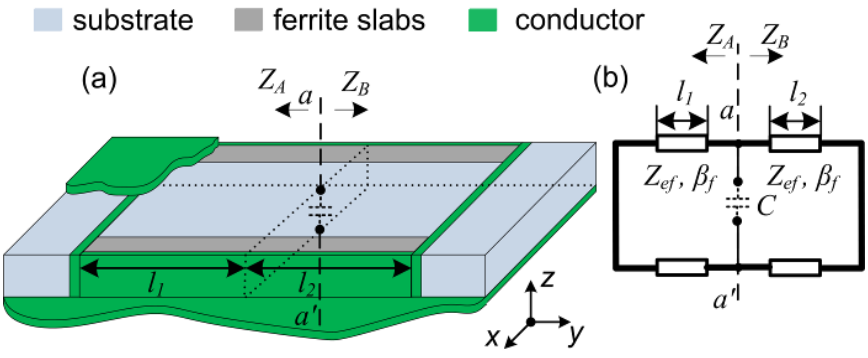

Figure 4.2-9: An SIW cavity resonator loaded with ferrite slabs along the two sidewalls and a capacitor at the center of the cavity (a) cross-sectional view (b) equivalent transmission line model.

In order to determine the reactance slope parameter given by (4.9) (4.10) and (4.11), the cavity resonant frequency f_0 and slope dX_f/df are first determined. Fig. 4.2-9(a) and Fig. 4.2-9(b) illustrate the representation of an SIW cavity resonator loaded with two ferrite slabs and its equivalent transmission line model. Similar to the theoretical analysis of the single cavity resonator presented in the previous section, the sum of the reactance at the cavity resonance frequency is equal to zero. Hence, seen from the reference plane defined by aa' the characteristic equation from Fig. 4.2-9 is,

$$\mathrm{Im}\left[\frac{Z_A\cdot(2X_c)}{Z_A+(2X_c)}+\frac{Z_B\cdot(2X_c)}{Z_B+(2X_c)}\right]=0. \tag{4.12}$$

where,

$$\begin{aligned} Z_A &= jZ_{0f}\tan(\beta_f l_1),\\ Z_B &= jZ_{0f}\tan(\beta_f l_2). \end{aligned} \tag{4.13}$$

In (4.12), "Im" represents the imaginary part of the term inside the bracket and, Z_{0f} and β_f are the guide impedance and propagation constant of the TE_{10} mode respectively. In order to determine the value of β_f, a characteristic equation of twin ferrite slabs loaded SIW transmission line is considered, which is given by [Lax, and Button (1962)]

$$\tan\left[k_s\left(W-2w_f\right)\right]=p/q, \tag{4.14}$$

where,

$$p=2\left(\frac{K_m\mu_s}{k_s\mu_e}\right)\cosh(K_m w_f)\sinh(K_m w_f), \tag{4.15}$$

$$\begin{aligned} q=&\left[1-\left(\frac{\beta_f\mu_s}{\mu_e\theta k_s}\right)^2\right]\sinh^2(K_m w_f)\\ &-\left(\frac{K_m\mu_s}{k_s\mu_f}\right)^2\cosh^2(K_m w_f), \end{aligned} \tag{4.16}$$

$$K_m^2=-(2\pi f)^2\varepsilon_f\mu_f+\beta_f{}^2, \tag{4.17}$$

$$k_s^2=(2\pi f)^2\varepsilon_s\mu_s-\beta_f{}^2, \tag{4.18}$$

$$\theta=\mu'/(-jk'), \tag{4.19}$$

In (4.16) and (4.17), ε_s and μ_s are the effective permittivity and effective permeability of the host

substrate, respectively. ε_f and μ_f are the effective permittivity and effective permeability of the ferrite material, respectively. The solution of (4.14) yields propagation constant value β_f of the SIW transmission line loaded with reciprocally biased twin ferrite slabs along its sidewalls.

In Fig. 4.2-10, the plot of propagation constant β_f values of an SIW transmission line loaded with two ferrite slabs along its sidewalls is presented. The β_f values are plotted for increasing values of applied magnetic field on ferrite slabs. In Fig. 4.2-10, the cut-off ($\beta_f=0$) frequency increases towards higher frequencies as the values of H_i increases. The increase in the cut-off frequency is non-linear for a linear increase in the value of H_i. This non-linear behavior is also displayed by μ_f and resonant frequency curves in Fig. 3.2-5.

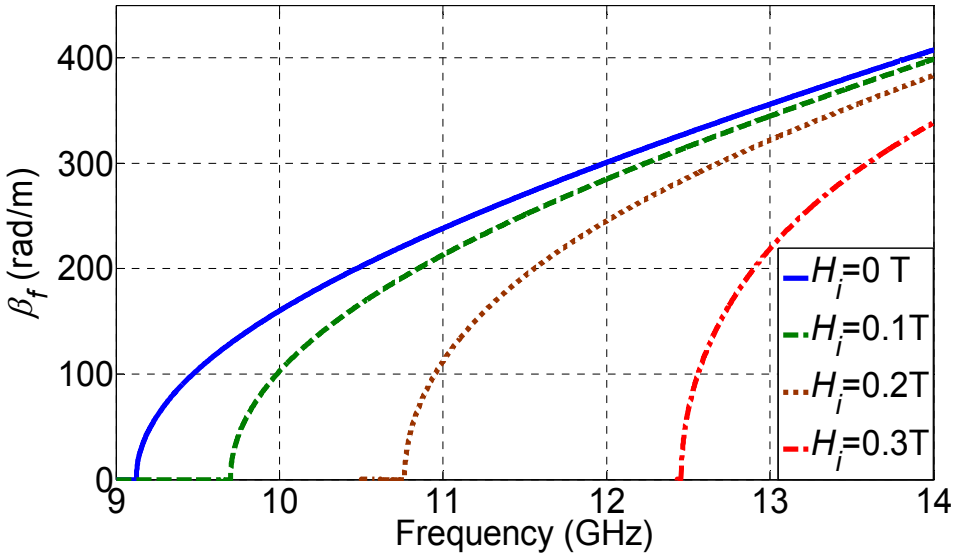

Figure 4.2-10: Calculated propagation constant β_f of an SIW transmission line loaded with ferrite slabs along its sidewalls.

In Fig. 4.2-11, α of the cavity resonators given by (4.11) are plotted. The plotted α values correspond to those of resonators *(1)* and *(2)* of the filter illustrated in Fig. 4.2-8. Since the two cavities are identical, both of them will exhibit the same α curves. For different capacitance C values, α values are also different. The α values for $C = 300$ fF, is higher than the α values for $C = 100$ fF. In Fig. 4.2-11, plotted are also the ideal α curves from (4.9) and (4.10) for different mean tuning frequencies $(f_0)_m$. The α values obtained from (4.9) and (4.10) leads to the development of a filter with constant response shape over the tuning range. Therefore, it is an objective to bring the α curves obtained from (4.11) as close as possible to those obtained from

(4.9) and (4.10).

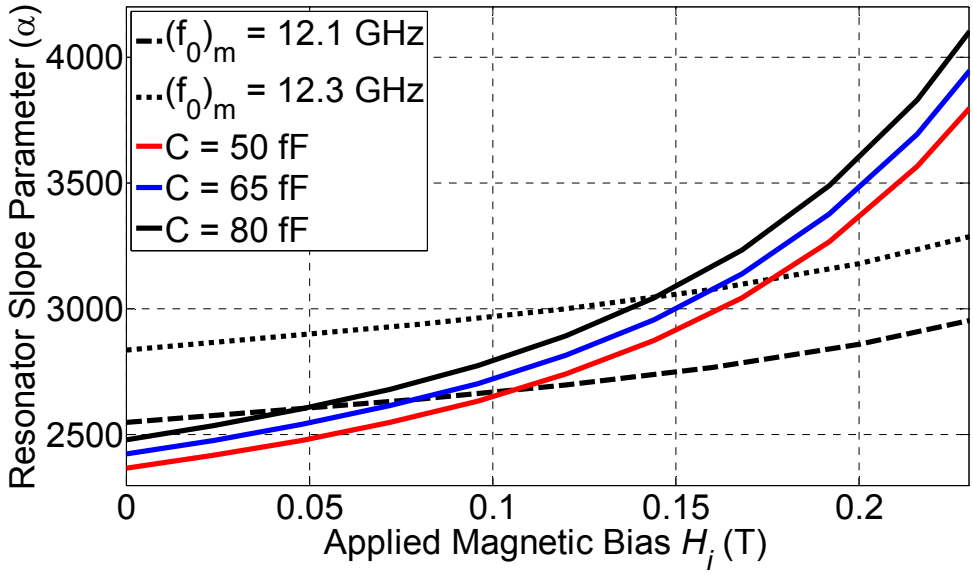

Figure 4.2-11: Calculated resonator slope parameter values versus applied magnetic bias (H_i).

In Fig. 4.2-11, assuming the initial value of C mounted on the cavity to be 80 fF, and selected $(f_0)_m$ to be 12.1 GHz. It can be seen that at lower value of H_i (up to 0.062 T), α curves obtained for $(f_0)_m$ = 12.1 GHz and C = 80 fF are closer to one another. As H_i value increases beyond 0.062 T, the difference between the two curves also increases. However, at this value of H_i, the α curve corresponding to C = 65 fF is in close agreement to $(f_0)_m$ = 12.1 GHz curve. Hence, in order to maintain constant filter response shape, the value of C must be changed from 80 fF to 65 fF. Similarly, for H_i value higher than 0.093 T, difference between α curves corresponding to $(f_0)_m$ = 12.1 GHz and C = 65 fF is increasing. Thus, in order to reduce the difference, value of C is again reduced to C = 50 fF. In this way, in order to realize a constant response filter the value of the capacitance C mounted on the cavity is reduced towards the lower values for a progressive increase in the value of applied magnetic field H_i.

In Fig. 4.2-12, a three-dimensional plot of the resonator slope parameter α is illustrated to obtain a design guideline, in realizing a simultaneous bandwidth and frequency tuning of the filter. It is therefore possible to realize either a constant-bandwidth variable frequency or a constant-frequency variable-bandwidth tuning. In Fig. 4.2-12, α values from (4.11) are plotted against C and H_i values. Ideal α values obtained from (4.9) and (4.10) are also plotted as overlapping isobandwith curves, in red, together with isofrequency curves, in black, obtained from (4.12). The constant-bandwidth curves are calculated for different pairs of $(f_0)_m$ and α_m values. Tuning the

cavities in accordance to the red curves change α and f_0 of the cavities according to the relation given by (4.9) and (4.10) provide a constant bandwidth tuning. In Fig. 4.2-12, they are represented as BW1, BW2, and so on. While the constant frequency curves correspond to the cavity resonant frequency f_0 for a given value of C and H_i and obtained from the solution of (4.12).

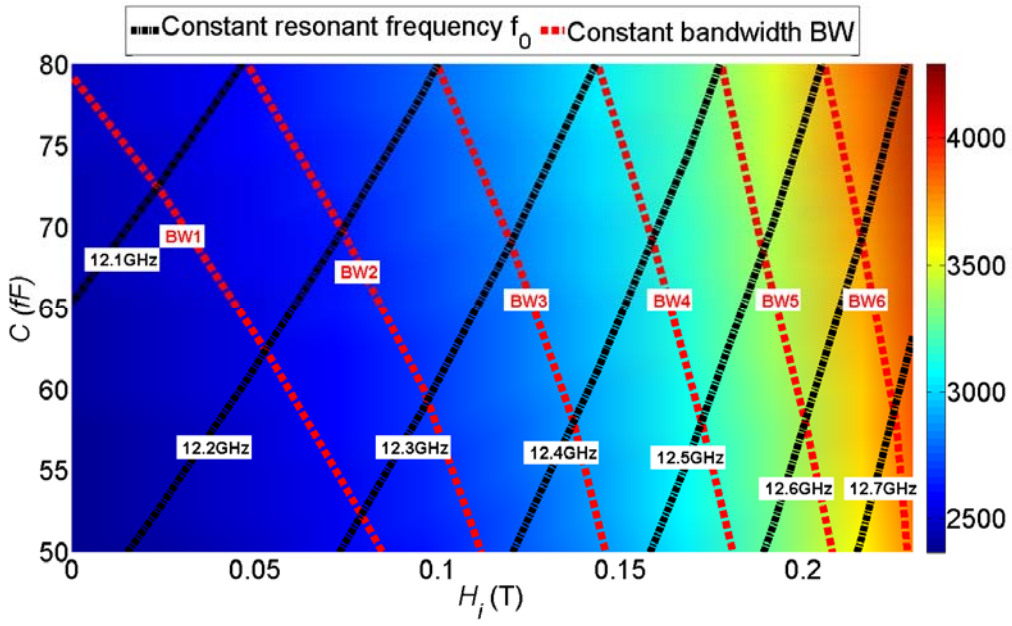

Figure 4.2-12: Calculated results of resonator slope parameter values and constant frequency and constant bandwidths isofrequency curves.

Fig. 4.2-12 provides a possibility to realize either a frequency tunable constant-bandwidth filter or a constant-frequency tunable-bandwidth filter. For example, tuning the C and H_i values along black-curves, a constant-frequency variable-bandwidth tuning of the cavity is achieved. And tuning the C and H_i values along red-curves, a constant-bandwidth variable-frequency tuning of the cavity is achieved.

4.2.3 Measurement results

In this section, measurement results of electric and magnetic two-dimensionally tuned SIW band-pass filter of Fig. 4.2-8 are presented. In Fig. 4.2-13, measurement results of a magnetically tuned SIW band-pass filter are presented. A capacitance value of 80 fF is mounted at the central region of the cavity.

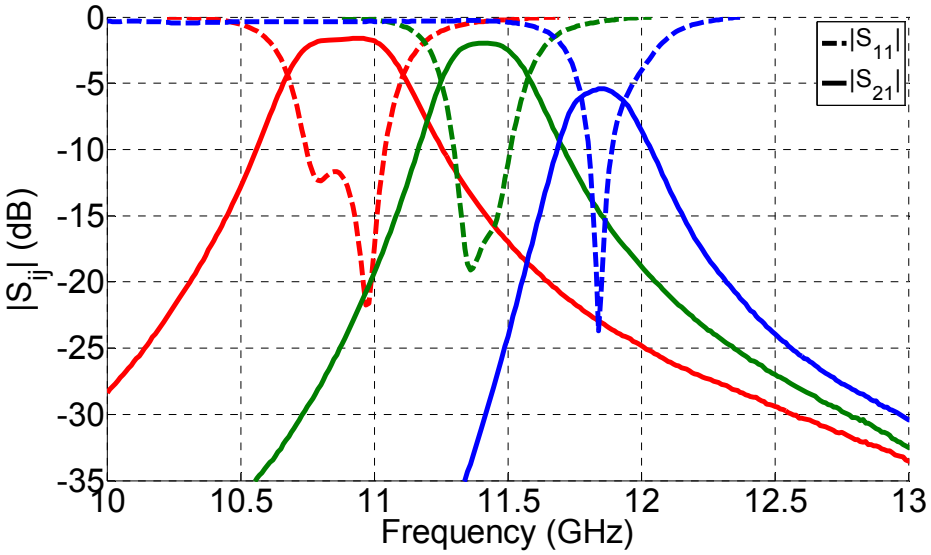

(a)

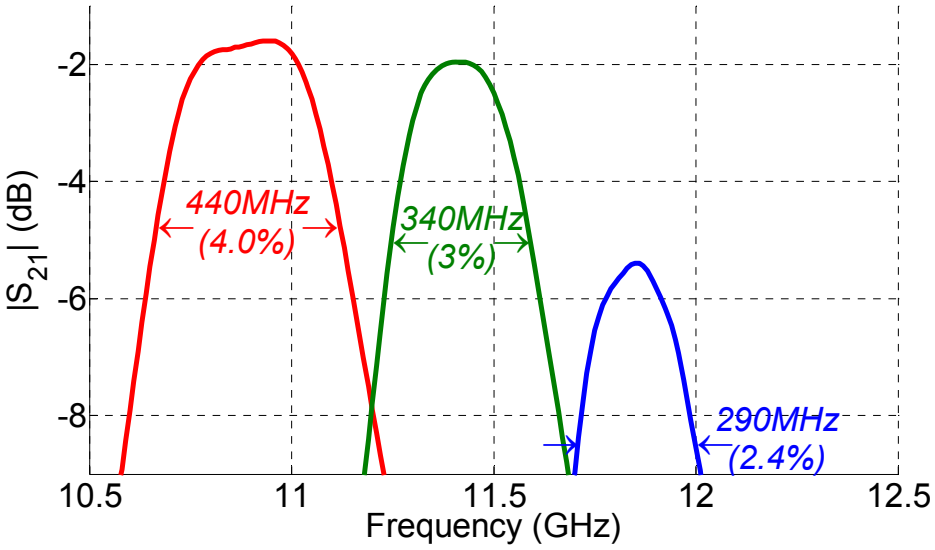

(b)

Figure 4.2-13: Measurement results of magnetically tuned (1-D) SIW cavity filter loaded with $C = 80$ fF capacitor at its center. (a) Measured S_{21} and S_{11} parameters. (b) Enlarged S_{21} parameters.

It can be seen that, keeping the capacitance value fixed and increasing only the externally applied magnetic bias H_0 (1-dimensional tuning), eventually deteriorates the filter response. It can be observed that from the enlarged S_{21} parameter curve images from Fig. 4.2-13 b), as the magnetic field is increased from $H_0 = 0$ T to $H_0 = 0.32$ T, the insertion loss is also increased from 1.7 dB to 5.4 dB. Moreover, the filter 3 dB bandwidth is reduced from 4 % at $H_0 = 0$ T to 2.4 % at

H_0 = 0.32 T.

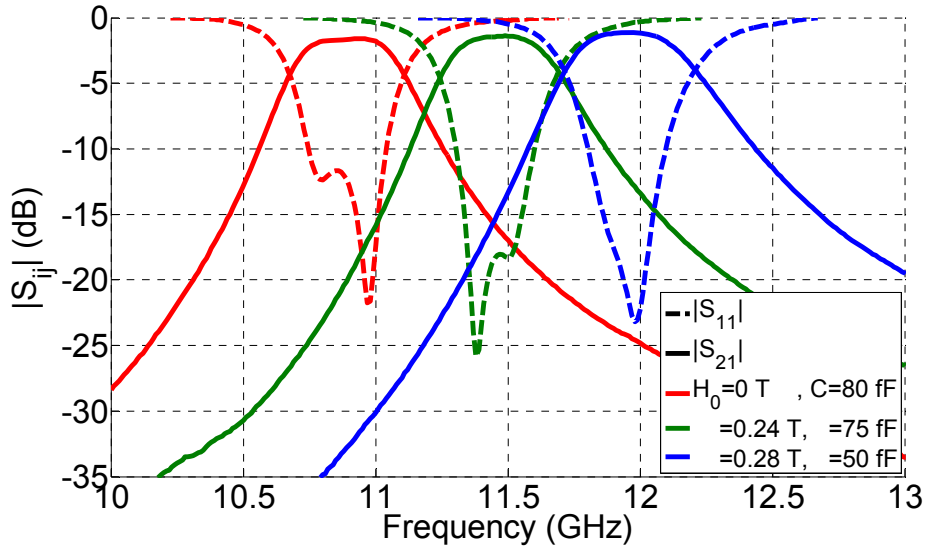

(a)

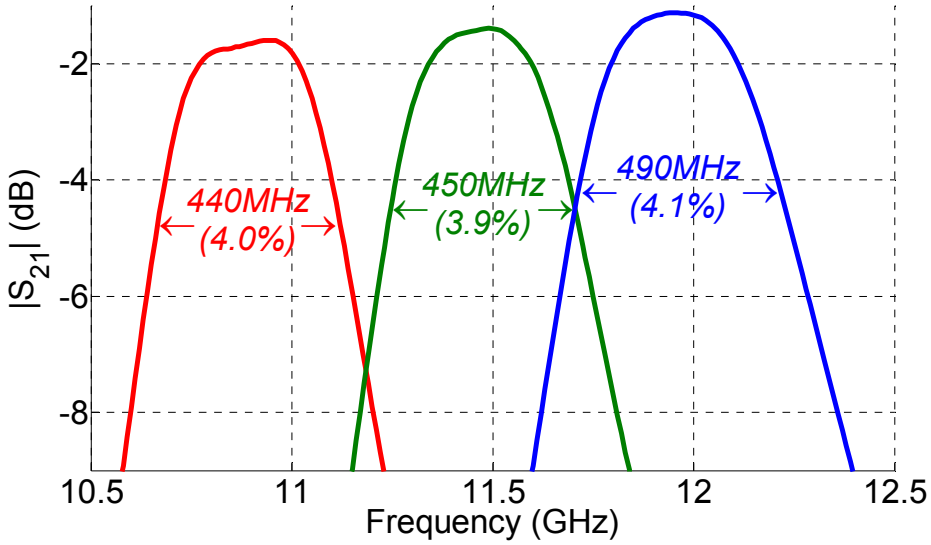

(b)

Figure 4.2-14: Measurement results of 2-D tuned SIW cavity filter loaded with a) measured S_{21} and S_{11} parameters b) enlarged S_{21} parameters.

In Fig. 4.2-14, a filter response of E- and H- field two-dimensionally tuned band-pass filter is presented. It can be seen that, with the increase in H_0 values, the filter response has not been deteriorated as it was in the case of 1-dimensionally tuned filter response presented in Fig. 4.2-13. A key difference in these two tuning methods is the value of the surface mounted capacitor C

as shown in Fig. 4.2-8 is no longer fixed at 80 fF. Instead, its value is reduced as the magnetic bias H_0 is increased. In Fig. 4.2-14, as the external magnetic bias H_0 is increased from 0 T to 0.28 T, the capacitance value C is also changed from the initial value of 80 fF to 50 fF. The reduction in the value of the capacitance as the frequency tuning progresses towards the higher frequency value has enabled preserving the same filter response. It can be noted from Fig. 4.2-14 b), for H_0 = 0 T, 0.24 and 0.28 T, the 3 dB bandwidth of the filter is maintained around 4 %, but for each values of H_0, capacitance C values are different, which are C = 80 fF, 75 fF and 50 fF respectively. It can also be observed theoretically from Fig. 4.2-11 that, in order to maintain a constant bandwidth at higher frequencies, the value of the capacitance needs to get reduced while the amount of magnetic bias H_0 is increased. Moreover, the amount of magnetic field required to achieve the same amount of frequency tuning range has also reduced. It can be observed from Fig. 4.2-13 b) that, keeping C constant at 80 fF, it requires H_0 =0.32 T to change the filter center frequency from 10.8 GHz to 11.86 GHz. While in Fig. 4.2-14 b), only 0.28 T of magnetic field produces a frequency shift from 10.8 GHz to 11.95 GHz.

In Fig. 4.2-15, the measurement results of an SIW band-pass filter with variable bandwidth is presented. It can be seen from Fig. 4.2-8 that, the center frequency of the filter for all three filter responses is fixed at 11.4 GHz. By a suitable variation of magnetic bias H_0 applied on ferrite slabs and capacitor C values, a variable bandwidth of 5 %, 4 % and 3 % is respectively achieved at the same center frequency. In Fig. 4.2-5, a constant frequency curve indicated by black color should be followed in order to realize a variable bandwidth filter. With a suitable combination of C and H_i values a variable bandwidth performance can be achieved at a desired frequency of operation.

It can be seen from Fig. 4.2-15 b) that, the insertion loss of the filter increases as the filter response becomes narrower. For H_0 = 0 T and C = 50 fF the insertion loss is approximately 1 dB, while for H_0 = 0.28 T and C = 80 fF the insertion loss has increased to 2 dB.

Fig. 4.2-13, Fig. 4.2-14 and Fig. 4.2-15 present the measurements that were performed using high Q, UQCL2AXXXBAT2A series ceramic capacitors from AVX Corporation. The capacitors were used for the proof of concept and to know its effect on frequency response shape and bandwidth of the filter for a given value of capacitance. In order to achieve a continuously E- and H- field

tuned band-pass filter, the ceramic capacitor is now replaced by a varactor diode MSV34060-0805-2 from Aeroflex.

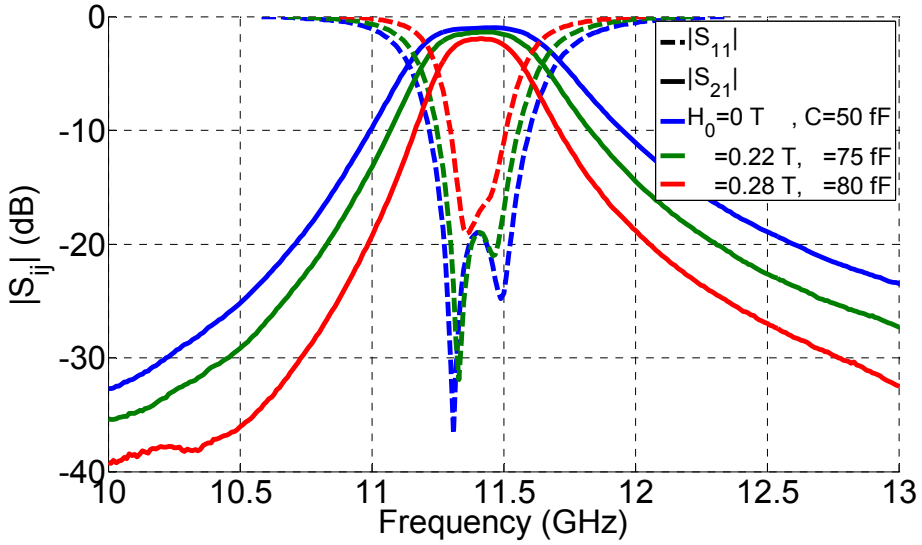

(a)

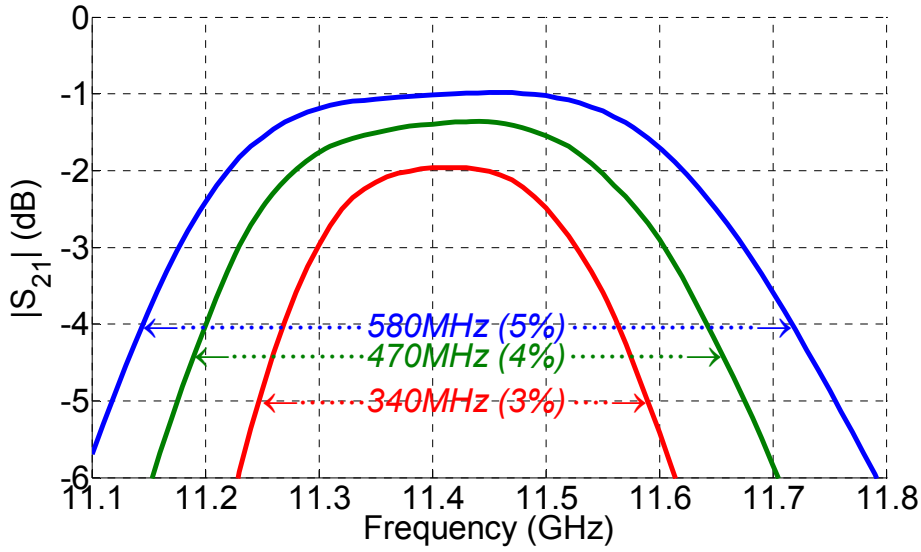

(b)

Figure 4.2-15: Measurement results of 2-D tuned variable bandwidth SIW band-pass filter a) Measured S_{21} and S_{11} parameters and b) Enlarged S_{21} parameters.

In Fig. 4.2-16, the measurement result of a magnetically tuned varactor loaded band-pass filter is presented. In this measurement, the varactor diode biasing voltage is kept constant at 0 V. Similar to only 1-dimensionally tuned band-pass filter of Fig. 4.2-13, with the increase of magnetic bias,

the filter response gets narrower and the insertion loss seems to increase. At $H_0 = 0.36$ T, the filter 3 dB bandwidth has reduced from 4.7 % to 3.1 %.

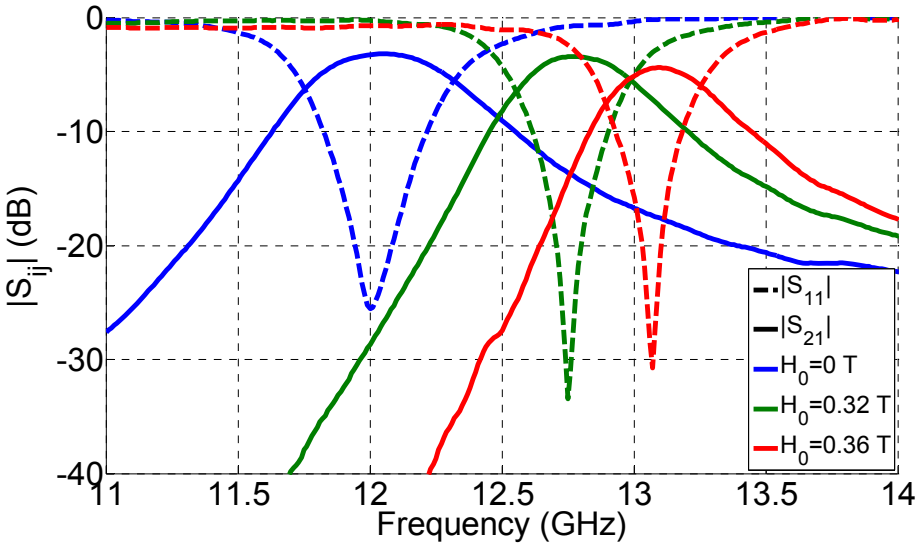

(a)

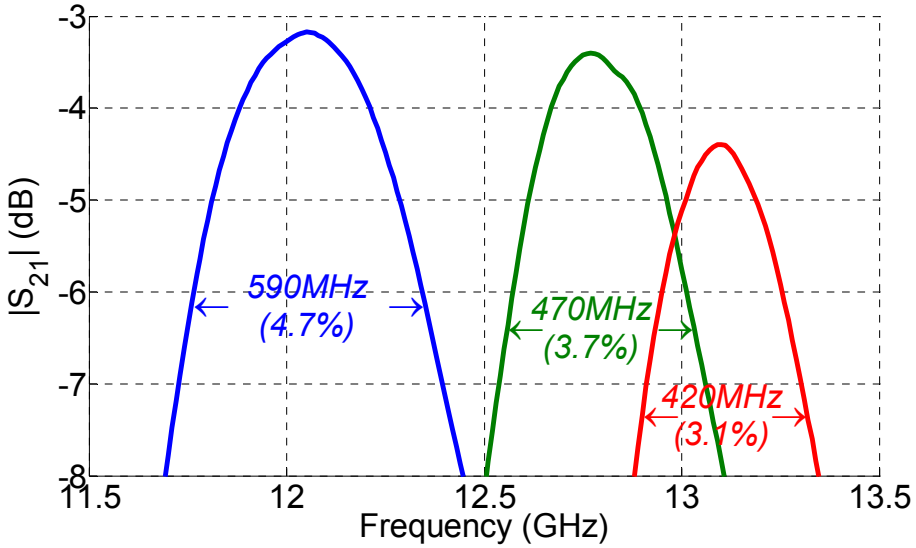

(b)

Figure 4.2-16: Measurement results of 1-D tuned SIW cavity filter using ferrite slabs a) Measured S_{21} and S_{11} parameters b) Enlarged S_{21} parameters.

In Fig. 4.2-17, the measurement results of two-dimensionally tuned band-pass filter using YIG and varactor diode are presented.

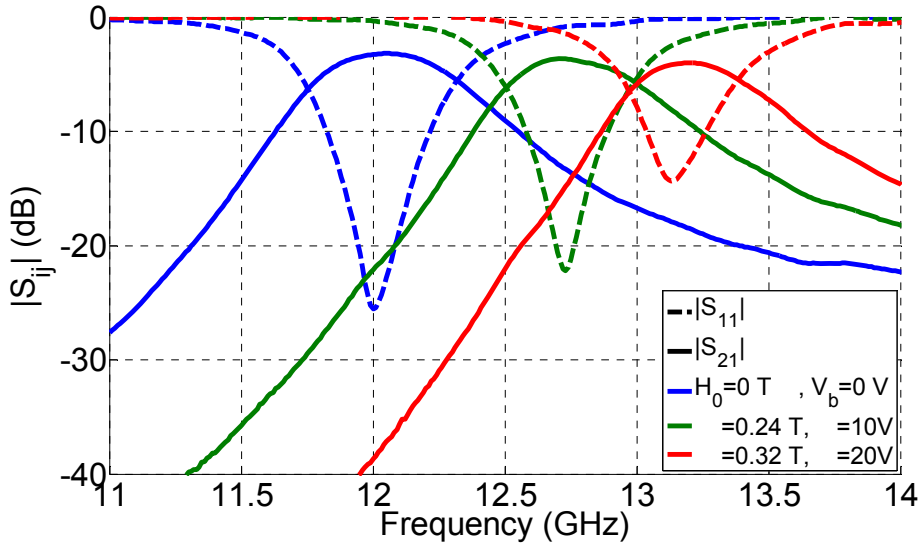

(a)

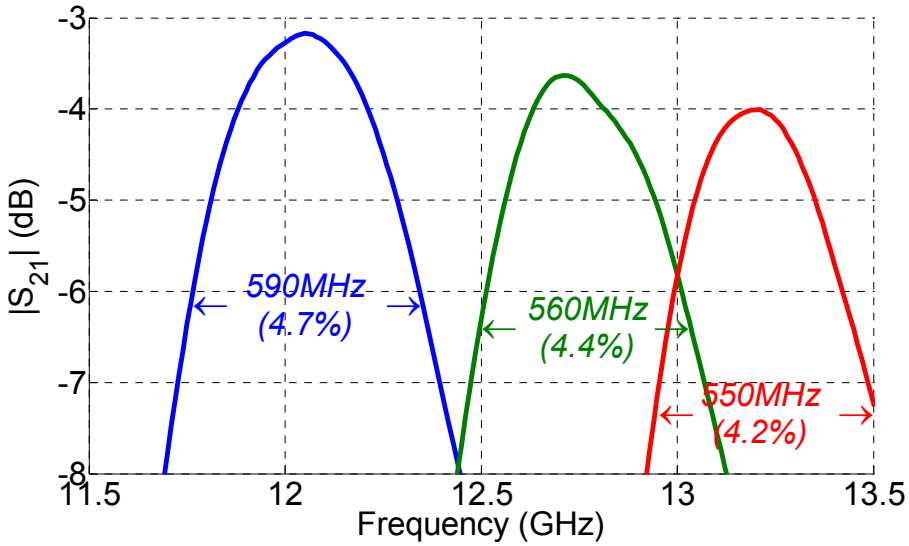

(b)

Figure 4.2-17: Measurement results of 2-D tuned SIW cavity filter using varactor diode and ferrite slabs a) Measured S_{21} and S_{11} parameters b) Enlarged S_{21} parameters.

For an applied bias voltage in the range of $V_b = 0$ V to 30 V, the variation of the nominal capacitance is between 0.3 pF and 0.5 pF. However, this range of capacitance is too high to realize a good matching condition for the filter. Therefore, a capacitance value of 0.1 pF is added in series to the varactor diode in order to reduce the total capacitance value to 80 fF. However, in Fig. 4.2-17, with 80 fF of net capacitance, the center frequency is approximately at 12.1 GHz, unlike Fig. 4.2-13 where the filter center frequency for $H_0 = 0$ T is at 10.8 GHz. This could be

caused by the parasitic effects coming from the series connection of a varactor diode and the capacitor. This is illustrated in Fig. 4.2-8(b), where a bottom view of the band-pass filter is presented. It can be seen in Fig. 4.2-8(b), two 0.1pF capacitors in series are connected to a via island at the bottom surface of the filter. Since the top and bottom surface of each cavities of the filter are connected by a via hole. The varactor diode mounted on the top surface will therefore be connected with the bottom surface capacitors in series. As can be seen from Fig. 4.2-17 that, by changing the varactor voltage to 20 V, the 3 dB bandwidth of the filter has been reduced only to 4.2% unlike in Fig. 4.2-16 where it has been reduced to 3.1% at the highest value of applied magnetic field.

4.3 Two dimensionally (2-D) tunable SIW cavity backed slot antenna

As shown in Section 4.1, the dual tuning of the cavity can be advantageously used to both increase the frequency tuning range and at the same time optimize the matching condition. Based on the cavity introduced in Section 4.1 and on previous work reporting a fixed frequency SIW cavity backed antenna [Luo, Hu, Dong, and Sun (2008)], an electrically and magnetically tuned cavity backed slot antenna is presented in this section. As expected, it is experimentally demonstrated that, the concept of simultaneous electric and magnetic tuning increases the total frequency tuning range of the antenna and improves the matching at the same time.

4.3.1 Cavity backed antenna topology

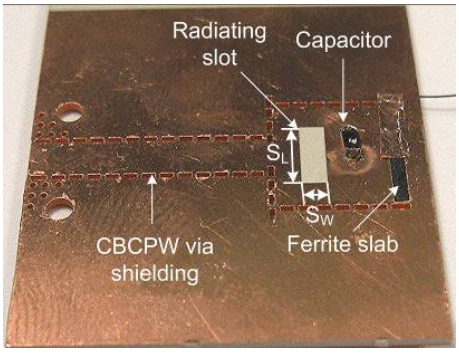

Figure 4.3-18: Fabricated SIW cavity backed antenna loaded with capacitor and ferrite slab S_L =5.5 mm, S_W = 1.9 mm.

Similar to SIW cavity resonator presented in the previous section, the cavity-backed antenna also operates with the dominant TE_{101} mode. The ferrite slab is loaded at an end-wall of the cavity and

a capacitor is loaded at the center. The SIW cavity contains a CBCPW current probe on one side for the feeding purpose and a rectangular slot on the other side as illustrated in Fig. 4.3-18.

4.3.2 Measurement results

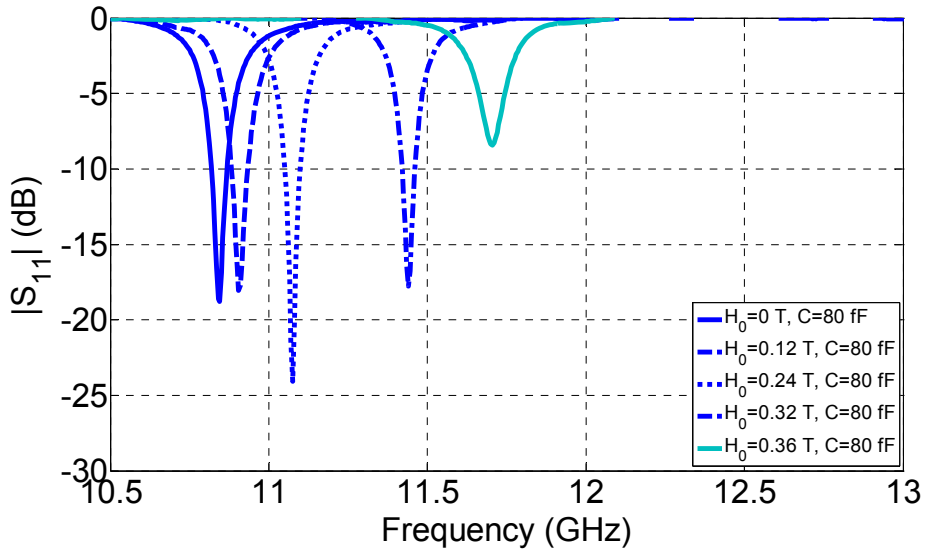

(a)

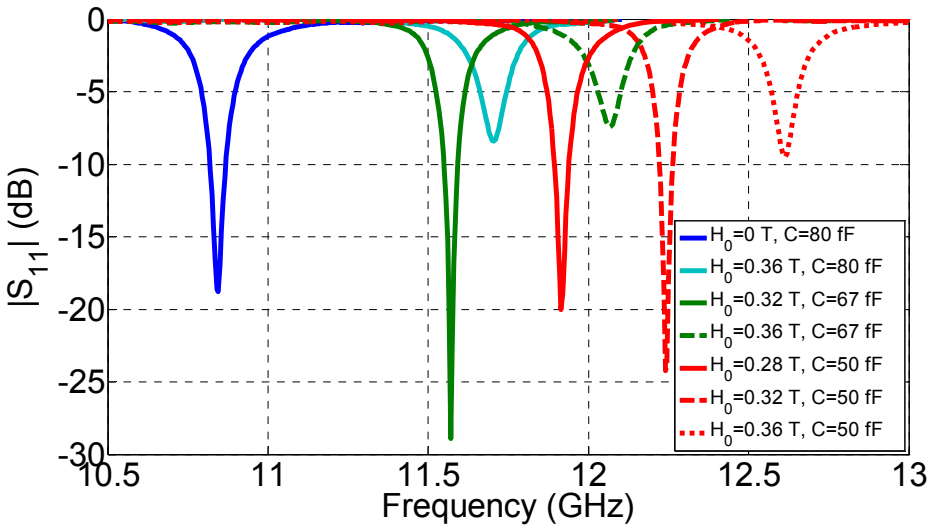

(b)

Figure 4.3-19: Measured S_{11} parameter of cavity backed antenna with a) one dimensional magnetic tuning b) two-dimensional electric and magnetic tuning.

In Fig. 4.3-19 a), a one-port measurement result of one-dimensional magnetic tuning of the cavity-backed slot antenna is presented. In this measurement the value of the capacitance mounted on the cavity is fixed at 80 fF. The external magnetic bias H_0 is increased from initial

value of 0 T to 0.36 T. With the increase in the value of applied magnetic bias, the resonant frequency shifts towards higher frequency values. At $H_0 = 0.36$ T, the return loss becomes significant. This loss increase at higher value of magnetic bias is also reported in previous chapter. A total frequency tuning range considering up to the frequency point where the return loss is better than 10 dB is equal to 590 MHz, i.e. for the applied magnetic bias from $H_0 = 0$ T to $H_0 = 0.32$ T. From Fig. 4.3-19 a) and Fig. 4.3-19 b), it is clear that the losses arising at the higher frequency value is not related to the magnetic loss due to its operation near the ferromagnetic resonance region, but it is related to the mismatch produced at the cavity feeding. Reducing the value of capacitance also improves the mismatch; thereby increasing the total frequency tuning range and optimizing the antenna return loss and overall efficiency.

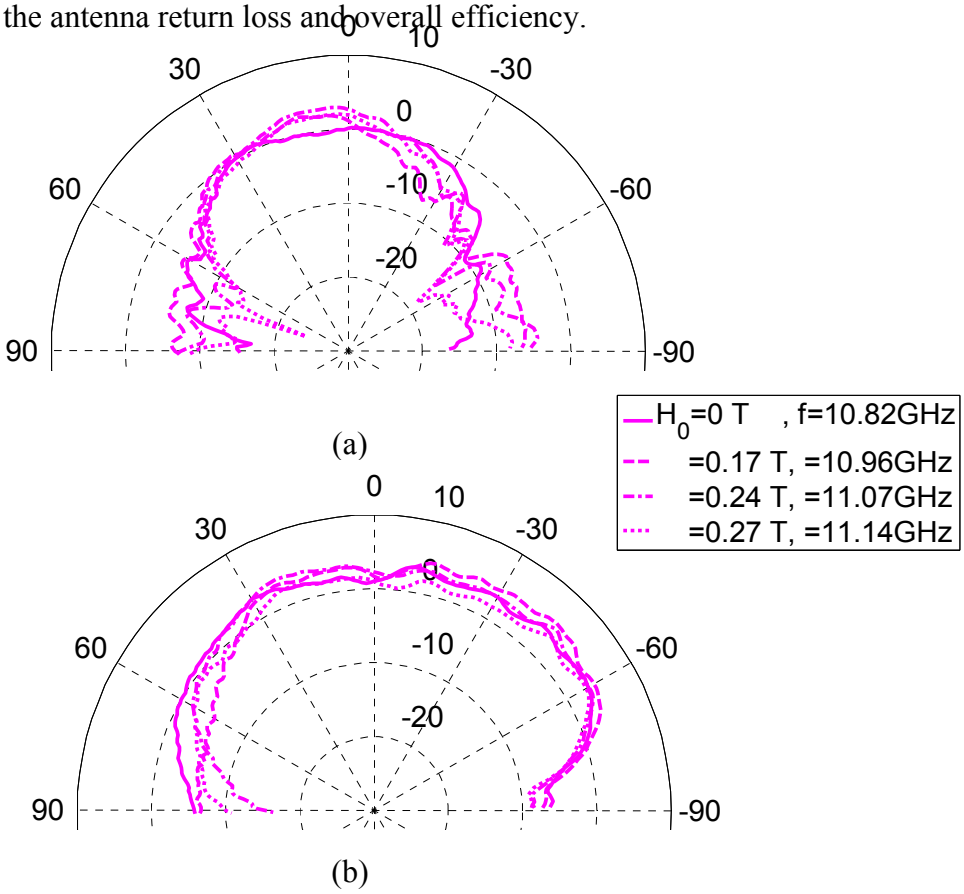

Figure 4.3-20: Measured radiation pattern, in dBi, of one-dimensional magnetic tuned cavity backed slot antenna: a) H-plane and b) E-plane.

In Fig. 4.3-20 and Fig. 4.3-21, the measured radiation patterns of the cavity backed slot antenna are presented respectively for one and two dimensional tuning. In Fig. 4.3-20, the E- and H-plane radiation patterns are plotted for magnetically tuned cavity-backed slot antenna with value

of the capacitance mounted on the cavity fixed at 80 fF, while Fig. 4.3-21 presents the radiation pattern where the antenna is tuned by changing the value of capacitor and the applied magnetic bias. It can be observed that there is no significant difference in radiation patterns shapes. The un-symmetricity in E-plane pattern is caused by the unequal ground plane length between the cavity feeding side and the side where the ferrite slab is loaded.

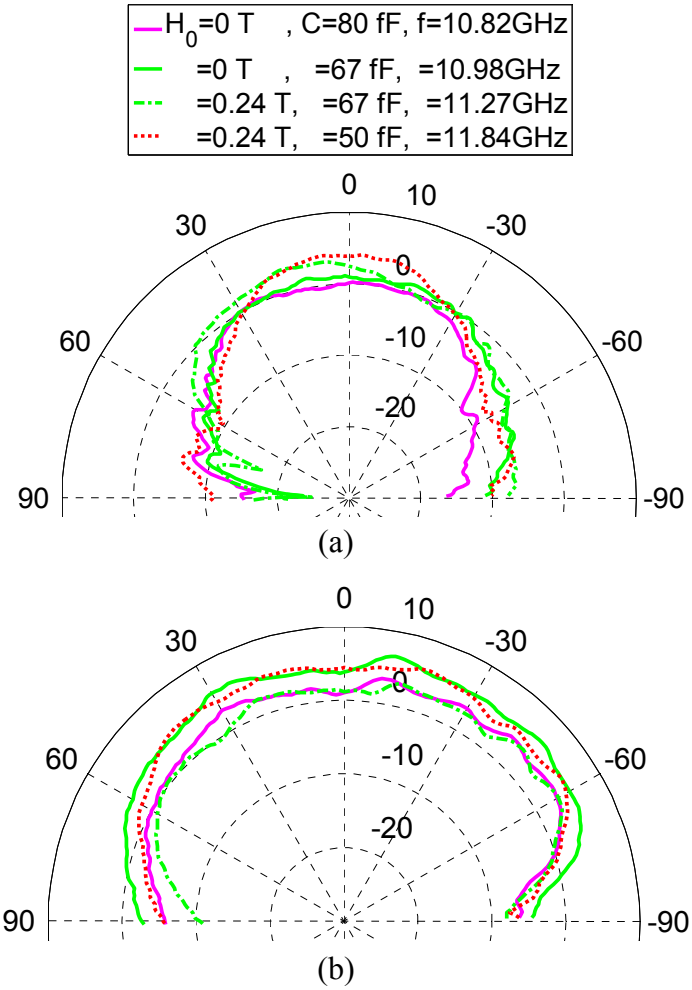

Figure 4.3-21: Measured radiation pattern, in dBi, of two-dimensional magnetic tuned cavity backed slot antenna: a) H-plane and b) E-plane.

4.4 Conclusion

A concept of simultaneous electric and magnetic two-dimensionally tuning has been presented and demonstrated with a number of theoretical and experimental cases studies. SIW-based devices including a cavity resonator, band-pass filter, and cavity-backed slot-antenna employing the proposed 2-D tuning concept have been successfully designed and fabricated. It can be seen

theoretically and experimentally that simultaneous electric and magnetic 2-D tuning not only significantly increases the total frequency tuning range compared to sole electric or magnetic tuning, but it is also useful in tuning other key design parameters including the factor, input matching, and bandwidth. A filter with simultaneous frequency and bandwidth tuning has been successfully demonstrated. As a matter of fact, the 2-D tuning is related to the resonant mode tuning in our cavity case studies. This mechanism may be of interest to be extended into other structures.

CHAPTER 5 NON-RECIPROCAL FERRITE LOADED SIW DEVICES

Anisotropic materials are very useful in realizing a wide variety of non-reciprocal microwave components and devices. Ferrites and ferromagnetic materials are promising anisotropic materials that have been used from the beginning to design microwave devices such as circulators, phase-shifters, tunable filters [Fay, and Comstock (1965)], [Boyd (1971)], [Uher, Bornemann, Arndt (1988)]. Most of these ferrite components and devices were developed based on rectangular waveguide technology. Within the topology of a rectangular waveguide, for a given mode of operation (for example TE_{10} mode), the regions of the highest electric and magnetic fields are clearly defined. Electric field strength is highest around the central region while magnetic fields are highly confined along the sidewalls. Since ferrite materials tend to have a strong interaction with magnetic fields, they should be placed within the locations of strong magnetic fields in order to generate any material commanded effects. Therefore, for a given application, ferrite materials are usually loaded along the sidewalls of the rectangular waveguide. Moreover, rectangular waveguide solutions offer lower loss and they can also carry much higher power in comparison to planar transmission line technologies. However, due to the three-dimensional mechanical and bulky-geometry, they are not compatible with the requirement of component and device integration and planarization. Attempts have already been made to develop and design ferrite-based two-dimensional and planar components that retain the benefits of a rectangular waveguide. In [D'Orazio, and Wu (2006)], a millimeter-wave degree-2 circulator for two different substrate thicknesses were successfully studied, designed and demonstrated. In [Bray, and Roy (2005)], anti-symmetrically biased rectangular waveguide phase shifter was embedded in a low temperature co-fired ceramic package. In the previous chapter, ferrite loaded magnetically tunable SIW based cavity resonator, band pass filter, and cavity backed antenna were proposed and demonstrated. In this chapter, SIW technology is used in support of the design of non-reciprocal magnetically tunable phase shifters that not only inherit all the qualities of a rectangular waveguide, but also are fully compatible with other planar circuits and devices.

In this work, Yttrium Iron Garnet (YIG) and Nickel (Ni) ferrite, having different values of saturation magnetizations, are considered for the demonstration of the SIW based magnetically tunable phase shifters. It is suggested theoretically and experimentally that materials with higher saturation magnetization offer higher phase shifting for the same value of applied DC magnetic

bias. Since YIG has a lower value of saturation magnetization compared to that of Ni ferrite, a comparison of results between those two classes of materials is also presented. It is discussed, for a given biasing condition, which one of the two materials could be possibly used in the realizing of a gyrator. Gyrator is a device having a unidirectional phase shift of 180°. Subsequently, the demonstrated gyrator is used in realizing an SIW based 4-port circulator at 12 GHz.

5.1 Theoretical study of ferrite materials

In this work, two different non-reciprocal phase shifters based on SIW technology using Yttrium Iron Garnet (YIG) and Nickel ferrite ($NiFe_2O_4$) are presented. YIG is a ferrimagnetic material whereas Nickel ferrite is composed of Nickel and Oxides. Ferrimagnetic materials possess higher resistivity and anisotropy compared to ferromagnetic materials [Pozar (2005)]. Both YIG and Nickel (Ni) ferrite are manufactured at National Magnetics Groups TCI ceramics, PA, USA. Based on the provided datasheet, saturation magnetization of YIG is Ms = 1780 G, dielectric constant ε_f = 15 and line width ΔH = 17 Oe. Similary, provided saturation magnetization of Ni ferrite is Ms = 5000 G, dielectric constant ε_f = 13.1 and line width ΔH = 198 Oe. It is a purpose of this work to compare the performance of YIG and Ni ferrite in terms of differential phase shift and loss when used as anisotropic elements in realizing SIW based non-reciprocal phase shifters.

Before using the ferrite materials to realize non-reciprocal phase shifters, it is necessary to analyze their behaviour when applied with a small AC (microwave) magnetic field. In the analysis, it is assumed that ferrite materials are biased by an application of transverse static DC magnetic field.. From the relationship between a torque exerted on the magnetic dipole of the ferrite and the applied magnetic field, a tensor permeabilities for different direction of magnetic bias is derived. For a ferrite biased along transverse z-direction, the tensor permeability is given by [Pozar (2005)],

$$[\mu] = \mu_0 \left([U] + [\chi] \right) = \begin{bmatrix} \mu & j\kappa & 0 \\ -j\kappa & \mu & 0 \\ 0 & 0 & \mu_0 \end{bmatrix}. \qquad (5.1)$$

In (5.1), μ_0 is the free space permeability, $[U]$ is a unit vector, and χ is a susceptibility tensor. By considering the effect of magnetic loss, the components of permeability tensor becomes complex, giving rise into dissipative and dispersive components of tensor permeability.

In Fig. 2.1-3 and Fig. 2.1-4, calculated dissipative and dispersive components of YIG and Ni ferrite are plotted against the internal magnetic field H_i. The permeability components of an infinite ferrite medium are plotted based on the provided values of *Ms* and ΔH values of YIG and Ni ferrite. The permeability components are calculated at an intended design frequency of 12 GHz.

In Fig. 2.1-3 and Fig. 2.1-4, the ferromagnetic resonance region occurs near 0.45 T of applied magnetic bias H_i. Since the line width value (ΔH) of Ni ferrite is much higher than that of YIG, in Fig. 2.1-3, the magnetic loss due to Ni ferrite begins to increase significantly even from 0.2 T of applied magnetic bias H_i. When the applied magnetic bias approaches near the ferromagnetic resonance region. the Ni ferrite suffers from much higher losses compared to YIG. Due to higher magnetic loss near the ferromagnetic resonance region, the non-reciprocal phase shifters presented in the next sections will be designed in the region below the ferromagnetic resonance. Similary in Fig. 2.1-4, it can be noted that the rate of change of dispersive permeability component μ' of Ni ferrite below the ferromagnetic resonance region is much higher compared to YIG. This suggests that even a low value of magnetic bias should be sufficient to produce a significant change in the dispersive permeability component value of Ni ferrite. Hence, it can be concluded that, due to the low loss property, YIG is more suitable in the design of low loss devices where the tunablitly is not important. Whereas, Ni ferrite is suitable in the design of highly tunable devices where some magnetic losses are tolerable.

5.2 Topology of SIW non-reciprocal phase shifter

Magnetic anisotropy is known to be induced in ferrites and ferromagnetic compounds by applying an external DC magnetic bias. Once the ferrite material is placed and becomes subjected to a DC magnetic bias, the dipole moments tend to align along the direction of the applied bias, thus producing a non-zero magnetic dipole moment. The applied magnetic bias makes the dipole moments undergo precession at a certain frequency. A strong interaction takes place between the applied electromagnetic signal and the ferrite material, if the precession of the dipole moments and the circular polarization of the applied signal are in the same orientation. Of course, a signal having a different orientation of circular polarization remains unaffected by the presence of ferrites. The use of this property of ferrite allows the realization of very useful non-reciprocal or anisotropic components and devices.

In this section, a magnetically tunable non-reciprocal phase shifter based on SIW technology is presented. SIW is known to present attractive low loss property and planar geometry, which presents an outstanding and unique compromise between waveguide solutions and planar technologies.

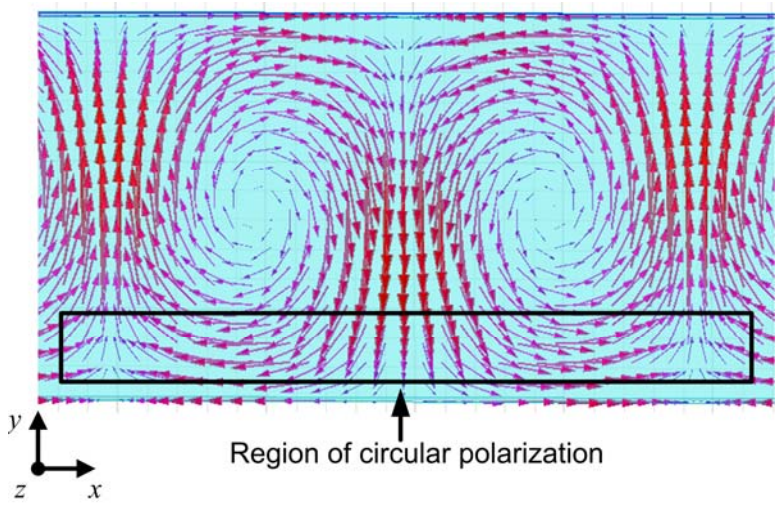

Figure 5.2-1: Simulation of a magnetic field vector inside SIW transmission line using Ansoft HFSS 15.0. Magnetic vector field illustrate the circular polarization behaviour near the SIW sidewall.

Fig. 5.2-1 illustrates a simulated SIW transmission line using Ansoft HFSS 15.0. In Fig. 5.2-1, the top-view image of magnetic field vectors of TE_{10} mode when looking in the *xy*-plane is plotted. The region of circular polarization inside the SIW line is indicated by the rectangular box. In these natural regions of circular polarization, as the time progresses the magnetic field vector remains constant in magnitude but its direction changes in a circular fashion as the time progresses forward. When the ferrite slabs are placed in these regions, circularly polarized waves are excited in the ferrites. The sense of rotation of such a circularly polarized wave depends upon the direction of the wave propagation inside the SIW. For a given polarity of external magnetic bias, a strong interaction between the electromagnetic wave and the ferrite material will occur if the precession of the magnetic dipoles and the circularly polarized wave orientation of rotation become coincident along the same direction. In the SIW representation of Fig. 5.2-1, as the ferrite material is placed along only one side wall, there will be an interaction between the ferrite material and the electromagnetic wave travelling in one direction. In such a topology, the wave travelling in the opposite direction will propagate as if no ferrite material is present. Thus, the structure (phase shifter) of Fig. 5.2-1 has a non-reciprocal phase shifting property, where the

phase shifting of the wave travelling in one direction is different from that of the wave travelling in opposite direction.

5.3 Theory and measurement results of single ferrite loaded SIW phase shifter

In this section, a theory and measurement results of an SIW based non-reciprocal phase shifter are presented. YIG and Ni ferrite are seperately considered for the design. The topology of phase shifter consists of a single ferrite slab loaded along one of the sidewalls of an SIW transmission line.

The SIW phase shifter is fabricated on a Rogers RT/duroid 6010 substrate, whose dielectric constant and the loss tangent (Tanδ) values at 10 GHz are $\varepsilon_s = 10.2$, and Tan δ = 0.002 respectively. Rogers 6010 is chosen for the design of the phase shifters because of its high dielectric constant value. As the dielectric constant values of YIG and Ni ferrite are 15 and 13.1, placing them inside Rogers's 6010 substrate which has dielectric constant of 10.2 will reduce the mismatch effects to some extent. However, Rogers 6010 has a higher dielectric loss tangent (Tan δ) value, which could have an effect on the overall loss performance of the phase shifter and the 4-port circulator.

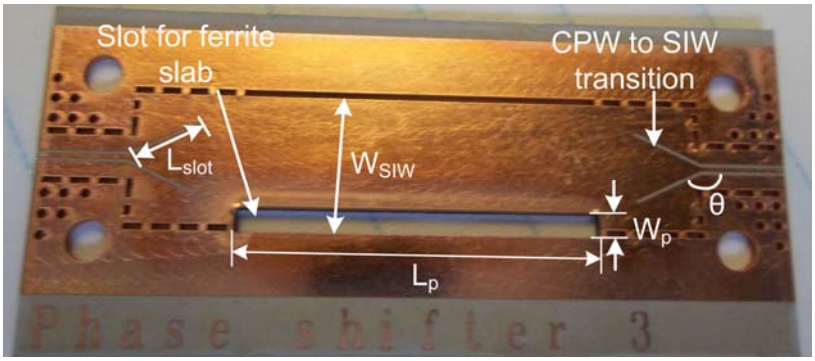

Figure 5.3-2: Fabricated tunable non-reciprocal FLSIW phase shifter with $L_p = 18$mm, $W_p = 1$mm, θ =25°, $L_{slot} = 3.8$mm, $W_{SIW} = 6.5$mm.

In Fig. 5.3-2, the fabricated prototype of an SIW section of transmission line is presented. In order to accommodate a ferrite slab inside the SIW, a rectangular slot of length L_p and width W_p is made along one of the sidewalls of the SIW. Nickel (Ni) ferrite and YIG are used in the design of the non-reciprocal phase shifter. Ni ferrite has $4\pi M_S = 5000$ G and $\Delta H \leq 198$ Oe, while YIG has $4\pi M_S = 1780$ G. and $\Delta H \leq 17$ Oe. To provide a constant metallic wall to preserve the TE_{10}

mode in SIW, only the outer wall of the slot is metallized along its length. As explained earlier, a non-reciprocal phase shifting is achieved by loading the ferrite slab on the sidewall slot of the SIW transmission line and applying an external DC magnetic bias on it. In order to facilitate the measurement of the phase shifter, a transition from SIW to CBCPW is made. The two port measurement of the phase shifter is performed, by connecting it to input and output terminals of Agilent's general purpose network analyzer (PNA).

5.3.1 Theory of single ferrite loaded non-reciprocal phase shifter

In [Collin (1960)], a theory on special case of a partially filled rectangular waveguide is presented, where a ferrite slab is loaded along one of the sidewalls of the waveguide. Since SIW inherits almost all the properties of a rectangular waveguide, the same theory is also used in the evaluation of a single ferrite loaded SIW transmission line.

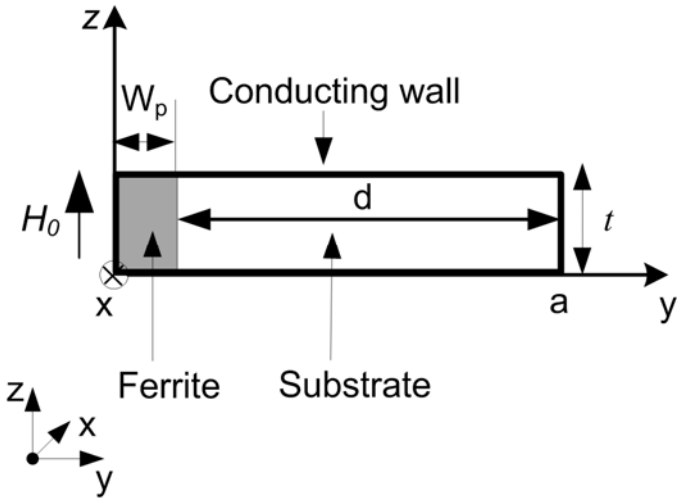

Figure 5.3-3: Cross-sectional view of the tunable non-reciprocal FLSIW phase shifter.

In Fig. 5.3-3, a cross-sectional view of an SIW line loaded with a single ferrite slab is illustrated. The ferrite slab is loaded only along one of the sidewalls of the SIW. A static magnetic bias H_0 is applied along z-direction. The widths of the ferrite slab and substrate section are represented by W_p, and d, respectively.

The characteristic equation is the simplified form of a complex transcendental equation, which assumes that the gap between the waveguide wall and the ferrite slab is zero. The equation is written as a sum of two functions given by [Collin (1960)],

$$f_1(\beta) = l\cot(lt) + \frac{\mu_e}{\mu_0} h\cot(hd), \tag{5.2}$$

$$f_2(\beta) = -\frac{\beta\kappa}{\mu} \tag{5.3}$$

In (5.2), l and h are the wave numbers in ferrite and substrate regions, and μ_e is the effective permeability of a plane wave, which is propagating transverse to the direction of applied DC magnetic bias. In Fig. 5.3-3, x-direction is the direction of the propagation of the wave, while the static magnetic bias H_0 is applied along z-direction. The effective permeability of the ferrite is given by,

$$\mu_e = \frac{\mu'^2 - \kappa'^2}{\mu'^2}, \tag{5.4}$$

where μ' and κ' are the components of tensor permeability.

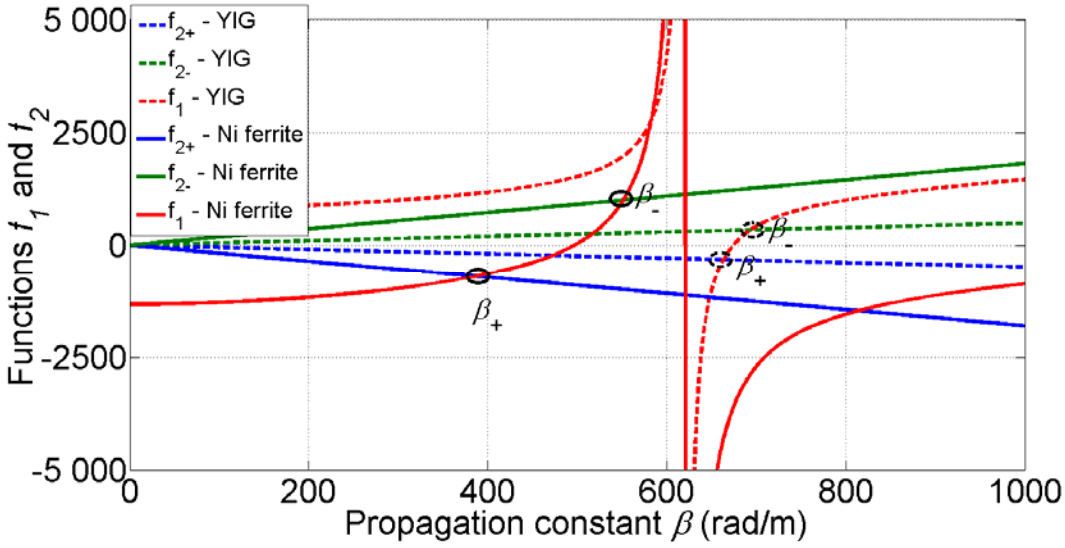

Figure 5.3-4: Calculated dispersive permeability components of YIG and Nickel (Ni) ferrite.

In Fig. 5.3-4, functions f_1 and f_2 versus propagation constant for YIG and Ni ferrite are plotted. It is assumed in the calculation that SIW width is 6.5 mm, and ferrite width is 2 mm, such that the value of d in (5.2) is equal to 4.5 mm. The solution for the reverse propagating wave is obtained by simply reversing the sign of f_2. The curves for YIG are represented by "dashed lines"; while for Ni ferrite they are represented by "solid lines". The points where f_1 and f_2 intersect give the solution of propagation constant values for the forward and reverse travelling waves. For YIG, f_1 and f_2 intersect at $\beta_+ = 660$ and $\beta_- = 700$, thus resulting differential propagation constant value is

$\Delta\beta$ = 40 rad/m. Similarly, for Ni ferrite β_+ = 390 and β_- = 550 and $\Delta\beta$ = 160 rad/m. Therefore, at 12 GHz, for the applied magnetic bias of 0.125 T, the differential propagation constant value of Ni ferrite is higher than YIG by four times. Since propagation constant value is directly proportional to the phase, hence from the solution of f_1 and f_2 plotted in Fig. 5.3-4, the differential phase shift produced by Ni ferrite is four times higher than the phase shift produced by YIG.

5.3.2 Measurement results of single ferrite loaded non-reciprocal phase shifter

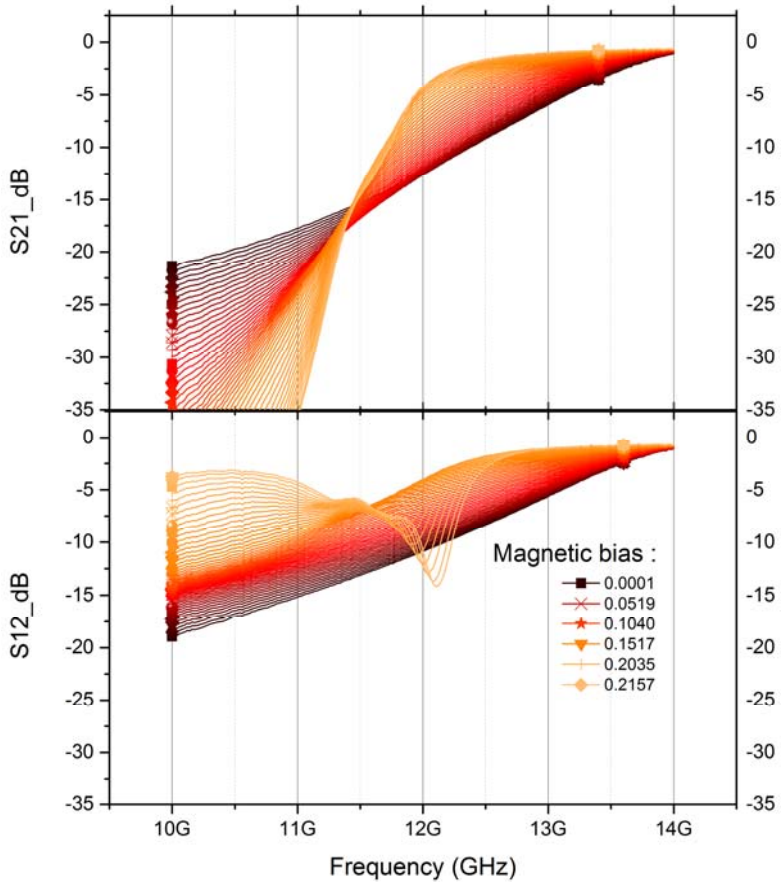

Figure 5.3-5: Measured insertion losses of a 2 mm wide Nickel (Ni) ferrite loaded SIW phase shifter. Traces are plotted for different magnetic bias value ranging from 0 to 0.2 T with steps of approximately 0.05 T.

Fig. 5.3-5 presents the measured two port S-parameters of 2 mm wide Ni ferrite loaded in an SIW transmission line. At 12 GHz for low value of applied magnetic bias, the insertion losses in both directions (S_{12} and S_{21} parameters) are higher than 10 dB. As the applied magnetic bias is increased, the insertion loss reduces. The permeability value decreases with the increase in the value of applied magnetic bias. Since the cut-off frequency of an SIW line is inversely

proportional to the permeability value, the cut-off frequency should therefore increase with the value of applied magnetic bias. But in Fig. 5.3-5, for S_{21} and S_{12} parameters with the increase in applied magnetic bias, the insertion loss reduces and it appears that the cut-off frequency moves towards lower frequency values instead of moving towards higher. An explanation for this behavior could be, due to low-field loss of Ni ferrite, the insertion loss at zero bias condition is very high. As the applied magnetic bias is increased, the low field loss also begins to reduce. The rate of reduction of the low field loss with the applied magnetic bias is much higher than the rate of change of cut-off frequency. Once enough magnetic bias is reached to compensate the low field loss, the cut-off frequency of SIW then appears to move towards higher frequency values.

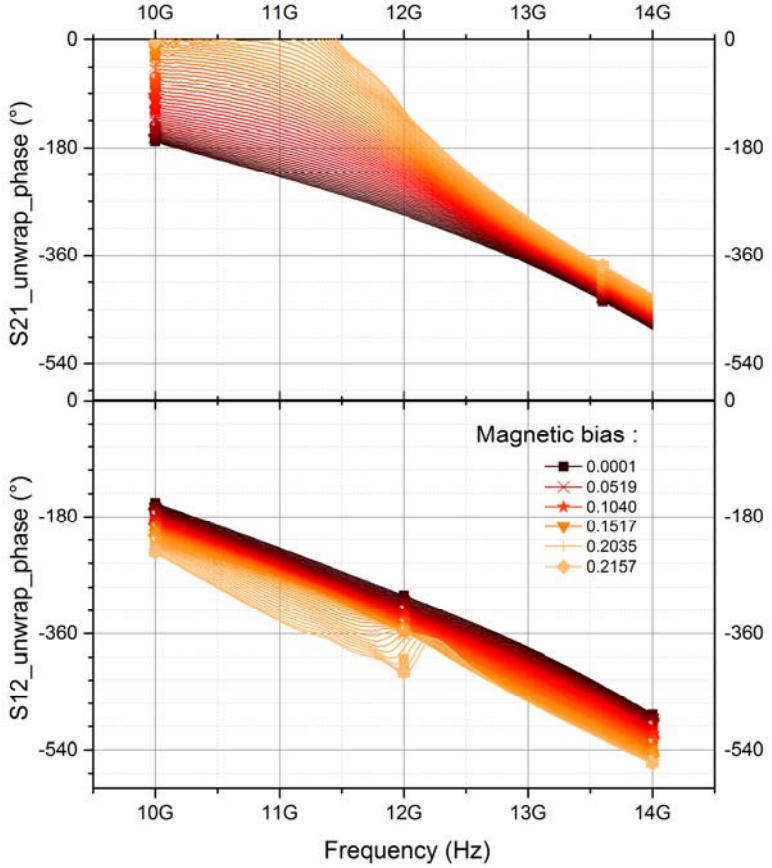

Figure 5.3-6: Measured phase shift from port 1 to 2 and from port 2 to 1 of a 2 mm wide Nickel (Ni) ferrite loaded SIW phase shifter. Traces are plotted for different magnetic bias value ranging from 0 to 0.2 T with steps of approximately 0.05 T.

In Fig. 5.3-6, measurement results of S_{21} and S_{12} phases are presented. Due to non-reciprocal phase shifting, with the increase in magnetic bias, S_{21} phase is increasing while the phase of S_{12} is becoming more negative. The rate of change of phase of S_{21} parameter is much higher compared

to S_{12} parameter. Similar results are also observed in the theoretically calculated solutions of (5.2) and (5.3). In Fig. 5.3-6, for a given ferrite material, the positive and negative propagation constant values β_+ and β_- are not changing at the same rate. It can be observed that the change in β_- is higher compared to β_+. Ideally for only one ferrite loaded SIW type of transmission line, one of the two propagation constant values should stay constant. But in reality it is changing in a smaller rate in opposite direction as illustrated. This phase shift in opposite direction has a huge impact on the design of a four port circulator where the phases of the signals are very import to achieve a higher isolation. In the later sections, the impact of the non-reciprocal phase shifter on the overall performance of the four port circulator will be discussed in a greater detail.

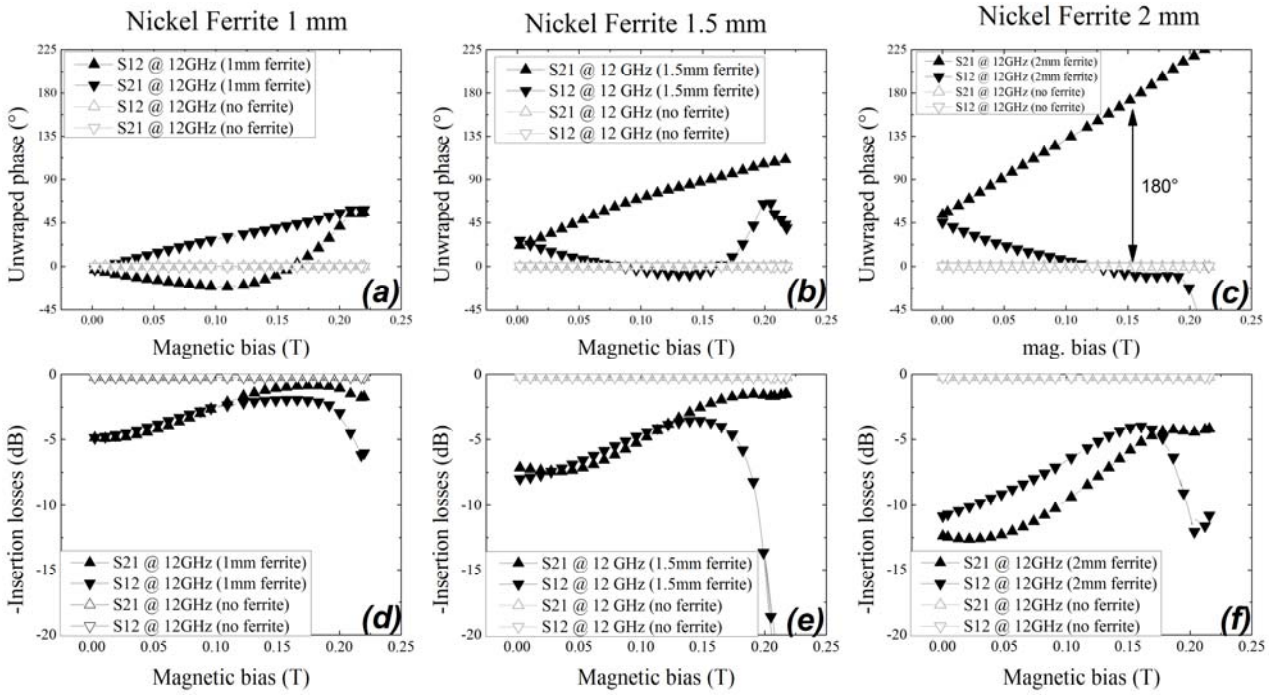

Figure 5.3-7: Measured forward and reverse phase shifts and insertion losses for different widths of a ferrite slab, compared to phase shifts and insertion losses of an unloaded SIW. (a): phase of 1 mm Nickel ferrite slab loaded in SIW; (b): phase of 1.5 mm Nickel ferrite slab loaded in SIW; (c): phase of 2 mm Nickel ferrite slab loaded in SIW; (d): insertion losses of 1 mm Nickel ferrite slab loaded in SIW; (e): insertion losses of 1.5 mm Nickel ferrite slab loaded in SIW; (f): insertion losses of 2 mm Nickel ferrite slab loaded in SIW.

In Fig. 5.3-7 and Fig. 5.3-8, two sets of measurement results of a non-reciprocal phase shifter loaded with Ni ferrite and YIG are presented. The measurements of the phase shifter are

performed at 12 GHz and the length of the ferrite slab in SIW phase shifter is 18 mm. In order to study the effect of ferrite size on the overall performance of the phase shifter, measurements are also performed for different widths of the ferrite slabs that are loaded inside the SIW line.

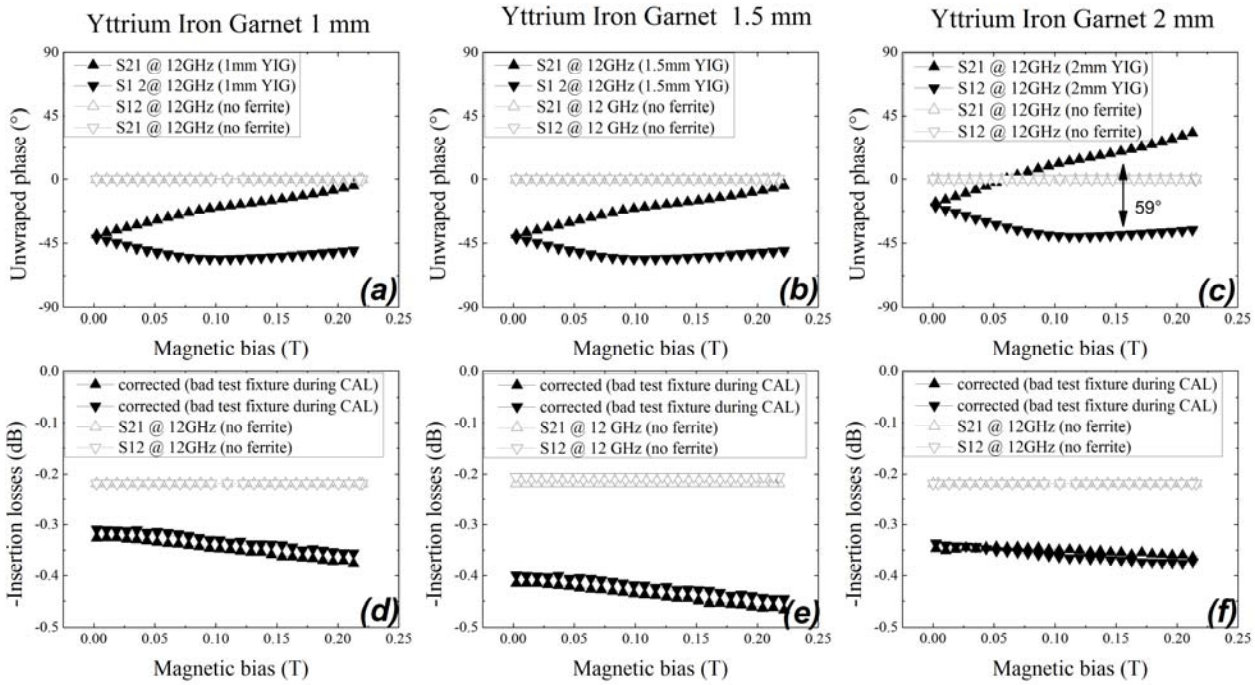

Figure 5.3-8: Measured forward and reverse phase shifts and insertion losses for different widths of ferrite slab, compared to phase shifts and insertion losses of an unloaded SIW. (a): phase of 1 mm YIG slab loaded in SIW; (b): phase of 1.5 mm YIG slab loaded in SIW; (c): phase of 2 mm YIG slab loaded in SIW; (d): insertion losses of 1 mm YIG slab loaded in SIW; (e): insertion losses of 1.5 mm YIG slab loaded in SIW; (f): insertion losses of 2 mm YIG slab loaded in SIW.

In Fig. 5.3-7, measurement results for Ni ferrite indicate that at low values of applied magnetic bias the insertion loss is much higher. At zero bias condition, increasing the width of the ferrite slab from 1 mm to 2 mm increases the insertion loss from 5 dB to almost 13 dB. While the results of YIG ferrite as illustrated in Fig. 5.3-8 show that the insertion loss is almost negligible and is comparable to that of SIW line without any ferrite slab. For Ni ferrite when the applied magnetic bias is increased, the insertion loss improves significantly. For 1 mm ferrite width, the insertion loss at 0.18 T is better than 5 dB while for 2 mm ferrite width it is close to 5 dB. The higher loss at low values of applied magnetic bias could be due to the low field loss of Ni ferrite. In the polycrystalline ferrite, at low magnetic bias there is a random distribution of crystallite direction

and domain orientations [Fuller (1987)], which produces higher losses on the propagating electromagnetic wave. As the magnetic bias is increased, the crystallite direction and domain orientations changes towards the direction of applied magnetic bias and therefore the low field loss reduces. Therefore, it can be concluded that Ni ferrite has higher low field loss compared to YIG and it is suitable for use as magnetically controlled device only at higher values of applied magnetic bias.

In Fig. 5.3-7, the unwrapped phase measurement results for different widths of Ni ferrite are presented. It can be seen that S_{12} and S_{21} phases are changing in opposite direction with the applied magnetic bias. By increasing the ferrite width, the splitting between S_{12} and S_{21} phase also increases. The increase in the phase of S_{21} is higher compared to S_{12}. Similar effect was also observed from theoretically calculated curves presented in Fig. 5.3-4. It can be seen from Fig. 5.3-7 (c), the differential phase shift of 180° is achieved for an applied magnetic bias value of 0.15 T. Therefore, for this value of magnetic bias and ferrite width, the two port non-reciprocal phase shifter operates as a gyrator. It is also important to note from Fig. 5.3-7 (c), that at 0.15 T, the S_{12} phase is close to the phase of an unloaded SIW transmission line.

5.3.3 Thermal behaviour of single ferrite loaded non-reciprocal phase shifter

Since SIW technologies and ferrite materials are known to have higher power handling capabilities, their combination to realize a tunable phase shifter is very suitable for high power applications. Due to the application of high power to the ferrite loaded SIW section, a heat is generated inside the ferrite material due to the losses. In the lack of a good thermal conductivity, the generated heat could not only destroy the property of a ferrite material, but at the same time can also degrade the performance of the device. Hence, it is necessary to understand the thermal behaviour of the ferrite material, when used for higher power applications.

In order to characterize the thermal behaviour of the ferrite loaded phase shifter of Fig. 5.3-2, it is placed inside a temperature controllable chamber as illustrated in Fig. 5.3-9. For this measurement the 2 mm ferrite slab loaded inside SIW was biased using two permanent magnets mounted on each side of the PCB providing an estimated DC magnetic bias of 0.2 T.

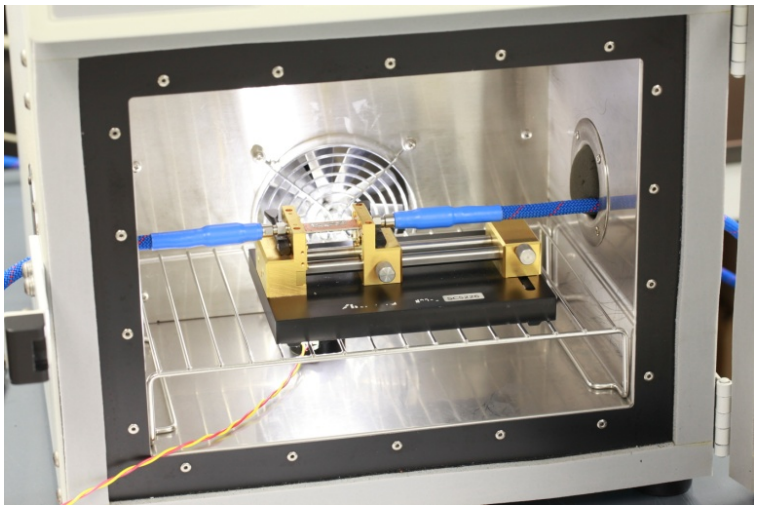

Figure 5.3-9: Photograph of the thermal measurement set up.

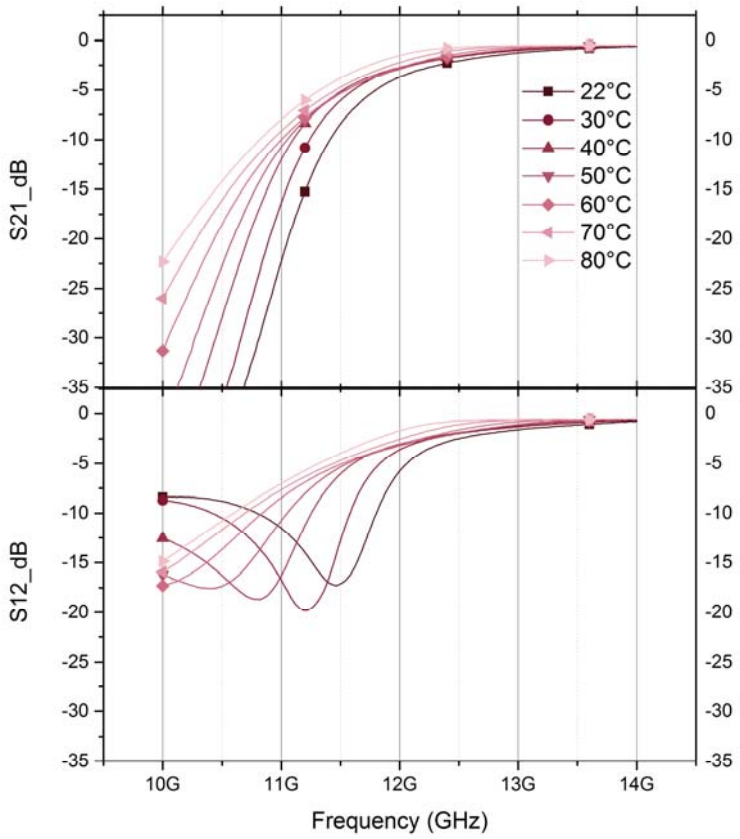

Figure 5.3-10: Measured amplitude of S_{21} and S_{12} parameters of the phase shifter versus temperature for 2 mm wide Nickel ferrite slab loaded inside the phase shifter.

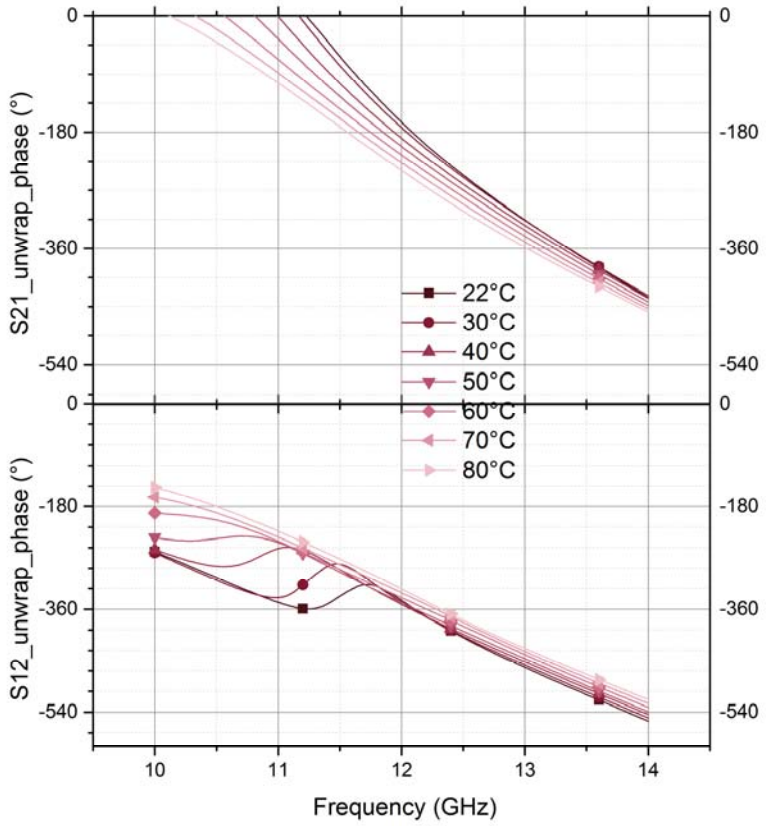

Figure 5.3-11: Measured angle of S_{21} and S_{12} parameters of the phase shifter versus temperature for 2 mm wide Nickel ferrite slab loaded inside the phase shifter

Fig. 5.3-10 and Fig. 5.3-11 respectively show the measured forward and reverse insertion loss and phase shift versus frequency at temperature values ranging from ambient to 80°C.. When comparing the results to Fig. 5.3-5 and Fig. 5.3-6, it can be concluded that, the effect of increasing the temperature on the ferrite loaded SIW line is similar to decreasing the value of magnetic bias applied on it. There are two magnetic materials involved in this measurement: permanent magnet to bias the ferrite, and the ferrite itself. Therefore, this behavior of reduced magnetic bias is caused by their combined effects. Due to the increase in temperature, the magnetic dipole moments of both ferrite and permanent magnet will begin to disorient themselves thereby reducing their magnetic property. At the highest value of the temperature in this measurement, the field produced by the permanent magnet was reduced from 0.2 T to 0.1 T. Thus, in order to avoid the influence of the temperature for high power applications, it is necessary to couple a heat sink to the design of phase shifter to thermally conduct the heat away from the ferrite material.

5.4 Four port circulator

In the previous section, theory and measurement results of non-reciprocal ferrite loaded SIW phase shifters were presented. It was demonstrated, for a ferrite slab loaded along the sidewall of an SIW transmission line, a non-reciprocal phase shifting between two ports can be achieved. It was noted that this differential phase shift between two-ports of SIW can be increased or decreased by increasing or decreasing the value of applied transverse DC magnetic bias. In this section, instead of varying the values of applied DC magnetic bias, it is set at a constant value such that the differential phase shift between the two ports is close to 180°. This type of a two-port non-reciprocal device having a differential phase shift of 180° is known as gyrator. A combination of gyrator as a non-reciprocal device together with reciprocal directional couplers leads to a realization of very useful four-port circulator [Lax and Button (1962)].

5.4.1 Topology of four port circulator

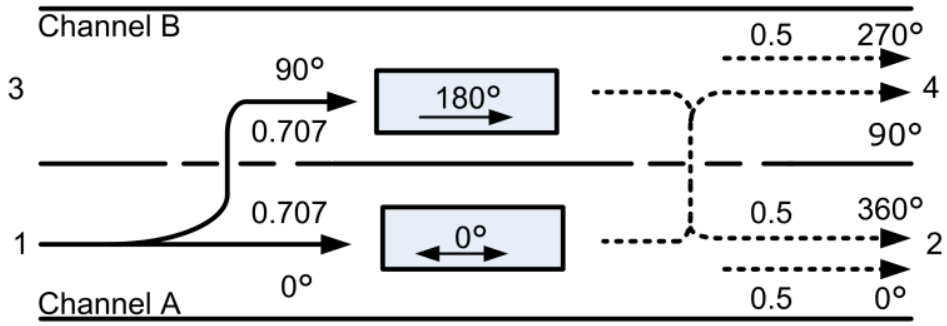

Figure 5.4-12: Topology of a four port circulator.

In Fig. 5.4-12, the topology of a four port circulator is presented. It consist of a gyrator with 180° unidirectional phase shift and a transmission line having a 0° bi-directional phase shift, which are cascaded between two 3-dB directional couplers. The 3-dB coupler has a property that, it couples half of the input power from channel A to channel B with 90° of phase difference. Assuming port 1 to be an input port, half of the input power is coupled through the directional coupler to channel B with 90° of phase advance. The gyrator provides additional 180° of phase shift such that the signal arriving at port 4 undergoes a total of 270° of phase advancement. Before reaching port 4, half of the total input power that underwent 270° phase shift re-enters channel A again such that by the time it reaches port 2, it has reached a phase advancement of 360°. Similarly, the other half of the input power that did not couple into channel B via the first coupler propagates

unhindered through a reciprocal (0° bi-directional phase shift) transmission line until it reaches the second coupler. At the second coupler, half of it reaches port 4 with 90° of phase advancement and the other half reaches port 2 with still 0° of phase advancement. Therefore, due to destructive interference the signal powers arriving at port 4 cancel each other to produce net output power of zero, while at port 2, the two powers sum up constructively to produce a net output power of one. A similar analysis on all the four-ports will result in a circulation of the input signal from 1->2->3->4->1->⋯. Therefore, for the functioning of the circulator it is very important that the signal powers undergo accurate constructive and destructive interferences at the desired output ports. Hence, the design of the couplers and the gyrator will determine the overall performance of the circulator.

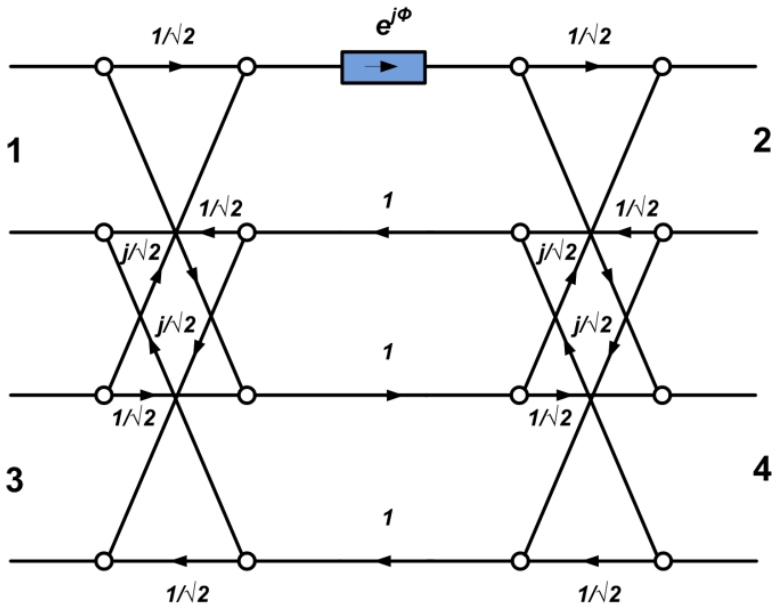

Figure 5.4-13: Signal flow graph representation of four port circulator.

Fig. 5.4-13 illustrates the signal flow graph representation of the four port network consisting of two directional couplers and a gyrator. The signal flow graphs of the directional couplers indicate the unit amplitude wave incident at port 1 is equally divided between port 1 and port 3 with 90° phase difference. It is a property of directional coupler that, it is reciprocal, matched and lossless. However, for a lossless four port network to be matched at all its ports, it is required that every input must be coupled only to the two other ports, such that the remaining last port will be an isolated port [Gardiol (1983)]. Hence in signal flow graph of Fig. 5.4-13, the reflected and isolated signal flow lines are not indicated. The non-reciprocal phase shifter is represented by t

section of transmission line with a variable phase term $e^{j\varphi}$. The scattering matrix of Fig. 5.4-13 can be written as,

$$[S]=\begin{bmatrix} S_{11} & S_{12} & S_{13} & S_{14} \\ S_{21} & S_{22} & S_{23} & S_{24} \\ S_{31} & S_{32} & S_{33} & S_{34} \\ S_{41} & S_{42} & S_{43} & S_{44} \end{bmatrix} = \begin{bmatrix} 0 & 0 & 0 & j \\ \frac{1}{2}\left(1-e^{j\phi}\right) & 0 & \frac{j}{2}\left(1+e^{j\phi}\right) & 0 \\ 0 & j & 0 & 0 \\ \frac{j}{2}\left(1+e^{j\phi}\right) & 0 & \frac{1}{2}\left(e^{j\phi}-1\right) & 0 \end{bmatrix} \tag{5.5}$$

The diagonal terms of the scattering matrix are zero indicating that ideally the four port network of Fig. 5.4-13 is matched. Moreover, the scattering matrix also suggests that ports 1 and 3, and 2 and 4 are well isolated from each other. However, the above assumptions of perfect match and isolation are valid only for an ideal network. In the later sections, simulation and measurement results of a four port circulator are presented, where the parameters affecting the matching and isolation conditions are discussed in a greater detail.

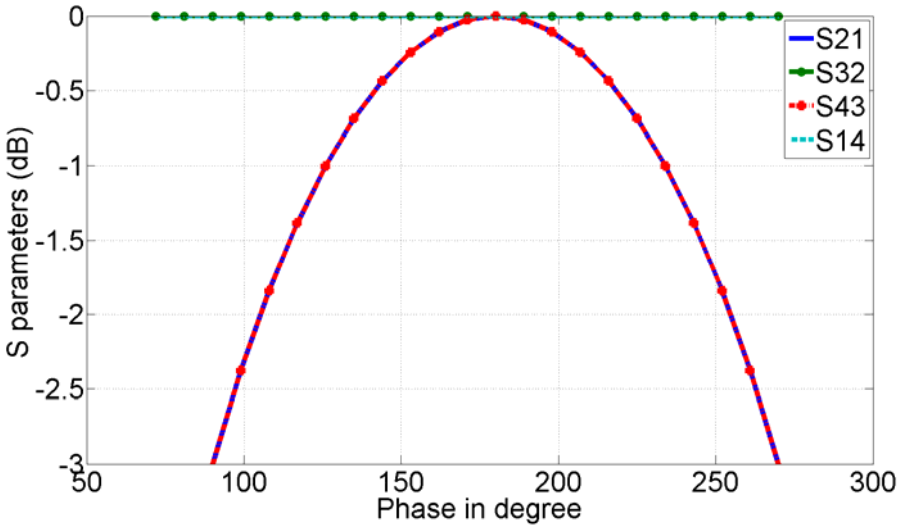

Figure 5.4-14: Calculated S-parameters of an ideal four-port circulator.

Based on the S-matrix given in (5.5), in Fig. 5.4-14 and Fig. 5.4-15, S-parameters of a four port circulator are plotted. The S-parameters are plotted against the values of ϕ, which are varied

between 72° and 270°. It can be seen from Fig. 5.4-14, the S-parameters representing transmission from port 2 to port 3 and port 4 to port 1 are independent of ϕ. Similarly, the isolations between port 2 to port 1 and port 3 to port 4 are also independent of the values of ϕ. In Fig. 5.4-14 and Fig. 5.4-15, ideal transmission and isolation conditions occur when the value of ϕ is equal to 180°. In the later section, based on measurement results, the S-parameter matrix of (5.5) is modified to take into account the phase variation of a non-reciprocal phase shifter with the applied magnetic bias and losses in the transmission lines. Therefore, the final equation could then be used to model a practical four-port circulator.

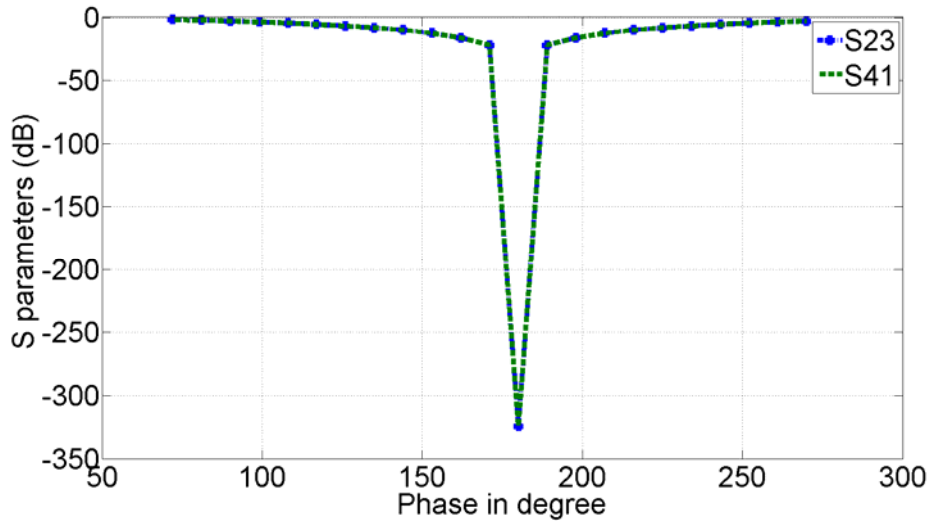

Figure 5.4-15: Calculated S-parameters of an ideal four-port circulator.

5.4.2 HFSS simulation results

In this section, simulation results of a four-port circulator using Ansoft's HFSS 15 are presented. It is seen from the previous section, Ni ferrite offers larger differential phase shift compared to YIG. Therefore, Ni ferrite is used in the simulation of the circulator, so that the desired gyrator and circulator can be realized at a low value of applied DC magnetic bias. Rogers RT/Duroid 6010 substrate having a relative permittivity value of $\varepsilon_{rs} = 10.2$ is chosen for the design and simulation of the circulator. Planar ferrite slab is loaded along a sidewall of an SIW transmission line to realize the non-reciprocal phase shifter. The relative permittivity value of Ni ferrite is $\varepsilon_{rf} = 13$. Therefore, a high permittivity substrate like Rogers RT/Duroid 6010 is chosen for the design to reduce the mismatch effects.

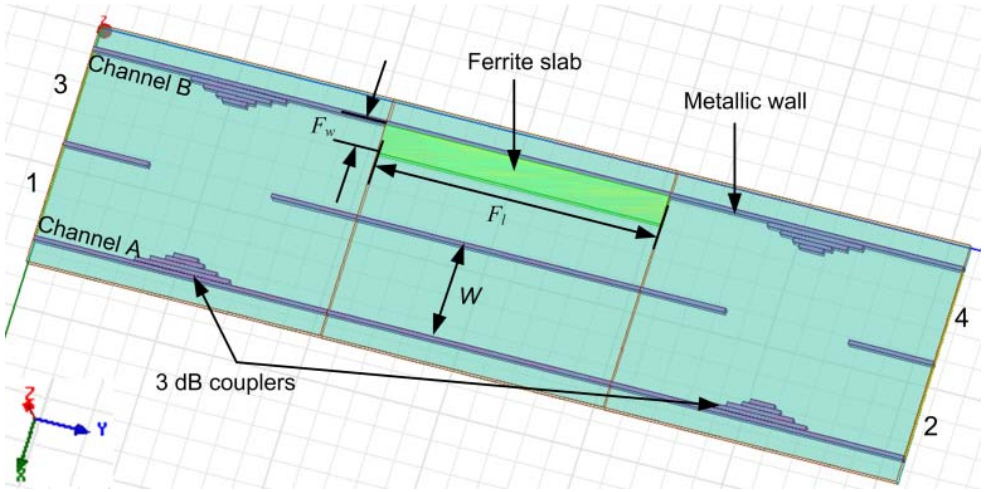

Figure 5.4-16: Four port circulator geometry in Ansoft's HFSS 15, Fw = 2 mm, W = 6.5 mm, and F_l = 18 mm.

In Fig. 5.4-16, four-port circulator geometry in Ansoft HFSS 15 is illustrated. It can be seen that, the circulator is designed using SIW technology. The gyrator section is realized by loading a planar ferrite slab of width *Fw* along a sidewall of an SIW line in channel B, while the SIW line on channel A is left unloaded. The gyrator and SIW line on channel B and channel A are cascaded between two 3-dB couplers that are also designed using SIW technology. A uniform static magnetic bias is applied on ferrite slab along positive *z*-direction. In HFSS simulation, it is observed that while simulating a ferrite material with a very high value of saturation magnetization, a large differential phase shift is observed even for zero value of applied magnetic bias. Since Ni ferrite has a $4\pi M_s$ = 5000 G, with this value of saturation magnetization, a differential phase shift of more than 300° was observed for a single ferrite loaded SIW line when the applied DC magnetic bias was still at 0 A/m. Therefore, a parametric sweep was performed, where the saturation magnetization value of the ferrite was increased in a step from 0 G to 5000 G keeping applied magnetic bias *H0* constant at 0 A/m. It was observed that for $4\pi M_s$ = 3400 G and *H0* = 0 A/m, between unloaded SIW line of Channel A and ferrite loaded SIW line of Channel B, a differential shift of approximately 180 G was observed at 12 GHz. Therefore, in the simulation of the circulator presented in Fig. 5.4-16, $4\pi M_s$ = 3400 G and *H0* = 0 A/m are used as the applied magnetic biasing condition.

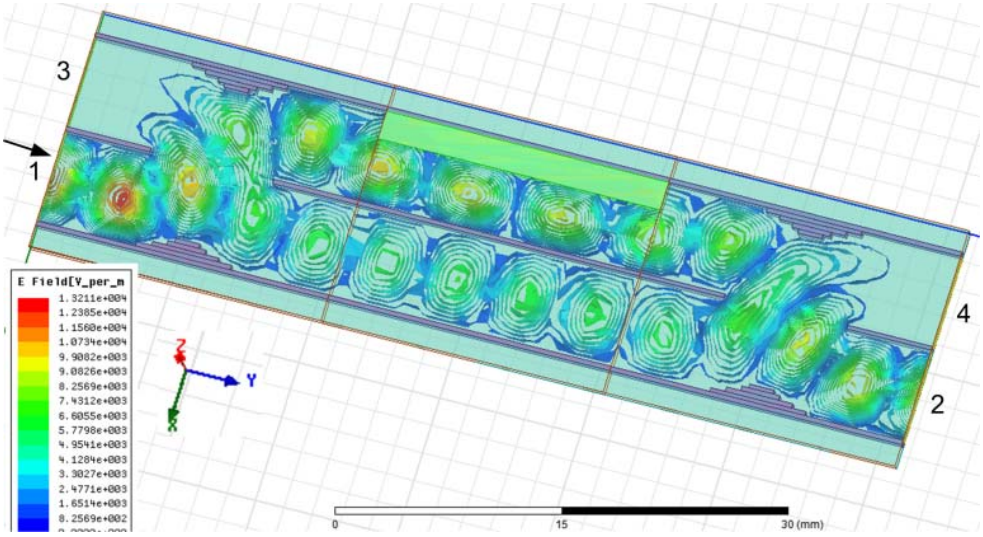

Figure 5.4-17: A snap-shot of electric field simulation of four-port circulator in HFSS 15, port 1 is the input port.

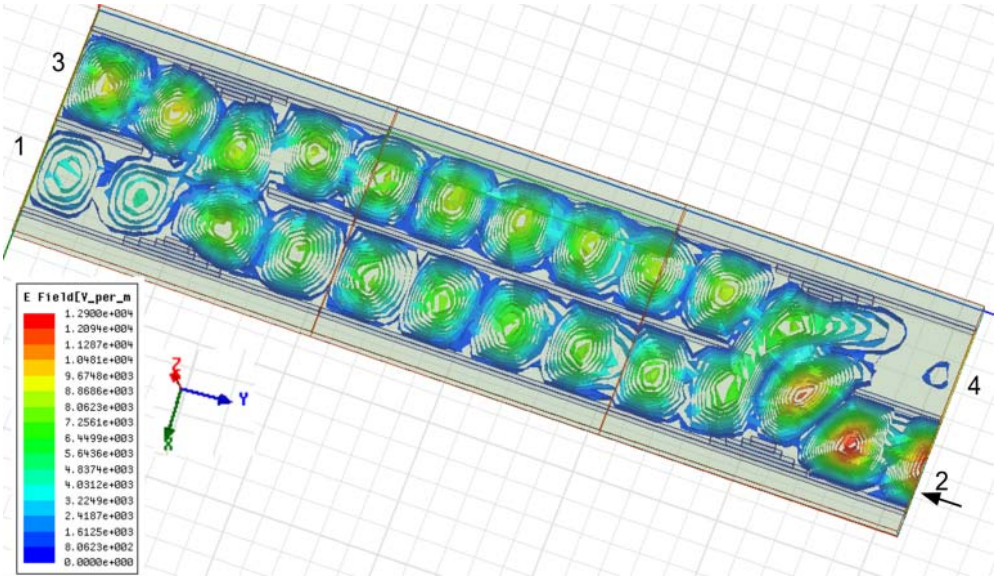

Figure 5.4-18: A snap-shot of electric field simulation of four-port circulator in HFSS 15, port 2 is the input port.

In Fig. 5.4-17 and Fig. 5.4-18, electric field simulations of a four port circulator are presented, where magnitudes of electric fields of an SIW line operating in TE_{10} mode at 12 GHz are presented. In Fig. 5.4-17, the input port is defined at port 1. As mentioned previously, due to the

non-reciprocal differential phase shift of 180° provided by gyrator, the signal at port is only transmitted to port 2 due to constructive interference with the signal arriving from channel B. While the net output power of the signal arriving at port 4 is zero, due to destructive interference with the signal arriving from channel A. It is observed from Fig. 5.4-17, that a good isolation is achieved between port 1 and port 4. Similarly in Fig. 5.4-18, the field simulation of a four port circulator with port 2 as an input port is presented. It can be seen that, the input power is transmitted from port 2 to port 3 while, port 4 and port 1 are isolated from port 2. Ideally in this case, the ferrite loaded SIW section should not produce any additional phase shift on the signal coupled from port 2 into channel B. But in simulation it was observed that, the gyrator produces some phase delay for a signal propagating from port 4 to port 3. Therefore, the signal arriving at port 1 does not undergo the total cancellation due to destructive interference hence the isolation between port 2 and port 1 is not ideal. Therefore, some method of phase compensation for a gyrator is required so that it only provides a unidirectional phase shift of 180°.

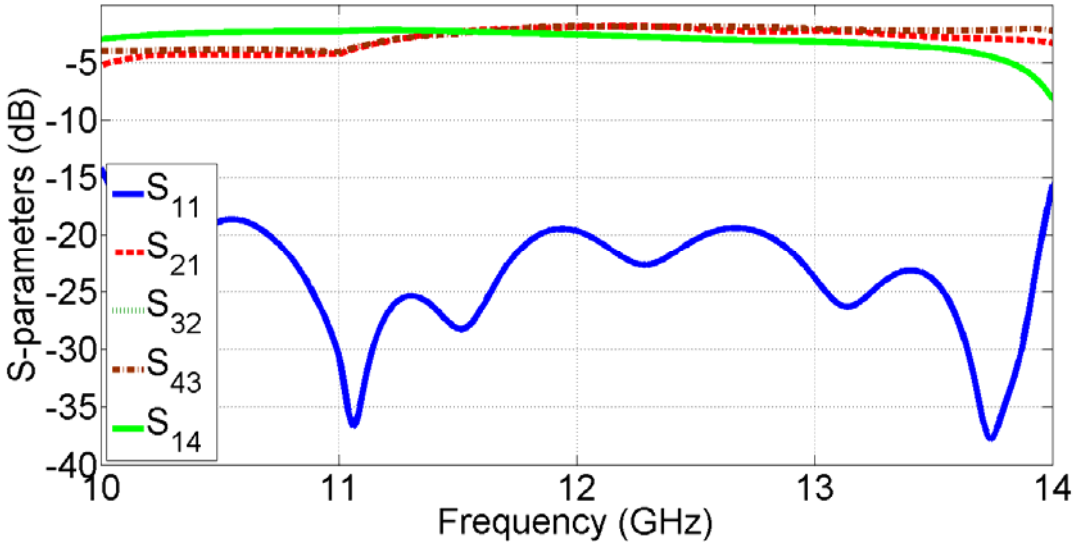

Figure 5.4-19: Simulation results of four port circulator consisting of single ferrite loaded gyrator in HFSS 15.

In Fig. 5.4-19 and Fig. 5.4-20, simulation results (S-parameters) of four port circulator are presented. The simulation results are presented for the ferrite material having a saturation magnetization value $4\pi M_s = 3400$ Gauss, $H0 = 0$ A/m, and ferrite width $F_w = 2$ mm. It can be seen from Fig 5.4-19, the insertion loss of signals from ports 1->2->3->4->1->⋯ are better than 3 dB at 12 GHz.

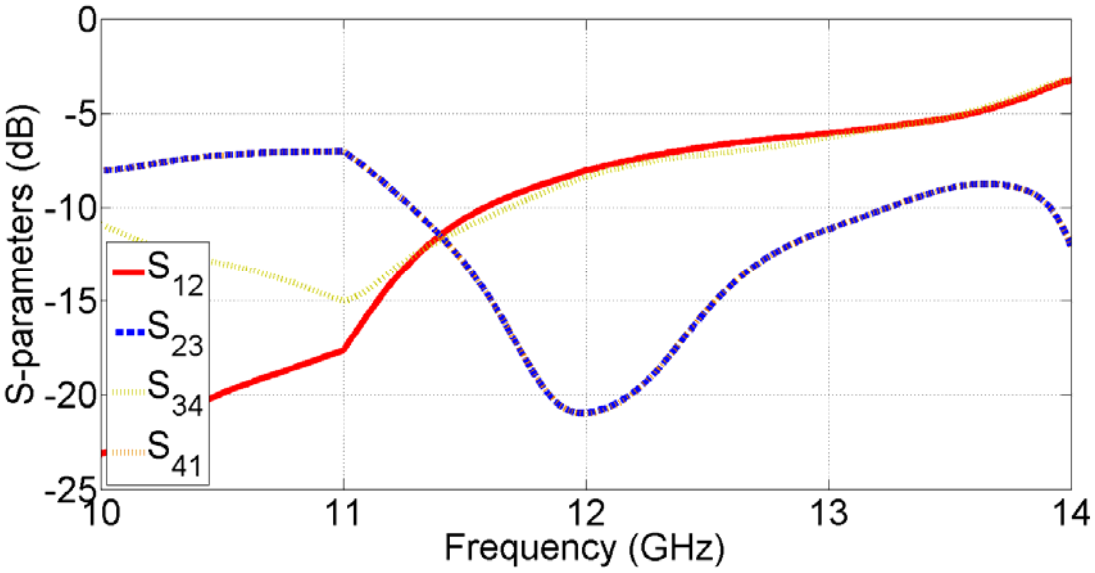

Figure 5.4-20: Simulation results of four port circulator consisting of single ferrite loaded gyrator in HFSS 15.

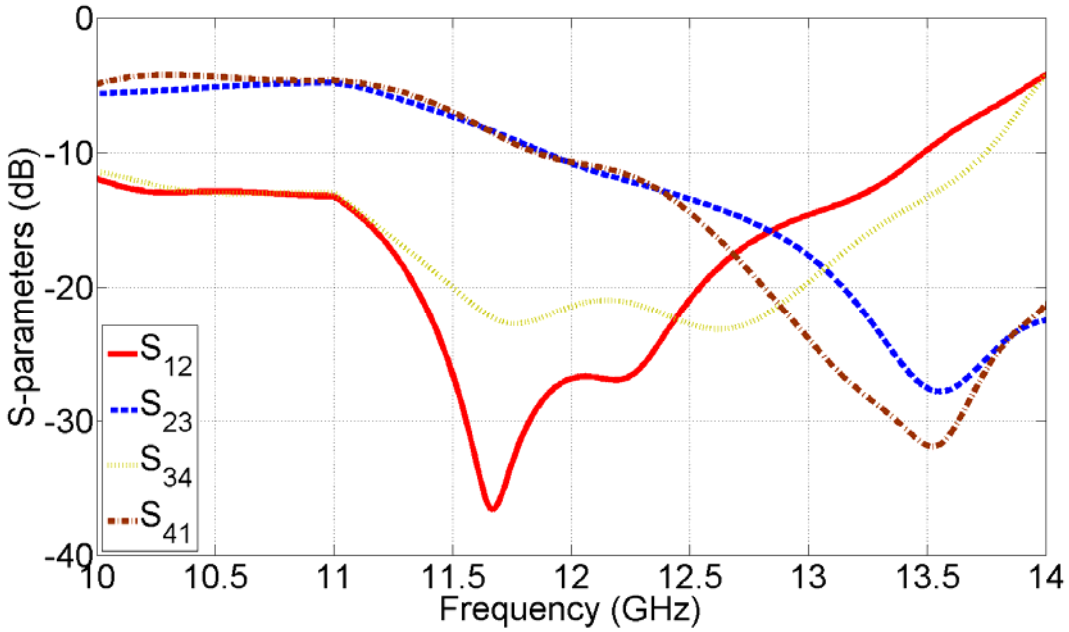

Figure 5.4-21: Simulation results of improved four port circulator consisting of single ferrite loaded gyrator in HFSS 15 (An additional phase shift of approximately 50° was added in channel A).

In Fig. 5.4-20, the isolation between consecutive ports (between 2 -> 1, 3 -> 2, 4 -> 3, and 1 -> 4) are illustrated. It can be seen that at 12 GHz, the insertion loss between ports 2 and 3, and 4 and 1 are better than 20 dB, while the insertion loss between ports 1 and 2, and 3 and 4 are

approximately 8 dB. The reason for low isolation between 1 and 2, and 3 and 4, is due to the unwanted phase shift in the opposite direction of the gyrator. It was observed in simulation that the unwanted phase shift from port 4 to port 3 was approximately equal to 50°. In Fig. 5.4-21 a phase compensated simulation is presented. An additional phase shift of approximately 50° was added in channel A to compensate the phase error of the gyrator. It is observed in Fig. 5.4-21, the isolations between 1 and 2, and 3 and 4 have improved, but the isolation between 2 and 3, and 1 and 4 has shifted towards higher frequency value. With optimum phase compensation, the isolation between the ports can be further improved.

5.4.3 Measurement results

In this section, measurement results of the fabricated four port circulator are presented. The circulator is fabricated on Rogers RT/Duroid 6010 substrate. The substrate has a dielectric constant of $\varepsilon_s = 10.2$ and thickness $h = 0.635$ mm. Nickel ferrite with saturation magnetization value of $4\pi M_S = 5000$ G and line width of $\Delta H \leq 198$ Oe is loaded along the sidewall of an SIW line to realize a gyrator. As it is seen from the previous section, for a given value of applied DC magnetic bias, Ni ferrite produces much larger differential phase shift compared to YIG. Therefore, in the realization of the gyrator Ni ferrite is chosen.

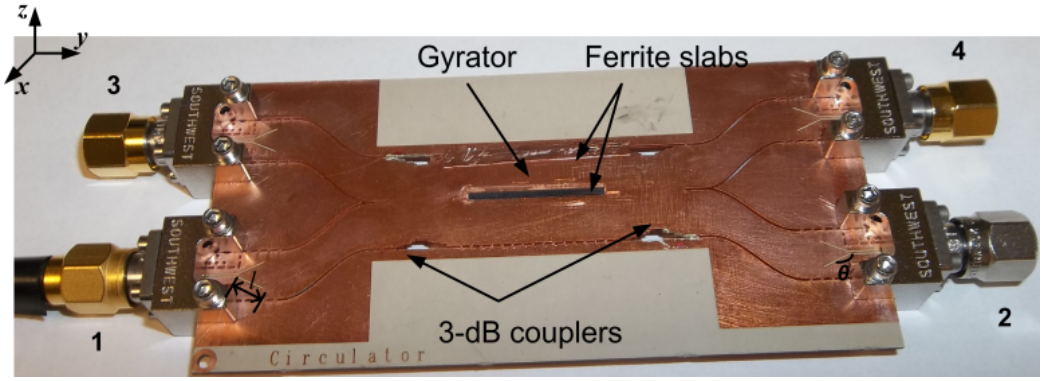

Figure 5.4-22: Fabricated four port circulator on Rogers 6010, 25 mil substrate with $l = 3.5$ mm, and $\theta = 25°$.

In Fig. 5.4-22, the fabricated four port circulator is presented for demonstration. As indicated, the circulator consists of two 3-dB couplers, a gyrator loaded with a single ferrite slab, and CBCPW to SIW transitions to facilitate the measurements using Vector Network Analyzer (VNA). Four Southwest K connectors are used for measurement purpose. Fig. 5.4-23 illustrates the

measurement set-up of the circulator. In order to vary the magnetic bias, the gyrator section of the circulator is placed between the two rods of the electromagnet, where the static magnetic field crosses the ferrite loaded cavity perpendicularly.

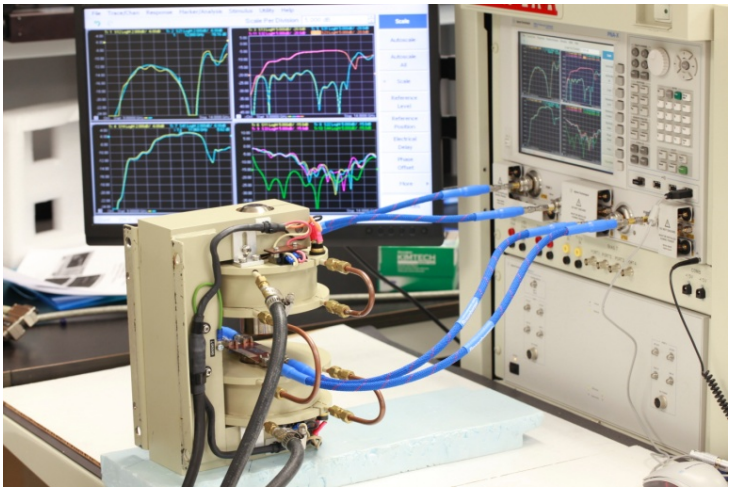

Figure 5.4-23: Photograph of the measurement set up of the four port circulator.

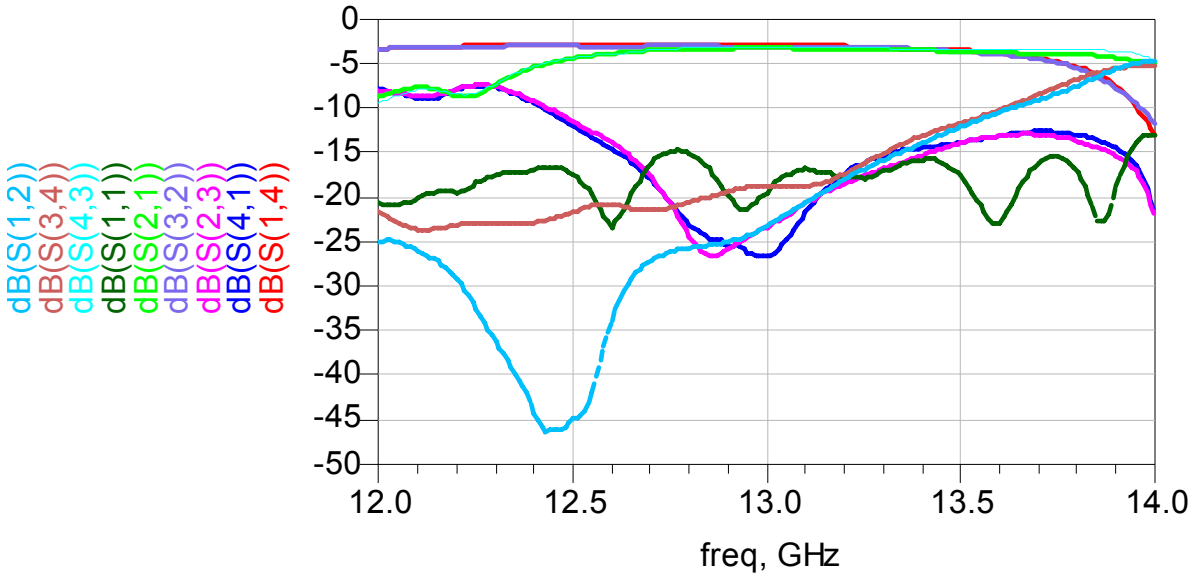

Figure 5.4-24: Measurement results of the four port circulator.

In Fig. 5.4-24, measurement results of the four port circulator are presented. Compared to the simulation results presented in Fig. 5.4-19 – Fig. 5.4-21, the design frequency of the circulator is shifted from 12 GHz to approximately 12.8 GHz. This could be due to the tolerances in the fabrication of the oscillator, and the definition of the ferrite material in HFSS 13.0. As previously mentioned, in simulation a ferrite material with $4\pi M_s = 3400$ Gauss, $H0 = 0$ A/m was defined.

But this definition does not exactly correspond to the Ni ferrite in practicality. However, with this definition a phase splitting of approximately 180 degree was observed between forward and reverse waves. It can also be noted from Fig. 5.4-24, similar to simulation results that isolations between ports 2 -> 1 is slightly offset with its optimum occurring at 12.5 GHz. However, at 13 GHz, the isolations between all the ports are better than 15 dB.

5.5 Conclusion

A magnetically tunable non-reciprocal ferrite loaded SIW transmission line has been presented and demonstrated with a number of theoretical and experimental cases studies. The use of two different magnetically tunable materials, Yttrium Iron Garnet (YIG) and Nickel ferrite ($NiFe_2O_4$), has been compared in term of insertion loss and phase shifting. SIW-based devices including a non-reciprocal phase shifter, a gyrator, an isolator and a circulator employing the proposed non-reciprocal FLSIW have been successfully designed and fabricated. One advantage of the proposed magnetically tunable FLSIW line compared to integrated circuits is a higher power handling. For this reason a measurement versus temperature was presented. The proposed non-reciprocal ferrite loaded SIW line could be advantageously used for integrated front-end design at microwave frequencies.

CHAPTER 6 MAGNETICALLY TUNABLE HALF-MODE SIW

Half-mode substrate integrated waveguide (HMSIW) is an emerging transmission line technology which is very useful for low-loss, compact and high power microwave and millimeter wave applications. From the geometry, HMSIW is a miniaturized form of substrate integrated waveguide (SIW). For an SIW line operating with dominant TE_{10} mode, the symmetric plane along the direction of propagation represents the perfect magnetic wall. The electric and magnetic fields are unaltered if the SIW line at the symmetric plane is cut into half. Thus, HMSIW is realized by implementing rows of via or metallic slots only on one side of the metal coated substrate, which makes it half of the size of an SIW transmission line [Hong, et al. (2006)]. Therefore, the dominant mode of transmission in HMSIW line can be considered as $TE_{(0.5)0}$ mode. Apart from being miniaturized form of SIW, HMSIW inherits almost all the properties of SIW transmission line. Similar to SIW, it is lower in loss, has a planar geometry, and lower in cost. In literature HMSIW has been used in the realization of number of microwave and millimeter wave components and devices including band-pass power dividers [Liu, et al. (2006)], and filter [Wang, et al. (2007)]. Apart from the fixed frequency devices, it has also been used for the realization of an electrically tunable evanescent mode HMSIW resonator working at S-band [Senior, et. al (2012)].

In this Chapter, a magnetically frequency tunable HMSIW is presented. The magnetic tuning is achieved by loading a single planar ferrite slab along the metalized sidewall of an HMSIW section. As an application, the magnetically tunable HMSIW is further developed to realize a tunable band-pass filter. In addition to magnetic tuning, lumped capacitances are loaded near the central regions of the filter's cavities, to make it bandwidth tunable.

6.1 Magnetically tunable HMSIW transmission line

In this section magnetically tunable HMSIW transmission line section is presented. Comparative measurement results between magnetically tunable HMSIW and SIW sections in terms of switching, tunability, losses, and phase shifting are reported and discussed.

6.1.1 Topology and design consideration

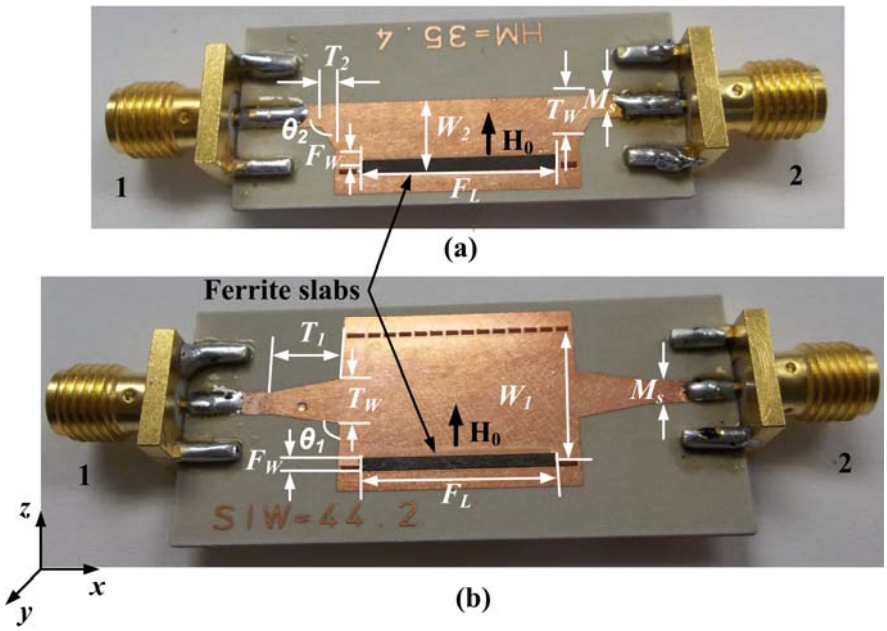

Figure 6.1-1: Fabricated prototypes of ferrite loaded a) HMSIW b) SIW, with F_L = 15 mm, F_W = 1.25 mm, M_s = 1.97 mm, T_W = 3.9 mm, W_1 = 11 mm, W_2 = 5.5 mm, T_1 = 5.6 mm, T_2 = 1.2 mm.

Fig. 6.1-1(a) and Fig. 6.1-1(b) illustrate the fabricated prototypes of magnetically tunable HMSIW and SIW transmission line sections. To achieve the magnetic tunability, planar ferrite slabs of length F_L and width F_W are used. Transitions to microstrip lines are implemented to permit the measurements using a vector network analyzer (VNA). Both HMSIW and SIW sections are fabricated on Rogers RT/duroid 6002 substrate with the dielectric constant value of 2.94, loss tangent of 0.0012 and a thickness of 0.762 mm. Low loss Yttrium Iron Garnet (YIG) with saturation magnetization value ($4\pi Ms$) of 1780 Gauss, and line width (ΔH) of 17 Oe is chosen as the magnetic tuning element. The ferrite slab thickness is the same as that of the substrate i.e. 0.762 mm. As illustrated in Fig. 6.1-1, for a comparison, YIG slabs loaded inside HMSIW and SIW sections have the same dimensions. The measurement reference planes are defined such that the total lengths of HMSIW and SIW lines containing the ferrite slabs are equal.

6.1.2 Results and discussions

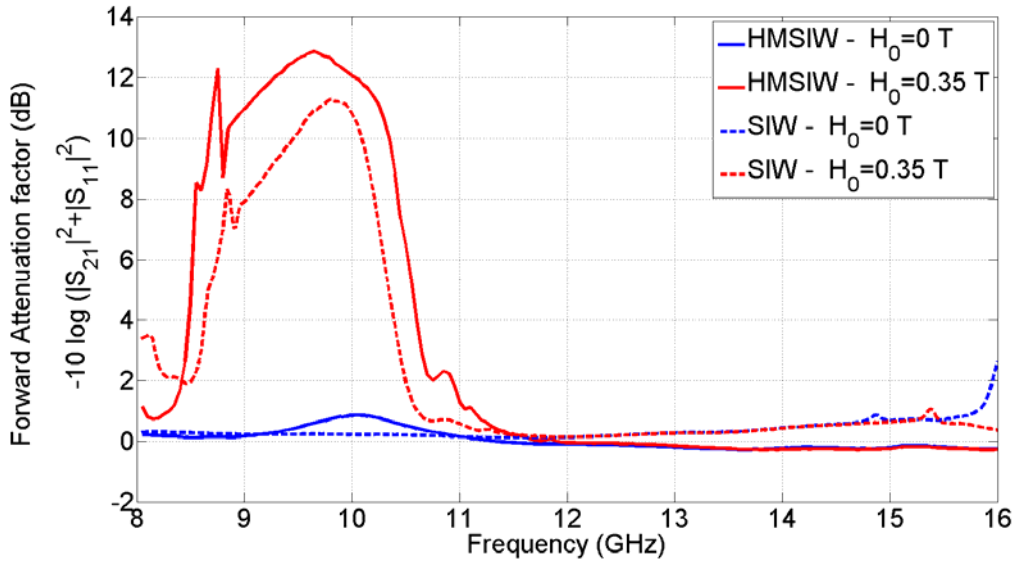

Figure 6.1-2: Measured forward attenuation constant values of ferrite loaded HMSIW and SIW sections for H_0 = 0 T, and H_0 = 0.35 T.

In Fig. 6.1-2 measurement results illustrating the forward attenuation factors of single ferrite slab loaded HMSIW and SIW lines at H_0 = 0T and H_0 = 0.35 T are presented. It can be observed for $H0$ = 0T, that the ferrite loaded HMSIW and SIW sections exhibit minimum losses. However, for an SIW line the tendency of the total loss near 16 GHz is increasing. This is due to the presence of the second order TE_{20} mode. But as the magnetic bias H_0 is increased the cut-off frequency of both TE_{10} and TE_{20} move towards higher frequency values. Therefore, for a ferrite loaded SIW line at H_0 = 0.35 T, the attenuation peak at 16 GHz no longer exists. Due to the geometry, TE_{20} mode does not exist in HMSIW. Therefore, in HMSIW the frequency tunable bandwidth is not limited by the presence of TE_{20} mode. Similar results were also obtained for S_{12} and S_{22} parameters. However, the isolation between S_{12} parameters at H_0 = 0T and H_0 = 0.30 T were limited to approximately 10 dB for both HMSIW and SIW sections.

From the forward attenuation factor presented in Fig. 6.1-2, ferrite loaded SIW and HMSIW sections could find an application as a microwave switch, or as a low-loss filter. When used as a switching device, HMSIW offers a higher value of isolation compared to SIW at 9.65 GHz. At the same time, when used as a filter it offers lower insertion loss both at lower and upper frequency values when magnetic bias is increased from H_0 = 0T and H_0 = 0.35 T.

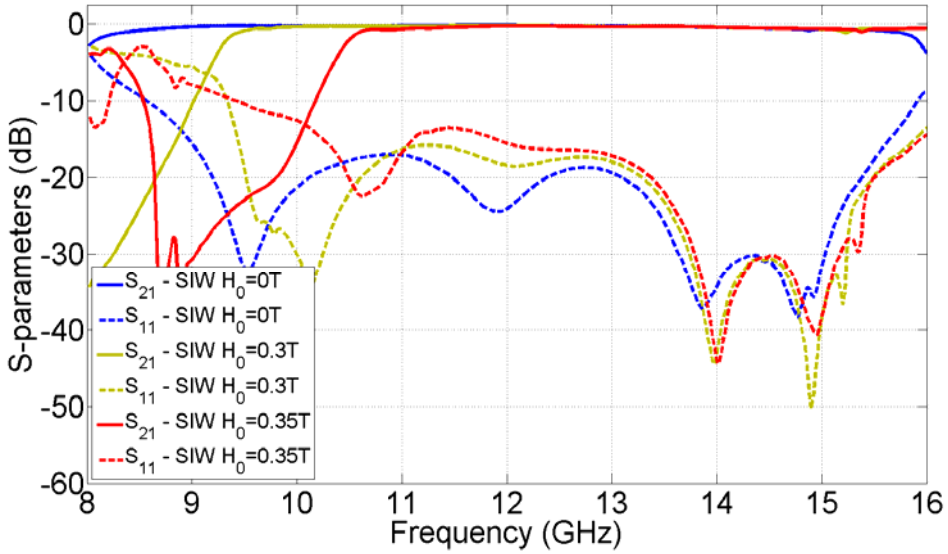

Figure 6.1-3: Measured S-parameters of SIW transmission line.

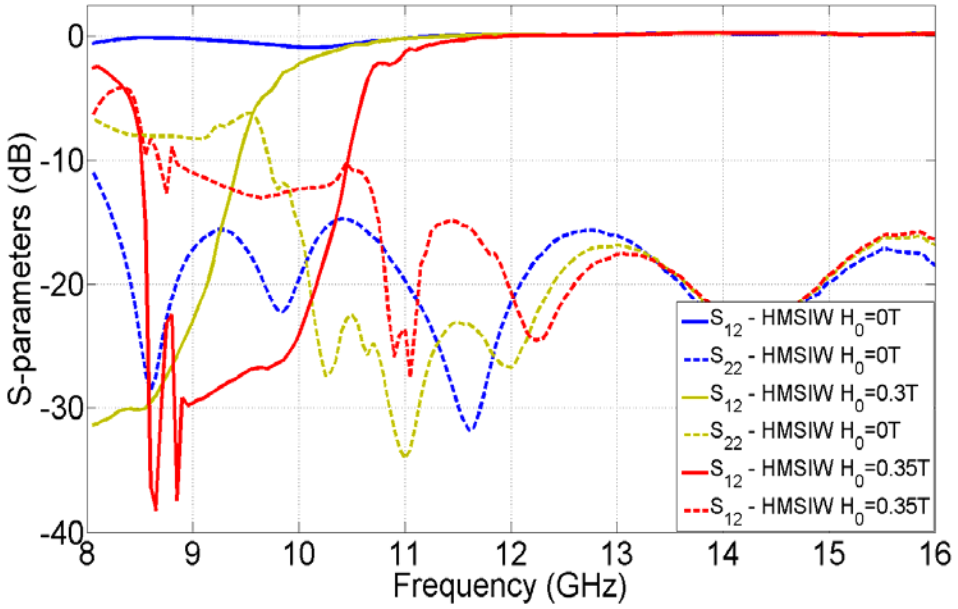

Figure 6.1-4: Measured S-parameters of HMSIW transmission line.

In Fig. 6.1-3 and Fig. 6.1-4, measured S-parameters of ferrite loaded SIW and HMSIW are plotted. For linear increase of magnetic bias H0, the cut-off frequency of SIW and HMSIW also increase towards higher frequency value. It can be observed, HMSIW although being symmetrically half produces the same level of frequency tuning as SIW.

The functions f_1 and f_2, obtained from the theoretical design equation presented in [Collins,

(1960)], are used to calculate the non-reciprocal differential phase shift of a single ferrite loaded SIW line.

$$f_1(\beta) = l\cot(l \cdot F_W) + \frac{\mu_e}{\mu_0} h\cot(hd). \tag{6.1}$$

$$f_2(\beta) = \pm\frac{\beta\kappa}{\mu}. \tag{6.2}$$

In (1) and (2), h and l are the wave numbers of substrate and ferrite sections, μ_e is the effective permeability of the ferrite, and d is the width of the substrate section, μ_0 and μ are the permeability values of free-space and substrate respectively.

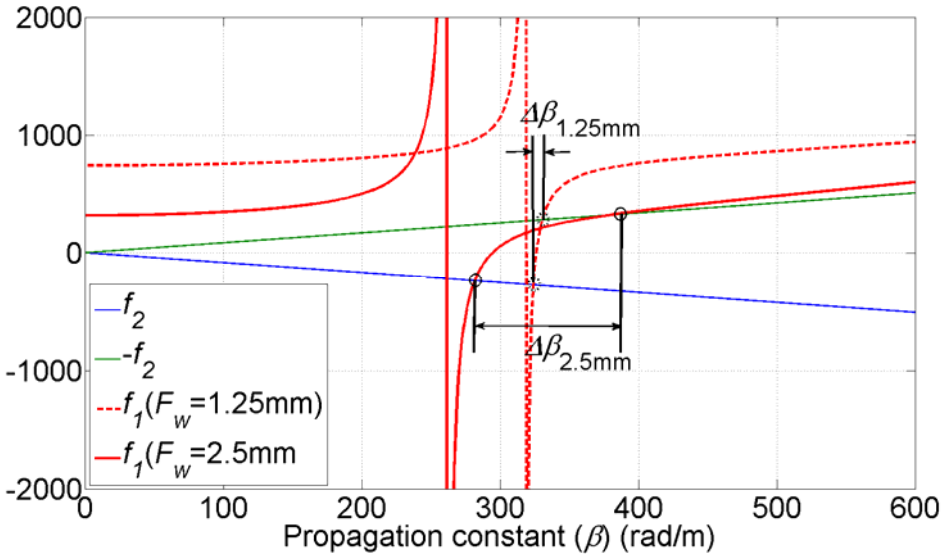

Figure 6.1-5: Plot of f_1 and f_2 to find the propagation constant of ferrite loaded SIW.

In Fig. 6.1-5, f_1 and f_2 are plotted at 12 GHz when applied internal bias is at H_i = 0.1 T. The detail derivations of f_1 and f_2 can be found in [Collins, (1960)]. The values of β, where f_1 and f_2 intersect each other are the required solutions of forward and reverse propagation constants. In Fig. 6.1-5 differential propagation constants $\Delta\beta$ = 6 rad/m and $\Delta\beta$ =106 rad/m are obtained for F_W = 1.25mm and F_W = 2.5 mm respectively. Thus, increasing the width of the ferrite loaded inside SIW also increases the value of $\Delta\beta$. For F_L = 15 mm, the value of $\Delta\beta$ = 6 rad/m corresponds to the calculated phase difference of $\Delta\varphi \approx 6°$.

In Fig. 6.1-5, functions f_1 and f_2 are plotted for an internal magnetic field H_i, while in measurements it is only possible to measure the external magnetic field H_0. From The relation

between external and internal magnetic fields is given in (3.23) for $F_W = 1.25$ mm and $F_L = 15$ mm, using closed form relation given in [Aharoni, A. (1998)], demagnetization factor of $N_z = 0.5907$ is calculated. Thus, for the given dimensions of the YIG slab, the internal magnetic field $H_i = 0.10$ T corresponds to the external field of $H_0 = 0.205$ T.

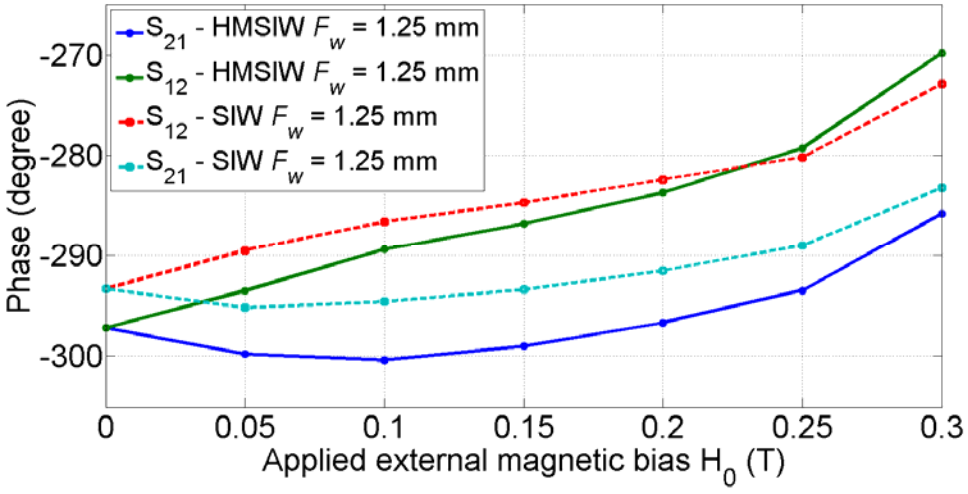

Figure 6.1-6: Plot of measured values of forward and reverse phase shift of ferrite loaded HMSIW and SIW.

In Fig. 6.1-6, measured forward and reverse phase shifts of HMSIW and SIW are presented at 12 GHz for increasing value of H_0. For SIW approximately at $H_0 = 0.20$ T, the value of $\Delta\varphi$ is close to 8°, which is slightly higher than the calculated value of 6°. It can be concluded from Fig. 6.1-6, that the non-reciprocal differential phase shifting produced by ferrite loaded HMSIW is higher compared to SIW for increasing values of magnetic bias H_0. It is due to the area occupied by YIG in HMSIW which is larger compared to that of SIW.

6.2 Two dimensionally tuned HMSIW band-pass filter

In this section a ferrite loaded magnetically tunable HMSIW band-pass filter is proposed as an application. In Fig. 6.2-7, the fabricated ferrite loaded HMSIW band-pass filter is presented. It is a three-pole filter consisting of two HMSIW cavities, which are formed by sections of HMSIW between two transverse slots [Wang, et al. (2007)]. Planar YIG slabs are loaded in each HMSIW cavities to produce the magnetic tuning. To achieve the bandwidth tuning, lumped capacitances are also added near the centre regions of the cavities, where the electric field strength is highest. Changing the value of capacitances changes the electric field distributions which in turn changes

the coupling between two cavities

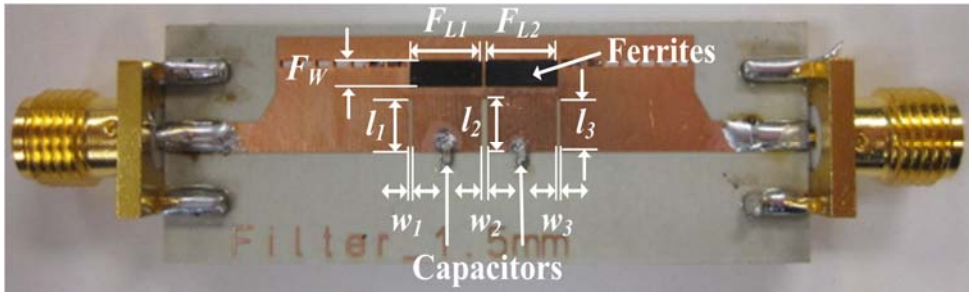

Figure 6.2-7: Fabricated prototypes of ferrite loaded a) SIW b) HMSIW with $F_{L1} = F_{L2}$ =5 mm , $l_1 = l_2 = l_3$ = 3.4 mm, $w_1 = w_3$ = 0.15 mm, w_2 = 0.4 mm.

6.2.1 Measurement results

For the band-pass filter of Fig. 6.2-7, the lower sideband of the filter is formed by the high-pass function of the HMSIW. The high-pass function of HMSIW is combined with the band-pass function of the couple resonators to achieve the desired band-pass characteristics.

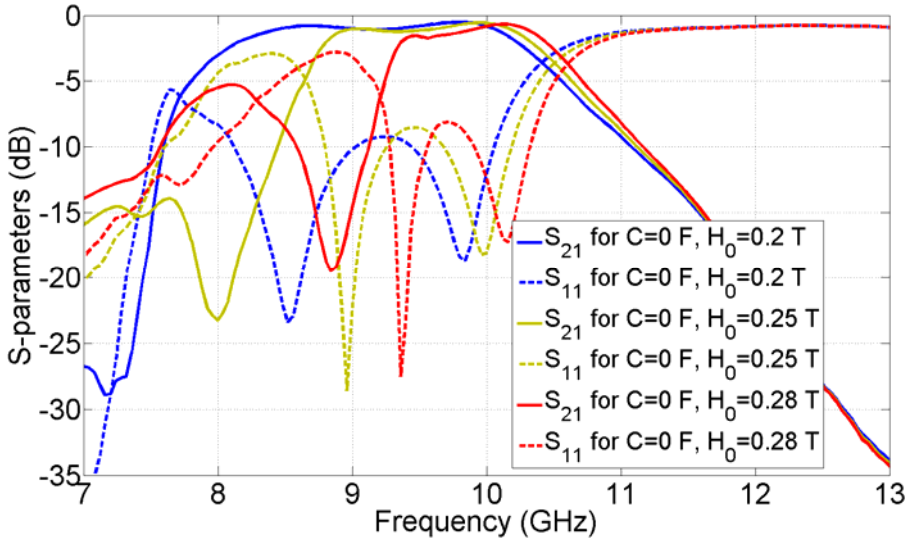

Figure 6.2-8: Frequency response curves of magnetically tuned HMSIW band-pass filter.

In Fig. 6.2-8, frequency response curves of magnetically tunable HMSIW filter are presented. It can be noticed, with the increase in magnetic bias, only the lower sideband of the filter is shifted towards higher frequencies, while the upper sideband of the filter remains fixed. Therefore, the effect of magnetic bias on ferrite slabs loaded along the sidewalls of the filter cavities, only changes the cut-off frequency of HMSIW but it does not change the inter-resonator couplings.

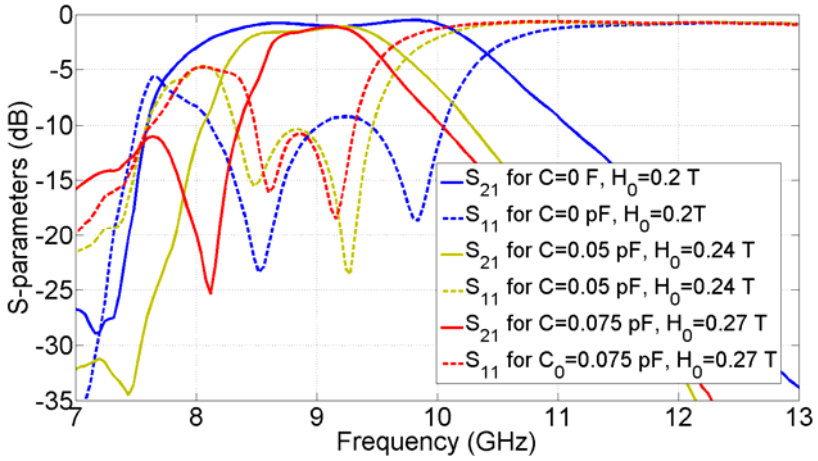

Figure 6.2-9: Frequency response curves of magnetic and capacitive tuned HMSIW band-pass filter.

In Fig. 6.2-9, frequency response curves of capacitive and magnetic tuned filter is presented. It can be noticed that, loading the lumped capacitors along the central regions of HMSIW cavities has an effect of shifting the lower and upper sidebands (i.e. the center frequency) towards the lower frequency values. Thus, with the dual magnetic and capacitive tuning, the designed filter can be used as a bandwidth tunable filter at a fixed center frequency. It can also be noticed from Fig. 6.2-9, the total insertion loss of the filter have remained approximately constant for all bandwidths.

6.3 Conclusion

A magnetically tunable half mode substrate integrated waveguide (HMSIW) transmission line and a band-pass filter were presented. The magnetic tuning was achieved by placing low loss YIG slabs along the sidewalls of the HMSIW. From the measurement results, performances of tunable HMSIW in terms of switching, losses and phase shifting are found superior compared to ferrite loaded SIW. Using dual capacitive and magnetic tuning, a bandwidth tunable HMSIW filter is also demonstrated.

CONCLUSION

The present wireless communication systems are becoming every day more complex in nature. New features are added into a single device to satisfy the growing customer needs. A small hand-held device is expected to have multiple functionalities with an excellent performance quality. In order to meet the growing complexities of RF front-end, its design must be adaptive and flexible in nature. An adaptive RF front ends can be realized by incorporating multi-band or multi-channel circuits to satisfy the several wireless system standards. One way of realizing the multi-band or multi-channel communication systems is by incorporating the tunable microwave components, circuits and devices into them. This not only will make the device operate in multiple frequency bands, but at the same time a single tunable device will replace the requirement of multiple devices to achieve the same functionalities. Moreover, the use of a single tunable device will also reduce the total size and the cost of the whole RF and microwave system.

The tunable devices for RF and microwave applications are realized by incorporating special type of tuning elements into them. The most widely and commercially used tuning elements include: semiconductors (varactor diodes, PIN diodes, and transistor), micro-electro-mechanical systems (MEMS), ferroelectrics materials, and ferromagnetic materials. Each of these tuning elements or techniques has their own advantages and disadvantages. Their use largely depends upon, the required type of tunability (discrete or continuous), operating power, design frequency, and also manufacturing complexity and total cost.

In this Ph.D. thesis, using ferromagnetic material and SIW technology new types of tunable components and devices are proposed, developed and demonstrated. Originally, rectangular waveguides were used in order to realize number of ferrite based non-reciprocal devices including circulators [Fay, et al. (1956)] and resonant cavities [Fay, et al. (1965)]. There could have been several reasons, why metallic waveguides were always chosen to be used together with ferrite materials. Metallic hollow waveguides are well known for their low-loss and high power handling properties. Ferrite materials are also popular tuning elements for high power applications. Therefore, a combination of metallic hollow waveguide and ferrite material would have yielded very useful non-reciprocal and tunable devices especially for high power applications. Thus, development of low-loss high power devices could have been a fundamental reason to associate ferrite material with rectangular waveguide. Although, ferrite loaded metallic

waveguides have many advantages including lower loss, high power handling capability, easy integration of ferrite and it's biasing, but due to their 3-dimensional geometry they cannot be easily integrated into planar circuits. The modern day communication systems require RF and microwave circuits not only to be lighter in weight but also they are required to have planar form to be integrated with other circuitries. Therefore, it is a purpose of this thesis to realize a magnetically tunable ferrite loaded components and devices that inherit all the properties of rectangular metallic waveguide and also at the same time it is planar in nature. Since, SIW is a planar or two-dimensional form of rectangular waveguide, it is chosen for the realization of magnetically tuned devices. Planar polycrystalline ferrite slabs are inserted or fitted inside the SIW devices to realize magnetically tunable planar microwave components and devices for high power applications.

In this work, number of microwave components and devices based on ferrite loaded SIW were presented. As a first step, a magnetically tunable ferrite loaded SIW cavity resonator was presented. The design of magnetically tunable cavity resonator was very important in order to understand the behaviour of SIW when it is loaded with ferrite material. From both theory and measurement it was observed that, when the cavity loaded with ferrite material is applied with static magnetic bias, the resonant frequency of the cavity had a tendency of shifting towards higher frequency values. It was noticed that this shift was non-linear in nature. The measurements were performed for one, two and four-ferrite slabs loaded cavity resonators. The measurement results indicated increasing the effective area of the ferrite slab also increases the total frequency tuning range. For the four ferrite slabs loaded cavity resonator, the frequency up to 16% was measured. The design of the ferrite loaded cavity resonator provided valuable information about total losses, frequency tuning range and physical design requirements.

A cavity resonator is a basic building block of any microwave system design. It can be used as a foundation circuit, and all other system`s components and devices can be derived from it. In this work, the tunable SIW cavity resonator was further developed to realize other active and passive components and devices all working at 12 GHz.

One of the devices designed on the basis of magnetically tunable cavity resonator was a tunable feedback-loop oscillator. The oscillator consisted of ferrite loaded magnetically tunable cavity resonator, which was connected between input and output ports of an amplifier. The frequency of

oscillation was tuned to higher frequency value by the application of DC magnetic bias on the ferrite loaded cavity resonator. A biasing mechanism was proposed, which consisted of a U-shaped soft iron metal connected between the two ferrite slabs. A similar soft iron metal plate was also soldered on the bottom of the substrate, to create a return path for the magnetic field. Copper solenoid was wounded around the metal core. To produce the magnetic field in the soft metal core, the two terminals of the wire was connected to the power supply. It was also demonstrated, that by replacing the DC current supplied on the metal core with AC, the oscillator output frequency was modulated by the frequency of the applied AC current source. The designed oscillator can be used as a signal generator for FMCW radar applications.

The proposed and demonstrated SIW based magnetically tunable devices exhibited very promising performances at the design frequency of 12 GHz. However, it was noticed that at highest value of applied magnetic bias ($H_0 = 0.4$ T and beyond), their performances started to degrade gradually. In the case of cavity resonator, there was a significant reduction in the magnitude of the resonance peak values. In the case of tunable band pass filter, the total frequency tuning range was limited due to the degradation of the filter shape and bandwidth. In order to improve the performance of magnetically tunable devices, a new concept of simultaneous electric and magnetic two-dimensional tuning was introduced.

With the new concept of two-dimensional tuning, electric and magnetic field components are simultaneously tuned to achieve the highest performance quality. Again SIW cavity resonator was considered to demonstrate and validate the concept of two-dimensional tuning. Planar ferrite slabs were loaded along the sidewall slots of the cavity, while a lumped capacitance was placed near the central region of the cavity where the electric field strength is highest. It was demonstrated that with the simultaneously changing the values of applied magnetic bias and the capacitance, the total frequency tuning range of the cavity was increased by two-folds. The same concept was also implemented on a band-pass filter, which was realized by cascading the two cavities together. This time, varactor diodes were connected along the central region of the cavity to achieve the desired electrical tuning. With the simultaneously changing the electric and magnetic fields applied on varactor diodes and ferrite slabs, a frequency tunable constant bandwidth as well as constant frequency tunable bandwidth filters were realized and successfully demonstrated. The same concept was also applied to enhance the total frequency tuning range of a cavity backed antenna.

The magnetically as well as simultaneous magnetically and electrically tunable devices mentioned above do not display any non-isotropic properties. In this work, the non-reciprocal aspects of ferrite loaded SIW devices were also investigated. To begin with, a simple non-reciprocal transmission line consisting of a single ferrite loaded SIW was demonstrated. Two separate ferrite materials (Nickel ferrite and YIG) with different value of magnetization were considered to investigate the non-reciprocal behavior. It was noticed, that the material with the higher saturation magnetization produces higher value of differential phase shifts when applied with the same value of magnetic bias. With Nickel ferrite, a differential phase shift of 180° was obtained for an applied magnetic bias of 0.16 T, while with YIG a differential phase shift of only 50 could be achieved. Using Nickel ferrite a four-port circulator was successful fabricated and demonstrated. The four-port circulator consisted of ferrite loaded non-reciprocal phase shifter (gyrator) and two 3-dB couplers. Isolations for more than 15 dB between each of the four ports were obtained.

As a final step, the concept of magnetic tuning was also implemented on HMSIW. From the geometry, HMSIW is symmetrically half of SIW. Therefore, it was interesting to compare the performance between magnetically tunable ferrite loaded SIW and HMSIW. From the measurement results, it was observed that HMSIW performance was very close and in some cases even better than that of SIW in terms of losses, switching, and tuning. Similar to SIW, using a principal of electric and magnetic tuning a bandwidth tunable band-pass filter was successfully demonstrated.

In this work, a novel magnetically tunable microwave components and devices are developed and demonstrated using SIW technology. The performances of the magnetically tunable devices were further enhanced by incorporating both electric and magnetic tuning on the single device. The designed tunable and non-reciprocal circuits, components and devices are very useful in the realization of high power communication and radar system designs.

Outlook:

The proposed concept of one-dimensional and two-dimensional tuned SIW devices can be further used in the realization of many other interesting microwave applications. Some of the possible components and devices that could be realized are listed and explained below:

Latched phase shifters: By using ferrite materials with high value of remnant magnetization, a latched phase shifters can be realized. The realized phase shifter will be able to produce the desired phase shifts with minimum energy consumption.

High power applications of ferrite: A ferrite material displays a non-linear behaviour when applied with high power microwave signals. The high power property of ferrite can be explored to realize interesting non-linear devices including parametric amplifier.

Other 2D and 1D tuned devices: In this thesis, not all the tunable devices using the concept of 1D and 2D tuning were realized. Some of the other 2D tuned devices which could be realized include: travelling wave antennas, waveguide slot antennas, self-oscillating mixers, 2D-tuned oscillator to realize AM and FM modulations.

Biasing circuit: The presented biasing circuit can be further improved by reducing the remnant magnetization produced in the coil.

System realization: A system totally based on ferrite loaded SIW can be realized. The designed will be a first of its kind, which will consist of 1D- and 2D- tuned devices integrated together to produce an entire system.

REFERENCES

Abbaspour, T., Dussopt, L., and Rebeiz, G. M. (2003), «Miniature and tunable filters using MEMS capacitors», *IEEE Transactions on Microwave Theory and Techniques*, vol. 51, no. 7, pp. 1878-1885.

Aharoni, A. (1998), «Demagnetizing factors for rectangular ferromagnetic prisms», *Journal of Applied Physics*, vol. 83, no. 6.

Armendariz, M., Sekar, V., and Entesari, K. (2010), «Tunable SIW band-pass filters with PIN diodes», *Proceedings of European Microwave Conference*, pp. 830-833.

Bakhit, A. A., and Wong, P. W. (2013), «Switchable microwave band-stop to all phass filter using stepped impedance resonator», *Progress in Electromagnetics Research*, vol. 52, pp. 99-115.

Boyd, C. R. (1971), «An accurate analog ferrite phase shifter», *IEEE MTT-S Microwave Symposium Digest* 1971, pp. 104-105.

Bray, J. R., and Roy, L. (2004) «Development of a millimeter-wave ferrite-filled anti-symmetrically biased rectangular waveguide phase shifter embedded in low-temperature co-fired ceramic», *IEEE Transactions on Microwave Theory and Techniques*, vol. 52, no. 7, pp. 1732-1739.

Brito-Brito, Z., Llamas-Garro, I., Pradella-Cara, L, Corona-Chavez, A. (2008), «Microstrip switchable bandstop filter using PIN diodes with precise frequency and bandwidth control», *Proceedings of European Microwave Week (EUMA)*, pp. 1707-1711.

Carter, P. S. (1961), «Magnetically-tunable microwave filters using single-crystal Yttrium-Iron-Garnet resonators», *IRE Transactions on Microwave Theory and Techniques*, vol. 9, pp. 252-260.

Cassivi, Y., Wu, K. (2003), «Low cost microwave oscillator using substrate integrated waveguide», *IEEE Microwave and Wireless Component Letters*, vol. 13, no. 2, pp. 48-50.

Chan, K. Y., Fouladi, S., Ramer, R., and Mansour, R. R. (2012), «MEMS switchable interdigital band-pass filter», *IEEE Microwave and Wireless Component Letters*, vol. 22, no. 1, pp. 44-46.

Chandler, S.R., Hunter, I.C., and Gardiner, J.G. (1993), «Active varactor tunable band-pass filter», *IEEE Microwave and Guided Wave Letters*, vol. 3, no. 3, pp. 70-71.

Collins, R. E. (1960), *Field theory of guided waves*, McGraw-Hill Book Company, ch. 3, pp. 248-253.

Courreges, S., Li, Y., Zhao, Z., Choi, K., Hunt, A. T., and Papapolymerou, J. (2009), «Two-pole X-band-tunable ferroelectric filters with tunable center frequency, fractional bandwidth and return loss», *IEEE Transactions on Microwave Theory and Techniques*, vol. 57, no. 12, pp. 2872-2881.

D'Orazio, W., and Wu, K. (2006), «Substrate Integrated Waveguide circulators suitable for millimeter wave integration», *IEEE Transactions on Microwave Theory and Techniques*, vol. 54, no. 10, pp. 3675-3680.

Djoumessi, E. E., Tatu, S. O., and Wu, K. (2010), «Frequency-agile dual-band direct conversion receiver for cognitive radio systems», IEEE Transactions on Microwave Theory and Techniques, vol. 58, no. 1, pp. 87–94.

Fay, C. E., (1956), «Ferrite tuned resonant cavities», *Proceedings of the IRE.*, vol. 44, pp. 1446-1449.

Fay, C. E., and Comstock, R. L. (1965), «Operation of the ferrite junction circulator», *IEEE Transactions on Microwave Theory and Techniques*, vol. 13, no. 1, pp. 15-27.

Fourm, E., et al. (2003), «Bandwidth and central frequency control on tunable band-pass filter by using MEMS cantilevers», *IEEE MTT-S International Microwave Symposium Digest*, vol. 1, pp. 523-526.

Fukuda, A., Kawai, K., Furuta, T. and Narahashi, S. (2007), «MEMS-based reconfigurable RF circuits for future mobile terminals», in *Asia–Pacific Microwave Conference.*, pp. 1–4.

Fuller, A. J. B. (1987), *Ferrites at Microwave Frequencies*, Peter Peregrinus Ltd., pp. 226.

Gardiol, F.E., *Introduction to Microwaves*, Artech House Publishers, 1983.

He, F., Chen, X-P., Wu, K., and Hong, W. (2009), «Electrically tunable substrate integrated waveguide reflective cavity resonator», *Asia Pacific Microwave Conference*, pp. 119-122.

He, F., Wu, K., Hong, W., Han, L., and Chen, X. (2010), «A low phase-noise VCO using an electronically tunable substrate integrated waveguide resonator», *IEEE Transaction on Microwave Theory and Techniques*, vol. 8, pp. 3452-3458.

Hong, W, et al. (2006), «Half mode substrate integrated waveguide: A new guide wave structure for microwave and millimeter wave application», *In Proceedings of Joint 31st Int. Conf. Infrared and Millimeter Waves and 14th International Conf. on Terahertz Electronics*, Shanghai, China, pp. 219.

Hunter, I. C., and Rhodes, J. D. (1982), «Electronically tunable microwave band-pass filters», *IEEE Transactions on Microwave Theory and Techniques*, vol. 30, no. 9, pp. 1354-1360.

Hwang, R.B., and Pan, J.L. (2007), «A band-pass filter using via hole-wall cavity», *Microwave and Optical Technological Letters*, vol. 9, pp. 1456-1459.

Jiang, H., Lacroix, B., Choi, K., Wang, Y., Hunt, A.T., and Papapolymerou (2012), «A compact ferroelectric tunable band-pass filter with flexible frequency responses», *IEEE International Conference on Wireless Information Technology and Systems (ICWITS)*," pp. 1-4.

Jones, G. R. (1956), «Magnetic tuning of resonant cavities and wideband frequency modulation of klystrons», *Proceeedings of the IRE*, vol. 44, pp. 1431-1438.

Joshi, H., Sigmarsson, Sungwook Moon, H. H., Peroulis, D., and Chappell, W. J. (2009), «High narrowband tunable filters with controllable bandwidth», *IEEE MTT-S International Microwave Symposium Digest*, Jun. 7–12, pp. 629–632.

Karim, M. F., Guo, Y-X., Chen, Z. N., and Ong, L. C. (2009), «Miniaturized reconfigurable and switchable filter from UWB to 2.4 GHz WLAN using PIN diodes», *IEEE MTT-S International Microwave Symposium Digest*, pp. 509-512.

Kim, J-M., et al. (2006), «Digitally frequency-controllable dual-band WLAN filters using micro-machined frequency-tuning elements», *IEEE International Conference on Micro-Electro-Mechanical Systems*, pp. 158-161.

Kim, J-M., Lee, S., Park, J-H., and Kim, J-M. (2005), «Low loss K-band tunable band-pass filter using micromachined variable capacitors», *Digest of Technical Papers in Solid-State Sensors, Actuators and Microsystems*, vol. 1, pp. 1071-1074.

Lax, B., Button, K. J.(1962), *Microwave ferrites and ferrimagnetics*, McGraw-Hill Book Company, ch. 4, pp. 154-155.

Lin., J., and Itoh, T. (1992), «Tunable active band-pass filters using three-terminal MESFET varactors», *Proceedings of IEEE MTT-S International Microwave Symposium*, pp 921-924, vol. 2, pp. 1-5.

Liu, B., Tian, L., Zhu, H-B., and Wu, K. (2006), «Half mode substrate integrated waveguide (HMSIW) multi-way power divider», *Proceedings of Asia Pacific Microwave Conference*, pp. 917-920.

Lourandakis, E., Schmidt, M., Fischer, G., and Weigel, R. (2009), «A ferroelectric tunable combline filter with improved stopband transitions», *IEEE Radio and Wireless* Symposium, pp. 340-343.

Lugo, C., and Papapolymerou J. (2004), «Electronic switchable band-pass filter using PIN diodes for wireless low cost system-on-a-package applications», *IEE Proceedings on Microwave Antenna and Propagation*, vol. 151, no. 6.

Luo, G. Q., Hu, Z. F., Dong, L. X. , and Sun, L. L., (2008), «Planar slot antenna backed by substrate integrated waveguide cavity», *IEEE Antennas Wireless Propag. Lett.*, vol. 7, no. 8, pp. 236–239.

Makimoto, M., and Sagawa, M. (1986) «Varactor tuned band-pass filters using microstrip-line ring resonators», *IEEE MTT-S International Microwave Symposium Digest*, pp. 411-414.

Matthaei, G. L., Young, L. and Jones, E. M. T. (1964), *Microwave Filters, Impedance-Matching Networks, Coupling Structures*. Norwood, MA: Artech House, pp. 1001–1014.

Meskoob, B., and Prasad, S. (1992), «Loop-gain measurement and feedback oscillator design», *IEEE Microwave and Guided Wave Letters*, vol. , no. 9, pp 375-377.

Moon, H-U., Choi, S-U., Cho, Y-H., Yun, S-W. (2008), «Size-reduced tunable hairpin band-pass filter using aperture coupling with enhanced selectivity and constant bandwidth», *IEEE MTT-S International Microwave Symposium*, pp. 747-750.

Murakami, Y., Ohgihara, T., and Okamoto, T. (1987), «A 0.5-0.4-GHz tunable band-pass filter using YIG film grown by LPE», *IEEE Transactions on Microwave Theory and Techniques*, vol. 35, pp. 1192-1198.

Musoll-Anguiano, C., Llamas-Garro, I., Brito-Brito, Z., Pradell, L., and Corona-Chavez, A. (2002), «Fully adaptable band-stop filter using varactor diode», *Microwave and Optical Technological Letters*, vol. 52, pp. 554-558.

Norwood, M. H., and Shatz, E (1968), «Voltage variable capacitor tuning: A review», *Proceedings of the IEEE*, vol. 56, no. 5.

Oates, D. E., Dionne, G. F., and Slattery, R. L. (2009), «Voltage tunable microwave filter resonator», *IEEE MTT-S International Microwave Symposium Digest*, pp. 641-644.

Ocera, A., Farinelli, P., Mezzanotte, P., Sorrentino, R., Margesin, B., and Gaicomozzi (2006), F., «A novel MEMS-tunable hairpin line filter on silicon substrate», *Proceedings of European Microwave Conf.*, pp. 803-806.

Ouaddari, M., Delprat, S., Vidal, F., C., Mohamed, and Wu, K. (2005), «Microwave characterization of ferroelectric thin-film materials», *IEEE Transactions on Microwave Theory and Techniques*, vol. 53, no. 4, pp. 1390-1397.

Pantoli, L., Stornelli, V., Leuzzi, G. (2012), «A single-transistor tunable filter for bluetooth applications», *Proceedings of European Microwave Integrated circuits Conference*, pp. 889-892.

Papapolymerou, J., Lugo, C., Zhiyong, Z., and Wang, X. (2006), «A miniature low-loss slow-wave tunable ferroelectric band-pass filter from 11-14 GHz», *IEEE MTT-S International Microwave Symposium Digest*, pp. 556-559.

Park, J-H., Lee, S., Kim, J-M., Kim, H-T., Kwon, Y., and Kim, Y-K. (2005), «Reconfigurable millimeter-wave filters using CPW-based periodic structures with novel multiple-contact MEMS switches», *Journal of Microelectromechanical Systems*, vol. 14, no. 3.

Popov, M. A., Murthy, D.V.B., Zavislyak, I.V., and Srinivasan, G. (2012), «Magnetic field tunable 18-36 GHz dielectric band-pass filter», *Electronic Letter*, vol. 48, no. 2, pp. 98-99.

Pozar, D. (2005), *Microwave Engineering*, New York Wiley, 3rd edition, pp. 441.

Rhea, R.W. (2010), *Discrete Oscillator Design*, Artech House 2010, pp 11.

S. L., Delprat, C., Durand, J., Oh, M., Chaker, and Wu, K. (2007), «Correlation between the lattice parameter and the dielectric tunability in nonepitaxial Ba0.5Sr0.5TiO3 thin films», *Applied Physics Letters*, vol. 91, pp. 063513-063513-3.

Sekar, V., Armendariz, M., and Entesari, K. (2011), «A 1.2-1.6 GHz substrate-integrated-waveguide RF MEMS tunable filter», *IEEE Transactions on Microwave Theory and Techniques*, vol. 59, no. 4, pp. 866-876.

Senior, D. E., et. al (2012), «Electrically tunable evanescent mode half-mode substrate integrated-waveguide resonators», *IEEE Microwave and Wireless Comp. Letters*, vol. 22, no. 3, March 2012.

Sirci, S., Martinez, J. D., and Boria, V. E. (2013), «Low-loss 3-bit tunable SIW filter with PIN diodes and integrated bias network», *Proceedings of the European Microwave Conference*, pp. 1211-1214.

Soohoo, R. F. (1959), «A ferrite cut-off switch», *IRE Transaction on Microwave Theory and Techniques*, vol. 7, no. 3, pp. 332-336.

Swartz, G. A., Wern, D. W., and Robinson, P. H. (1980), «Large-area varactor diode for electrically tunable, high-power UHF band-pass filter», *IEEE Transactions on Electron Devices*, vol. 27, no. 11, pp. 2146-2151.

Tai, C. S., and Qiu, G. (2009), «Wideband microwave filters using ferromagnetic resonance tuning in flip-chip YIG-GaAs layer structures», *IEEE Transactions on* Magnetics, vol. 45, pp. 656-660.

Tatarenko, A. S., Gheevarughese, V., and Srinivasan, G. (2006), «Magnetoelectric microwave band-pass filter», *Electronics Letters*, pp. 540-541, vol. 42.

Torregrosa-Penalva, G., Lopez-Risueno, G. and Alonso, J. I. (2002), «A simple method to design wideband electronically tunable combline filters», *IEEE Transactions on Microwave Theory and Techniques*, vol. 50, no. 1, pp. 172–177.

Uher, J., Bornemann, J., and Arndt, F. (1988), «Tunable microwave and millimeter-wave band-pass filter», *IEEE Transactions on Microwave Theory and Techniques*, vol. 36, no. 6, pp. 1014-1022.

Wang, Y., Hong, W., Dong, Y., Liu, B., Tang, H. J., Chen, J., Yin, X., and Wu, K. (2007), «Half mode substrate integrated waveguide band-pass filter», *IEEE Microwave and Wireless Components Letters*, vol. 17, no. 4, pp. 265-267.

Wu, K., Deslandes, D., Cassivi, Y. (2003), «The substrate integrated circuits – a new concept for high-frequency electronics and optoelectronics», International Conference on *Telecommunication in Modern Satellite, Cable and Broadcasting Service*, pp. 2-9.

Xu, R. F., Izquierdo, B. S., and Young, P. R. (2011), «Switchable substrate integrated waveguide», *IEEE Microwave and Wireless Component Letters*, vol. 21, no. 4, pp. 194-196.

Yang, G.-M., Lou, J., Wu, J., Liu, M., Wen, G., Jin, Y., and Sun, N. X. (2011), «Dual - and -field tunablemultiferroic band-pass filterswith yttrium iron garnet film», *IEEE MTT-S International Microwave Symposium Diest*, pp. 1-4.

Yi, C. C., and Rebeiz, G. M. (2011), «A tunable three-pole 1.5-2.2 GHz band-pass filter with bandwidth and transmission zero control», *IEEE Transaction Microwave Theory Techniques*, vol. 59, no. 11, pp. 2872-2878.

Yu, F. L., Zhang, X. Y., and Zhang, Y. B. (2012), «Frequency-tunable band-pass filters with constant absolute bandwidth and improved linearity», *Progress in Electromagnetics Research Letters*, vol. 33, pp. 131-140.

Zhang, N., Deng, Z., and Sen, F. (2013) «CPW tunable band-stop filter using hybrid resonator and employing RF MEMS capacitors», *IEEE Transactions on Electron Devices*, vol. 60, no. 8, pp. 2648-2655.

Zhang, X. Y., Chan, C. H., Xue, Q., and Hu, B.-J. (2012), «RF tunable band stop filters with constant bandwidth on a doublet configuration», *IEEE Transactions on Microwave Theory Techniques*, vol. 59, no. 2, pp. 1257–1265.

APPENDIX 1 – LIST OF PUBLICATIONS & AWARDS

1. Peer-reviewed journal publications

1.1 Published papers

[J1] **S. Adhikari**, and K. Wu, "Developing One-Dimensional Electronically Tunable Microwave and Millimeter-Wave Components and Devices towards Two-Dimensional Electromagnetically Reconfigurable Platform", ***Progress In Electromagnetics Research***, 143, 821-848, 2013.

[J2] K. Wang, **S. Adhikari**, A. Ghiotto, K. Wu, "Multiharmonic Generator for Large-Signal-Network-Analyzer Verification", ***IEEE Microwave Magazine***, vol.15, no.1, pp.120,128, Jan.-Feb. 2014.

[J3] **S. Adhikari**, A. Ghiotto, K. Wu, "Simultaneous Electric and Magnetic Two-Dimensionally Tuned Parameter-Agile SIW Devices", ***IEEE Transactions on Microwave Theory and Techniques***, vol.61, no.1, pp. 423-435, January 2013.

[J4] **S. Adhikari**, A. Ghiotto, K. Wang, K. Wu, "Development of a Large-Signal-Network-Analyzer Round-Robin Artifact", ***IEEE Microwave Magazine***, vol.14, no.1, pp.140-145, Jan.-Feb. 2013.

[J5] A. Ghiotto, **S. Adhikari**, K. Wu, "Ferrite-Loaded Substrate Integrated Waveguide Switch", ***IEEE Microwave and Wireless Component Letters***, Volume 22, Issue 3, Pages 120-122, March 2012.

[J6] **S. Adhikari**, Y-J Ban and K. Wu, "Magnetically Tunable Ferrite Loaded Substrate Integrated Waveguide Cavity Resonator," ***IEEE Microwave and Wireless Components Letters***, vol.21, no.3, pp.139,141, March 2011.

2.2 Submitted papers

[J7] **S. Adhikari**, S. Hemour, A. Ghiotto, K. Wu, "Magnetically Tunable Ferrite Loaded Half Mode Substrate Integrated Waveguide", ***IEEE Microwave and Wireless Component Letters***, Submitted on March 2014.

[J8] **S. Adhikari**, A. Ghiotto, C.-W. Park, and K. Wu, "Self-Packaged Magnetically Tunable and Frequency Modulated Substrate Integrated Waveguide Oscillator for High-Power Applications", ***IEEE Transactions on Components, Packaging and Manufacturing Technology***, Submitted on February 2014.

2. Conference papers

[C1] S. Hemour, **S. Adhikari**, A. Ghiotto, K. Wu, "Low magnetic biased SIW-based isolator -- Effect of the rising temperature on the performance of the isolator", ***IEEE Wireless and Microwave Technology Conference***, Tampa, June 2014.

[C2] **S. Adhikari**, A. Ghiotto, S. Hemour, K. Wu, "Tunable Non-Reciprocal Ferrite Loaded SIW Phase Shifter", ***IEEE MTT-S International Microwave Symposium (IMS2013)***, Seattle, 2-7 June 2013.

[C3] **S. Adhikari**, A. Ghiotto, K. Wu, "Low-cost frequency modulated ferrite loaded SIW oscillator for high-power microwave transmitter", ***IEEE MTT-S International Microwave Symposium (IMS2013)***, Seattle, 2-7 June 2013.

[C4] **S. Adhikari**, A. Ghiotto, K. Wu, "Simultaneous Electric and Magnetic Two-Dimensional Tuning of Substrate Integrated Waveguide Cavity Resonator", ***IEEE MTT-S International Microwave Symposium (IMS2012)***, Montreal, 17-22 June 2012.

[C5] A. Ghiotto, **S. Adhikari**, K. Wu, E. Kerhervé, "Atténuateur micro-onde réflectif variable basé sur un guide d'onde intégré au substrat chargé de ferrite", ***18èmes Journées Nationales Microondes***, Paris, 14-17 Mai 2013.

3. Awards

[A1] **MTT-S 2013 Graduate Fellowship** from the IEEE Microwave Theory and Techniques Society.

[A2] **First prize** in the student design competition of a Large-Signal-Network-Analyzer Round-Robin Artifact at the IEEE MTT-S International Microwave Symposium 2013, Seattle, June 2013.

[A3] **Best Student Paper Finalist** at the 2012 International Microwave Symposium of the IEEE Microwave Theory and Techniques Society.

[A4] **First prize** in the student design competition of a Large-Signal-Network-Analyzer Round-Robin Artifact at the IEEE MTT-S International Microwave Symposium 2012, Montreal, June 2013.